Infrared Thermography and Ultrasonics to evaluate porosity of Carbon Fibre Reinforced composites

Cinzia Toscano

Tesi di Dottorato in

Ingegneria Aerospaziale

Università degli Studi di Napoli

Federico II

Scuola di Dottorato in Ingegneria Industriale

Dottorato di Ricerca in Ingegneria Aerospaziale, Navale e della Qualità

Ciclo XXIV

Indirizzo Ingegneria Aerospaziale

Coordinatore Chiar.mo Prof. Luigi De Luca

Relatore Ing. Carosena Meola

Tutor Ing. Stefania Cantoni

Quando l'acqua sale, il pesce mangia la formica;
quando l'acqua scende, la formica mangia il pesce.
(Proverbio Thailandese)

Acknowledgements

First of all my thanks go to CIRA and to the Department of Aerospace Engineering of University of Naples Federico II for allowing me to perform the present thesis.

I would like to express my deep and sincere gratitude to my supervisor Ing. Meola for her infinite patience, her participation and closeness.

My heartfelt thanks goes to Lorenzo for his lively critical attitude, his support and also for the simple fact of being there.

I would like to thank Ing. Maria Chiara Iorio for her help during the first part of the research.

My special thanks go to my "Matlab consultant" Ing. Giancarlo Totaro and also to Dott.ssa Angela Ferrigno for her help with optical microscopy.

This research would not have been possible without the courtesy of Flir® and Roberto Rinaldi, who provided me with the flash system.

Heartfelt thanks go to everyone who even when things seemed to go wrong, has supported me and encouraged me, especially my supervisor Ing. Meola and my chief in CIRA, Ing. Felice De Nicola.

Finally, thanks to the "dance room" and all my friends who gave me "oxygen" and cheerful times in the most difficult moments.

Contents

Introduction

The present dissertation is conceived as part of research and technological innovation activities performed at the Advanced Materials & Technology laboratory of the Italian Aerospace Research Centre (CIRA). This laboratory, among other tasks, is involved in developing new manufacturing methodologies for the production of composites for aeronautical applications. Such a purpose is pursued with both numerical and experimental approaches and, often, with an integrated approach. The experimental output may serve as input to numerical models for the ultimate design of the material fabrication process and numerical models may help in optimizing the experimental activities. Once a component is produced, specific testing (mechanical, chemical, thermal, etc.) follows in order to optimize the material ingredients (type of matrix and reinforce as well as stacking sequence), the manufacturing process (hand lay-up, filament winding, etc.) and the curing cycle.

In this context, non-destructive testing plays a fundamental role. In fact it allows, at the end of the manufacturing process, to non-invasively verify the integrity of the produced components as well as their compliance with the design requirements; usually this is the first feedback about the quality of the product. Non destructive testing also acts as support and complement to the mechanical tests, because it allows also to verify whether the component has been damaged as a consequence of the applied mechanical load.

The procedure described above is usually adopted also by composites manufacturing companies for the optimization and fine tuning of the production processes, as well as for the quality control of final products.

In this context, CIRA, already equipped with instrumentation and trained personnel for non-destructive testing with the Ultrasonic technique (UT), has, recently, decided to investigate the suitability of InfraRed Thermography (IRT), attracted by the considerable advantages offered by such a remote 2D and fast inspection technique. To venture into this new field CIRA decided to promote and fund a PhD in cooperation with the Department of Aerospace Engineering

of the University of Naples, Federico II, under the guidance of Ing. Carosena Meola who is a well-recognized expert in this field, both in Italy (member of ITANDTB and UNI commissions) and abroad (member of European Committee CEN/TC).

InfraRed Thermography is currently adopted in aeronautics in order to check the integrity of the components, allowing easily and rapidly the inspection even of large surfaces. On the other hand, its employment is still somehow limited, due to a partial assessment and due to the lack of an exhaustive validation. Specifically the IRT capability to provide a quantitative estimation of porosity is still not completely validated by an extensive comparison with the Ultrasonic method which is actually the most adopted technique. The possibility to use IRT instead of UT is of great interest because it allows a contactless inspection without any use of contaminating substances, which potentially may penetrate porous materials.

The main objective of this dissertation is to contribute to the assessment of infrared thermography as technique to be used to estimate the porosity amount and its distribution in a carbon/epoxy composites, as well as detect thin delaminations in presence of porosity. The ultimate goal is to setup an experimental arrangement and testing protocol to be used in the industrial processes for fast and effective evaluation of the porosity content in composites.

It is worth noting that porosity, depending on its volumetric percentage and on shape and size of pores, can greatly reduce the mechanical properties as well the overall performance of composites. On the other hand, as can be seen from literature it is possible to affirm that, although UT is the most commonly used non-destructive method, it suffers from some limitations in presence of a porous medium. In general, results depend on the used equipment and method as well as on the material under analysis and its manufacturing process. Therefore, UT is most effective when associated to consolidated and repetitive manufacturing processes. In addition, UT may be affected by many problems linked to the surface finishing and it is not effective in presence of a porous surface.

Recently, scientific literature highlighted IRT, in particular flash thermography, as a promising alternative of the UT for porosity measurements.

The use of flash thermography is therefore herein investigated as a method to infer measurements of porosity through measurements of thermal diffusivity.

The approach and the results discussed in this dissertation may be of considerable utility for aeronautical companies that deal with production of CFRPs. In fact, flash thermography is a simple and fast (potentially a few seconds more than the time needed to take a picture) to be used for estimation of the percentage of porosity within the material. This can be achieved by simply performing a calibration process (analogous to the one herein described) for each specific material under analysis. Moreover, flash thermography allows also to discover different types of discontinuities in the material, such as inclusions and delaminations.

With regard to the content of the present dissertation, it is subdivided into different Chapters. The first Chapter gives a look at the world of composites and at the standard non destructive testing techniques which are used in the aeronautical industry. Further, the problem of the presence of porosity in CFRP is addressed with also a description of the consequences it entails from the component mechanical performance point of view. In the subsequent Chapters 2 and 3, the two non-destructive techniques, UT and IRT, are described from both theoretical and experimental points of view. Chapter 4 introduces to the core of the experimental activity, which continues on Chapters 5 and 6. In particular, a section of Chapter 4 is devoted to the description of specimens, which are specifically manufactured with a certain percentage of porosity and with also a thin kapton disk to simulate a local delamination. The porosity amount is then estimated through destructive and non-destructive methods; in particular, results obtained with UT and IRT are shown and discussed in Chapters 5 and 6.

Chapter 1

Composite materials: manufacturing methods and characterization

In the last years, the word *composite* became of very common use. In fact, composite materials are being ever more massively employed in automotive, aerospace and naval structures components. The success of composites is mainly related to their involved possibility to both choose the raw materials and, to conceive the production process so as to obtain a final product that is perfectly responding to the design requirements.

Among the broad variety of composites, Carbon Fibre Reinforced Polymers (CFRP) are amongst the most used ones in military as well as in civil aviation, for both primary and secondary structures. In civil aviation they are highly appreciated especially for their favourable stiffness to weight ratio, because it involves a significant decrease of the fuel burnt per seat, per mile and, as a consequence, airlines have achieved to substantially reduce CO_2 emissions, which complies with the modern need of the environment preservation. Moreover, CFRP provide the answer to specific issues such as the need of improvement of the passengers comfort, related to the noise level on departure and landing.

Due to the complex processes required for CFRP production, special care is devoted to the monitoring of the involved parameters, especially in the aeronautical industry where very high quality levels are required. Actually, during the manufacturing process, some defects, like delamination and/or porosity, may be induced in the composite structure. In particular, pores may act as starting sites for formation of cracks in service. However, whichever the type of defect, it may unpredictably grow when the component (like a vehicle structure) undergoes the typical loading of the life in service. Of course, this makes the manufactured structure potentially dangerous if flaws are not pre-

emptively detected and evaluated. Besides, flaws in composites may occur on aircraft components, during either take-off or landing, when small debris are raised against the vehicle, or during maintenance operations, due to drop of tools on the structure. This is why Non Destructive Evaluation (NDE) is nowadays a fundamental need both for quality assessment in industrial production, as well as a mean for defect characterization in order to comply with specific part rejection criteria.

Generally, under the term NDE, several methodologies, competencies as well as instruments are included, all having in common the characteristic of allowing inspection of materials without damaging them. Some of the NDE techniques, which are largely used in aeronautics especially the standardized ones, will be illustrated in a section to follow (sect. 1.3).

1.1 Some basics on composites technology

Materials, which are nowadays mostly employed in industrial applications, can be grouped into three main families: ceramics, metals and polymers. In order to enhance the properties of a single material, two or more of them can be combined to obtain a new material, which is generically called composite material [1,2]. Most kind of composites [3,4] are obtained by inserting a fibrous, or particulate material (reinforce) within a matrix, so as to form a relatively homogeneous structure.

Composites can be classified owing to the type of matrix used, as: Ceramic Matrix Composites (CMC), Polymeric Matrix Composites (PMC) and Metal Matrix Composites (MMC). Some of them are often named as "advanced" because of their enhanced properties as compared to the more traditionally used structural materials, like aluminum and steel. Composites are very attractive not only for their superior properties, but especially for their versatility. Indeed, once specific structural and mechanical requirements are assigned, the composite material can be *ad hoc* designed. In the past, designers were accustomed to start with the raw material and after to select a consolidate manufacturing process to obtain the desired component. The introduction of composite materials changed this approach: once the shape and the purpose of a component are assigned, both the raw materials to be used and the manufacturing process are conceived and fitted to match the required characteristics. Moreover, due to the composite inhomogeneous nature, some properties can be strongly not isotropic, so the reinforcement location or orientation, as well as its density, can be chosen depending on the final loads distribution foreseen during their use.

Ceramic [5] is particularly appreciated for its resistance to aging and to high temperatures. Conversely, it is brittle: defects in its microstructure could be responsible for the formation of micro-cracks which can unpredictably grow under load, so affecting the component overall effectiveness. Different techniques have been used to reinforce this type of material. In particular, in the

aerospace field, ceramic is often reinforced with carbon fibres, as in the Thermal Protection System (TPS) used in the Discovery nose that is shown in Fig.1.1. A very typical TPS material is carbon-reinforced silicon carbide (C/SiC), which combines the superior strength and stiffness of carbon fibres at high temperatures with a more oxidation resistant matrix [7,8].

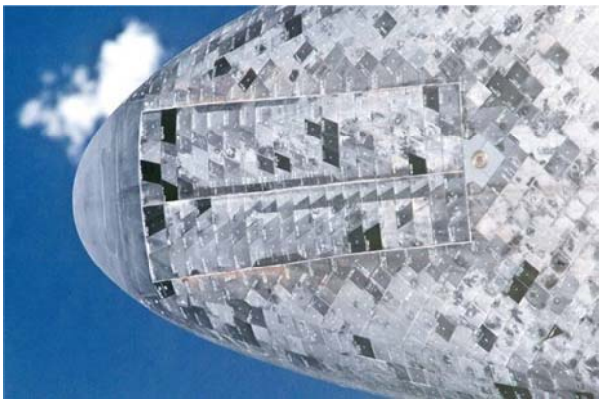

Figure 1.1**: The underside of the nose of Discovery (NASA) [6]. TPS tiles are clearly visible.**

MMCs are composed of a metal matrix and a reinforcement, or filler material, which confers excellent mechanical performance [9]. Aluminum and its alloys are the mostly used matrix component, but magnesium and titanium are used too. The reinforce is generally made of particles, or fibres, of silicon carbide or graphite. They are particularly appreciated for their enhanced specific strength and stiffness, low density and high temperature strength. Magnesium matrix composites are used for manufacturing aircraft parts for gearboxes, transmissions, compressors and engine. Titanium Matrix Composites are used for manufacturing structural components of the F-16 jet's landing gear [9] and turbine engine components (fan blades, actuator pistons, synchronization rings, connecting links, shafts and discs). Moreover, in the aerospace field, Al-SiC, Al-B, Mg-C, Al-C, Al-Al2O3, with either continuous or discontinuous strengthening, are widely used for frames, reinforcements and aerials joining elements [11].

PMCs are conceived in such a way that the reinforce provides the stiffness and rigidity which is missed in the lonely polymeric matrix material [12]. In these composites, the reinforce is mainly demanded to carry the load whereas the

matrix keeps together the constituents of the reinforcement and distributes the loads. PMC could be divided in two types: reinforced plastics and advanced composites; the latter possess higher mechanical properties. Reinforced plastics are generally made of polyester resins and glass fibres, are cost effective and widely used for boat hull, corrugated plates, pipes and automotive panels. Advanced composites are manufactured with a high density of continuous fibres which could be glass, aramid, or boron fibres. In the aeronautical industry, carbon fibres are the preferred reinforcement for primary load-bearing structures, because of the best combination of strength and cost provided.

1.1.1 Carbon Fibre Reinforced Polymers (CFRP)

Carbon fibres Reinforced Polymers, as their name indicates, are made of a polymeric matrix, like epoxy resin or other thermosetting materials, reinforced with carbon fibres obtained from graphite.

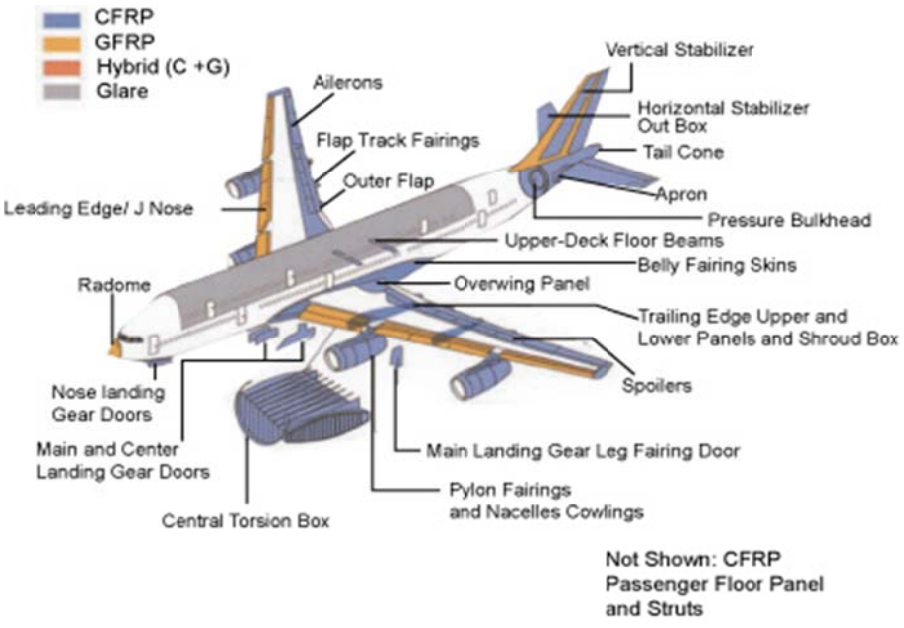

Figure 1.2: CFRP deployed for primary and secondary structures in Airbus A380.

CFRP are characterized by low weight and high strength. Some of these composites can be stronger than steel, but much more lighter. Because of this,

they can be used to replace metals in many applications, ranging from parts of racecars and space shuttle, to tennis rackets and fishing rods.

Fibrous composites have been used for military aviation components since 1960 and for civil aviation since 1970. During the 80's, fibrous composites have been used for a variety of secondary wing and tail components such as rudder and wing trailing edge panels.

In the 2000s a major breakthrough was achieved when Airbus launched the production of the A380 (fig. 1.2), the world's largest passenger aircraft, in which these materials have been deployed extensively in primary load carrying structures. In the A380, the 25% by weight is made of composites such as glass-fiber reinforced plastic and aluminum-glass-fiber laminate, and in particular, the central wing box is entirely made of CFRP.

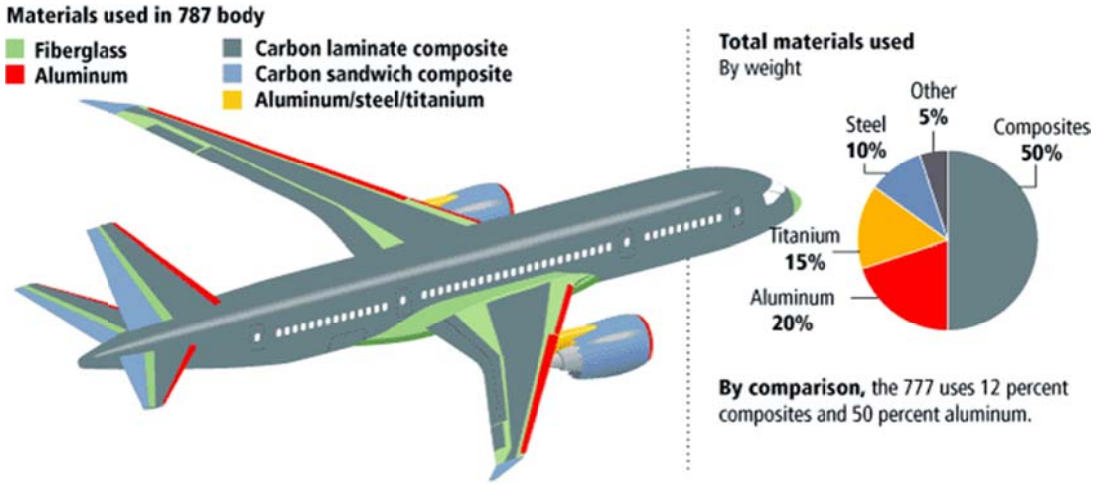

Figure 1.3: Boeing's Dreamliner composite materials employment.

Most recently, the Boeing 787 Dreamliner (fig. 1.3) has been conceived with almost 50% of composite materials, with the consequent 20% of fuel saving and 20% off of CO_2 emission [13]. However since their first application, composites exhibited many drawbacks when compared to metallic materials, in terms of type and occurrence of flaws from their production to their in-service life.

The duration of a metallic component is dependent on the possible formation of a crack and its growth. Linear elastic fracture mechanics is often adequate to develop models, which are able to define the size of critical flaws and, as a

consequence, to establish rejection/acceptance criteria of components on the basis of the designer requirements. On the contrary, CFRPs are strongly inhomogeneous and then, many models have been developed to describe their behavior related to embedded defects such as interlaminar deboding, matrix degradation, fiber rupture and total or partial separation of the matrix from the fibres [14].

At the moment, none model is able to completely describe the complexity of the failure starting point as well as its propagation in composites and, as a consequence, it is impossible to establish an *a priori* rejection/acceptance criterion. Consequently, a "Damage Tolerance" approach is preferred and continuously under development [15].

1.2 Main manufacturing techniques

Manufacturing processes of composites entail many parameters. Such parameters, together with the characteristics of the mixed materials have a strong influence on the quality of the final product and on its mechanical and structural properties.

In this section the most used manufacturing processes will be described with attention to the related problems that may induce formation of hidden defects.

CFRPs for structural application are often obtained by lamination of thin layers. This method allows choosing the orientation of the fibres and their percentage amount to deal with specific design requirements [16].

One of the most used manufacturing technique is the Lay-Up, which is based on the superimposition of pre-impregnated laminas, i.e. laminas of unidirectional or woven fibres partially impregnated with resin, of thickness in the range 0.125 ÷ 0.25 mm. These laminas are generally found in rolls or tapes then, they are cut and superimposed according to assigned shape and stacking sequence; the latter entails the orientation of fibres and the whole thickness. Once the laminas are stacked, a vacuum bag is applied and an autoclave cycle curing is performed. Generally, the curing cycle involves cooperation between temperature and vacuum in order to reach the correct viscosity level of the resin and to allow its flowing to achieve the correct fibres impregnation, as well as to take off the entrapped air or other gases.

Pre-preg laminas are expensive, to both buy and store; indeed in order to avoid room temperature curing of the resin, they require preservation in a cold chest at –18 ^{o}C. Moreover, autoclaves are expensive and pose limitation to production of very large or complex shape components. That is why new emerging manufacturing processes had entered the aeronautical manufacturing industry. In the following, some of the mostly used technologies are described.

- **Resin Transfer Molding**

Resin Transfer Molding, RTM (figure 1.3), is accomplished with two matched metallic molds in which a series of dry fiber plies are settled and kept together by stitching, or by binders. Then, the two molds are clamped together and heat and vacuum are applied in the cavity they generate [17,18]. A part from that, the resin is heated in order to reduce its viscosity so as to allow a better injection in the mold. The main advantages of RTM are the composite dimensions, which depend only on the mold shape.

The obtained composites have good surface finish on both sides and they are ready to be used without need of further processing. This process is cost effective to produce a large amount of components and thick parts. Many aerospace components are manufactured by RTM, such as door pillars, stringers, stiffened panels, rudder tips and ribs.

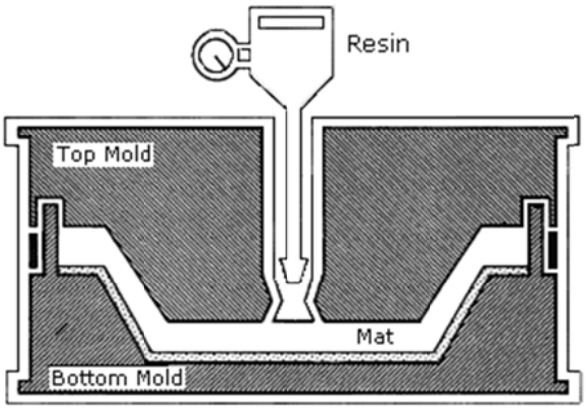

Figure 1.3: Typical RTM set up [19].

- **Resin Film Infusion**

Unlike RTM, this process requires just one male or female mold of the desired shape [20]. A thin film or sheet of pre-catalyzed solid resin is laid into the mold and the pre-form (in the shape of the desired part) is laid on the top of the resin film. The mold is hermetically closed by sealant tapes and then, vacuum is created through a vacuum bag. The resin is thermally cured in an oven, or in autoclave, while vacuum is applied. This process allows to reach high specific strength but generally, it is not used for manufacturing of structural parts.

Airbus A380 radar domes and rear pressure bulkheads are prepared with RFI [21]

- **Resin Infusion**

This process is similar to the Resin Film Infusion [22] with the difference that only dry fibres are put in the mold which is closed in a vacuum bag. With a pump, air is sucked off, and the liquid resin, stored in large mixing containers, migrates throughout the mold thanks to the existing vacuum. Once the resin saturates the entire stack of fibres, the vacuum is kept on for several hours until complete curing.

This process has been used since the 60's for the production of yacht parts. One of its main advantages resides in the possibility to produce large and thin parts, which has made this process attractive also for aerospace and transportation applications.

- **Filament winding**

This process requires tows of pre-impregnated fibres and a mandrel (figure 1.4).

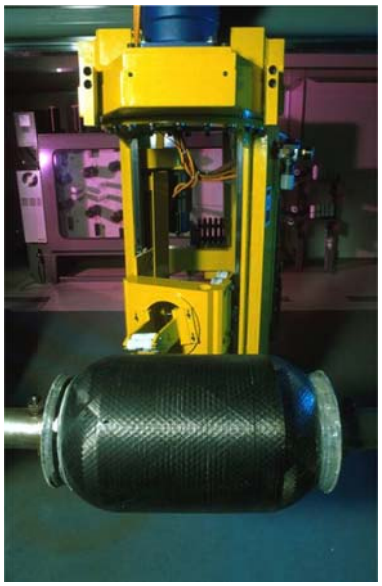

Figure 1.4: Filament wound tank at C.I.R.A. laboratory.

The tows are continuously wound onto the mandrel following an *ad hoc* design by dedicated software in order to obtain a specific fiber orientation and quantity [23]. After winding, the wounded mandrel is put in a vacuum bag and then in

autoclave for curing. As a highly automated procedure, the filament winding is usually precise and accurate. Filament wound structures have high strength to weight ratio, so they are attractive for manufacturing of pressure vessels, aircraft bodies, power poles, pipes, and much more.

A process similar to that above described is the Fiber Placement, in which the deposition head can not only provide the tow winding, but also it can cut and stop the deposition as well as it can restart the tow winding onto a new surface. This of course can accomplish specific design requirements related to fibres orientation and thickness of the component.

- **Pultrusion**

This process is cost effective for high volume production of constant cross section parts, and it is well known since the '50s, when it was created by the person who is considered by many to be "the father of composites" W. Brant Goldsworthy [24]. In the case of CFRP, carbon fibres are pulled from a series of reels and impregnated within a thermoset resin bath. The resin-impregnated fibres are then preformed to the shape of the profile to be produced and the resin in excess is removed. The obtained composite is passed through a heated die where an exothermic reaction cures the resin matrix. The component is continuously pulled; it exits the mold as a hot, constant cross sectional part which is cooled by forced air and then cut into the desired dimension (figure 1.5). Pultruded composites are the favored candidates to be used for high strength and light weight applications, for example as consumable wings for weapons or UAVs, and stiffening ribs to be incorporated into the wing.

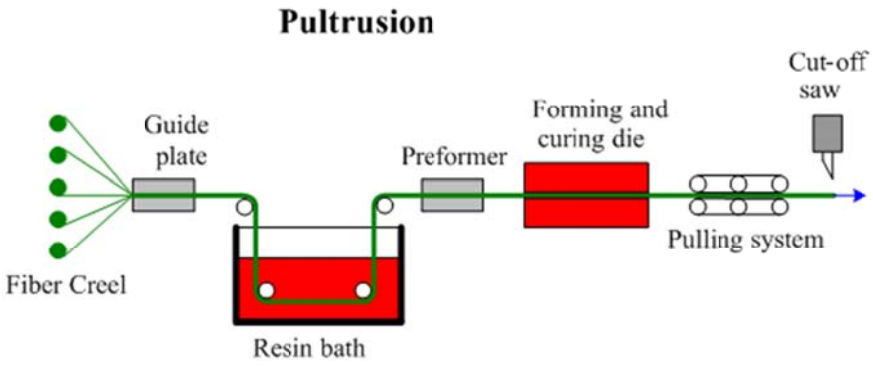

Figure 1.5: Typical pultrusion set up [25].

1.3 Main types of defects in composites

Defects can be inadvertently induced in composites during the manufacturing process. Indeed, the manufacturing process is probably the primary responsible of defects occurrence, especially for porosity formation, (i.e., presence of voids between the fibres and the matrix or within the matrix). Porosity is typically produced by an incorrect curing process due to uncontrolled or unexpected variations of the several involved parameters, such as temperature, pressure, timing, etc.

As a main effect, the presence of porosity can reduce the Inter Laminar Shear Strength causing delamination (inter lamina debonding). On the other side, the presence of regions of fibres unsupported by the matrix can induce local stress concentration, with consequent severe degradation of strength and stiffness in-service. That is why the porosity level must be checked, as will be more extensively explained in the following paragraphs.

The typical plies made by fibres pre-impregnated with resin are generally prepared by either hands or by automated processes; in both cases the introduction of foreign bodies may occur ranging from backing film to just greasy marks from fingers or, in case of composites made by moulding processes, by slag in the moulds if not perfectly cleaned.

More recently, low cost manufacturing processes, involving the impregnation of dry fibres laying in moulds, have introduced new types of defects as the fibre misalignment or waviness, both in, or out, of plane [26,27]. The stitching of fibres tows [28], typically used in order to avoid the latter cited defects, are themselves responsible of the introduction of voids in the areas close to the stitch.

However, the main weakness of composites is their vulnerability to impact damage that may happen during manufacturing and in service. Impacts typically occur during take-off and landing due to the rising of small debris from the landing strip, or during maintenance due to the drop off of tools.

Impacts can produce matrix cracking and delaminations of the ply layers [29] (figure 1.6).

Figure 1.6: Typical inter laminar debond induced by an impact.

Particularly crucial are impacts at low velocity/low energy that do not produce surface perforation but, in most cases, a mere indentation. In this case the damage is defined as "Barely Visible Impact Damage" (BVID), even if the damage produced in the internal part of the material could be more extended [30]. The main problem related to delamination is its enlargement in service with unpredictable and also catastrophic consequences [31]. A method for reducing impact damage, involving a damping layer interleaving within the stacking sequence, has been recently investigated [32].

1.3.1 Porosity in CFRP

One of the most used methods for CFRP manufacturing [33] consists of stacking laminas, generally named pre-preg, of carbon fibres pre-impregnated with resin and to cure the obtained stacked sequence with an autoclave curing cycle. This allows to convert the laminate into a rigid and stiff object. The autoclave cycle involves the combined effort of heat at certain temperature together with vacuum (fig. 1.7). Proper temperature is needed to activate and to control the chemical reactions in the resin, while pressure is used to squeeze off the resin in excess, to consolidate the stacked plies and to minimize the amount of air between the plies and within the resin [34].

So the action of temperature and pressure, as well as the duration of the applied cycle, are the main parameters to keep under control in order to assure the effectiveness of the curing process.

Generally, the curing cycle is planned starting from empirical models in order to reduce the number of experimental tests, such as the ones that can be found in literature [35-37].

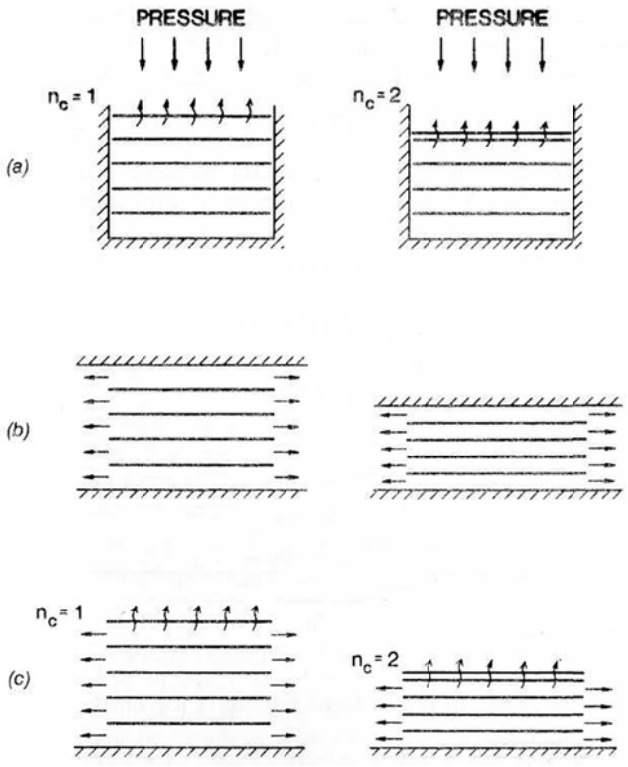

Figure 1.7: Pressure can influence the resin flowing in a direction orthogonal (a) or parallel (b) to the fibres, or in a direction in between (c) [35].

As can be expected, the quality of the manufactured component, in terms of structural and mechanical characteristics and its compliance with specific design requirements, is strongly dependent on these parameters and on the applied procedure for curing.

Generally the curing temperature, indicated by the materials providers, is found by carrying out specific thermo-physical tests to monitor the dependence of the resin viscosity on the temperature and by measuring the Glass Transition Temperature[1]. The application of heat at proper temperature assures that the structural performance of the obtained components will be uniform. On the contrary, the amount of vacuum and the duration of its application are more

[1] The glass-liquid transition (or glass transition for short) is the reversible transition in amorphous materials (or in amorphous regions within semi-crystalline materials) from a hard and relatively brittle state into a molten or rubber-like state. This transition occurs at the glass transition temperature T_g.

difficult to assess and, as a consequence, this latter emerges as the parameter to be carefully monitored [38-40]. Indeed, if the pressure level and its application duration are not optimized, voids could rise in the laminate (figure 1.8).

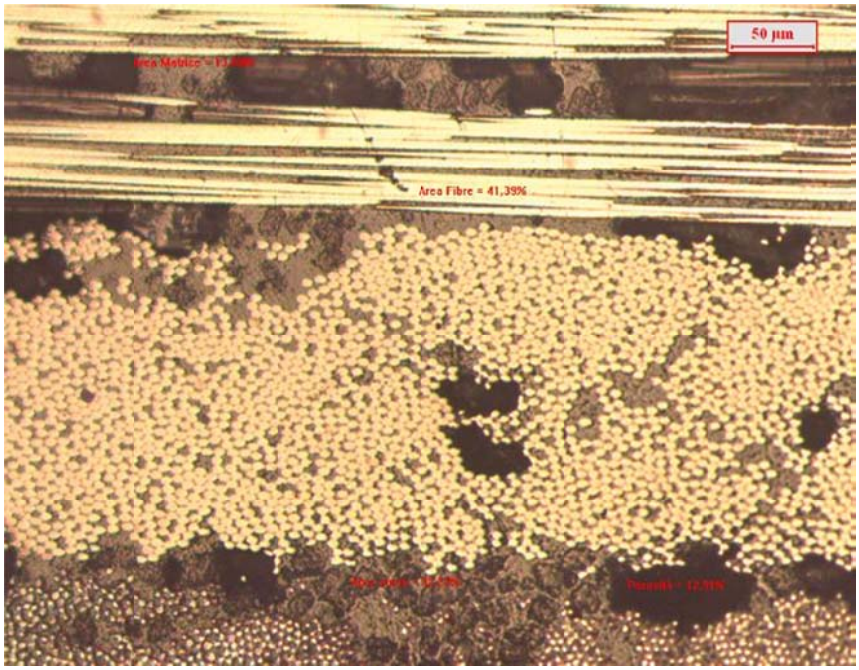

Figure 1.8: Metallographic microscopy on a CFRP laminate with porosity. Magnification 550x.

Among the several mechanisms determining the void formation, two of them have been deeply studied by scientists because they are considered to be the most probable ones:

- gas entrapment (humid air typically) during the process of fibres impregnation by the resin or during the lay-up of the pre-preg laminas;
- rising of volatile gases due to the curing of the resin.

Further, the volume of voids can grow due to the influence of the temperature in itself, because of air diffusion or due to the fusion of closest voids to create agglomerates.

Some authors have demonstrated that [41-43] the mechanical properties of CFRP laminated composites are heavily influenced and in most cases, downgraded, by the presence of voids [39,44-46]. In literature a plethora of works can be found, which are devoted to the mechanisms of voids formation during the curing process and to methods for voids reduction and, in particular,

concerned with the effects of voids on the final laminate properties. All of them are unanimous in considering that, in a unidirectional laminate, the mechanical properties in the fibres direction are not significantly influenced by the voids.

On the contrary, properties such as longitudinal compressive modulus and strength, transverse tensile modulus and strength, as well as bending and shear properties, are modified by the presence of voids, although this effect could be very different from case to case.

From experimental results, it seems that Interlaminar Shear Strength (ILSS) of unidirectional CFRP laminates is the property most affected by the presence of porosity thus, it can be taken as a reference.

As can be appreciated in figure 1.9, for a [0°/90°] lamination type, both strength and moduli decrease with increasing the void content [39]. However, the drop-off rate is different and the decreasing percentage for ILSS is the largest.

Otherwise, it must be borne in mind that the ILSS of two formerly identical laminates can be significantly different, also for the same void content. This implies that the mechanical properties, in which the role of the matrix is predominant, are influenced not only by the amount of voids but also by their spatial distribution in the laminate direction, or through the thickness direction, as well as by the voids dimension and shape [47].

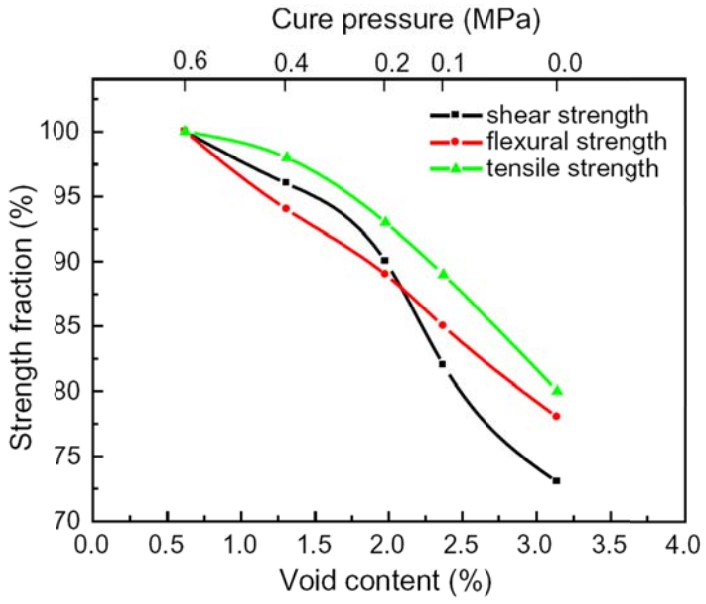

Figure 1.9: Mechanical properties dependence on void content [39].

Furthermore, due to location and volume occupied by the voids, inhomogeneous stress concentration may arise in the direction perpendicular to the laminate.

It has also been demonstrated that, generally, bigger voids rise in between the plies, so determining local fibre deformation and/or inadequate fibre impregnation. Therefore when the tensile stress is applied in the fibre direction, the decreasing of the longitudinal tensile strength due to the void amount can be explained by taking in consideration the local fibre deformation above cited.

The effects of voids are similar to micro-debonding between the fibres and the matrix, so when matrix, fibres and interfaces are all uniformly loaded, as in the case of transverse tensile modulus and strength tests, the local discontinuity between matrix and fibres determines the decreasing of both quantities.

Three point bending tests have demonstrated that, also in the case of identical voids amount, flexural and bending modulus can decrease differently. This is due to the role played by the voids dimension and shape. Further, ILSS tests have demonstrated that the strength is smaller when voids are concentrated between the plies and so, as in the previous case, dimension and shape play a fundamental role.

Works devoted to the study of the influence of voids on mechanical properties have demonstrated that a porosity of only 4% can determine the failure of 28% of coupons during ILSS (Interlaminar Shear Strength) tests [48]. Moreover, it has been observed that a 10% decrease of compressive strength can be ascribed to a 1% increase of void content [49]. On the contrary, due to their more uniform fibre distribution, woven fabric laminates are less influenced by porosity with respect to other laminate stacking sequences.

In spite of the enormous progress in the materials development and the even more sophisticated methods for resin reinforcing, the problems related to porosity occurrence are still open, that is why scientists are still facing the challenge of finding new instruments and more performing methodologies for porosity assessment and for prediction of its effects on the affected components.

1.4 Non Destructive Evaluation of CFRPs

Due to the heterogeneous nature of composite materials and to the continuous evolution of the employed raw materials and manufacturing processes, the methodologies used for Non Destructive Evaluation (NDE) require continuous upgrading. In fact, effective NDE methods are required for assessment of the products quality with the consequent rejection of parts not complying with the acceptance or rejection criteria, and also for investigation of the causes of failure in service. This latter is nowadays gaining a primary role in the aeronautical industry with the aim to better understand the behavior of damaged structures and to make as reliable as possible their remaining forecasted life.

Since the introduction of the Non Destructive Inspection (NDI) concept in the industrial materials production, many techniques have been developed. With the term Non Destructive (ND), one refers, in general, to all the methodologies which are able to inspect parts or components, without damaging them. Often, acronyms NDT, which stands for Non Destructive Testing, and NDE, which stands for Non Destructive Evaluation, are used indifferently with the same meaning. Generally, the first action is spent in testing and recording an output, while the second consists in the successive data processing, with dedicated software, to obtain the evaluation. Owing to the final output, in this chapter, we use the term NDE.

1.4.1 NDE techniques in the Aerospace field

The today NDE methods for which the certification of personnel can be obtained in the Aerospace frame (EN 4179: 2009 Aerospace series - qualification and approval of NDT personnel) are the following:

- Liquid penetrant (PT)
- Magnetic particle (MT)
- Eddy current (ET)

- Ultrasonic (UT)
- Radiography (RT)
- Thermography (IRT)
- Shearography (ST)

The above listed techniques can be used for a variety of materials ranging from metals to complex composites.

Basically, depending on the type of component to be inspected and on the type of defect to be detected, different methodologies could be used [50-52] for nondestructive characterization of composite media, in particular, some are very effective for CFRP inspection and also certified; others are not yet certified but largely employed and especially conceived for materials investigation. In the following, each of them will be illustrated with also some historical hints.

- **Liquid Penetrant**

  Liquid Penetrant inspection is a method for revealing surface defects especially in metals (cracks or welds) and ceramics (cracks). On the surface of the inspected part is applied a colored liquid (penetrant) which is sucked into defects thanks to the capillarity action. After a period of time, named *dwell*, the excess of liquid is removed and a developer applied. So the penetrant is drawn from the flaw to reveal its presence. Two main types of penetrants are used: colored, which needs a very good white lightening to get the proper contrast, and fluorescent which needs ultraviolet light ("black light") to be revealed.

  This method, although a change of the used substance occurred, is very old, since it is possible to trace signs of a similar procedure already in the latter part of the 19th century to approximately 1940. To inspect steel and iron components of railways, the "oil and whiting" method was used. More specifically, parts were submerged in oil diluted with kerosene, then after removal and careful cleaning, they were coated with a fine suspension of chalk in alcohol, so that a white surface layer formed once the alcohol evaporated. The object was then subjected to vibration being

struck with a hammer, causing the residual oil in any surface cracks to seep out and stain the white coating. This method was abandoned when the magnetic particles method was introduced, due to its better effectiveness with ferromagnetic materials.

In the 1940 the Magnaflux in Chigago introduced in the market oil with very visible red dyes, and during the 1942, the Magnaflux Zyglo included fluorescent dyes in the penetrant oil [53] to enhance defects visibility.

This method requires very trained personnel with excellent eyesight [54]; it is still largely used for welding inspection (fig. 1.10).

Figure 1.10: Liquid Penetrant testing of metal welded joints [55].

- **Magnetic Particles**

Magnetism was known since ancient Greeks, but the very first use for non-destructive evaluation was carried out during 1868, when cannon barrels were inspected. The cannon was magnetized by sliding a magnetic compass along the entire length of the barrel, then by observing the changes in the orientation of the needle, the first inspectors were able to detect flaws.

In the early 1920s William Hoke noticed that colored magnetic particles (metal shavings) could be used together with magnetism to reveal flaws in metals. Hoke discovered that a surface, or subsurface flaw, in a magnetized material caused the magnetic field to distort and extend beyond the part. The idea was based on the application of magnetic powder on the inspected part and on observation of the powder

distribution. In correspondence of flaws, indeed, the powder tends to store up providing a clear indication of the defect (fig. 1.11). Thanks to its effectiveness in the inspection of ferromagnetic materials, in the '30s, this method replaced the oil penetrant method used for railway inspection.

Magnetic particles is nowadays still largely used to check the integrity of components or welded parts, especially in automotive and bridge engineering [56].

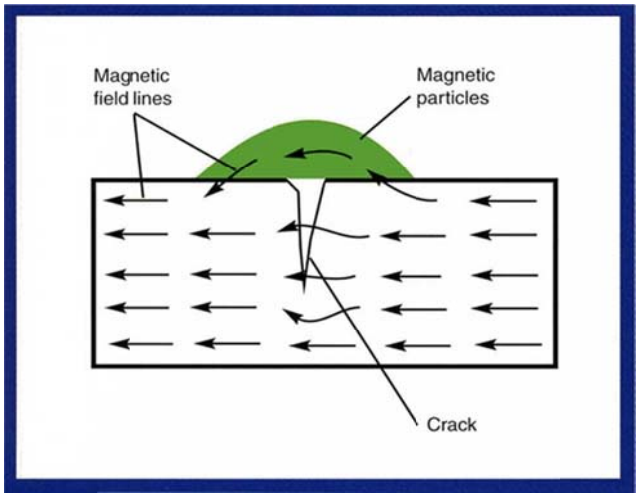

Figure 1.11: Magnetic particle testing of a surface crack [57].

- **Eddy current Testing**

Eddy current testing is based on the electromagnetic induction. This phenomenon was discovered in 1831 by Michael Faraday, the English chemist/physicist who is recognized as the discoverer of electromagnetic induction, electromagnetic rotations, magneto-optical effect, diamagnetism, and other phenomena. On this bases, High in 1979, noticed that the electrical properties of a coil tend to change when it is put in contact with a metal of different electric conductivity and permeability.

If an electric coil is put close to the surface of an electrically conducting material, eddy currents are induced into it (fig. 1.12). These currents flow parallel to the coil in a region limited to nearby the probe and their density decreases exponentially with distance (*skin effect*).

Eddy currents interact with its inductive primary field, so, when a defect is present in the material, such as a micro-crack, there the eddy currents are modified determining a change in the resistance and in the inductive reactance of the coil in the probe. These changes are directly related to the defect position and extension [58,59]. Nowadays eddy current instruments may be arranged in a different ways, but generally, all have in common an alternating current source, a coil of wire connected to this source, and a voltmeter to measure the voltage change across the coil. An ammeter could also be used to measure the current change in the circuit instead of using the voltmeter.

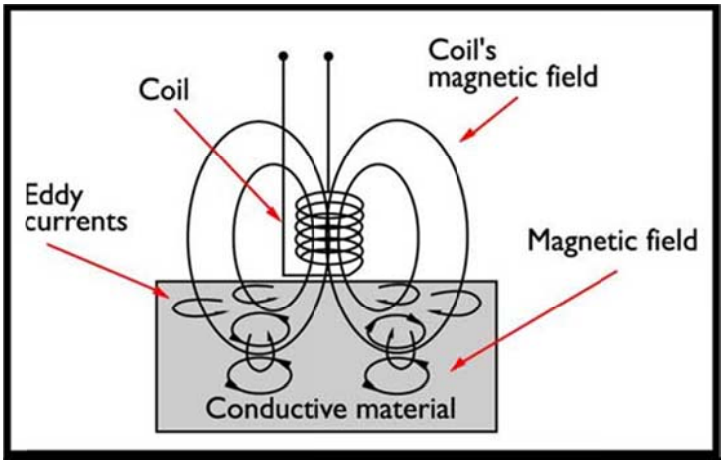

Figure 1.12: Eddy current testing principle [60].

- **Ultrasonic Testing**

Ultrasonic Testing (UT) [61,62] is one of the most used non-destructive method, due to portability of instrumentations and to the easiness of data interpretation.

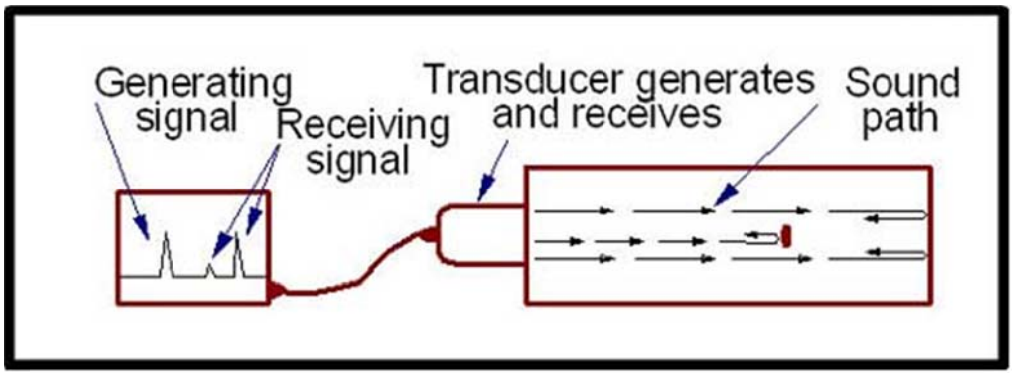

Figure 1.13: Schematic of the typical set up for Ultrasonic Pulse-Echo technique [63].

UT is very effective in the detection of most of the common CFRP defects, such as porosity, slag inclusions and delamination. This method is based on the principle that a ultrasonic wave, of a given frequency, is modified by passing through a material; in particular, it undergoes both amplitude reduction and reflection at interfaces between parts of different acoustic impedance (fig. 1.13). The very first application of ultrasonic waves for NDE was in between 1929 and 1935, when S.Y. Sokolov [64] demonstrated the reliability of metal components examination using methods based on ultrasounds; this became the main application of ultrasounds during World War II [65]. Since their first use, they have experienced a huge enhancement of both instrumentation and techniques, and nowadays ultrasounds has become an essential method for materials assessment ranging from metals to reinforced plastics [66]. Typically, the used techniques are Pulse-Echo and Through-Transmission, respectively involving one or two transducers whose effectiveness is of course related to the type of the defect and to the possibility to access just only one or both sides of the inspected component.

This technique will be more extensively treated in the next chapter.

- **Radiographic Testing**

The radiographic inspection is perhaps the most effective ND method for a huge range of materials.

Within only a month after the announcement of the discovery of a new kind of ray, by Wilhelm Conrad Roentgen in 1895, many medical radiographers used it successfully both in Europe and in USA. Industrial applications appeared later due to the need of X-ray tubes able to withstand the high voltages required to produce rays of satisfactory penetrating power. This was reached in 1913 when the high vacuum X-ray tubes designed by Coolidge became available. The high vacuum tubes were an intense and reliable X-ray source, operating at energies up to 10^5eV (hard X rays). This was followed by a rapid development of devices,

also new technologies were investigated thanks to the discovery, by Becquerel, of natural radioactivity. In 1931 the General Electric Company developed 10^6eV X-ray generators, providing an effective tool for industrial radiography. In the same year, the American Society of Mechanical Engineers (ASME) permitted X-ray approval of fusion welded pressure vessels that further opened the door to industrial acceptance and use, also in the aeronautical industry, for inspection of composites.

Through X-ray inspection, anomalies become visible as local change of luminous intensity because radiation decays in different ways through different materials and thicknesses (i.e. the light/shade effect strongly depends on the density and thickness of the material) (fig. 1.14).

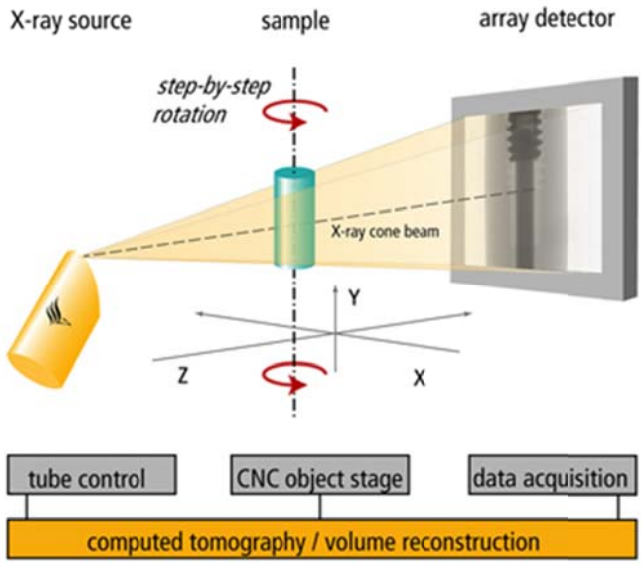

Figure 1.14: Schematic of a radiographic set up [70].

Thus a detailed profile of the internal defect distribution can be obtained [67]. A broad range of material thicknesses can be inspected, as well as complex shapes. The radiographic techniques are generally classified according to the type of radiation employed: X-ray (λ~Å), gamma (λ~10^{-4} Å), or neutrons, eligible for materials composition determination [68]. Radiography in the CFRP inspection is principally used to detect subsurface imperfections or discontinuities such as porosity, inclusions or fiber waviness [69]. Today X-ray inspection is filmless thanks to the

technology of digital imaging, and computers have become part of the commonly used set ups. The advanced type of radiographic inspection is the Computed Tomography which allows, by proper software, the 3D reconstruction of the inspected component.

Although radiography has numerous advantages, it is quite expensive and poses health risks, that is why it is not so common and used as other techniques.

- **InfraRed Thermography**

Infrared Thermography [71-73] is very attractive since it offers non-contact, fast inspection of wide areas and can be used as an alternative, or complement, to other inspection technologies.

The first use of an infrared device for NDE purposes goes back to the 1960 [74] and the first infrared sensor was patented in 1914 by Parker [75]. IRT can be performed with different approaches which allow detection of defects and reconstruction of their position in plane and in depth within the thickness of the inspected component. The most used IRT techniques for NDE are Pulsed, Lock-In, Pulsed Phase and Flash thermography and all of them involve the use of a heat source to warm up the inspected material and to stimulate infrared emission from it.

Figure 1.15: Thermography for fuselage inspection [76].

These methodologies are attractive for the aerospace industry (fig. 1.15) due to the absence of contact with the inspected object. Its effectiveness in detection of many of the most typical defects in composites such as

disbonds, inclusions, impact damage, porosity as well resin starved areas has been extensively proved. The use of Infrared thermography in NDE will be more deeply described in Chapter 3.

- **Shearographic Testing**

Detection of subsurface defects in thin structures can be effectively carried out also with an optical technique such as Shearography [77].

The electronic laser shearographic imaging interferometer was pioneered in the early 1980's by three researchers, Dr. John Butters at Loughborough University in the UK, Dr. S. Nakadate in Japan and Dr. Mike Hung at Oakland University in the USA [78]. Shearographic nondestructive testing has evolved considerably since its first use on a production aircraft program in the USA in 1986. This, thanks to the introduction of digital CCD cameras and high power solid-state lasers which have led to dramatic performance improvements in shearography instruments and systems [79]. The technique is based on interferometry; defects are detected by comparing the fringes obtained by a Michaelson interferometer related to the surface of the inspected material with the same image obtained when the material is under load.

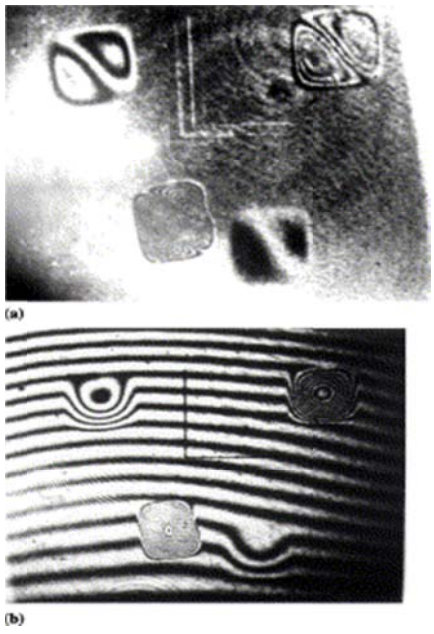

Figure 1.16: Fringe deformation due to debonding at various depths [80].

The load is induced by mechanical or thermal methods e.g., under either overpressure, or heating up the whole object. When a defect is located near the surface, the interference fringes are there modified due to the stress concentration around the defect; the fringes deformation allows the flaw detection (fig. 1.16). Defects such as debonding, delaminations [81], wrinkles, slag inclusions and out-of-plane deformation can be easily detected with an inspection rate of almost 1 m^2 per minute.

Shearography is currently in use on a wide variety of aircraft including F-22, F-35 JSF, Airbus, Cessna Citation X, Raytheon Premier I and the NASA Space Shuttle [82].

From the above brief description of the most used NDE techniques, it can be outlined that not all of them are suitable for composite inspection, especially for composites with polymeric matrices and carbon fibres. In a recent ASTM standard [83], the most effective techniques for PMC have been analyzed and their effectiveness for specific defect detection has been highlighted.

Type of Defect	Infrared Thermography	Radiography	Shearography	Ultrasonics
Delamination	X	X	X	X
Density Variation	X	X		X
Disbond	X	X	X	X
Fiber Debonding	X	X	X	X
Fiber Misalignment	X	X		
Fractures	X	X		X
Inclusions	X	X		X
Microcracks		X	X	X
Moisture	X	X		
Porosity	X	X		X
Thickness Variation	X	X	X	X
Voids	X	X		X

Table 1.1.

Among the techniques most used for aeronautic inspection, it is possible to resume their applicability and effectiveness in the following table 1.1.

From the table it can be appreciated that radiographic techniques are the most effective for the most part of defect detection, nevertheless UT and IRT are considered the best solution in terms of balance between costs, health risks and easiness to use.

1.5 NDE methods for porosity assessment in CFRP

Porosity and, in particular, scattered voids are very common defects occurring during composite manufacturing, especially in CFRP. Whatever is the reason for porosity occurrence in a laminate, its direct consequence is the presence of regions where fibres are deprived of resin supporting, or of areas with local stress concentration. For this reason porosity is considered one of the main causes of degradation of the structures mechanical properties; this is dramatically crucial when they undergone the typical loadings of life in service.

The overall effects of porosity on composites are strongly dependent on its extent as, for example, the decreasing of the density of the material as well as of moduli and strength. The measure of the level of porosity could be a complicated practical problem and generally, within the area of composites manufacturers, the percentage of porosity in a material is considered like a measure of the overall quality of the latter.

Porosity is generally assessed in terms of density measurements through destructive ways. The most common method is based on the sample's weight per volume (also known as volumetric method), which supplies information by statistical inference. Conversely, mainly in the aeronautical field, there is the need of having control of porosity distribution on the entire production. Then, it is justified the even increasing interest on the development of non destructive testing methods (NDT).

Most of the studies deal with qualitative estimation of porosity. Nevertheless, to reach the goal of quantitative measurements, a large data base of cases have to be created and the results obtained in different laboratories worldwide must be compared to obtain a general data correlation.

Amongst the NDE techniques for porosity assessment, UT is considered one of the most effective. Generally, it is carried out by directly producing ecographic images (c-scans), as either by correlation with a single ultrasonic frequency (narrowband approach), or by correlation with ultrasonic frequency slope (broadband approach).

The typical ecographic approach is very effective when the characteristic dimension of the pores (i.e. their diameter) is larger than the instrument resolution of the ultrasonic image; however, this technique may require further efforts in image elaboration, which makes the quantitative evaluation of porosity very difficult, or not reliable.

Amongst the empirical techniques, the measure of the attenuation variation of the signal is massively used since voids strongly scatter the elastic waves [84].

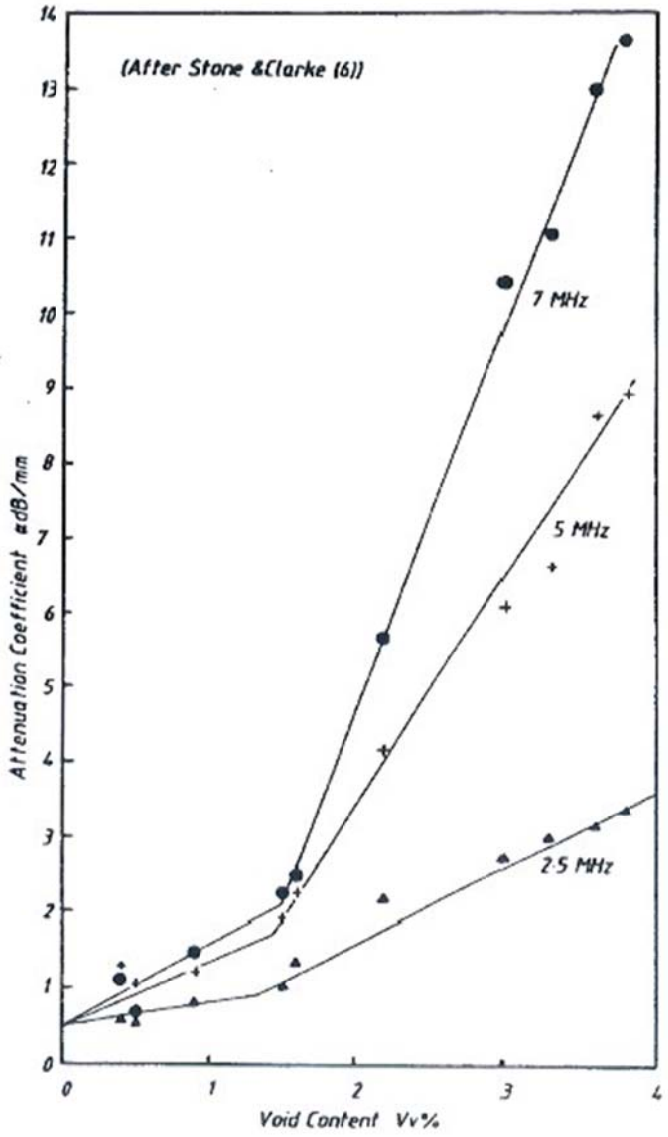

Figure 1.17: Ultrasonic attenuation dependence on void content [84].

Further, the correlation between the attenuation and the amount of porosity has been demonstrated and successfully applied to porosity evaluation [85], as well as the dependency of the attenuation on the ultrasonic wave frequency (fig.

1.17) [86]. In particular, Hsu [87] used the Through-Transmission technique for determining the amount of porosity as percentage of volume in CFRP. He demonstrated that the amount of voids is directly related to the attenuation slope (attenuation with respect to the used signal frequency).

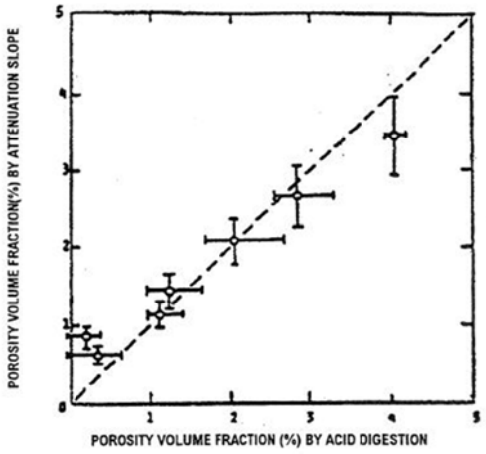

Figure 1.18: Ultrasonically determined void content in carbon-epoxy laminates (made from unidirectional pre-pregs) vs. void content determined by acid digestion[2] [87].

The author has measured the attenuation slope for frequencies ranging from 2 up to 16 MHz in carbon/epoxy and carbon/polyamide: up to 6 % voids in non-woven unidirectional and quasi-isotropic laminates (fig. 1.18) and up to 12 % voids in woven laminates (fig. 1.19).

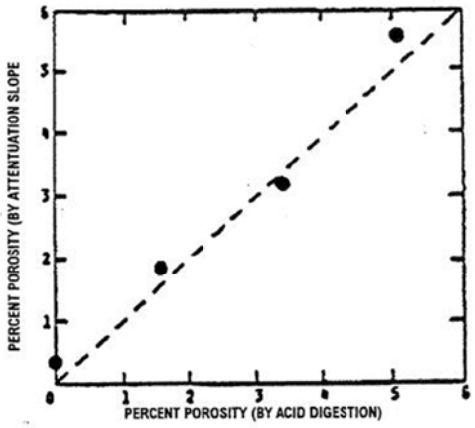

Figure 1.19: Ultrasonically determined void content in woven carbon-epoxy laminates (made from unidirectional pre-pregs) vs. void content determined by acid digestion [87].

[2] This method consist of resin removal by acids (as an example fuming sulphuric acid) followed by weighting of the unaffected fibres for the determination of constituent fraction of the composite.

To study the amount of porosity, also the ultrasonic Pulse-Echo technique can be used as disclosed in the paper by Steiner [88]. He used a 2 mm thick sample, with porosity varying between 1,17% and 3,57% and carried out tests by using a robotized probe holder. Within such set up, he was able to perform digitized full-volume waveform analysis and to appreciate the effects of porosity of the full ultrasonic wave. Specifically, he observed that almost no echoes activity was present in low porosity samples between the entry echo and the back-wall echo, whereas a huge amount of echoes appear when high porosity samples were inspected.

Laser based Ultrasounds were used by Karabutov, et al. [89]. They used a short laser pulse to generate ultrasounds in graphite-epoxy composite materials. The inspected samples included different percentages of porosity (<0.1%, 0.4%, and 1.2%). Laser was used to induce thermo-elastic expansion of the impinged layer with the consequent production of acoustic pressure waves, which propagate into the absorbing and transparent media as ultrasonic pulses in the range 1-5 MHz. They observed that the higher the porosity amount the greater the acoustic attenuation coefficient and that the noise component of the scattered acoustic signal increased with porosity. Then, authors suggest that spectral representation should be used to further analyse laser-induced ultrasonic signals.

In a recent study, performed at CIRA, it has been demonstrated, through attenuation measure by the Pulse-Echo technique, that porosity, which forms during the curing cycle, depends also on the laminate stacking sequence [90].

Since the detection of porosity in resin-starved areas of polymer matrix composites is very difficult and generally not reliable with the ultrasonic method, the attention is being devoted towards infrared thermography. An early investigation involving thermography and laser based Ultrasonics has been carried out by Steiner et. al. (1996) to monitor porosity in thermoplastic composite fabrication [91].

Later, Grinzato, et al. [92] used Infrared Thermography to inspect an actual CRFP aeronautical component and demonstrated that by mapping local

thermal diffusivity and effusivity, the determination of the amount of voids is more effective than the estimation obtained by using ultrasonic based methods.

A similar study was carried out by Ciliberto et al. [93] who obtained useful results for a fuselage panel (manufactured by bonding process between a CFRP skin and honeycomb nomex), by comparing thermal diffusivity with ultrasonic results.

In a recent review on NDE methods for porosity assessment in fibre reinforced polymers, Brit and Smith [94] stated that none of the current NDE techniques can be considered as a reference technique due to the dependence of the instrument response to the pores morphology as well as to the intrinsic nature of the fibre and matrix in themselves. Nevertheless, in a more recent study carried by NASA [95] it is stated that in the industrial production environment UT can be the most effective technique for porosity assessment. This can be achieved thanks to the use of processes and materials strictly under control, which can reduce the generally randomly variable factors, such as the porosity morphology, as well as by using well known instrumentation and adequately trained personnel.

On the base of the above considerations and experience by international scientists, in this dissertation Ultrasonics and Infrared Thermography are both considered for porosity assessment in CFRP samples with different percentages of induced porosity; porosity is also measured by the destructive gravimetric method for data comparison.

Chapter 2

Ultrasonics: theory and testing approaches

Ultrasonic inspection is one of the most widespread and old approach for materials assessment.

Since World War II, this type of inspection emerged as a fundamental mean for metals flaw detection and, thanks to the huge progress in development and enhancement of instruments and techniques, is nowadays one of the preferred methods in aeronautic and aerospace industries, also for composite inspection. It is greatly useful for inspection of components during and at the end of the manufacturing process, as well as for rapid and reliable checking of components, as parts of a vehicle, during their life in service.

Several are the ultrasonic techniques conceived to inspect different types of materials and structures, but the more used inspection arrangements are known as Reflection technique (or Pulse-Echo) and Transmission technique (or Through-Transmission).

Special transducers, which work thanks to the piezoelectric effect, are used for producing a ultrasonic wave which is properly forced to travel within the material to be inspected. The detected signal, and its changes with respect to the originally incident wave, are all elements full of information about the nature of the material, and the in-homogeneities which may be present within it. This method allows to inspect materials, without damaging them, and to know where flaws are present, how much space they occupy in the whole component and how deep is their position. This knowledge, allows to apply specially conceived acceptance/rejection criteria which are fundamental tools to enhance the production quality within the industrial frame. Moreover Ultrasonic inspection results can be the base for mathematical models able to foreseen or,

better, to estimate the future life of the component in the case of the flaw would enlarge once the component, as part of a more complex structure, is under use. Ultrasonic Testing (UT) is one of the most effective tool to detect the most part of the common defects in CFRP, in particular it can be used successfully for porosity assessment.

2.1 UT historical hints

Ultrasounds are special acoustic waves with frequencies above the upper limit of human audibility (approximately 20 kHz).

At the end of the XVIII century, the speed of sound in air was already measured and the sound inability to propagate in vacuum had been demonstrated. The existence of sound waves with frequencies inaudible by human hears was highlighted in 1794, when the Italian biologist, Lazzaro Spallanzani, demonstrated that bats can fly in the darkness thanks to their ability to detect echoes, i. e. sound reflections, coming from objects in the environment. Some years later, in 1826, the Swiss physicist Jean-Daniel Colladon measured the speed of sound in the water of the Geneva Lake (almost 1480 m/s) thanks to his underwater bell [96]. In the following years, physicists were working to mathematically describe the propagation of sound waves and their interaction with matter but only in 1877, the famous treatise "The Theory of Sound" by Lord Rayleigh was published [97]. In this treatise, for the first time, sound waves were mathematically described, opening the way for the future theoretical developments and successive applications.

The first reproduction of very high frequency sounds is due to the English scientist Francis Galton in 1876, when he created his so called Galton whistle (fig.2.1) [98], but the real breakthrough in the study of high frequency sounds was achieved in 1880 when the *direct piezoelectric effect* was discovered by Pierre Curie and his brother, Paul Jacques, in Paris [99]. They succeeded in measuring the electrical charges appearing on the surface of specially prepared crystals (tourmaline, quartz, topaz, cane sugar and Rochelle salt among them), when subjected to mechanical stress.

The property that crystals exhibiting the direct piezoelectric effect would also exhibit the *converse piezoelectric effect* (mechanical stress in response to an applied electric field) was, firstly, mathematically deduced from fundamental thermodynamic principles by Lippmann in 1881 [100] and, subsequently, experimentally confirmed by the Curies brothers.

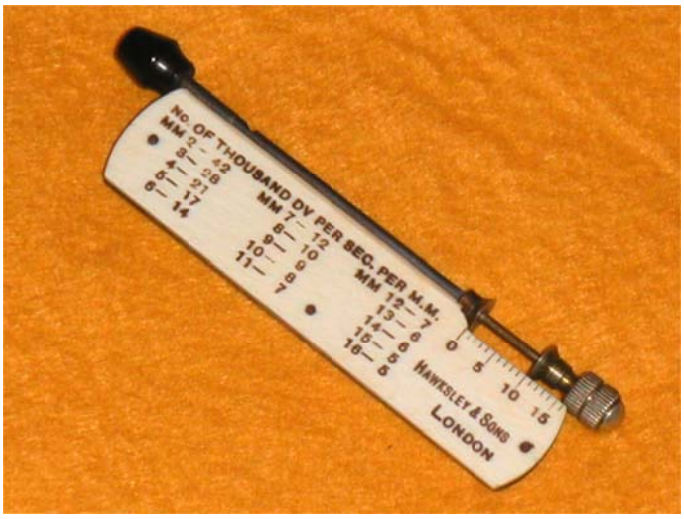

Figure 2.1: Galton whistle.

Thanks to this discovery, ultrasounds production and reception was then possible taking advantage of the piezoelectric crystals properties.

One of the first applications of the underwater ultrasound (*sonar*) detection was proposed in 1912 after the Titanic sinking. Within a month from the disaster, the English meteorologist Lewis Richardson [101] claimed in its patent the possibility to detect icebergs by ultrasounds, but the first working sonar system was realized in the United States by the Canadian Reginald Fessenden only two years later, in 1914. Fessenden was studying a device to underwater transmit and receive electromagnetic signals, in order to allow communication between ships. He conceived and designed an oscillator including a copper tube (a strong electromagnet) with inside a central core made by a coil. To transmit low frequency ultrasonic waves, he joined the copper tube and a large diaphragm together. The alternate current flowing through the core coil induced a current in the copper tube, which started to move back and forth, causing vibration of the diaphragm. By putting the moving diaphragm in contact with water, the propagation of mechanical waves was obtained. The oscillator was also used as a receiver in fact, the incoming mechanical waves caused the diaphragm vibration, so, the copper tube magnet started to move back and forth. This induced a current flowing in the coil which was related to the received ultrasonic signal. This first sonar based on the Fessenden oscillator was able to detect an underwater iceberg 2 miles away.

In the same years, thanks to the application of diodes and triodes, ultrasonic apparatus with enhanced amplification were developed. This led the French physicist Paul Langévin and the Russian scientist Constantin Chilowsky (who was resident in France), to start developing devices based on ultrasounds to detect submarines [102] which were largely used during World War I. Such device, called *hydrophone* included an array of thin quartz crystals between two steel plates with a resonant frequency of almost 150 KHz.

Between 1929 and 1935, S.Y. Sokolov [64] demonstrated the reliability of metal components examination using methods based on ultrasonic waves, so he introduced the concept of Non Destructive Evaluation, NDE, i. e. materials examination without damaging them; this became the main application of ultrasounds during World War II. He proved that the ultrasonic signals, transmitted through metals, were affected by losses of energy; the ultrasonic energy variations were associated with the presence of flaws. Therefore, the detection of flaws was obtained by measurements of the ultrasonic energy attenuation. At Sokolov time, the resolution of this method was still quite poor, then he suggested the use of reflected signals instead of the transmitted ones, so he had the intuition of a method nowadays massively used which is the *Pulse-Echo* technique. Unfortunately, at that time, the available technology was inadequate for the complete exploitation of such idea.

A method for ultrasonic data visualization was introduced in 1936 in Germany by Raimar Pohlman [103]. His system was based on the transmission of acoustic waves which were transformed in images by acoustic lenses. This apparatus was widely used during World War II in order to allow quality controls of the ammunitions for the flak in Berlin.

During the 1940's ultrasounds for investigation of materials was improved in the United States by Floyd Firestone, who was the inventor of the Reflectoscope [104]. He modified a radar instrument and developed an amplified transmitter with short pulses (fig. 2.2).

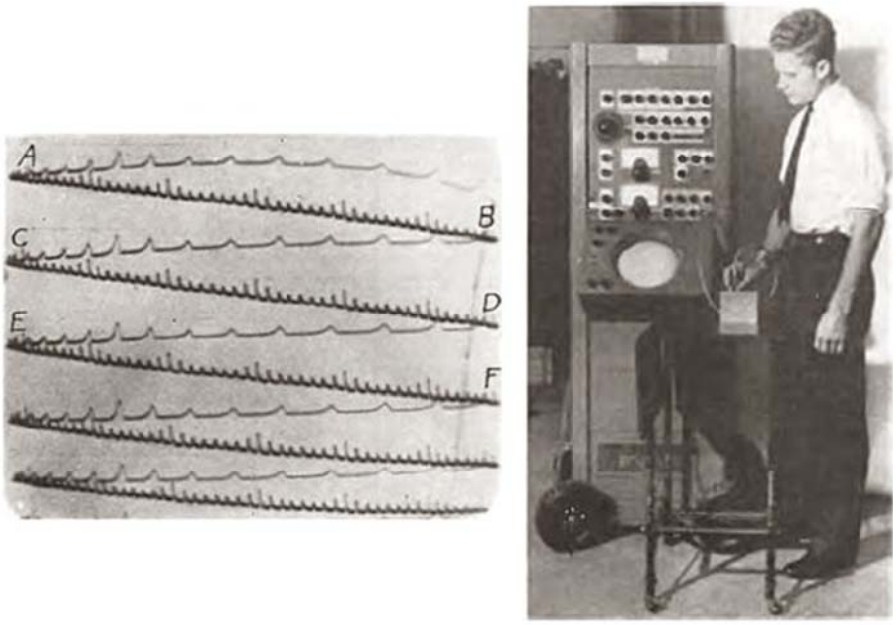

Figure 2.2: First supersonic Reflectoscope [105].

In the same period, Donald O. Sproule in Great Britain and Adolf Trost in Germany, although they had no knowledge of each other, started to apply a transmission technique based on separated transmitter and receiver probes. They put the two probes in contact on the opposite sides of a plate, on the same axis, via a mechanical device; continuously flowing water was used as coupling media between the probes and the investigated surfaces. This technique is now commonly used to inspect materials and it is known as *Through-Transmission* or *Transmission technique.*

In Germany, during 1949, the Reflectoscope invented by Firestone was investigated independently by Josef Krautkrämer in Cologne and Karl Deutsch in Wuppertal. Josef Krautkrämer and his brother Herbert, both physicists, were able to develop ultrasonic instruments in their company the KRAÜTKRAMER, while Karl Deutsch, a mechanical engineer, found a partner in Hans Werner Branscheid to set up the KARL DEUTSCH. These two companies producing ultrasound instruments for flaw detection, within only one year entered into a competition which endured since few years ago.

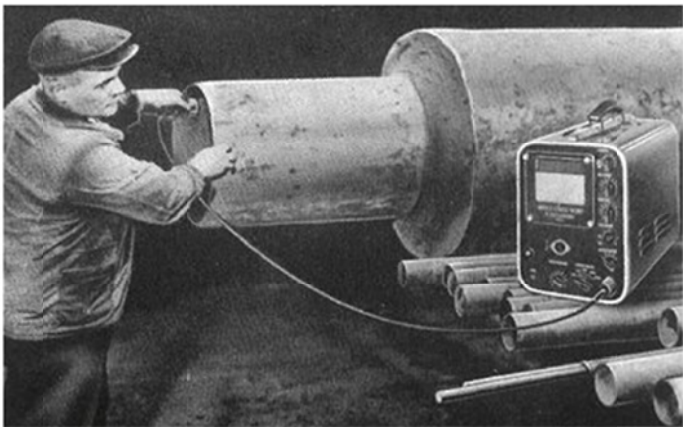

Figure 2.3: Pipe testing with Krautkrämer apparatus (1950s) [105].

Even if this chapter is devoted exclusively to ultrasonic applications for NDE, it has to be pointed out that ultrasound applications for medical purposes have been developed in parallel with those devoted to the inspection of metal components. Rather, most of the results obtained for medical purposes act as inspiration for conceiving instrumentation specifically thought for materials investigation. Between 1920 and 1930 the use of ultrasounds for the ablation of tissues, such as carcinomas, was already been experimented by William Fry at the University of Illinois [106], and their application to rehabilitation were already been put in practice.

Around 1940, ultrasounds were taken into consideration as diagnostic tools. Between 1942 and 1947, Dussik presented some results [107] concerning human organs inspection. He put two transducers on the opposite side of the head of a patient. The inspected parts of the head with both transducers were immersed in water to effectively transmit ultrasonic energy. The received signals were impressed upon a photographic thermo-sensitive paper.

Around 1949, doctor George D. Ludwig active as junior Lieutenant at the Naval Medical Research Institute in Bethesda, Maryland, succeeded in measuring the ultrasound speed in human tissues (almost 1540 m/s), value which is still used today [108]. His studies provided an important contribution to the creation of a scientific community involved in the investigation of ultrasounds medical applications. Some years later, in 1959, Professor I. Donald, in Scotland, succeeded to detect clear echoes from the foetus head, and within only few years, the pregnancy monitoring from beginning to end was possible. These

were the first steps in human diagnostics which had led to what today is known as *echography* [109].

Since the introduction on the market of the first ultrasound based instruments, it was evident that the primary purpose of using ultrasounds in industrials applications was the detection of defects. The possibility of defect detection led to develop the "safe life" approach aimed to prevent and reject potentially dangerous components from service in order to avoid disruptions.

During the 1970's the technological progress allowed improving instrumentation performance leading to the detection of smaller defects. In the industrial production, this caused the increase in the amount of the rejected components although the probability of failure had not changed. Thanks to the development of the fracture mechanics theory, it has become possible to predict the growth rate of cracks under cyclic loading (fatigue). This has formed the basis for the new philosophy of "damage tolerance" design, i.e. the possibility to accept structures containing defects, if the characteristics of such defects were known and verifiable. Therefore, the evaluation of defect type and size, became a mean to establish a critical size below which defects may remain to prevent failure. Quantitative details, about flaw size, were used as input for fracture mechanics predictions to achieve information on the remaining life of a component. This approach was adopted particularly in the military and nuclear power industries, leading to the Quantitative Non Destructive Evaluation (QNDE) .

2.2 Theoretical principle for application of UT to NDE

As seen in the previous paragraph, the mechanical stress is at the origin of the elastic waves, which can propagate in fluids and in solids.
For NDE applications, ultrasounds are emitted and/or received by transducers, whose working mode is based on the piezoelectric effect.
The ideal elastic wave equation for the completely general (anisotropic) case is given by [110]:

$$\rho \frac{\partial^2 u_i}{\partial t^2} = \lambda_{iklm} \frac{\partial^2 u_m}{\partial x_k \partial x_l} \tag{2.1}$$

Where in eq. 2.1, ρ is the density, u_i are the components of the displacement vector, λ_{iklm} is the elastic modulus tensor (the Einstein summation convention is followed).
If the material is isotropic and its microstructure can be ignored (i.e. small with respect to the wavelength), the same equation becomes:

$$\rho \frac{\partial^2 u_i}{\partial t^2} = G \frac{\partial^2 u_{mi}}{\partial x_k^2} + (K + 4/3G) \frac{\partial^2 u_l}{\partial x_i \partial x_l} \tag{2.2}$$

In eq. 2.2, *G* and *K* are respectively the *shear* and the *bulk modulus*. So, in a unbounded isotropic media, two kind of waves, i.e. modes, can propagate in principle, and each of them describes a different type of particle motion along the propagation direction [61], which are (fig. 2.4):

- longitudinal waves (or compressional) – the average particles motion is parallel to the propagation direction, i.e. the wave behaves as a compression and a consequent expansion of the medium (fig. 2.4, part a);
- transverse waves (or shear) - the particles motion is orthogonal to the propagation direction within the medium (fig. 2.4, part b).

Both longitudinal and transverse modes are characterized by their specific propagation velocity c, which depends on the physical properties of the materials.

Longitudinal waves velocity, c_l, depends on the material Young modulus E, density ρ and Poisson ratio μ, through:

$$c_l = \sqrt{\frac{E}{\rho}\frac{1-\mu}{(1+\mu)(1-2\mu)}} \tag{2.3}$$

transverse waves velocity c_t is, with respect to c_l, mainly related to the Shear modulus G, through:

$$c_t = \sqrt{\frac{E}{\rho}\frac{1}{2(1+\mu)}} = \sqrt{\frac{G}{\rho}} \tag{2.4}$$

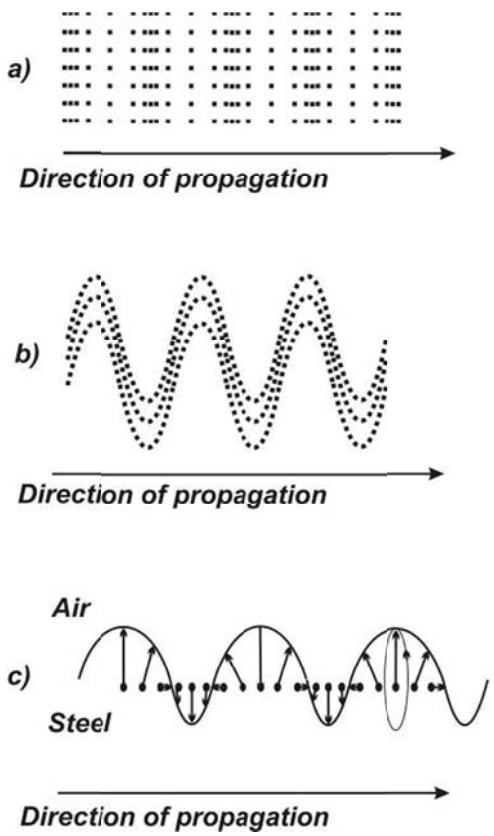

Figure 2.4: Particles motion in the Longitudinal wave mode (a), in the Transverse wave mode (b) and in the Rayleigh wave mode (c).

Depending on the material and geometry of the part to be inspected, different types of modes can propagate. When the particles motion is constrained to the surface, a Rayleigh wave is produced (fig. 2.4, part c). In this case the particles move on an ellipse around the propagation direction. For a solid with thickness less or equal to the wave length, the Rayleigh waves degenerate in Lamb waves (*plate waves*) [111,112]. Moreover, in the inspection of constant cross sectional structures, such as railhead or pipelines, the so called guided waves can be used, which are obtained by the interference between longitudinal and transverse waves in confined structures.

The basic principle of ultrasonic testing is linked to the reflection/transmission phenomena, which occur when ultrasonic waves travel across an interface between media of different acoustic impedance.

The acoustic impedance is defined as:

$$Z=\rho c \tag{2.3}$$

being ρ the density of the medium and c the ultrasonic wave velocity. Consequently, Z is strictly related to the material nature (table 2.1).

MATERIAL	ULTRASONIC VELOCITY				
	Longitudinal		Transverse (Shear)		Impedance
	in / μs	mm / μs	in / μs	mm / μs	Z
Fiberglass	0.124	3.15	0.068	1.727	6.04
Graphite/Epoxy	0.117	2.972	0.077	1.956	4.65
Boron/Epoxy	0.131	3.327	0.072	1.829	6.38
Aluminum 2024-T4	0.251	6.375	0.124	3.150	17.6
Steel 4340	0.230	5.842	0.128	3.251	45.6
Concrete	0.167-0.207	4.242-5.258	0.135	3.429	12.4
Glass (Plate)	0.227	5.766	No Shear Component		14.5
Quartz, Natural	0.226	5.74	0.139	3.531	15.2
Water (20C)	0.058	1.473	No Shear Component		1.48
Air (20ºC)	0.014	0.356	No Shear Component		0.00041

Table 2.1. Some of the most common materials acoustic properties.

As the Snell's law for electromagnetic waves allows reconstruction of transmitted and reflected waves directions in media with different refraction index, similarly for ultrasounds, the angles of the reflected and the transmitted

waves are linked to the velocity in both media A and B (fig. 2.5), by the following relation:

$$\frac{sin\alpha_I}{sin\alpha_T} = \frac{c_I}{c_T} \tag{2.4}$$

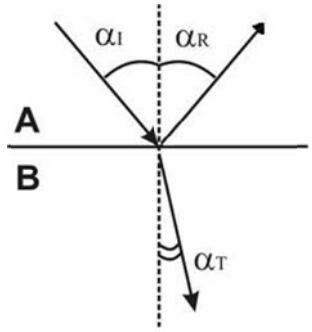

Figure 2.5. Snell's law for ultrasounds.

Unlike what happens to the electromagnetic waves, depending on the incidence angle, more than one propagation mode could be induced in the material (as an example, both the longitudinal and the transverse mode can be induced).
In some cases, for example, in presence of defects, having orientation parallel to the propagation direction which cannot be detected using the common longitudinal incidence waves, the most effective induced mode must be selected. For this reason, transducers with adjustable angular wedges in order to choose the proper incidence angle, are available on the market. Crossing an interface between two medias with impedances Z_A and Z_B, the wave intensity changes as explicitly expressed by the relation:

$$\frac{I_T}{I_I} = \frac{T^2 Z_A}{Z_B} \tag{2.5}$$

where T is the transmission coefficient.
Being I_I the incident intensity, Eq. 2.5 provides an estimation of the transmitted intensity I_T. From this relation, it rises clearly the reason why, for NDE purposes, a suitable coupling medium between the transducer and the material has to be used; indeed, it assures that the highest incident ultrasonic intensity enters into the inspected material, with the consequent reduction of energy

losses at the interfaces. As an example, if longitudinal waves are used, considering an air/CFRP interface, which involves an interface between two materials with strongly different impedance, the transmitted intensity is almost 0.03%, otherwise, it increases to 70% if water is used as coupling media instead of air.

These last are not the sole responsible of energy losses. A reduction of intensity is also associated with the wave propagation inside the material. In fact, materials can absorb and scatter ultrasonic waves, due to their intrinsic structure (in which there may be also slag inclusions, impurities or voids).

In NDE, a defect within a CFRP is schematically represented as an interface between different media, then reduction of the ultrasonic intensity is expected. Generally, when the defect size exceeds the wavelength, as in the case of delaminations or inclusions within laminas, the ultrasonic wave can be totally reflected according to the Snell's law (mirror like reflection). If the defect size is smaller than the wavelength, as, for example, could be metallic debris from cutting tools (due to manufacturing) or slag inclusions, the wave will be scattered under an angle, which depends on the ratio between the size of the defect and the wavelength. For very small defects (e.g., pores), the overall effect on the ultrasonic wave is a consistent energy attenuation, which is a function of the amount of pores.

2.3 Ultrasonic transducers for NDE

NDE based on ultrasound methodologies are based on the use of different types of probes depending on the inspection technique, shape and size of the inspected part, as well defect type.

The main part of a ultrasound probe (fig. 2.6) is the transducer which is made of a piezoelectric material [113]. The first type of transducer was made by quartz crystals [114] but most of the ultrasonic transducers used today are made by piezoelectric ceramic materials, which can be cut in various ways to produce different wave modes. Indeed, as soon as piezoelectric ceramics were introduced, they became the dominant material for transducers due to their good transmission properties and to their ease to manufacture into a variety of shapes and sizes. Such materials also operate at low voltage and are usable up to about 300°C. The firstly employed piezo-ceramic material was the barium titanate [115,116], principally used for contact transducers, which are probes where the transducer is in direct contact with the material surface. During the 1960's zirconate titanate based compounds entered the market [117,118]; such materials, at present, are the most commonly employed ceramics for transducers.

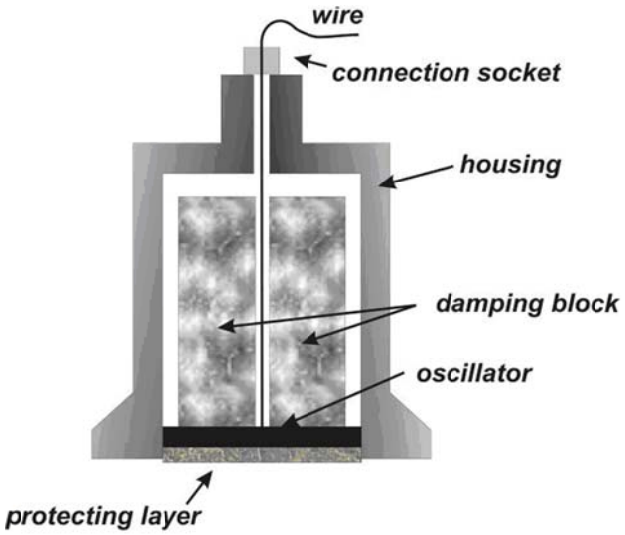

Figure 2.6: Schematic of a ultrasound probe with a piezoelectric plate.

When these transducers are employed in immersion testing (i.e. tests in which both the transducer and the sample are immersed in water), protection by water-tight covering layers is required. Usually the protection is made of cold-hardening resin, which is also used to assure the coupling impedances matching. The transducers surface geometry can be designed in such a way so as to obtain a focused ultrasonic wave beam or a better matching with non-flat sample surface. For special applications in which transversal mode wave is needed, the transducers are joined together with a plastic wedge which assures the proper inclination with respect to the plane of incidence of the wave beam, which guarantees the proper wave mode propagating within the material.

Progress in materials research had led to conceive the Ultrasonic Array (fig. 2.7) [65]. Such a device includes an array of piezoelectric elements which are arranged in order to increase inspection coverage and/or inspection speed. Each element is much smaller than the conventional ones used for a single transducer, and the excitation can be supplied either to each separate element, or to groups of them. This operational mode allows generation of wave-fronts which can be directionally controlled and shaped, by simply introducing a proper delay among elements [119].

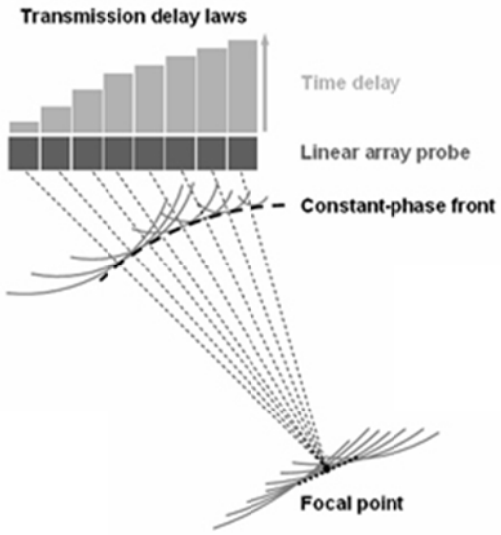

Figure 2.7: Principle of functioning of a ultrasonic array probe [120].

In the last fifteen years a big effort has been devoted to the development of probes and special signals treatment in order to make effective "air ultrasonic"

testing, which consists in testing without any media needed to couple the material and the transducer. Air is responsible of dramatic energy losses and this effect increases with increasing the probe frequency [121], so the major attention is put in creating probes and amplifiers able to compensate such energy losses. At present, devices for low-frequency applications (30Hz up to 100Hz) or for medium frequency applications (0.5 MHz up to 3 MHz) are available on the market; this last type is particularly useful for honeycomb composite inspection [122].

2.4 Inspection techniques

Two main techniques are used for ND ultrasonic testing: Through-Transmission (TT) and Pulse-Echo (PE) [123].

Through-Transmission, also known more simply as *transmission* technique, requires two transducers coupled at the opposite sides of the component under inspection; in such a way they face each other having the material in between. One transducer acts as transmitter while the other one as receiver (Fig. 2.8 part a). This configuration allows measuring the attenuation variations of the received signal, which is due to the passage within the material. Defects are outlined through the higher intensity decrease registered in correspondence of in-homogeneities with respect to the intensity reduction (attenuation) measured in sounds parts of the component. For the effectiveness of the inspection, it is important to carefully put the transducers aligned and perfectly orthogonal to the sides of the component under inspection.

TT is particularly suitable for detection of porosity [124], moreover, it has been demonstrated that the slope of the attenuation curves, which depends on the frequency of the applied ultrasonic signal, can be directly related to the amount of porosity in the material under inspection [84-86].

For the Pulse-Echo, (Fig. 2.8, part b) only one transducer is used, which works, alternatively, as transmitter and as receiver. In this way, information about the presence of flaws are provided by the amplitude and the time of flight of the reflected signal. To effectively carry out the test, the period of the excitation pulses of the unique transducer must be long enough, and its duration short, to avoid overlapping between transmitted and reflected waves. Thanks to this method, knowledge about the planar extension of the defects, their position through the thickness, as well as their 3D representation can be obtained [125]. The PE technique is widely used for porosity detection, fibre/matrix distribution [88], fibres orientation [126], interlaminar debonding as well as for detection of impact damage [127].

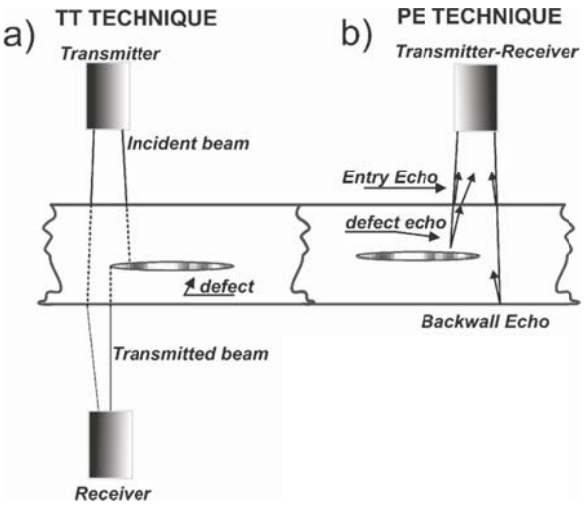

Figure 2.5: A schematic of the two most common inspection techniques: Through-Transmission (TT Technique) (a) and Pulse-Echo (PE Technique) (b).

An interesting combination of the two techniques is disclosed in patent US7823451 [128], in which, the time of flight and amplitude data coming from PE are compared to the amplitude data coming from TT in order to discriminate low porosity zones from other anomalies.

Both TT and PE can be applied using contact transducers; thus, special gels or oils are needed to assure the proper coupling with the inspected material. TT and PE can be carried out also in immersion; then, all the transducers and the material under investigation are submerged in water. To carry out ultrasonic immersion testing, a water pool is required and, depending on the dimensions of the tested component, a quite large pool is often required. When a large pool cannot be realized or the parts to be inspected are very large, jet probes (*squirters*) are preferred. The latter are transducers provided with a laminar water jet which impinges on the component surface acting as a wave guide for the ultrasound beam as described in Patent US 4507969 [129]. Water jet probes are widely used to carry out Trough-Transmission testing allowing a very quick control of large components.

Another largely used technique is the Double-Trough-Transmission (DTT). It is a sort of Pulse-Echo which involves a transducer headed to one side of the sample material and a glass mirror put nearby its opposite side. Because of the very large impedance with respect to water, the glass mirror acts as a perfect

reflector. In this way, the signal passes through water, the sample material, and then to water and vice versa. Being known both the distance of the mirror from the sample surface and the ultrasound velocity in water, the attenuation due to the material can be measured. Moreover, by DTT, the sample thickness and the ultrasound wave velocity in it, can be also measured [130], as well as the porosity as shown in Patent US6684701 [131].

Thanks to the glass mirror, separated echoes from each interface can be displayed, and, as a consequence, more accurate measurements of the interfaces position are obtained. In immersion, the transducer must be positioned precisely orthogonal to the sample surface that is usually achieved by computerized automatisms.

Regardless of the used technique, the received signals are turned into electrical signals by the transducers; thus, they can be amplified and displayed on an oscilloscope screen and/or acquired by suitable computer software which provides data visualization/representation.

2.4.1 Imaging techniques

Once the ultrasonic signal is received by a transducer it can be then easily displayed on an oscilloscope screen. This allows to study the signal and to understand the nature of the material inspected. In the following the most used imaging techniques are described.

A-scan

The simple signal representation on the oscilloscope screen, similar to that schematically shown in fig. 2.9, is known as A-scan. This imaging method is especially useful to assure correct positioning of the transducer, when it is required to be located orthogonal to the entry surface of the inspected material. Indeed, it can be monitored by moving the probe in order to maximize the signal of the echo produced at the entry surface (Entry-Echo, EE) of the material (fig. 2.9). Moreover, by choosing a transducer of proper frequency and diameter, the echo coming from the opposite side of the material is displayed; which is known as Back-Wall-Echo (BWE). When a defect is present, such as a delamination, the echo, which is due to the interface between defect and sound

material, is seen between the EE and the BWE. Depending on size and nature of the defect, the amplitude of BWE decreases as far as it disappears.

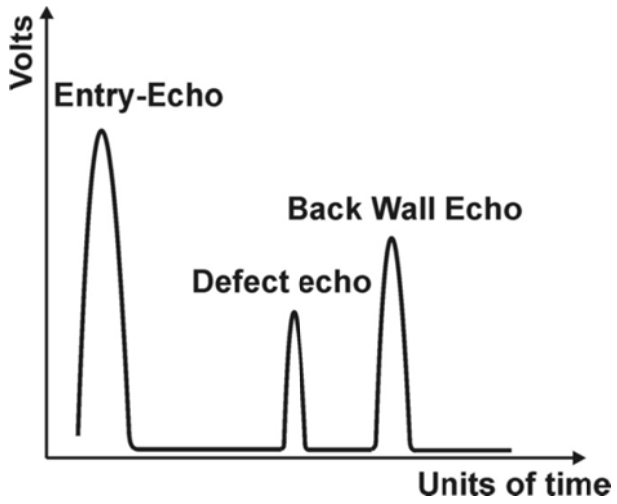

Figure 2.9: Schematic of the A-scan representation.

If the Pulse-Echo technique is used, by moving the transducer point by point on the sample surface, the signal, which is received by the transducer and displayed on the oscilloscope screen, appears like that schematically shown in fig. 2.9. Thanks to this technique, it is possible to reconstruct the distance of a defect from the surface. If the ultrasound velocity in the material is known, by measuring the time spent by the signal to reach the defect and came back to the transducer, known as *Time of Flight*, the depth of the defect can be calculated. It is important to notice that, for this type of test, the defect orientation plays an important role; indeed, a defect with its major dimension parallel to the ultrasound beam propagation may be undetected, even if widely extended.

In the A-scan imaging, the axial resolution depends on the wavelength and on the pulse duration. The spatial resolution depends on the distance between the transducer and the sample surface; indeed, it depends on the divergence of the beam and on the ratio between the transducer diameter and the wavelength.

B-scan

If the transducer is moved with a computed traversing system, it can acquire A-scans along a line (fig. 2.10a). Measurements can be graphically represented with the transducer position on the x axis and the time on the y axis. To each point of the obtained graph is associated a signal intensity, which is attenuated

by reflections and/or scattering phenomena, occurring nearby that point. Thanks to the B-scan, not only the position of a defect but also its extension along the scanning line is provided. The axial resolution is the same as for the A-scan, but the spatial resolution depends also on the scanning step (i.e. the distance between two successive acquisition points).

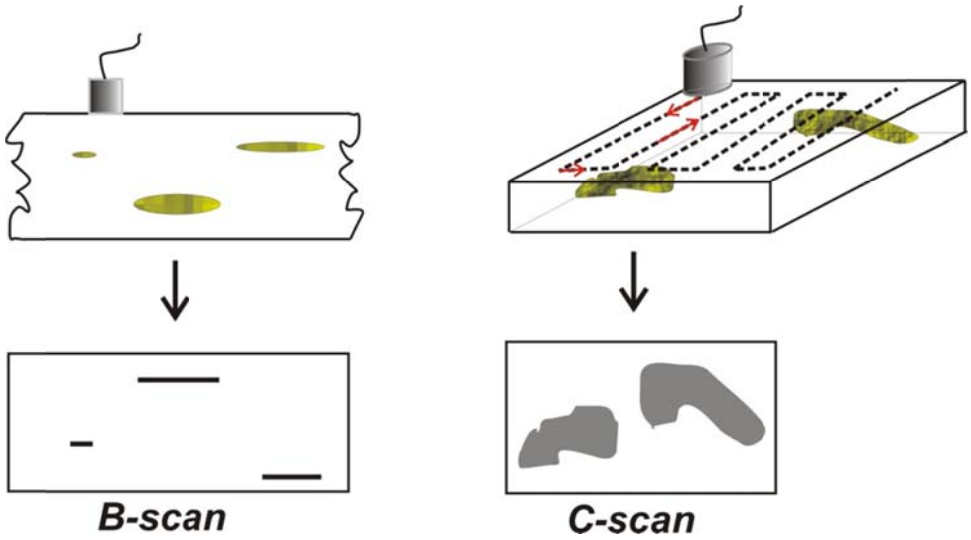

a) b)

Figure 2.10: A schematic of B-scan and C-scan imaging techniques.

C-scan

The C-scan is probably the most effective and used imaging technique. In this case, the transducer is forced to move along a Greek-fret pattern covering the entire sample surface as shown in fig. 2.10b. The C-scan supplies details about the planar extension of defects through their 2D projected image (see bottom of fig. 2.10b). When PE is used, a Time of Flight C-scan can also be obtained providing the position through the thickness of the defect.

Generally, the ultrasonic instrumentation is provided with "gates": time-amplitude windows in which only signals over/above a threshold are acquired in order to reduce the stored data.

Both axial and spatial resolution are the same as for the B-scan imaging.

2.5 UT for the detection of bulk porosity

As already stated in Sect. 2.3, the overall effect of porosity on the ultrasonic propagation within a media is recognizable through the appreciable reduction of the signal intensity across the material under inspection.

Moreover, it has been shown that there exists a strong correlation between the signal attenuation and the amount of porosity in a material. For lack of simplicity this result, already shown in the previous chapter (section 1.5), is here again reported in fig. 2.11.

In theory, both TT and PE techniques are suitable for gaining knowledge about the decreasing of intensity due to porosity, because both provide accurate attenuation measurements.

For the purposes of this dissertation, PE was chosen because, due to the double passage of the signal within the porous samples, the effect of porosity is, *de facto*, amplified.

In particular, PE in immersion is used. This techniques is performed by submerging in water both the transducer and the sample under test. This, thanks to the water coupling, assures a continuous and constant impedance matching between the piezoelectric transducer, producing and detecting the ultrasound, and the material to be analysed. Of course, that implies that specific transducers for ultrasonic immersion testing must be used.

Bearing in mind the schematic arrangement shown in fig. 2.5 (b), it is easy to understand that, in a PE inspection, the total attenuation $A_{T,}$ undergone by the signal, can be assumed as given by the sum of two principal contributions:

$$A_T = A_R + A_B \tag{2.6}$$

In equation 2.6, A_R are the losses due to the reflections of the signal at the encountered interfaces, which are water-specimen and specimen-water and A_B is the total bulk attenuation due to the double passage across the specimen. Therefore, the measure of the attenuation of the echo coming from the Back

Wall (fig. 2.9), provides the measure of the total attenuation experienced by the signal, A_T.

From literature [132], the intensity decrease of a ultrasonic signal I_0 propagating within a material, is well described by the classical Beer-Lambert law:

$$I(z) = I_0 e^{-\beta z} \tag{2.7}$$

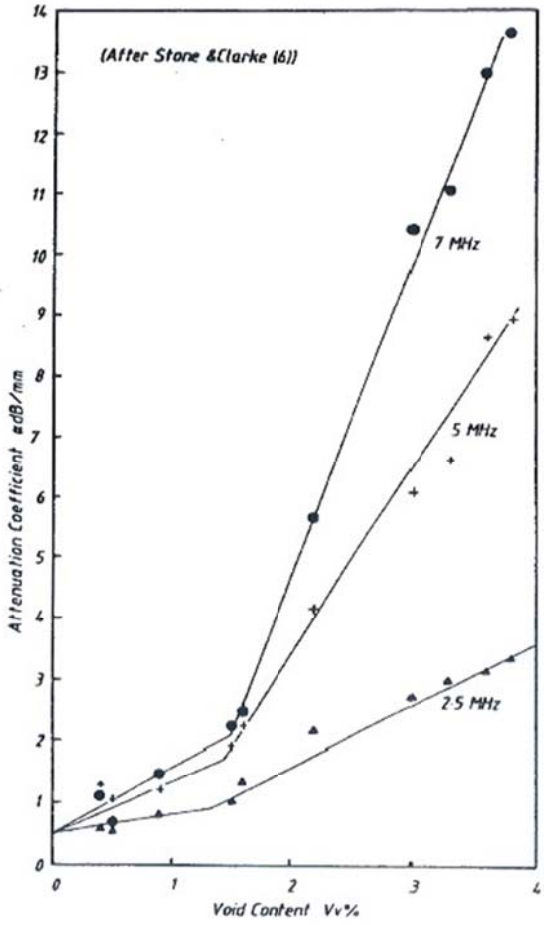

Figure 11: Attenuation coefficient vs. void content in CFRP [84].

In equation 2.7, z is the path length of the ultrasonic wave and β is the *attenuation coefficient* of the material.

From Eq. 2.7 and the Decibel definition, it follows that:

$$\beta z = 10\ Log \frac{I_0}{I} dB \tag{2.8}$$

So, the attenuation coefficient in dB, can be obtained from the total attenuation, $A_{T,}$ which is the right member of the eq. 2.8, and by dividing it for the thickness of the sample material.

In order to obtain the attenuation coefficient, related to the bulk material, it is needed to know the losses, or as the same, the attenuation due to the reflection at interfaces. This can be obtained experimentally with several methods; the method used in this dissertation will be described in the next chapter 5.

Chapter 3

Infrared Thermography: theory and nondestructive testing techniques

It is well known that every object at temperature T above absolute zero (i.e., $T > 0$ K) emits electromagnetic radiation in the form of rays which mainly fall into the infrared portion of the electromagnetic spectrum [133]. Such electromagnetic radiation, also called infrared radiation, or thermal radiation, moves from one place to another one through electromagnetic waves like visible light but of longer wavelength. To the "eye in the infrared" (i.e. an infrared imaging device), the world reveals features not apparent to the visible eye. In fact, through conversion of the detected energy into thermal images, every object, animal, or human being whose temperature is higher with respect to its background, can be discriminated regardless of the available visible light. In addition, in the infrared, visibility is improved in adverse conditions such as smoke or fog.

Infrared Thermography has to be considered as a relatively young methodology for NDE assessment of materials. Actually, infrared based techniques were known since the early part of the '900, but their major celebrity was achieved starting from the '80 with the understanding and exploitation of heat transfer mechanisms. Since then, a huge improvement followed leading to the addition of Thermography among the ASTM recommended practice for CFRP inspection; from that, also recommendations for qualification and certification of the personnel involved with IRT in NDE have been included in the Aeronautical Standard EN4179.

Infrared Thermography, due to its versatility and variety of applications, can also be used for thermo-physical materials characterization. Indeed, there are some specific techniques for emissivity coefficient measurement, as well as for thermal diffusivity and thermal conductivity. In this dissertation, a technique

for diffusivity evaluation has been used, as well as Lock-In thermography, both in reflection and in transmission modes, for NDE assessment of CFRP.

3.1 Some historical hints on Infrared Thermography

Infrared thermography (IRT) is generally considered a recent inspection technique because has been included among the ASTM standardized NDE methods only a few years ago. Nevertheless, the Russian scientist Vladimir Vavilov [134] has found traces of its use in non-destructive inspection during the early years of the '900. The first infrared device was patented in 1914 by Parker [135], which was used for icebergs detection, although he attempted also to distantly distinguish human and animal beings. Twenty years after, in 1934, Barker [136], proposed a system for forest fire detection. In the same period, Nichols suggested the first industrial application [137], to control the heating uniformity in steel strips.

However, the idea to produce the very first commercial infrared system (named AGA Thermovision) was conceived at the Swedish Defence Department (FOA) in cooperation with AGA in the 1950s. An almost complete historical evolution of infrared imaging devices can be found in [138]; herein, only some of the most important steps are reported. The first infrared camera prototype was devoted to military applications. It was based on a thermistor bolometer detector type, which is the technology mostly used nowadays. The principle of operation was pretty simple and smart, but the time required to obtain a thermogram was very long (about fifteen minutes). The initial devices, manufactured before the second world war, were based on semiconducting diode detectors obtained from indium antimonide or lead-tin-telluride materials; the single detector was provided with mechanical scanning to form a complete image.

It is reported of an airborne optomechanical IR imaging system developed by Barnes (USA) in 1954. This opened the way to the development of Forward Looking Infrared (FLIR) systems, which were mounted on aircraft and operated with line scanning only since the frame scanning was assured as due to the airplane movement.

The system evolution went on and at the end of the 1950s a second prototype named TS1 (Thermal Sight) was presented. To make the image presentation faster, a higher number of sensors was used involving both vertical and horizontal scanning. The demand for higher sensitivity and faster frame rate, made the researcher to move further on and, in the beginning of 1960s, the Swedish Defence Department started to use a new scanning principle together with a fast InSb LN2 cooled detector. In the meantime a new scanning concept was designed and patented by FOA and tested by AGA; the novelty resided in a fast refractive horizontal prism.

Figure 3.1: AGA Thermovision 661 in the 1960s. [138]

Between 1964 and 1965 the first commercial infrared system entered the market. This was the AGA Thermovision (fig. 3.1) which was firstly used for inspection of the electronic plants (fig. 3.2) and, successively, it was employed for specific NDE use to check the integrity of the Polaris missiles motor casings [139], and nuclear reactor fuel elements [140].

Being the first IRT approaches rather qualitative, in the frame of the NDE applications, at that time the interest was generally turned on other techniques much more reliable such as UT. This mainly because of lack of basic knowledge regarding the output of the infrared imaging device and the thermal behaviour of the part under inspection. At that time, there were no well assessed testing procedures and the interpretation of thermograms was rather difficult. Later, it

was thanks to the exploitation of heat transfer mechanisms [141] for the interpretation of thermograms that IRT received renewed attention.

Figure 3.2: AGA Thermovision 661 used for electronic plants inspection in 1969 [138].

From 1970 to 1990 there has been a huge development of infrared devices for civil applications by AGA, which later become Agema and further on Flir. The Thermovision 870, released by the Agema in 1986, represented a milestone since it was the first device equipped with a thermoelectric cooling system and the first of a generation of cameras capable to satisfy the most demanding IR applications for a long period of time. The reason of this success was the full range of detectors, lenses and accessories available. Another important event was the release of the Focal Plane Array (FPA) technology by the US military in the late 1980s, which entered the civil market in 1995 with the Thermovision 1000 by Agema. FPA is the technology actually in use coupled with both uncooled and cooled detectors.

This progress in the infrared cameras technology has led the American Society of Non destructive Testing (ASNT) to include the IRT among the standardized techniques for NDE applications. Indeed, in 2007 the ASNT updated the already existing recommended Practice for the personnel involved in nondestructive tests, including Flash Thermography between the NDE recommended techniques for the inspection of CFRP for Aeronautical applications [142].

3.2 IR radiation: theoretical principles

The theory of InfraRed Radiation is the result of over 40 years of research from many scientists starting with the Kirchhoff's enouncement of his law in 1859 and his blackbody definition in 1860, followed by the work of Stefan (1879) and Boltzmann (1884), the Wien's law in 1893, among others, and culminated with the enouncement of Planck's law in 1900.

In a paper published in 1900, Planck proposed a mathematical solution to characterize the radiant energy distribution over the entire frequency spectra. To explain this results, he conceived the revolutionary idea that energy is radiated in discrete units named *quanta*, rather than as a continuum stream as described by classical physics. He introduced a universal constant that he called *quantum of action*, which is better known as the Planck's constant, *h*. Although not fully understood at that time, Planck's concepts were gradually adopted by the scientific community forming the basis of the *Quantum Theory* and marking the beginning of a new era in Physics.

Following the Planck's theory, all matter regardless of its state or composition continuously emits Electromagnetic (EM) radiation, if its temperature is above the absolute zero. The emitted radiation can be viewed either as the transportation of tiny particles called *photons* or *quanta* or as the propagation of EM waves. This so called Wave-Particle Duality [143], is very convenient in describing EM behaviour.

For instance, the amount of energy radiated by a photon, E (i.e. a particle measure), can be directly related to the corresponding wavelength λ, or frequency *f*, of a wave, through the following relationship:

$$E = h \cdot f = \frac{hc}{\lambda} \tag{3.1}$$

where h = 6.6256 x 10^{-34} Js is a universal (or Planck's) constant, and c=2.9979 x 10^8 ms is the speed of light.

3.2.1 Black Body Radiation

In 1860, Gustav Robert Kirchhoff (1824-1887) defined a *blackbody* as a body that neither reflects nor transmits incident radiation. Instead, a blackbody absorbs all incident radiation coming from all directions and covering the whole wavelengths spectra. In addition, to be a perfect absorber, a blackbody is also a perfect radiator. Therefore, a blackbody is able to emit 100% of its energy; none body can emit more energy than a blackbody. In addition, a blackbody is a diffuse emitter, i.e. the emitted radiation is a function of wavelength and temperature but independent of the direction.

Max Planck found an expression describing the spectral distribution of the radiation intensity from a blackbody, which is known as the *Planck's Law*:

$$E_{\lambda,B}(\lambda,T) = \frac{C_1\lambda^{-5}}{e^{\left(\frac{C_2}{\lambda T}\right)}-1} \tag{3.2}$$

where $E_{\lambda,B}$ is the energy spectral density of the blackbody, C_1=3.742 x 10^{-16} W/m^2 is the *first radiation constant*, and C_2=1.4389 x 10^{-2} mK is the *second radiation constant*.

Equation 3.2 is plotted in figure 3 as a function of the wavelength for some specific temperature values.

In 1879, Josef Stefan (1835-1893) experimentally determined a simple expression relating radiant emission from a surface to its temperature. Stefan's results were theoretically confirmed in 1884 by one of his former students, Ludwig Boltzmann, (1844-1906).

The resulting expression, known as *Stefan-Boltzmann Law*, states that the total radiant emission of a black body, integrated all over the wavelengths, is proportional to the fourth power of its absolute temperature:

$$E_B = \sigma \cdot T^4 \tag{3.3}$$

where σ=5.6697·10^{-8} W/m^2 K^4 is the Stefan-Boltzmann constant. Eq. (3.3) can be obtained by integrating Planck's Law, eq. (3.2), over the entire spectrum ($0<\lambda<\infty$).

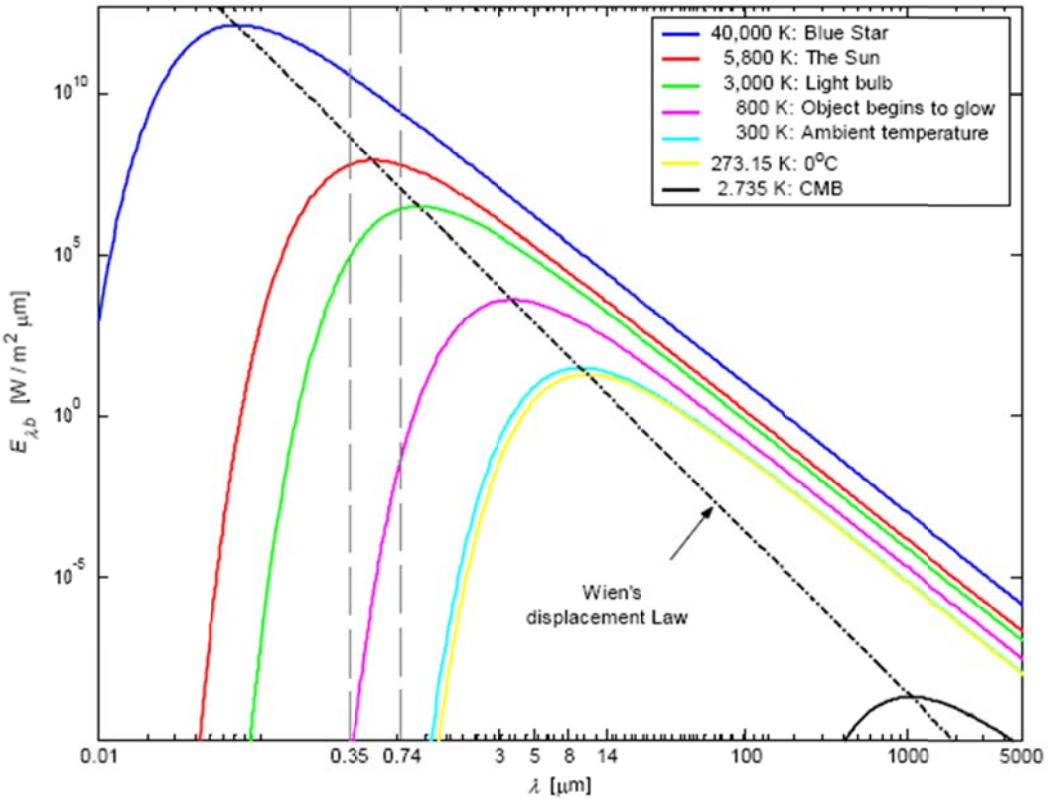

Figure 3.3: Planck's distribution at different wavelength [144].

Stefan-Boltzmann's Law gives the total flux integrated over all frequencies (or wavelengths). Now, the frequency (or wavelength) at which Planck's distribution has the maximum specific intensity (marked as a straight dotted line in fig. 3.3) is given by the *Wien's displacement Law*. In 1893, Wilhelm Wien (1864-1928) measured the spectral distribution of a blackbody at different temperatures. Wien found that the peak energy is emitted at a wavelength λ_{Tmax} which inversely varies with the temperature, that is:

$$\lambda_{Tmax} \cdot T = C_3 \tag{3.4}$$

where C_3=2897.8 μm K, is the *third radiation constant*. This relationship can be obtained by differentiation of eq. 3.2 with respect to λ, and setting the result equal to zero (in order to find the maximum).

Wien's law gives an indication of the "colour" of the thermal radiation. Wavelengths in the visible area of the electromagnetic spectrum, i.e. between 350 and 740 nm, see fig. 3.4, are associated with high temperatures.

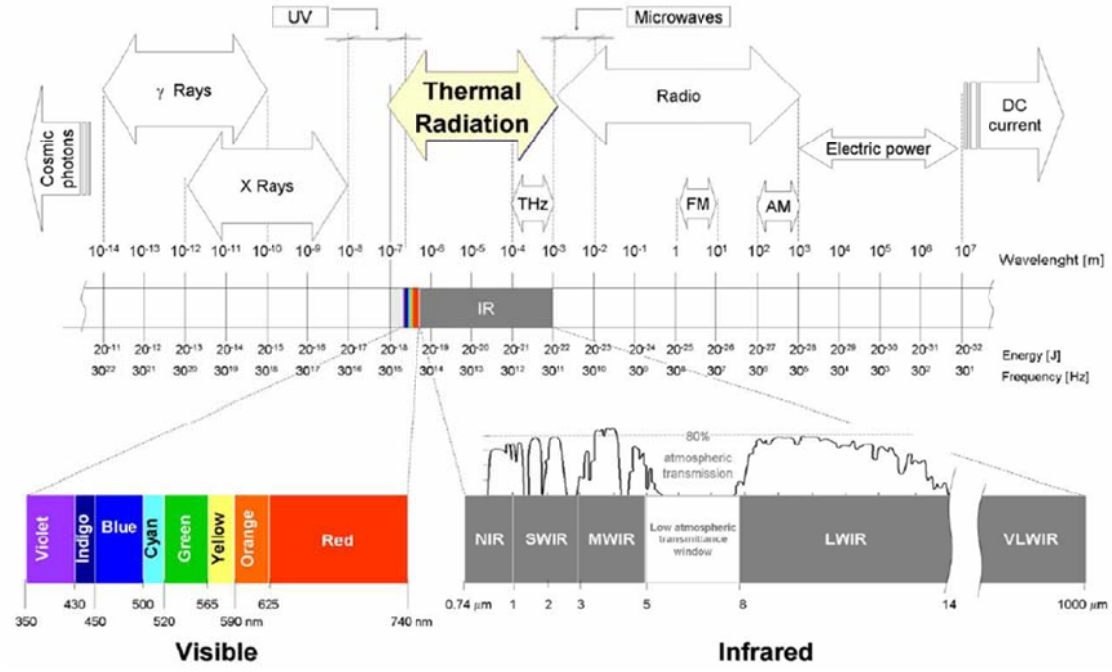

Figure 3.4: The EM spectra.

The thermal radiation band generally lies between 0.1 and 1000 μm (it is highlighted in fig. 4) enclosing part of the Ultraviolet (UV), the visible and the Infrared (IR). The infrared band of the spectrum (0.74÷1000 μm) can be, for the lack of convenience, further subdivided into five parts: Near Infrared (NIR) from 0.74 to 1 μm; Short Wavelength Infrared (SWIR) from 1 to 3 μm; Medium Wavelength Infrared (MWIR) from 3 to 5 μm; Long Wavelength Infrared (LWIR) from 8 to 14; and Very long Wavelength Infrared (VLWIR) up to 1000 μm. This subdivision is based on the atmosphere *transmissivity windows*, i.e. the wavelength bands where the atmosphere is the most transparent as possible for the IR radiation (fig. 3.5). In these windows the percentage of transmitted IR radiation can reach the 80%. Infrared detectors are generally conceived to work

in specific transmissivity windows; the mostly used are the MWIR and the LWIR.

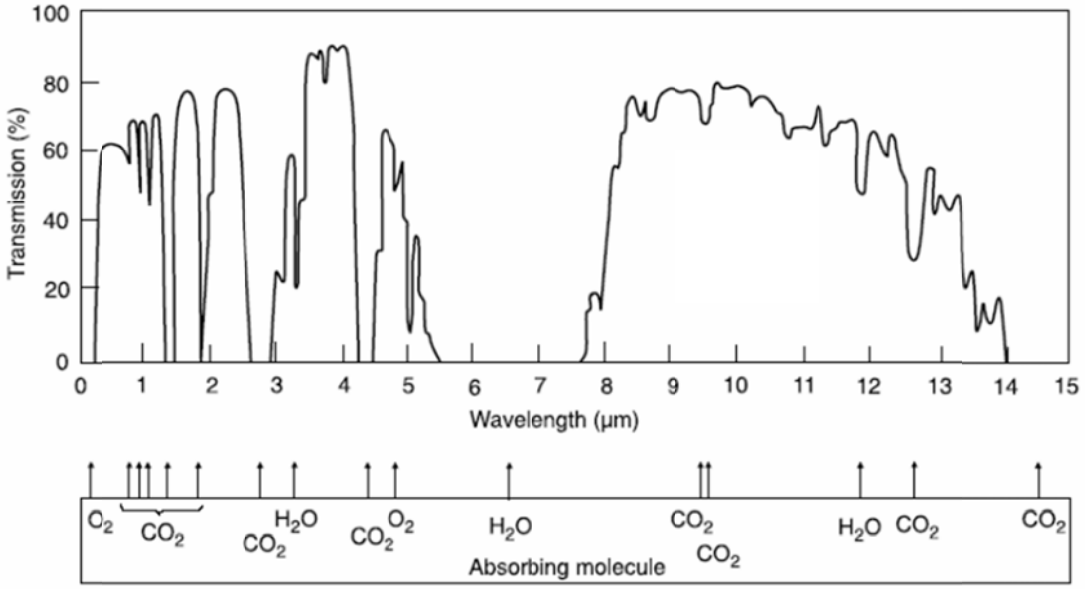

Figure 3.5: Atmospheric transmissivity windows [145].

3.2.2 Real Body Emission

Kirchhoff approached the problem of the EM emission of real bodies, defining the *emissivity* ε, as the ratio of thermal radiation emitted by a real surface with respect to that of a blackbody at the same conditions (temperature, wavelength and direction):

$$\varepsilon(\lambda, T) = \frac{E(\lambda,T)}{E_B(\lambda,T)} \tag{3.5}$$

From this definition, emissivity can vary between 0 and 1; depending on this value four types of sources can be distinguished [145]: a blackbody (perfect radiator), for which $\varepsilon(\lambda,T)$=1; a greybody for which $\varepsilon(\lambda,T)$ <1 is independent of λ; a whitebody (perfect reflector), for which $\varepsilon(\lambda,T)$=0; and a selective radiator, for which $\varepsilon(\lambda,T)$ varies with λ. It is worth nothing that with the term whitebody is indicated a perfect reflector not a white surface since the colour of a surface is not a significant parameter for emissivity; more specifically, a white paint may have higher emissivity with respect to a black one. In the NDE field, generally greybodies are inspected, and as a consequence, the Planck's Law becomes:

$$E_{\lambda,}(\lambda, T) = \varepsilon \frac{C_1 \lambda^{-5}}{e^{\left(\frac{C_2}{\lambda T}\right)} - 1} \tag{3.6}$$

In general, a body can absorb, transmit and reflect impinging radiant energy G. The absorptivity α, measures the fraction of energy absorbed by a surface, for the Kirchhoff's law:

$$\alpha = \varepsilon \tag{3.7}$$

and so α=1 for a blackbody, whilst α=0 corresponds to a white body; for real surfaces α<1. More specifically, a blackbody absorbs all the incident radiant energy G, a white body reflects back all the incident energy while a real surface absorbs a fraction α of the incident radiant energy G.

As was the case for emissivity, absorptivity depends on direction and wavelength, but is only slightly affected by surface temperature.

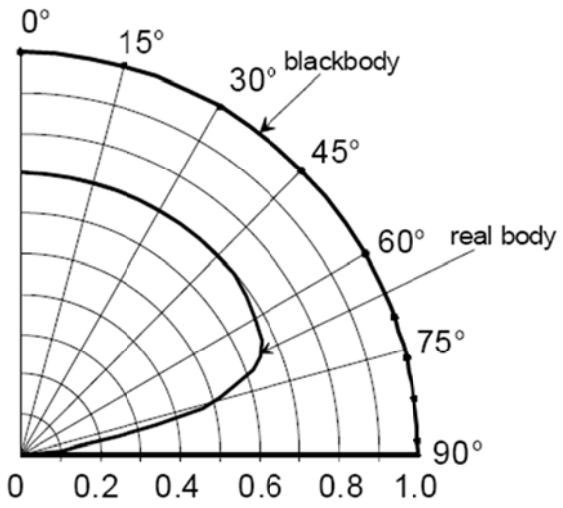

Figure 3.6: Directional emissivity.

It is worth nothing that emissivity is less sensitive to temperature variation for wide temperature ranges, while it is strongly dependent on the surface finish and on the angle of view, i.e., for a dielectric material, the maximum emission occurs in the direction normal to the radiating surface and decreases becoming null for a direction parallel to this surface. Only a blackbody emits radiation

uniformly in all directions and the distribution takes the appearance of semi-circumferences (fig. 3.6).

The reflectivity ρ is defined as the fraction of the incident radiation reflected by a real surface with respect to *G*. Although reflectivity depends on the direction of both the incident and reflected radiation, it is convenient to work with integrated average to avoid complication. If a surface reflects radiation in all directions regardless of the direction of the incident radiation, the surface is said to be diffuse. Conversely, if radiation is reflected with an angle equal to the incident one, the surface is said to be specular.

Absorptivity and reflectivity are responsible for our perception of colour. Colour is not the result of emission, since only objects at high temperature (higher than ~800 K) glow in the visible portion of the spectra. Instead, colour is the result of a balance between reflection and absorption. A surface is white if it reflects all incident radiation in the visible spectra, and it is black if it absorbs all the irradiation. Colour, however, does not give an indication of the absorbed or reflected radiation which mostly occurs in the IR band. The typical example is the snow, which is highly reflective at visible wavelengths (between 350 and 750 nm), but absorbs and emits IR radiation strongly, approximating a blackbody at longer wavelengths.

The transmissivity τ is defined as the ratio of the directly transmitted radiation after passing through a participating medium (slab, atmosphere, dust, fog) to the amount of radiation that would have passed the same distance through a vacuum. Dissolved colloidal and suspended particles cause further attenuation by absorbing and scattering effects. Higher attenuations are observed at long wavelengths. Transmissivity is of importance when selecting the spectral band of operation of the IR equipment.

So, the behaviour of a body, once it is impinged by a EM radiation, involves all the above described phenomena. In general, a body may absorb, reflect, and transmit a part of the incident energy *G*; for the energy conservation law (first law of thermodynamics) it follows:

$$G = \alpha G + \tau G + \rho G \tag{3.8}$$

which in terms of specific properties gives:

$$\alpha + \tau + \rho = 1 \tag{3.9}$$

3.3 IR detectors

Infrared detectors are transducers of radiant incident energy.

The more used infrared detectors can be grouped in two main types [146] (fig. 3.7):

- thermal detectors
- quantum/photon detectors

and can be classified as cooled and uncooled infrared detectors [147,148].

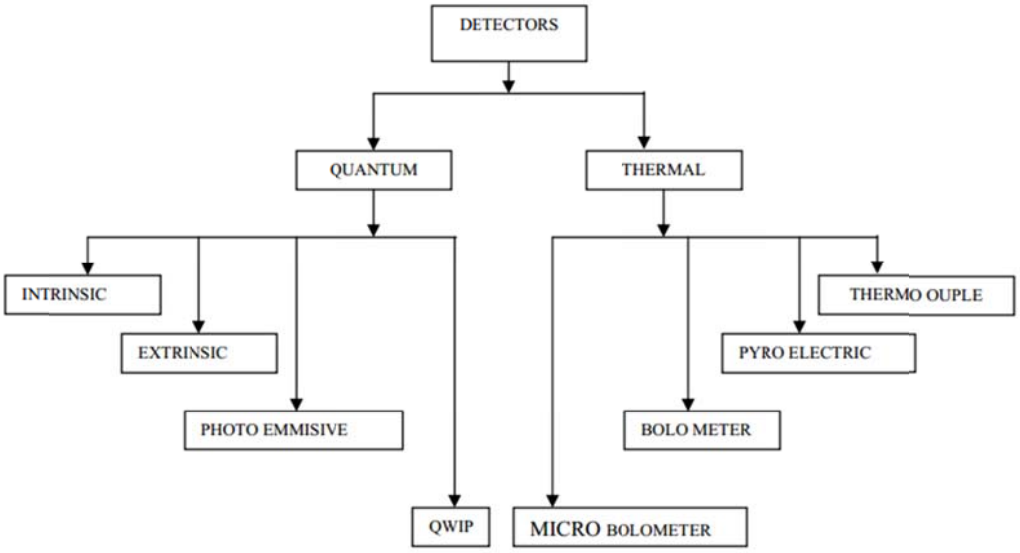

Figure 3.7: Types of IR detectors [146].

Cooled detectors need to be cooled down to temperatures greatly below to that of the ambient in order to get very rapid scanning rates, high sensitivity and low noise. In the past cooling systems were made with Dewar flask filled with liquid nitrogen LN_2 (77 K). Today systems include miniature coolers based on the thermoelectric Peltier effect or the Stirling cycle and do not require any external cooling source. Uncooled detectors work at ambient temperature using small elements for temperature control. The working mode of these devices is based on changes of some properties such as electrical resistance, voltage or current once they are impinged by infrared radiation. These changes are then

measured and compared to the values of the operating temperature of the sensor.

3.3.1 Thermal detectors

The working mode of thermal detectors is based on the variation of the electrical resistivity of a semiconductor once it is impinged by a radiation. The output signal is practically constant regardless of the frequency; the response time is higher than the time needed by the photons detectors. Thermal detectors can be classified as thermometers, thermocouples, thermopiles, bolometers and newer microbolometers and microcantilevers.

Thermopiles functioning is based on thermoelectric effect. They are obtained by a certain number of thermocouples connected in series. Each thermocouple is made by a junction between two different materials. Once the junction is heated, an electric potential difference rises across it due to the Seebeck effect. This electric potential is proportional to the induced temperature variation with respect to the ambient which allows to measure the actual temperature. The first thermopiles were simply made using thin wires of, as an example, copper-constantan. Nowadays these devices are made with thin films deposited on a substrate allowing reduced dimension, moreover their sensitivity can be enhanced by encapsulating the thermopile in a low thermal conductivity medium (i.e., to avoid losses to the surroundings).

Bolometers allow to measure temperature through electrical resistance variations induced by temperature changes [149]. Typically they are based on a weathstone bridge: once one of the two bridge's branches is heated by a thermal radiation it changes its resistance of a quantity proportional to the change of temperature. Today microbolometers can be found which are obtained thanks to micromachining of silicon: a grid of vanadium oxide or amorphous silicon heat sensors over a porous silicon bridge as thermal isolating and mechanical supporting structure. The microbolometer grid is commonly found in two sizes, a 320×240 array or less expensive 160×120 array.

Pyroelectric detectors as their name says, are based on the pyroelectric effect: once the temperature of the crystal increases its surface charge varies due to the

dipole moment changes. For continuous operation, the common technique is to incorporate a chopping device inside the optical system and to create an AC output signal; the spurious signals caused by low-frequency ambient temperature can be filtered. Triglycine sulfate (TGS), lithium tantalate ($LiTaO_3$) and polyvinyl fluoride (PVF2) are materials that exhibit the pyroelectric effects.
Microcantilevers are based on the thermal expansion of bimetals [150] e.g., silicon nitride and gold film. Due to the different expansion, when the bimetal temperature changes, one element will expand more than the other, causing the device to bend out of plane. The actual temperature can be measured if the degree of bending is known.

3.3.2 Photon detectors

Photon detectors convert incident photons directly into free current carriers by photoexciting electrons across the energy band gap of the semiconductor to the conduction band. This produces a current, voltage or resistance change of the detectors. The photoexcitation is caused by the radiation interacting directly with the lattice sites. Therefore, the temperature of the detector must be low enough so that the number of carriers thermally excited across the bandgap is less significant (i.e. the charges produced by the impinged radiation must be higher than the thermal noise charges). To maintain a low temperature, cooling systems are required, which increase the system cost.
Four main types of photodetectors can be found Photovoltaic, Photoconductive (intrinsic and exstrinsic) [151], photoemissive and newer QWIPs.
Photovoltaic (PV) intrinsic detectors structure is based on a P-N junction device. Under IR radiation, the potential barrier of the P-N junction leads to the photovoltaic effect. An incident photon with the energy greater than the energy band gap of the junction generates electron-hole pairs and the photocurrent is excited. PV devices operate in the diode's reverse bias region; this minimizes the current flow through the device that in turn minimizes power dissipation. In addition, PV detectors are low noise because the reverse bias diode junction is depleted of minority carriers. The best performances are obtained with

detectors fabricated from Si, Ge, GaAs, InSb, GaAs and MCT (Mercure-Cadmium-Telluride).

The photoconductive (PC) intrinsic detectors mechanism is to produce the conductance change under the IR radiation [152]. In this detectors, the free carriers generated by the photon energy cause increase of the conductance of photoconductive material under an applied constant electric field. The incident IR radiation is absorbed to generate holes and electrons. Under the applied constant bias, the resultant current level is proportional to the incident photon flux. Common materials are lead sulfide (PbS), lead selenide (PbSe) and mercury cadmium telluride (HgCdTe) [153].

Extrinsic detectors are based on Si (Si: X) or Ge (Ge: X) doped with impurities such as Boron, Arsenic and Gallium. They are similar to intrinsic detectors. However, in extrinsic detectors carriers are excited from the impurity levels and not over the bandgap of the basic material [154]. Both PV and PC types exist also as extrinsic. They have the advantage of being able to operate at much lower wavelengths than intrinsic type.

To avoid the extreme cooling demand of extrinsic semiconductor detectors and in some cases to reach even longer wavelengths, there is a third approach i.e. photoemissive detectors (PE), or freecarrier or Schottky-barrier detectors. In these detectors, a metallic compound, for example, platinum silicide (PtSi), is overlaid by doped silicon. A photon bounces an electron or a hole, out of the conductor into the silicon. The advantage of such devices is that the response does not depend on the characteristics of the semiconductor but on those of the metal, which are extremely uniform, so that high uniformity of response is much easier to achieve. However, absorption is proportional to the square of the wavelength, so for wavelengths of a few microns, efficiency and sensitivity are much less than for extrinsic devices.

The fourth main type of IR photon detector is the quantum-well IR photoconductor (QWIP) [155]. The operating principle is similar to that for extrinsic detectors. The dopants are used to alter the band structure. But in QWIPs, the dopants are concentrated into microscopic regions, creating quantum wells, where the band structure has shifted. Detection occurs when a

photon knocks an electron or hole out of the quantum well into the neighbouring band. QWIPs are much more sensitive than extrinsic types, because the entire quantum well, not just an individual dopant atom, acts as an absorber. Since quantum wells are 10-100 atoms across, their effective absorption area is much higher. QWIPs generally consists of layers of thin gallium arsenide (GaAs) alternated to layers of aluminum gallium arsenide (AlGaAs).

Most used sensors are effective in just one spectral band. In IRT the most used band windows are: NIR, MWIR and LWIR (fig. 3.3 and 3.4). In the midwave band the most used sensor is the InSb, photovoltaic type, especially effective in the range 3.5 ÷ 5.6 μm, which is the sensor of the thermal camera mostly used for this dissertation; usually together with this devices lens and other optical materials such as silica with antiglare coating are used, which assure the maximum transmittance at 5 μm.

3.3.3 Main characteristics of an infrared device

The modern infrared cameras, due to advanced detector materials and microelectronics, are mostly equipped with Focal Plane Arrays (FPA) (fig. 3.8) detectors which are now available in all the used (NIR, SWIR, MWIR and LWIR) spectral bands.

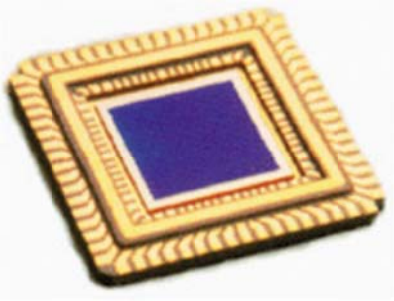

Figure 3.8: Example of FPA.

FPAs use either photon or thermal detectors. Photon detection is accomplished using intrinsic or extrinsic semiconductors and either photovoltaic, photoconductive, or metal insulator semiconductor technologies. Thermal

detection relies on capacitive or resistive bolometers. In all cases, the detector signal is coupled into a multiplexer and read out in a video format.

FPA where firstly conceived for military applications, but they entered the civil market in 1995 with the Thermovision 1000 by Agema. FPA is the technology mostly used for both cooled and uncooled detectors [156].

The performance of a detector is mainly evaluated through three parameters [157] that are: *Responsivity* R_v, *Noise Equivalent Power* (NEP) and *Detectivity D**.

The *Responsivity* R_v is a measure of the signal output S_{out} (voltage, or current) per incident radiation E_{in} over the active area of the detector A_{det}:

$$R_v = \frac{S_{out}}{E_{in}A_{det}} \tag{3.10}$$

The responsivity can also be written as:

$$R_v = \frac{\lambda \eta_q Q_e P_g}{hc} \tag{3.11}$$

with η_q the quantum efficiency, Q_e the electron charge, p_g the photoelectric gain.

The *Noise Equivalent Power* (NEP) defines the intrinsic noise level of the detector, or better the detection limit of the detector. It can be expressed by:

$$NEP = \frac{E_{in}A_{det}}{\frac{S_{out}}{N_{out}}\sqrt{\Delta f}} = \frac{N_{out}}{R_v\sqrt{\Delta f}} \tag{3.12}$$

where N_{out} the noise output and Δf the noise bandwith.

*Detectivity D** defines the resolving power of the detector and is expressed in terms of the signal-to-noise ratio with respect to the incident power:

$$D^* = \frac{S_{out}}{N_{out}}\frac{1}{E_{inc}}\frac{\sqrt{\Delta f}}{\sqrt{A_{det}}} = \frac{\sqrt{A_{det}}}{NEP} \tag{3.13}$$

The common units of D^* are cm $Hz^{1/2}/W$; often, in literature, this quantity is measured in Jones in honour to D. Clark Jones who defined this quantity in 1959.

Generally noise is due to two main causes: the noise intrinsic to the device circuits and electronics and to the environment radiation. Generally the first contribute is negligible, so the detection limit is evaluated by taking into account only the second contribution. This last is called Background Limited Infrared Photodetection (BLIP).

The radiation coming from the environment is known as background photon flux density or *dark current*. The amount of radiation received by the detector depends on its responsivity to the wavelengths contained in the radiant source and on its *Field Of View* (FOV) of the background.

A relevant parameter for infrared systems is the *Noise Equivalent Temperature Difference* (NETD); it is the temperature difference which would produce a signal equal to the camera's temporal noise, N_L. It is generally indicated as the minimum temperature difference which the camera can resolve and is given by:

$$NEDT = N_L \frac{\Delta T}{\Delta S_m} \tag{3.14}$$

In which ΔS_m is the signal measured for the temperature difference ΔT.

3. 5 IRT for NDE

IRT for NDE is aimed to the detection of subsurface features (presence of anomalies/defects), thanks to relevant temperature differences observed on the surface with an infrared camera. IRT can be carried out via two concepts: *passive* and *active*. The passive approach is addressed to test materials and structures which are naturally at a different (higher, or lower) temperature with respect to the ambient. On the contrary, the active approach involves an external stimulus in order to induce relevant thermal contrast in the object (supposing that the part under test is at thermal equilibrium with the ambient prior to testing).

In most of the applications, passive thermography is rather qualitative because its function consists of revealing temperature difference ΔT with respect to a reference one. However, thanks to proper modeling, also passive thermography could allow for quantitative measurements as can be found in literature mainly for maintenance of power generation [158] and electric facilities [159], for emissivity evaluation [160], for assessing the integrity of part of bridges [161] and so on.

For NDE purposes, the active approach is generally used. The active approach is characterized by the need of using a thermal stimulation source to get the needed information about the material, or the structure under inspection.

It allows, indeed, more accurate knowledge of the subsurface features, although an important condition must be accomplished for its effectiveness: the defect must be different enough from the rest of the hosting material, beyond a thermo-physical point of view, (i. e. its response to thermal stimulation must be different from the response of the surrounding material).

There exists not a single IRT technique to get information about the presence of flaws, their dimension, their position and so on. Moreover, the effectiveness of a test is strongly dependent on the nature of the material and its thickness, that is why several techniques have been developed starting from the *Heat Diffusion Theory*, such as Pulsed Thermography (PT), Stepped Heating (SH), Lock-In (LT), Pulsed Phase Thermography (PPT) and Vibrothermography (VT).

PT consists of exciting the material surface with a thermal pulse to increase its temperature of few degrees; this may be simply accomplished with a halogen lamp (or other methods). The behavior of the specimen is analyzed either during the rising surface temperature, or during the decay [162,163]. A transmission scheme is possible (infrared detector and stimulation unit on either side of the specimen) only if both surfaces are accessible, otherwise the reflection scheme must be adopted [164]. Anomalous temperature decay is the indication of presence of subsurface features. Stimulation could be of few millisecond duration in the case of highly conductive materials (metals) or of seconds in the case of lower conductivity materials (such as plastics, CFRP). It is very common due to the simplicity of application and interpretation of results.

SH consists of thermal excitation with a long pulse of low power. The heating pulse is long compared to the observation time and acts as a temporal step function. The start of the heating is synchronized with the thermal camera acquisition which covers the entire heating period. Also in this case variation of surface temperature (normalized with respect to the behavior in sound surface parts) with time are indication of subsurface anomalies. This technique is sometimes referred to as Time-Resolved-Infrared (TRIR) technique [165] and is particularly indicated for coating thickness evaluation [166] or of multilayered coatings.

LT is applied with a modulated heating source, such as a halogen lamp connected with a function generator, which launches a thermal wave inside the material to be inspected. The basic concept of modulated, or lock-in, thermography was described by Carlomagno and Berardi [167] and later further investigated by Beaudoin et al [168], Kuo et al [169], Busse et al [170] and Balageas et al. [171]. Subsurface features reflect the thermal wave, with a specific amplitude and phase delay. The term Lock-In refers to the need of monitoring of the exact time dependence between the output signal and the reference one (the modulated thermal source). This can be done by lock-in amplifier, or, in a more complex system, as the one used for this dissertation, by a computer software which provides module and phase maps. The phase maps are the major point of interest of this technique, due to their insensitivity to non uniform heating and from

surface features, further its penetration depth is almost twice that for module maps.

PPT combines the advantages of both PT and LT without sharing their drawbacks. It was introduced by Maldague and Marinetti in 1996 [172] and later analyzed by Vavilov and Marinetti (1999) [173]. For PPT applications the material is heated with a Dirak-like thermal pulse, so a mix of frequencies are launched in the object. By performing the Fourier transform of the temperature evolution over the field of view the phase, or magnitude, image can be presented as in LT. Deeper thicknesses can be inspected with less influence of surface infrared and optical features. A comparison between PT, LT and PPT applied to the evaluation of frescoes was performed by Carlomagno and Meola (2002) [174].

Vibrothermography is based on the heat generated by friction in discontinuity zones. Then, to apply vibrothermography, the structure under analysis is externally induced to vibrate, then heat is released by friction where the defects are located, at specific resonance frequency [175]. This local heating is revealed by the thermal camera.

In the following Fourier's Heat diffusion theory is briefly described since it is exploited for data interpretation. Some specific thermographic techniques are more deeply described, which are used for the experimental tests reported in this dissertation.

3.5.1 Heat transfer by conduction

It is known that, anytime there is a temperature difference T_1-T_2>0 in a physical system, a heat flux is generated which is directed from the hotter region to the colder one. This process continues until the physical system reaches a uniform temperature.

The way the heat flows depends on the nature of the transport mechanism which can be radiation, convection and conduction. In condensed matter the principal mechanism is the conductive one; so the rate of heat transferred per unit area in the direction x of a homogeneous material is governed by the *first Fourier's law*:

$$\dot{Q}_x = -k\nabla T(x) \tag{3.15}$$

where k, is the *thermal conductivity*.

Using eq. 3.15 in the energy conservation equation (the first principle of Thermodynamics) and assuming k constant, we obtain a parabolic differential equation, well known as the *heat diffusion equation*, often called *Fourier's second law*:

$$\nabla^2 T(x) - \frac{1}{\alpha}\frac{\partial T(x,t)}{\partial t} = 0 \tag{3.16}$$

The *thermal diffusivity* α depends on some physical properties of the material:

$$\alpha = \frac{k}{\rho c_p} \tag{3.17}$$

where ρ is the density and c_p is the *specific heat at constant pressure*.

Further, the product $\rho \cdot c_p = C$ is the *specific heat capacity*, or *heat capacity per unit volume*.

In a general sense, thermal diffusivity is the measure of thermal inertia. In a substance with high thermal diffusivity, heat moves rapidly through it because the substance conducts heat quickly relative to its volumetric heat capacity.

Another fundamental parameter is the *thermal effusivity* defined as:

$$e = \sqrt{k\rho c_p} = \frac{k}{\sqrt{\alpha}} = \rho c_p \sqrt{\alpha} \tag{3.18}$$

The effusivity determines the surface temperature of a body and its behaviour at interfaces in presence of periodic or transient heat sources.

A valid solution of eq. 3.16 [141, pg. 50] is given by the temperature pulse:

$$T(x,t) = \frac{1}{2\sqrt{\pi \alpha t}} e^{-\frac{x^2}{4\pi \alpha t}} \tag{3.19}$$

Eq. 3.19 is the well-known Gaussian function, which has the following property:

$$\int_{-\infty}^{+\infty} T(x,t)dx = 1 \qquad \text{for all t>0} \qquad (3.20)$$

The eq. 3.20 implies that heat diffuses all over the space (in this case along the x axis), whatever is *t*. This is known as the thermal paradox, because it involves the concept that heat diffuses with infinite velocity. This paradox, typical of parabolic equations, was resolved by Cattaneo [176]. He found that in equation 3.16, a term has to be added which is derived by the hypothesis that the heat flux does not depend only on the temperature gradient but also on the gradient of the temperature change rate:

$$\Phi_x = -k\nabla \mathrm{T}(x,t) + k\tau\nabla\dot{T}(x,t) \qquad (3.21)$$

In eq. 3.21, the time derivative term makes the heat propagation velocity finite, so the heat flux does not appear instantaneously but it grows gradually with the so called relaxation time, τ [177,178].
Using the 3.21 instead of the 3.15, we get a new diffusion equation where a second derivative of time appears: it is a hyperbolic equation also known as the Cattaneo equation:

$$\frac{\partial^2 T(x,t)}{\partial x^2} - \frac{1}{\alpha}\frac{\partial T(x,t)}{\partial t} - \frac{1}{v^2}\frac{\partial^2 T(x,t)}{\partial t^2} = 0 \qquad (3.22)$$

Here $v = (\alpha/\tau)^{1/2}$ is known as a (finite) velocity of propagation of the thermal signal, although it is just a collection of the terms α and τ.
For macroscopic solids at ambient temperature this time is of the order of 10^{-11} seconds so that for NDE purposes, where typically heating time is highly longer than the relaxation time of materials [179,180], the use of eq. 3.16 is adequate.

3.5.3 Pulse Thermography

Consider the case of a semi-infinite body of isotropic material, with the surface in x=0 which is subjected to a rapid thermal pulse with amplitude Q. The solid matter typically treated in NDE inspections, is generally of macroscopic

dimension, so, the proper starting equation for studying the heat propagation will be the eq. 3.16.

The one-dimensional solution of the Fourier Equation calculated in x=0 in this case is given by:

$$T(0,t) = T_0 + \frac{Q}{e\sqrt{\pi t}} \tag{3.23}$$

Where T_0 is the initial temperature.

Experimentally this situation can be reproduced with the arrangement shown in fig. 3.9, in the case that the reflected thermal signal is detected by the IR camera, and then processed by a proper software.

This allows to register the temperature-time trend on the surface of the inspected specimen. Specifically, what it is obtained pixel by pixel, is schematized in fig. 3.10.

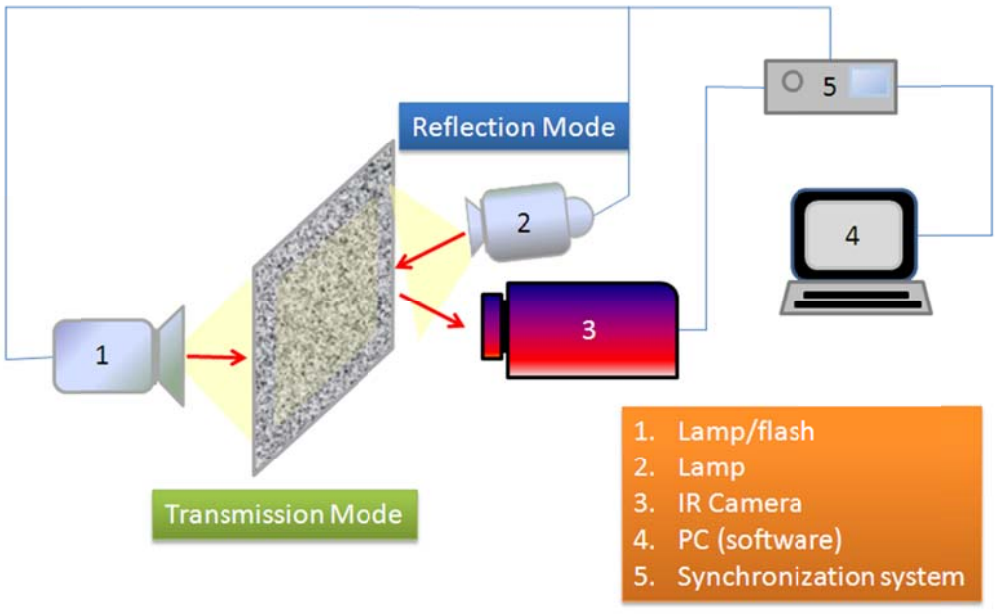

Figure 3.9: Typical arrangements used for NDE-IRT testing.

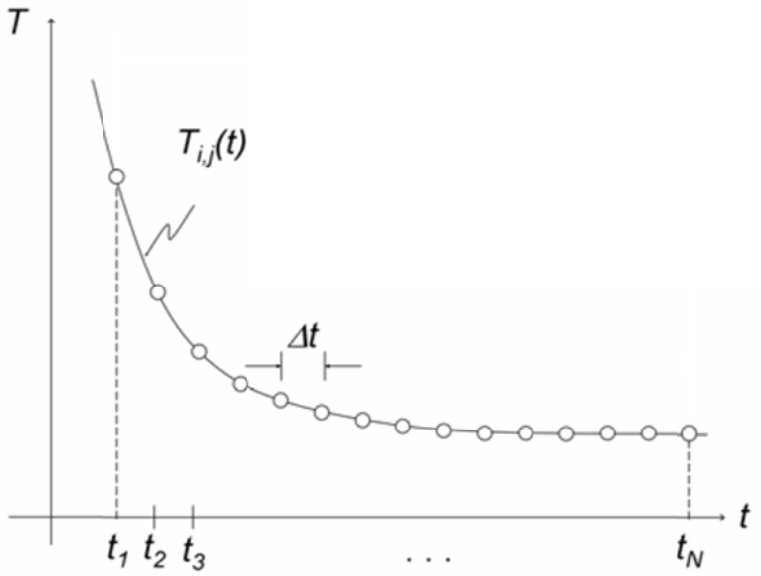

Figure 3.10: Temperature-frame cooling down registered by the single pixel i,j [144].

Once the maximum temperature is reached, the cooling down transient starts with a typical time-dependency like $t^{-1/2}$. Any deviation from this behaviour is related to the presence of subsurface features, like the example reported in fig. 3.11:

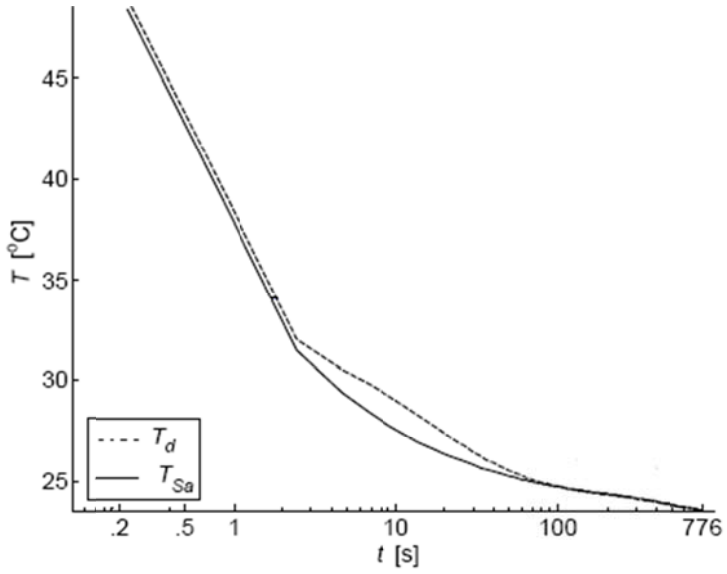

Figure 3.11: Temperature-frame cooling down registered by the single pixel i,j [144].

The temperature-time evolution of a defect area, T_d, shows a sort of bulge, with respect to that of the sound area, T_{Sa}, which is due to the reflection of the thermal signal at the interface between the material and the defect. The larger is the amplitude of the bulge the higher is the ratio between the effusivities of the two materials.

Thermal contrast defined as $\Delta T = T_d - T_{Sa}$ provides a good indication of defect characteristics (qualitative and quantitative) [181] when working with relatively shallow defects in homogeneous materials, which entail small non-uniformities at the surface , and the effect of non-uniform heating is the most reduced possible.
Indeed, the major difficulty in the application of PT is to obtain the proper uniform heating of the inspected surface. This can be easily reached if the surface is small with respect the used lamp, but for larger surfaces arrays of lamps can be used or, for some applications, it is convenient the Lateral Heating (LHT) method conceived by Grinzato et al. [182]. For the inspection of cavities and channels, when a strong heat pulse is required, the pulse thermography with *Injecting Water Vapour* (PTJV) may be convenient. PTJV was proposed by Meola et al. [183] to detect ceramic residuals in the tip of turbine blades.

3.5.2 Flash Thermography for diffusivity measurement

The measure of thermal properties of materials is constantly a matter of interest for scientists, especially in the field of NDE for two main reasons: first of all because this knowledge allows to develop models in order to predict the behaviour of materials and, as typically occur in experimental science, because from the measure of a single parameter many others can be estimated. This is the case of thermal diffusivity.
Due to the definition of thermal diffusivity, its measure can be very useful for materials characterization, due to the density and thermal conductivity dependence, which are affected by the presence of pores
This is well known for a specific class of materials such as the ceramic Carbon-Carbon, for which the linearly dependence between the amount of porosity and the diffusivity has been demonstrated [184]. Studies on other types of composites for Aeronautical applications have shown that the diffusivity measure is a very effective tool to evaluate porosity [185-189].
Among the possible methods involving IRT, the following described one is the first introduced in 1961, by Parker et al. [190] for the thermal characterization of materials through a thermal device and a Dirac-like heating source. It is a special

application of the Pulse Thermography above described and applied in the transmission mode.

The solution of the eq. 3.16 for an isotropic slab with parallel surfaces thermally insulated and uniform thickness L, will be [141, pg. 101]:

$$T(x,t) - T_0 =$$
$$= \frac{1}{L}\int_0^L T(x,0)dx + \frac{2}{L}\sum_{n=1}^{\infty} exp\left(\frac{-(n\pi)^2 \alpha t}{L^2}\right) cos\frac{n\pi x}{L}\int_0^L T(x,0)\, cos\frac{n\pi x}{L}dx \tag{3.24}$$

In the case that the side of the slab in x=0 is heated by a thermal Dirac-like pulse Q which is instantaneously and uniformly absorbed within a small depth δ from the front surface in x=0, the following boundary condition can be applied:

- in 0<x<δ

T(x,0)=Q/(ρc$_p$δ) (heat absorption within δ)

- in δ<x<L

T(x,0)=0 (no internal heating)

Therefore the solution becomes:

$$T(x,t) - T_0 =$$
$$= \frac{Q}{\rho c_p L}\left\{1 + 2\sum_{n=1}^{\infty} cos\frac{n\pi x}{L} sin\frac{(n\pi\delta/L)}{(n\pi\delta/L)} exp\left[\left(-\frac{n\pi}{L}\right)^2 \alpha t\right]\right\} \tag{3.25}$$

ρ being the density, c the specific heat, T_0 the initial constant temperature and t the time after pulse heating.

Since δ is very small for opaque materials, therefore it can be made the approximation $sin(n\pi\delta/L) \approx n\pi\delta/L$. So the above solution can be rewritten for the opposite side $x=L$, as:

$$T(L,t) - T_0 = \frac{Q}{\rho c_p L}\left\{1 + 2\sum_{n=1}^{\infty}(-1)^n exp\left[-\left(\frac{n\pi}{L}\right)^2 \alpha t\right]\right\} \tag{3.26}$$

Two dimensionless parameters can be introduced (T_M is the maximum temperature reached in $x=L$):

$$\left.\begin{aligned} V(L,t) &= \frac{T(L,t)}{T_M} \\ t_\alpha &= \frac{\pi^2 \alpha t}{L^2} \end{aligned}\right] \tag{3.27}$$

which allows to rewrite eq. 3.26 as:

$$V = 1 + 2\sum_{n=1}^{\infty}(-1)^n \exp(-n^2 t_\alpha) \tag{3.28}$$

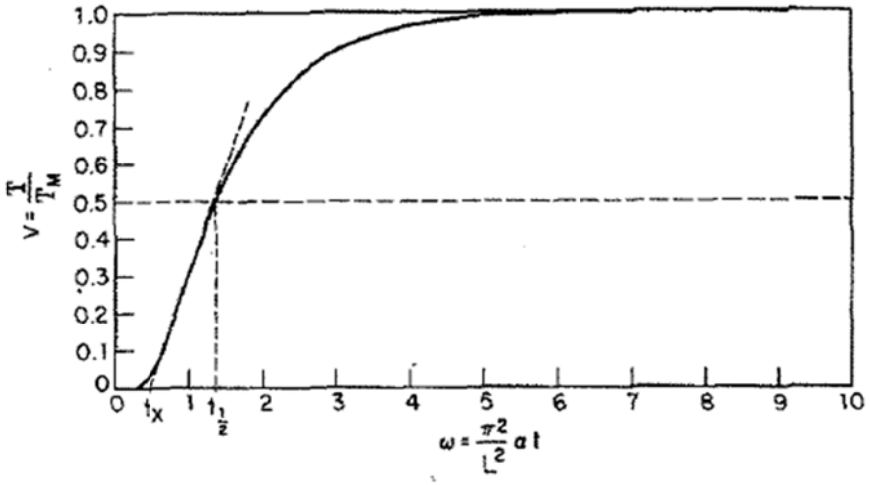

Figure 3.12: Warming up of the rear side of the slab [190].

When $T=T_M/2$, then $V=0.5$ and as a consequence $t_\alpha=t_{1/2}=1.38$ (see fig. 3.12) which is the time needed to the rear surface (transmission arrangement in fig. 3.9) to reach half of the maximum temperature. Therefore it follows that:

$$\alpha = \frac{1.38L^2}{\pi^2 t_{1/2}} \tag{3.29}$$

3.5.3 Lock-In Thermography

Lock-In Thermography, together with PT, is the most used Infrared based method for NDE purposes among the active approaches.

Basically, the thermographic Lock-In system is coherently coupled to a thermal wave source which is operated in such a way that a sinusoidal temperature

modulation results; this can be easily arranged with a halogen lamp connected to a function generator for sinusoidal driving. It is basically performed in reflection mode.

If the surface in x=0 of a semi-infinite solid is impinged by a sinusoidal heat source with modulation frequency ω, and its initial temperature is T_0, by considering photo-thermal methods applied to the lock-in amplifier which allows filtering the stationary component, the harmonic heat delivered at the surface (x = 0) of a homogeneous and semi-infinite material results in a (time dependent) thermal wave which propagates inside the material according to:

$$T(x,t) =$$
$$= T_0 e^{-\frac{x}{\mu}} cos\left(\omega t - \frac{x}{\mu}\right) - \frac{2T_0}{\pi^{1/2}} \int_0^{x/2(\alpha t)^{1/2}} cos\left[\omega\left(t - \frac{x^2}{4\alpha\xi^2}\right) e^{-\xi}\right] d\xi \quad (3.30)$$

where $T(x,t)$ is the periodic temperature component. It is worth nothing that $T(x,t)$ should be, more correctly, indicated as $\tilde{T}(x,t)$; however, the most simple way of $T(x,t)$ is largely used by people involved with lockin thermography measurements once the meaning is known. The first part of the second term of eq. 3.30 is related to the *steady oscillation* (asymptotic) solution, whilst the second term is a transient disturbance due to the initial thermal oscillation at the starting time t=0 which dies with increasing *t*.

Then the used solution is the first part of the second term of the eq. 3.30.

Eq. 3.30 includes the *diffusion length* μ and the *phase* φ (which is the delay of the propagating wave with respect to the thermal stimulation) defined respectively as:

$$\mu = \sqrt{\frac{2\alpha}{\omega}} = \sqrt{\frac{\alpha}{\pi f}} \quad (3.31)$$

$$\varphi(x) = \frac{x}{\mu} \quad (3.32)$$

Since the thermal diffusion length is inversely proportional to the modulation frequency, the higher is the frequency the shorter is the distance travelled by the

thermal wave, which implies that the inspection is restricted to the near surface region. On the contrary, low frequencies allows to probe more deeper but very slowly, that is why inspection of thick parts can take sometimes longer time, or, in the worst case, it could be ineffective.

It has to be noted that amplitude is insensitive to superposition of unmodulated radiation caused by reflection effects; the phase angle is also independent of local power density and thermal emission coefficient [191].

The depth range, for the amplitude image, is given by μ while the maximum depth, p, which can be inspected, for the phase image corresponds to $C_1\mu$, where C_1 can take values from 1.5 [191] to 2 [192], although, generally, the adopted values is 1.8 [193,194] and so the maximum penetration will be:

$$p = 1.8\mu \tag{3.33}$$

In the lock-in analysis, the system collects a series of images and compares their temperature computing amplitude and phase angle of the sinusoidal wave pattern at each point. In this way the resulting image may be an amplitude image or a phase image. Amplitude A and phase φ at each pixel are calculated from four thermographic images (fig. 3.13) S1 to S4 taken during one modulation cycle:

$$A(x) = \sqrt{(S_3 - S_1)^2 + (S_4 - S_2)^2} \tag{3.34}$$

$$\varphi(x) = arctg\left(\frac{S_3 - S_1}{S_4 - S_2}\right) \tag{3.35}$$

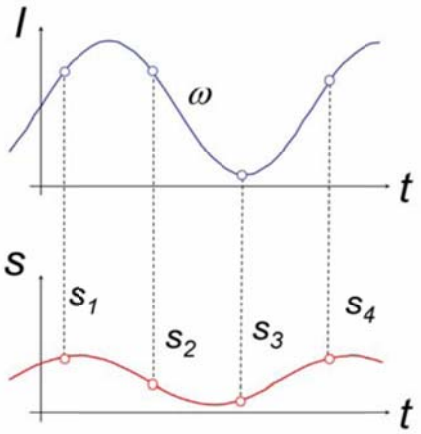

Figure 3.13: Amplitude and phase retrieval from a sinusoidal thermal excitation [144].

Similarly to the concept of temperature contrast, a definition for the absolute phase contrast $\Delta\varphi$, can be found in literature [195] which is defined as:

$$\Delta\varphi = \frac{\varphi_S - \varphi_D}{\varphi_S} \tag{3.36}$$

Where φ_S and φ_D are respectively the phase value of sound and defect area. Of course, due to eq. 3.32, the phase can change with frequency, and, it can assume positive or negative values; further, it varies also because of its dependency to the diffusivity of the defect, which can be higher or smaller than that of the sound area one. Of course, there exists a frequency for which the contrast is almost zero, which is known as *blind frequency*, f_B.

Thanks to eq. 3.33 the diffusivity of a slab with known thickness can be easily calculated. This can be done by putting a benchmark in contact with the rear side of the slab. Once the higher stimulation frequency allowing to obtain an appreciable $\Delta\varphi$ in the area occupied by the benchmark is found, this f can be used, together with the p, (which, in this case is the thickness of the slab, L) simply by inversion of the 3.33. we obtain:

$$\alpha = \pi f \left(\frac{L}{1.8}\right)^2 \tag{3.37}$$

By this approach, similarly, the depth of defects embedded in CFRP laminates can be obtained if diffusivity is known, simply through the f (this time using eq. 3.31 and 3.33), allowing a Quantitative IRT analysis [196-197]. A drawback of LT performed with optical heating is that it is sensitive to thermal boundaries, which sometimes does not allow reliable discrimination of the defective area with respect to the sound areas. This can be resolved by applying a different thermal stimulation source, as the case of mechanical elastic waves (ultrasound) in order to induce a selective heating stimulation. Indeed, only the defect areas produces local heating due to friction effect [198].

Chapter 4

Manufacturing of CFRP with preset amount of porosity

In order to study the effectiveness of Infrared Thermography for porosity assessment in CFRP, several coupons with induced porosity were manufactured.
From literature, it is known that porosity is a problem involved principally within the curing cycle, chosen for CFRP laminates, due to non optimized setting of pressure-temperature parameters. Specifically, the applied vacuum pressure plays a key role for both eliminating air entrapped during the lamination phase (hands-made)and removal of gases rising during curing of the resin in autoclave.
This awareness was exploited to perform a curing cycle suitable, contrarily to that is commonly done, to deliberately insert porosity within the laminate. Starting from the curing procedure suggested by the pre-impregnated laminas provider, which of course is conceived for achieving optimal material characteristics, the pressure parameter was modified in such a way to obtain specimens with induced porosity. More specifically, the pressure was set at different percentages of the bulk prescribed one to have specimens with different amount of porosity.
The obtained porosity percentages were firstly evaluated through destructive methods.
One of the most used and reliable method for porosity assessment is the "acid digestion", which implies elimination of the resin in the whole component in order to isolate the contained fibres. Nevertheless, the use of acids entails serious safety issues, which lead this method to be discarded in favour of two more feasible ones: gravimetric measures for density evaluation and optical microscopy.
Thus, the volumetric percentage of embedded voids was determined by the gravimetric method, while the voids location was highlighted by optical microscopy.

4.1 Coupons with induced Porosity

As previously observed in sections 1.3.1 and paragraph 1.5, porosity is a defect which typically rises when the autoclave curing is not perfectly performed. Specifically, the vacuum pressure is the parameter primarily responsible for entrapment of air in the laminate, as well as for stagnation of gases produced during curing of the resin.

These concepts were used to produce coupons with induced porosity. The idea was to apply an incorrect pressure-temperature cycle for the autoclave curing. Thus, starting from the optimum cycle, indicated by the provider of the pre-impregnated laminas, some changes were introduced. In particular, the vacuum pressure has been set to a lower value with respect to the recommended value (7 bar), whilst the temperature evolution versus time was not changed in order to allow, in any case, the decreasing of the resin viscosity to allow it flowing and melting.

Further, to obtain coupons with a certain amount of porosity, coupons were collected into several groups each of them cured at a different percentage of the prescribed pressure (7 bar). Specifically, the first group was cured by applying the full pressure in order to get reference laminates; then, the successive groups were cured at 75%, 50%, 25% and 0% of the prescribed pressure. A schematic of the coupons type produced can be found in the table 4.1.

4.4.1 Manufacturing procedure

The coupons were made of shits of unidirectional carbon/epoxy pre-preg laminas M21/IM7 (fig. 4.1) provided by HEXCEL®, which were cut at established dimensions in order to lay up them by hand. To investigate the possible influence of the fibres orientation (fig. 4.2) on the porosity formation, particularly the distribution of pores, coupons were conceived of four different stacking sequences (table 4.1). Moreover, a kapton® disk, made of two overlapped ones of thickness 0.0625 mm each, was inserted in the middle of the stacking sequence in order to simulate a slag inclusion, or a delamination (fig. 4.3 and 4.4). Then considering the

5 different curing pressures and the 4 stacking sequences, in total 20 coupons were manufactured.

Figure4.1: Pre-preg M21/IM7 by HEXCEL.

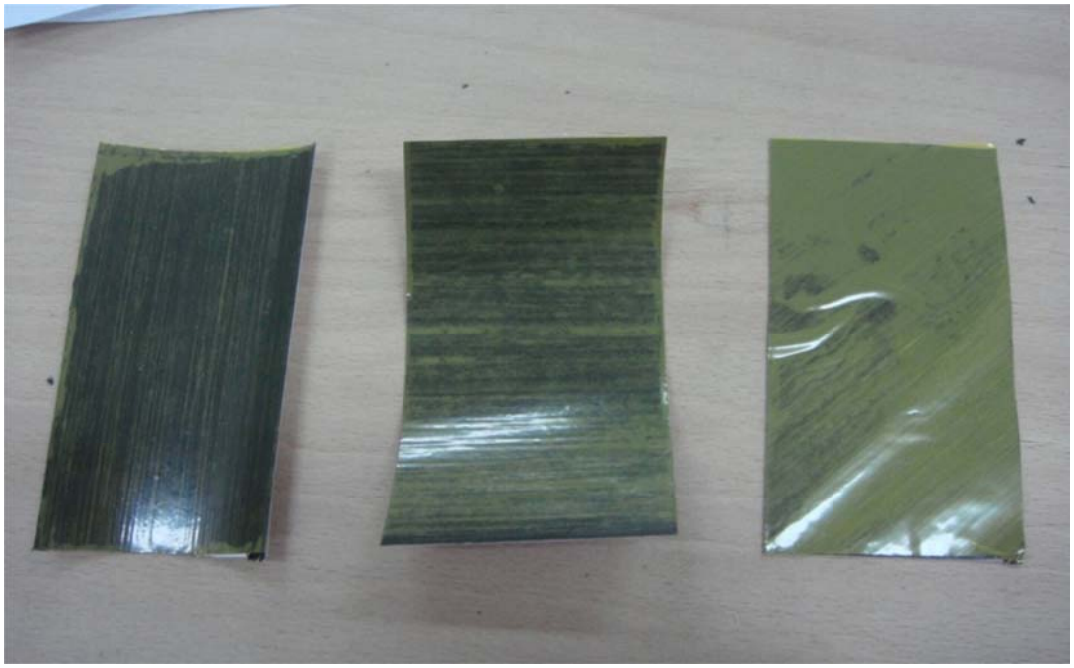

Figure 4.2: Plies were cut into rectangular shapes10cm x 5cm with fibres oriented at 0°, 90° and 45°.

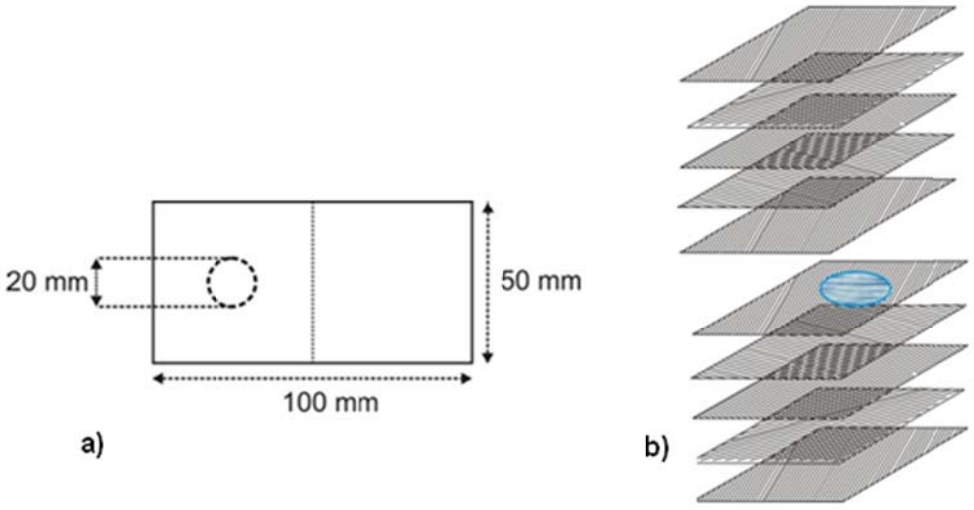

Figure4.3: Schematic of a coupon a) with indicated the position of the embedded inclusion, b).

Figure4.4: Position of two overlapped kapton disks.

During the stacking sequence, each lamina was forced to adhere to the underlying ones by a compression performed manually with a special roller tool. This allowed eliminating part of the air entrapped between laminas during deposition that may cause formation of macroscopic bubbles.

Coupon Type	Stacking sequence	# plies
P1	[0°]	24
P2	[90°]	24
P3	$[45°/-45°]_s$	24
P4	$[45/0/-45/90/45/0/-45/90//90/-45/0/45/90/-45/0/45]_s$	32

Table4.1:Types of produced coupons.

Finally, the obtained structures were placed on a planar metallic mold and covered with a vacuum bag, its perimeter was hermetically closed and attached to the mold. The bag was provided with just one vent for elimination of the air enclosed in it (figure 4.5). At this stage, the obtained structure was put in autoclave and subjected to the chosen curing cycle (figure 4.6).

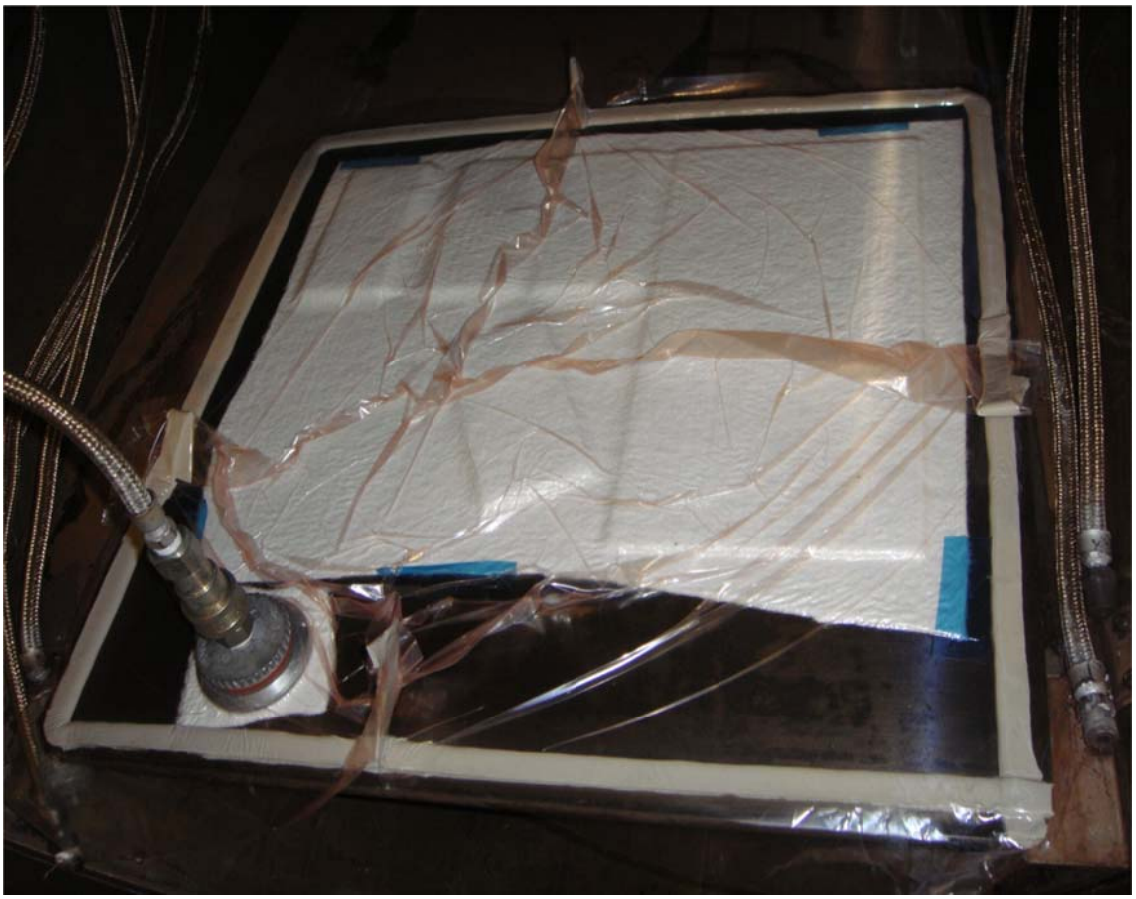

Figure 4.5:Vacuum bag with the vent in the left lower angle.

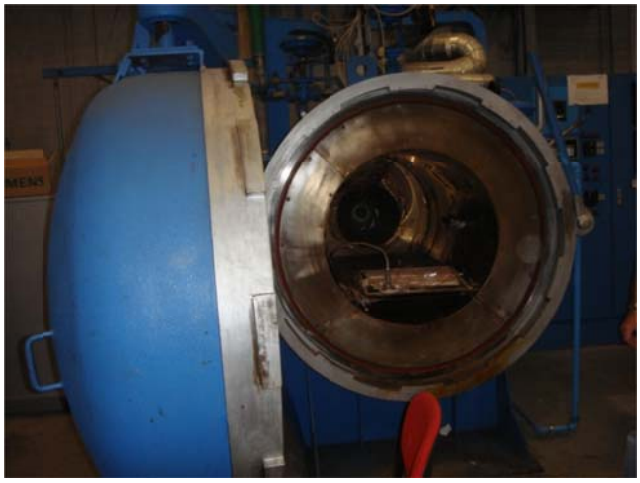

Figure 4.6:View of the autoclave inside.

In figure 4.7, it is shown a graph of the curing cycle for parts of thickness less than 15 mm, as suggested by Hexcel. Such a cycle, for application of the correct pressure, can be schematized in this way:

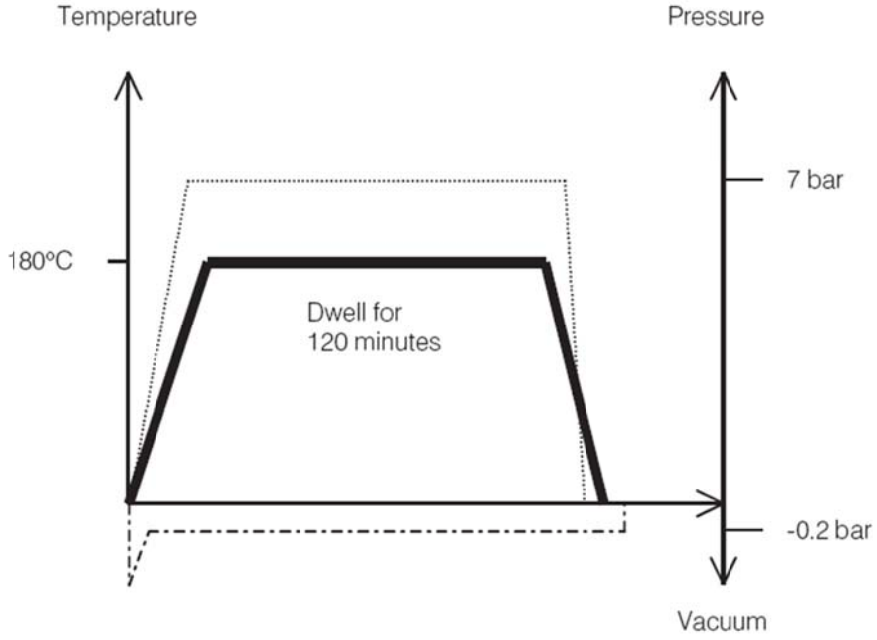

Figure 4.7: Typical Autoclave Cure of Monolithic Part, as provided by Hexcel.

1. Apply full vacuum (1 bar) (figure 4.5)
2. Apply 7 bar gauge autoclave pressure.
3. Heat-up at 1-3°C/minute to 180°C ± 5°C
4. Hold at 180°C ± 5°C for 120minutes ± 5 minutes.
5. Cool at 2-5°C/minute.
6. Vent autoclave pressure when the component reaches 60°C or below.

4.2 Induced porosity assessment

In order to estimate the amount of induced porosity, several techniques can be used. As shown in a report by MIT [199], and in many other literature sources, three are basically the most reliable techniques:

1) Volumetric method;
2) Microscopy;
3) Acid digestion.

First of all, the amount of voids can be evaluated by gravimetric analysis, as for example by density measures. Another widely used technique is the quantitative microscopic examination of a metallurgically polished interior section of the material, and last, specifically for CFRP (not for other types of composites), the so called *acid digestion*. All of them are destructive techniques: the first two can be applied on samples extracted from the whole component, whilst acid digestion can be applied on the whole component. Acid digestion, indeed, involves resin removal by acid attack, such as with fulming sulfuric acid, which does not damage the carbon fibres. The whole component is initially weighted, and after acid digestion, the remained fibres are weighted again. Then through easy calculations [200], the volume percentage of each component, including air (pores) can be estimated.

The latter method implies serious safety issues, for this reason the first two methods were herein preferred and applied, in particular, for density measures and for visualization of pores distribution.

4.2.1 Gravimetric measures for density assessment

For the gravimetric measurements, a mono-plate digital balance Sartorius (fig. 4.8), was used. The sample was firstly weighted in air and then in water.

Being known the density of water, the sample density was obtained through the following formula (from the Sartorious user manual):

$$\rho = \frac{W_a[\rho_{fl} - \rho_a]}{0.99983[W_a - W_{fl}]} + \rho_a \qquad (4.1)$$

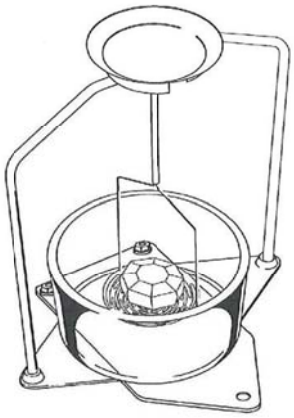

Figure4.8: Mono-plate digital balance.

where W_a is the weight of the sample in air, W_{fl} is the weight of the sample in water, ρ_a is the density of air at laboratory temperature, while ρ_{fl} is the density of water at laboratory pressure and temperature (ρ_{fl}= 0.0012 g/cm^{3}at 20°C and 1 atm).

In order to measure the density of each coupon, from each of them three small samples were cut and weighted, then the average density was calculated. The obtained density values were plotted against the curing pressure in fig. 4.9. As expected, the density of the coupons cured with the recommended curing cycles was found to be closest to the datasheet value (1.56 g/cm^3). In the following table 4.2, the average density values measured for each type of coupons are reported.

Cure Pressure %	Density (g/cm^3)			
	P1	P2	P3	P4
100	1.55	1.54	1.54	1.55
75	1.53	1.51	1.51	1.55
50	1.51	1.5	1.5	1.46
25	1.48	1.46	1.47	1.46
0	1.47	1.45	1.45	1.46

Table 4.2: Average density for each type of coupons.

4.2.2 Assessment of pores volumetric percentage

Starting from the obtained average density, the volumetric percentage of the embedded porosity was calculated. It was assumed the fiber volume ratio and the resin volume ratio to be the same for all the coupons, whereas the introduction of the porosity was responsible just only of volume variations. The above considerations can be translated into equations; for the theoretical density, ρ_T, by the law of mixtures, we have:

$$\rho_T = \frac{\rho_f V_f + \rho_r V_r}{V_f + V_r} \tag{4.5}$$

In which ρ_f, V_f, ρ_r and V_r are respectively the density and the volume of the lonely fibres and the lonely resin part. Due to the hypothesis above stated, the presence of the pores is responsible of a volume occupied by the voids, V_v, which is added to the volumes of the fibres and of the resin. So, it can be assumed that the real density, measured with the above described method, gives:

$$\rho = \frac{\rho_f V_f + \rho_r V_r}{V_f + V_r + V_v} \tag{4.6}$$

where ρ is the real density and $V_f + V_r + V_v = V_T$, e.g. the total volume of the coupon.
If equations 4.5 and 4.6 are multiplied and divided by V_T, the following relationships are obtained:

$$\rho_T = \frac{\rho_f V_{f\%} + \rho_r V_{r\%}}{V_{f\%} + V_{r\%}} \tag{4.7}$$

$$\rho = \rho_f V_{f\%} + \rho_r V_{r\%} \tag{4.8}$$

In which:

$$V_{f\%} = \frac{V_f}{V_T}$$

$$V_{r\%} = \frac{V_r}{V_T}$$

The ratio between equation 4.8 and 4.7 gives:

$$\frac{\rho}{\rho_T} = V_{f\%} + V_{r\%} \tag{4.9}$$

And from eq. 4.9 it is:

$$V_{r\%} = \frac{\rho}{\rho_T} - V_{f\%} \tag{4.10}$$

Putting eq. 4.10 into eq. 4.9, it can be obtained:

$$V_{f\%} = \frac{\rho - \frac{\rho_r \rho}{\rho_T}}{\rho_f - \rho_r} \tag{4.11}$$

And finally, the volume percentage of the voids is given by:

$$V_{V\%} = 1 - V_{r\%} - V_{f\%} \tag{4.12}$$

As a consequence, from eqs. 4.10, 4.11 and 4.12 the volume percentage of the fibres, of the resin and of the voids can be calculated, thanks to the provided datasheet densities (table 4.3).

ResinDensityρ_r(g/cm^3)	1.28
fibres Densityρ_f(g/cm^3)	1.78
Pre-preg densityρ_T (g/cm^3)	1.56

Table4.3:Properties of the used pre-preg.

The obtained porosity percentages, V_v%, are reported in table 4.4 and the distribution with the adopted pressure percentage can be appreciated in the figures 4.9-4.12.

Cure Pressure %	V_v%			
	P1	P2	P3	P4
100	0.68	0.98	0.99	0.93
75	1.89	3.00	2.90	0.89
50	3.46	3.78	3.92	6.21
25	5.45	6.67	5.60	6.18
0	5.76	7.06	7.24	6.18

Table4.4: Percentage of embedded pores for each type of coupons.

In the figures 4.9-4.12 the measured V_v%, normalized with respect to the porosity percentage obtained at a curing pressure P_c=100% is plotted against the applied curing pressure, P_c. Comparing the behaviors highlighted through the data representation, it can be noticed that the porosity amount is constantly increasing with decreasing pressures for all the coupons. In the following table 4.5, the slope of the best fitting curves parameters for each group of data are shown, together with the coefficient of determination R^2. As can be seen, a linear dependence exists between V_v% and the decreasing applied P_c, for the coupons P1, P2 and P3; on the contrary, the V_v% of the P4 type shows a stepped behavior. Moreover, it seems that there is some influence of the fibres orientation on the porosity occurrence, indeed, the P1 type has the larger slope absolute value which entails that this lamination sequence is characterized by a quite stronger tendency to retain voids.

Coupon type	Slope	R^2
P1	-0.08	0.97
P2	-0.06	0.96
P3	-0.06	0.99
P4	-0.07	0.74

Table4.5: Best fitting parameters.

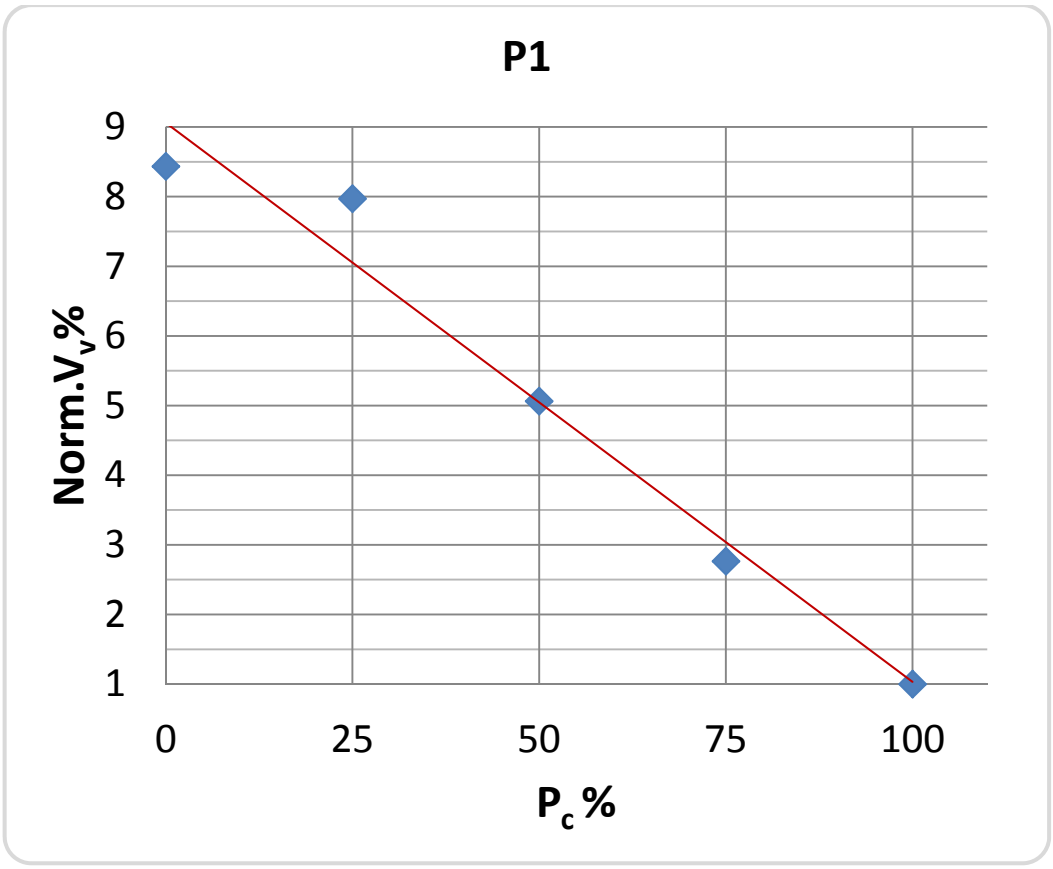

Figure 4.9: Normalized percentage of voids vs. P_c.

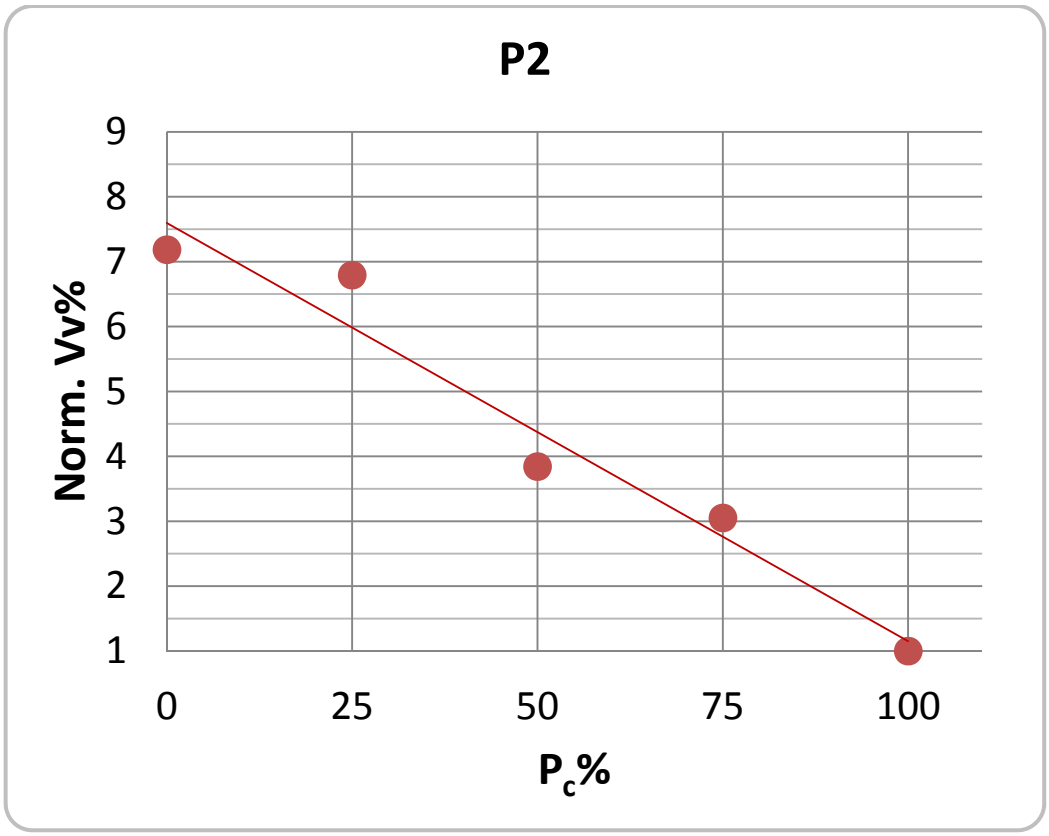

Figure 4.10: Normalized percentage of voids vs. P_c.

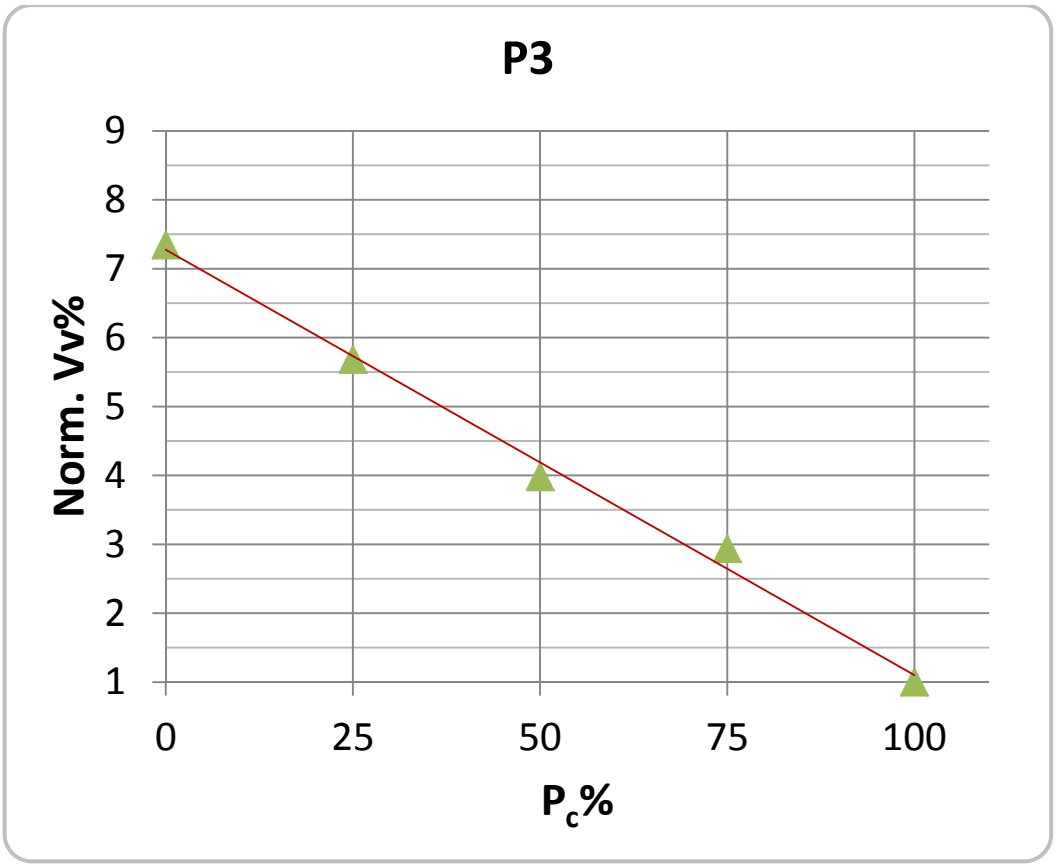

Figure 4.11: Normalized percentage of voids vs. P_c.

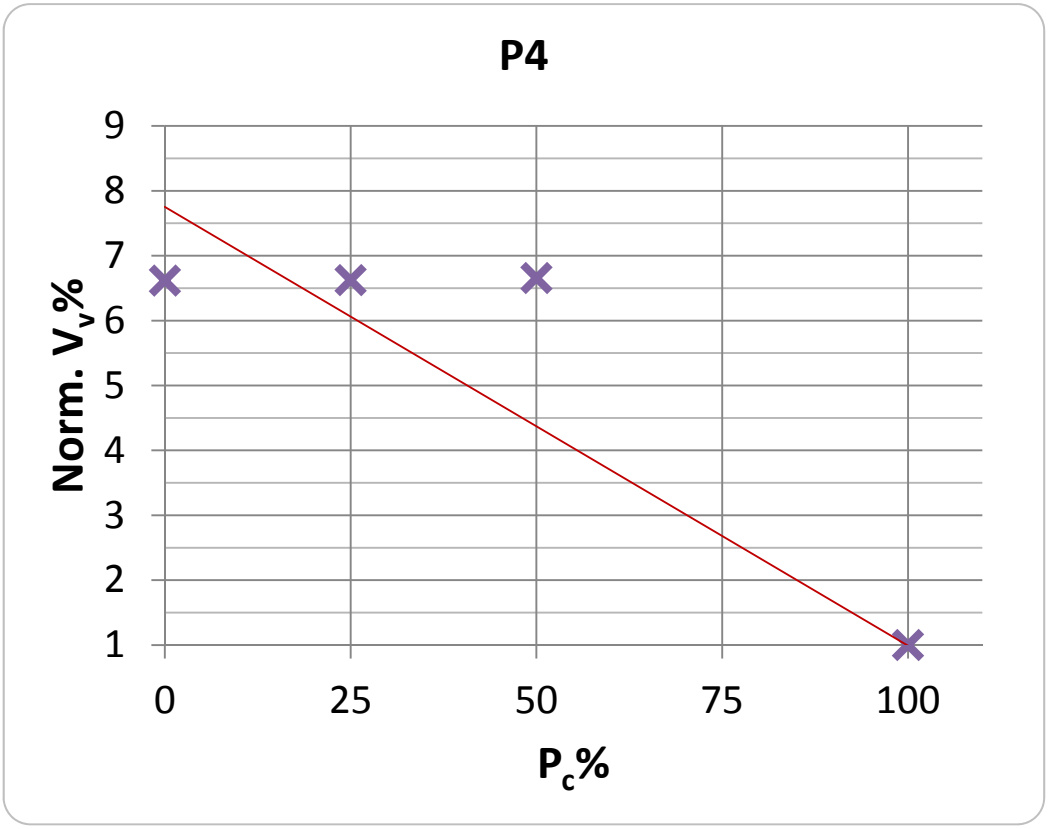

Figure 4.12: Normalized percentage of voids vs. P_c.

4.2.3 Porosity amount assessment through optical microscopy

To perform optical microscopy observations a small sample was cut from each coupon, as highlighted in figure 4.13. The same sample was previously part of the set used for the gravimetric method measures.

Then groups of samples were embedded into a resin mold and metallurgically polished in order to observe the internal surface of each of them (figure 4.14).

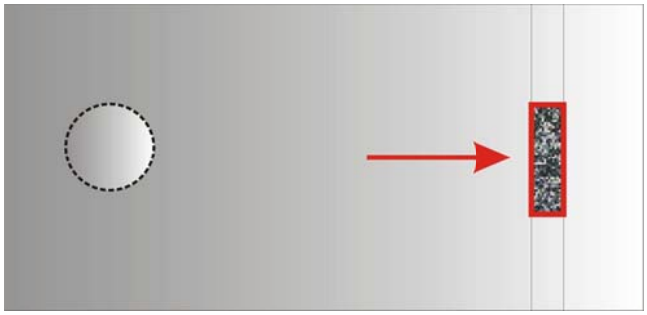

Figure4.13: Schematic of the sample extracted from the coupon; the red arrow indicates the internal section which was the observed one.

The surface was observed with a proper lens; by knowing the lens magnification factor, the software coupled to the microscope provided an estimation of the porosity distribution within the whole sample.

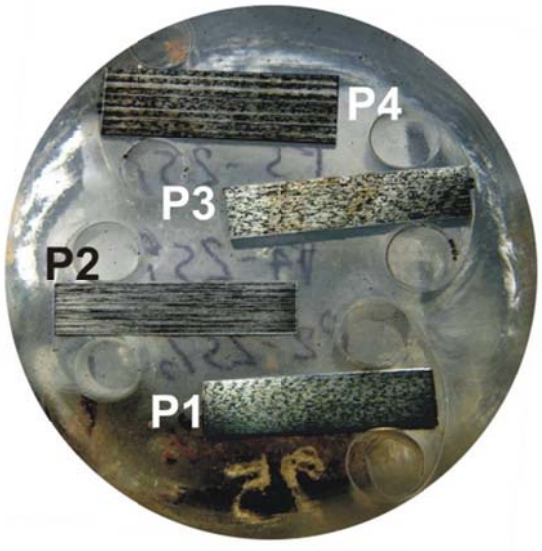

Figure4.14: Resin mold for the samples observation.

The obtained percentages of porosity are resumed in table 4.6. The normalized porosity percentages obtained through microscopy are plotted against the curing pressure in fig. 4.15-4.18.

Cure Pressure %	Porosity %			
	P1	P2	P3	P4
100	2.43	4.00	1.92	2.06
75	3.58	3.92	3.41	11.10
50	5.99	7.41	12.65	3.23
25	9.45	7.18	9.75	13.03
0	11.45	7.32	11.75	12.76

Table 4.6: Percentage of embedded pores for each type of coupons by optical microscopy.

In the following table 4.7, the slope of the best fitting curves for each group of data are shown, together with the coefficient of determination R^2.

Coupon type	Slope	R^2
P1	-0.04	0.98
P2	-0.01	0.73
P3	-0.05	0.70
P4	-0.04	0.50

Table4.7: Best fitting parameters.

The obtained graphs and the best fitting parameters shows clearly that just only for the coupon P1 a good agreement with a linear dependence by the pressure is achieved. It may be concluded that the applied pressure has a very complex relation with the induced porosity, nevertheless with decreasing pressures also the microscopy confirms that porosity increases as well. However, the obtained measures are in contradiction with those obtained with the gravimetric method. Actually, the results of both methods, gravimetric and microscopy, are strongly related to very small portions of the larger component under analysis; this, of course, affects the method reliability. More specifically, this makes the results unlikely to be extendable to the whole piece. It can also be observed that, being it

intrinsic to every statistical method, the analysis of a larger number of samples supplied more trustworthiness results.

It is very probably, that the use of the acid digestion as a method for porosity assessment should had supplied more reliable results because it involves the analysis of the whole component. Nevertheless the use of dangerous acids involves severe safety measures with additional costs for personnel training and specific equipment.

Within the aim of this dissertation and considering the safety issues, the results obtained with the gravimetric method have been considered acceptable.

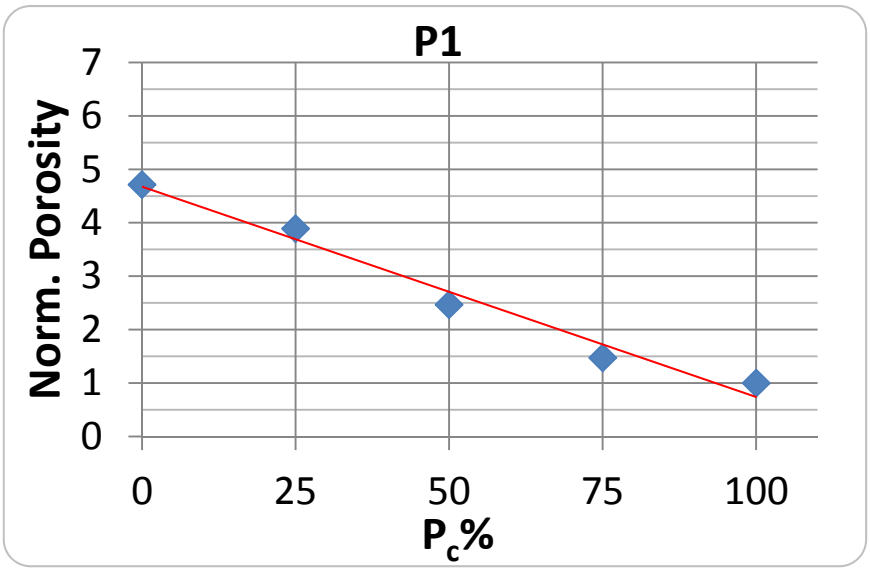

Figure 4.15: Normalized percentage of voids vs. P_c.

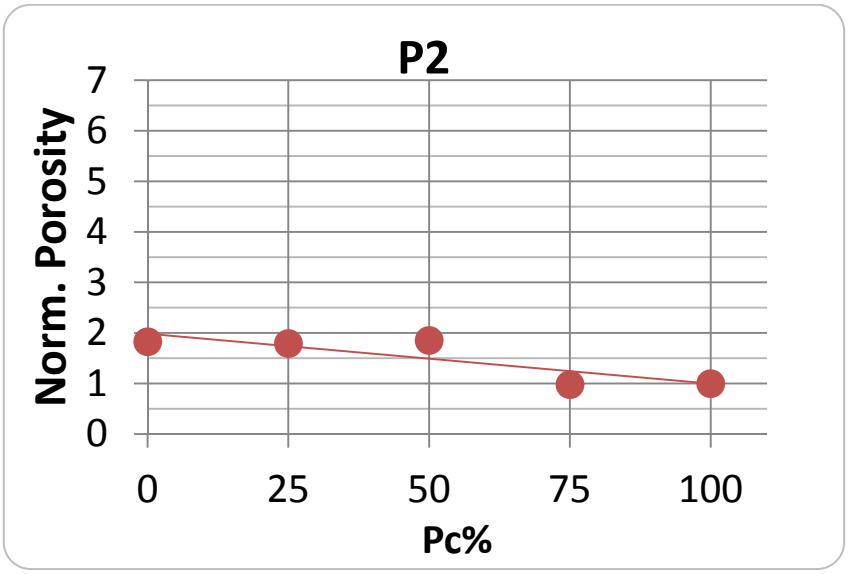

Figure 4.16: Normalized percentage of voids vs. P_c.

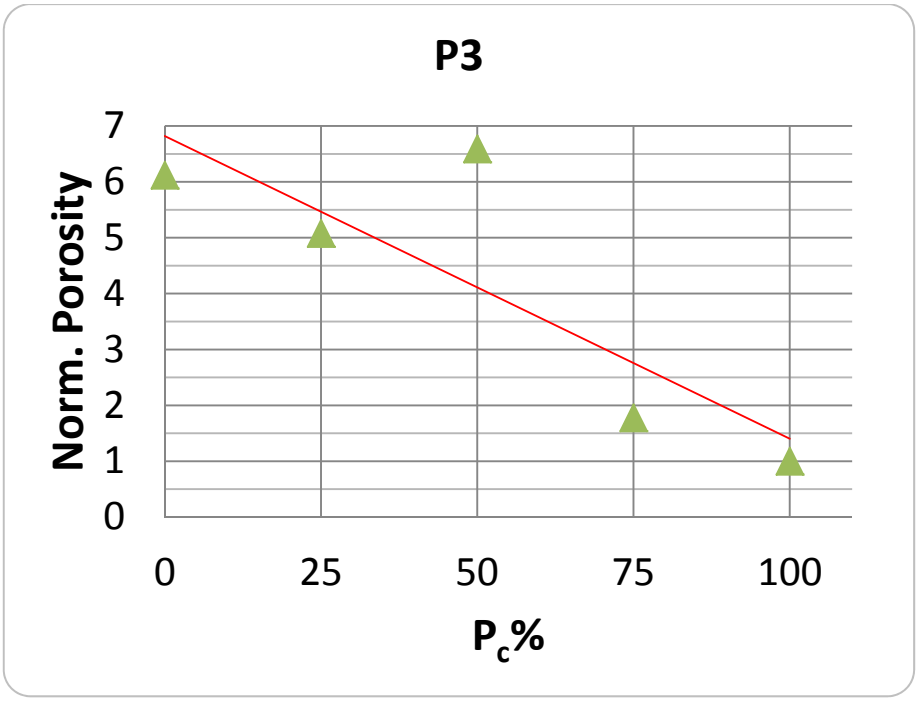

Figure 4.17: Normalized percentage of voids vs. P_c.

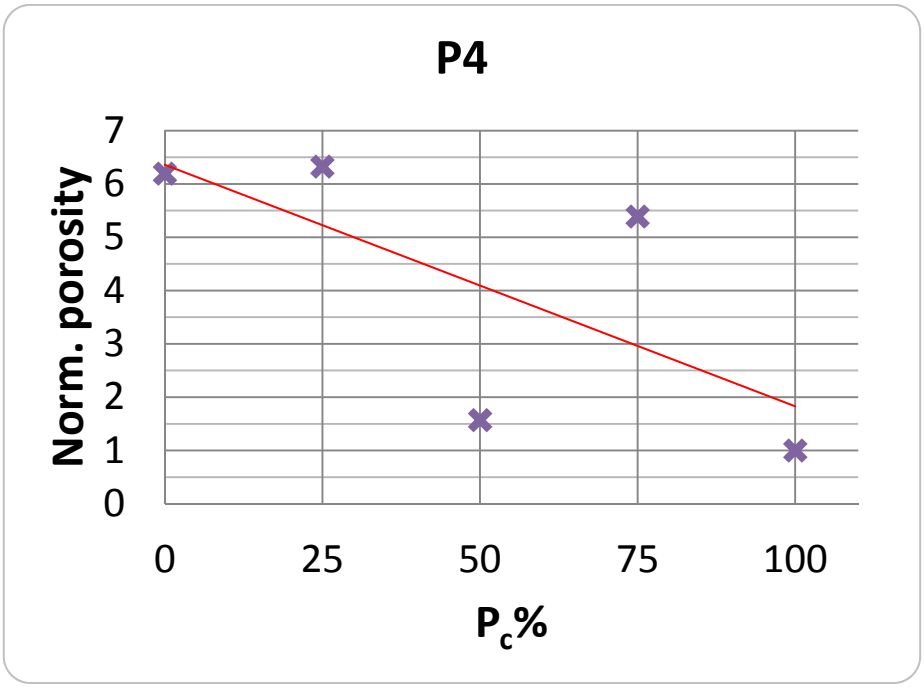

Figure 4.18: Normalized percentage of voids vs. P_c.

From figure 4.19 to figure 4.22 some images obtained with two magnification factors M=1100 and M=2750 are reported, in which the presence of the pores can be appreciated especially within the plies and among them.

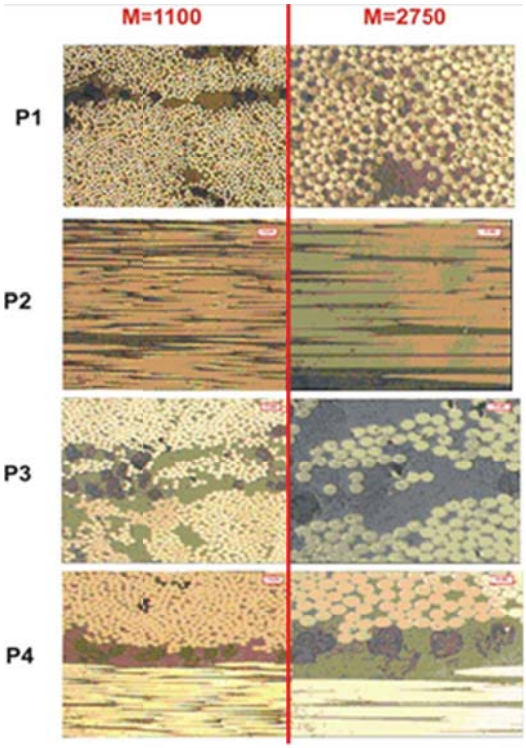

Figure 4.14: Samples cured with P_c=100%.

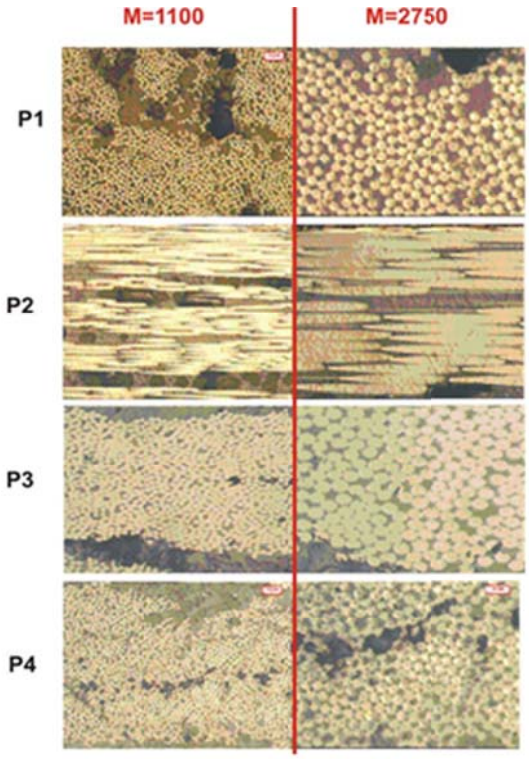

Figure 4.15: Samples cured with P_c=75%.

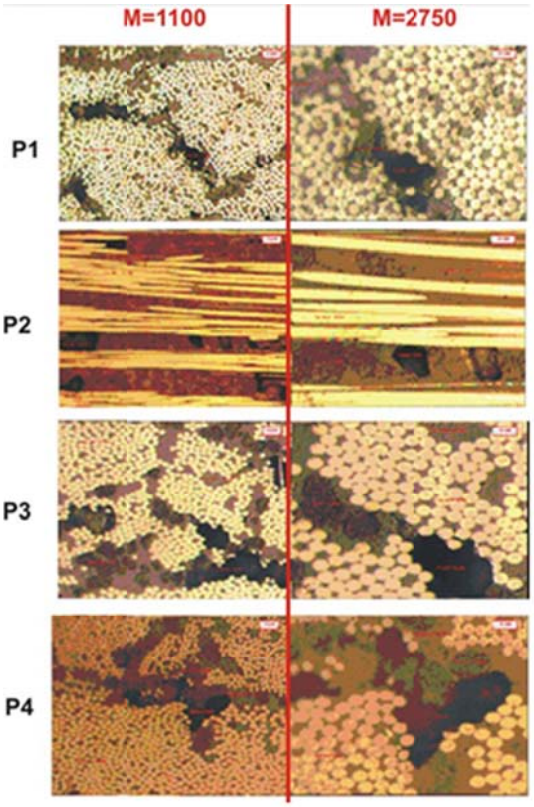

Figure4.16: Samples cured with P_c=50%.

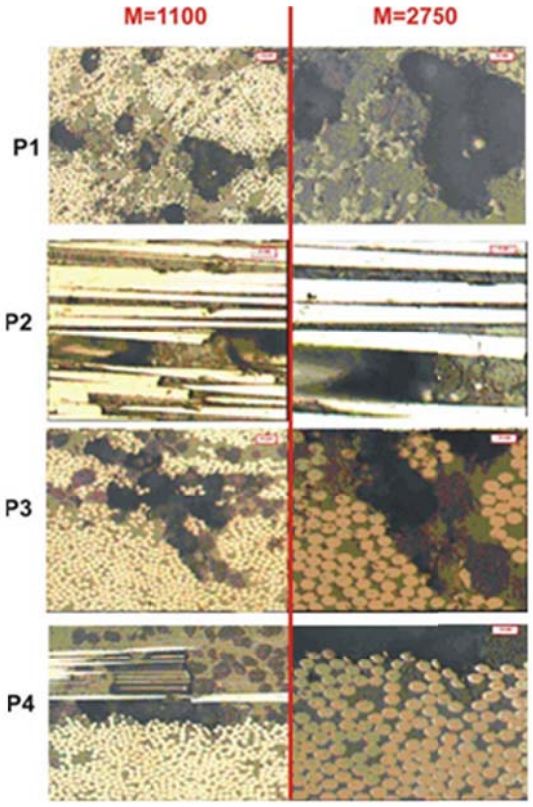

Figure 4.17: Samples cured with P_c=25%.

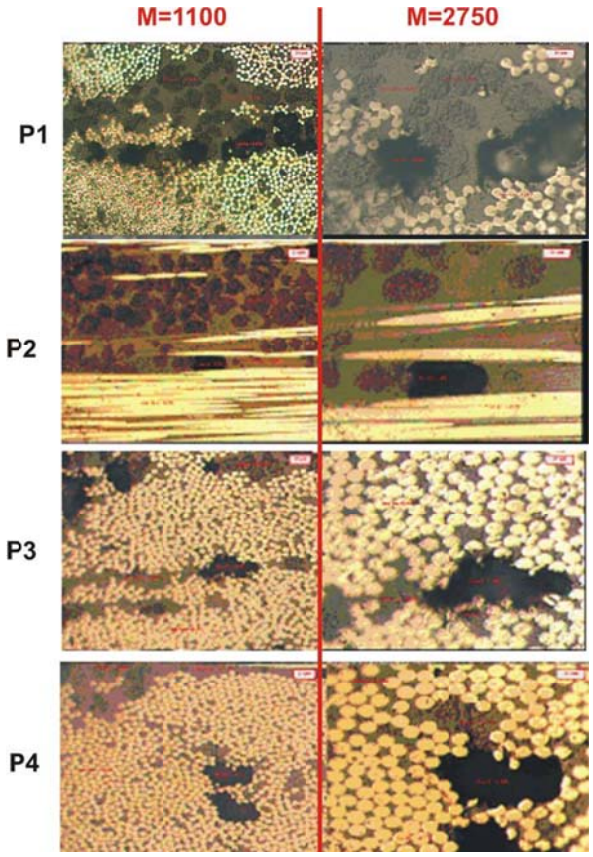

Figure4.18: Samples cured with 0% pressure.

Chapter 5

Ultrasonic testing and data analysis

In this chapter all the results obtained through the Ultrasonic Testing (UT) campaign are shown.

Firstly, all the lamination sequences adopted have been ultrasonically characterized by the construction of the Distance Amplitude Curve, which allows to measure the energy losses due to the reflection of the ultrasound wave at the interfaces between water and CFRP, as well as a first estimation of the ultrasonic attenuation coefficient, i.e. the attenuation per unit length undergone by the signal during its passage across the material, has been obtained.

Then, all the sets of coupons produced with induced porosity were analyzed.

It has been found that laminates of some specific stacking sequences seem more sensible to the pressure used during curing in autoclave.

Further, it has been shown that potentially ultrasonic testing could be a more reliable tool of porosity assessment if compared to the very largely used method, which is the gravimetric measure for porosity volumetric percentage estimation.

5.1 Ultrasonic characterization of CFRP laminates

The coupons specifically manufactured for porosity characterization have been described in the previous paragraph 4.1.1.

The next step is now to perform ultrasonic tests in order to measure the ultrasonic attenuation. This allows gaining information about the influence of the induced porosity on the overall attenuation of the signal and to obtain a general ultrasonic characterization of the defects enclosed in the coupons. As reported in paragraph 2.5 the total attenuation undergone by the ultrasonic signal in the *reflection* ultrasonic testing in immersion, is given by two contributions: the reflection at the interfaces between the CFRP surfaces and the water, which is due to the acoustic impedance mismatch, and the bulk attenuation due to the double passage of the signal within the material. In order to isolate this last contribution which is actually the part mostly affected by the presence of pores, it is needed to measure the contribution due to the surfaces.

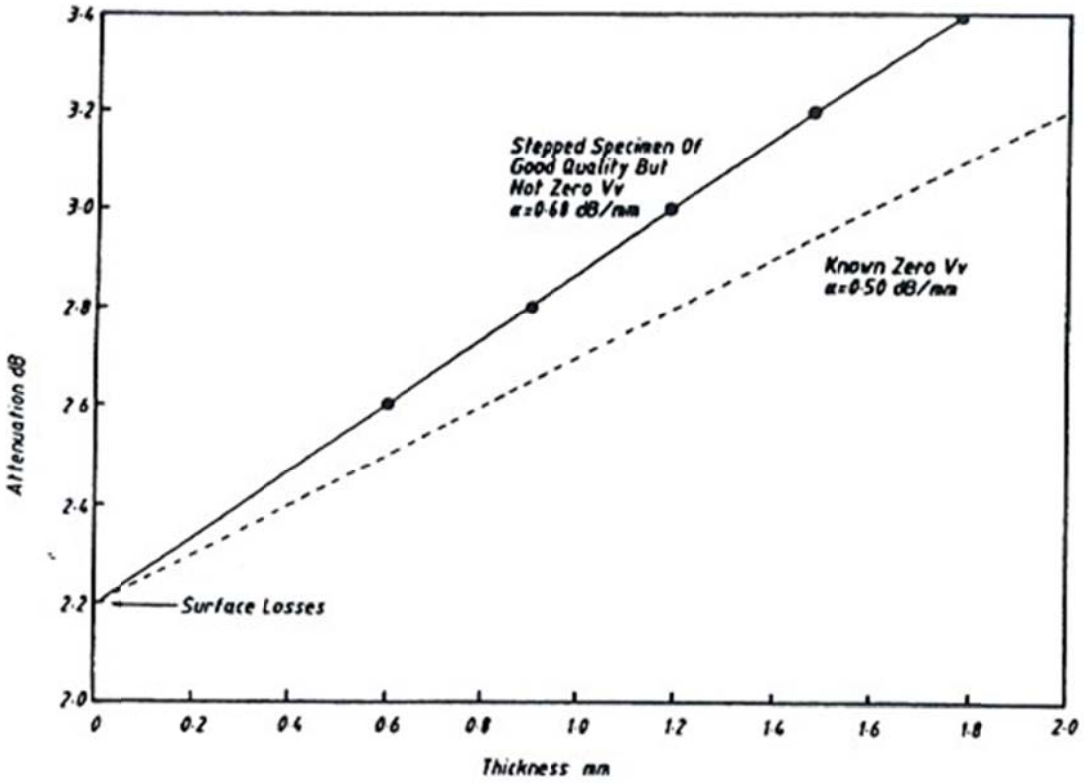

Figure 5.1: D.A.C.: Total Attenuation vs. thickness [75].

For this reason another special set of coupons was produced. These coupons are laminated of several different thicknesses (a different number of laminas) in order to get a step wedge. Of course, the ultrasonic signal attenuation will be affected by the bulk attenuation at each step of the wedge, and, the higher it is the thickness the higher will be the attenuation. This allows to calculate the attenuation per unit thickness. Plotting in a graph the measured attenuation against the thickness, as in fig. 5.1, the intercept of the almost linear distribution with the orthogonal axis gives the total contribution of the surface losses [75]. This kind of graph is known as DAC, i.e. Distance Amplitude Correction curve.

Taking into account the four stacking sequences considered for the construction of coupons with induced porosity, 4 different step wedges were manufactured in order to create the D.A.C. for each of them.

5.1.1 Reference specimens for DAC creation

The step wedges related to the P1 and P2 stacking sequences (see chapter 4) were made with four different thicknesses, whilst, P3 and P4 type, by only two different thicknesses, because for the latter lamination sequences the minimum number of plies and their mutual orientation is fixed in order to obtain a residual stress equilibrium during autoclave curing. This care assures their surface planarity after the autoclave curing. In order to avoid production of too thick parts, the P3 and P4 have only two steps. In the following figures 5.2 and 5.3 are shown the schemes of the different step wedges as well their lamination sequences.

The thickness of each step was measured with a Palmer caliper and the average values are reported in the following table 5.1 together with the lamination sequences.

Through the ultrasonic c-scan the average attenuation was measured at each step for each coupon, taking into account the double passage across the thickness. Then the DAC graph has been created for each step wedge by putting on the orthogonal axis the average attenuation in dB, and on the x axis the actually covered thickness in mm. Due to the linear correlation between the data, by a linear regression the slope and the intercept of the graphs are calculated. The slope is the *bulk attenuation*, i.e. the attenuation for unit length, and the intercept is an estimation of

the so called *surface losses*, i.e. the attenuation due to the reflection at both interfaces of the material.

	A		B		C		D	
	Lam.	*mm*	*Lam.*	*mm*	*Lam.*	*mm*	*Lam.*	*mm*
P1	$[0°]_8$	1.67	$[0°]_{16}$	3.12	$[0°]_{24}$	4.59	$[0°]_{32}$	6.01
P2	$[90°]_8$	1.62	$[90°]_{16}$	3.12	$[90°]_{24}$	4.52	$[90°]_{32}$	5.84
P3	$[45°/-45°]_8$	3.4	$[45°/-45°]_{8s}$	5.93	-		-	
P4	[45/0/-45/90/45/0/-45/90//90/-45/0/45/90/-45/0/45]	3.6	$[45/0/-45/90/45/0/-45/90//90/-45/0/45/90/-45/0/45]_s$	6.12	-		-	

Table 5.1: Lamination sequence and thickness of each step wedge coupon.

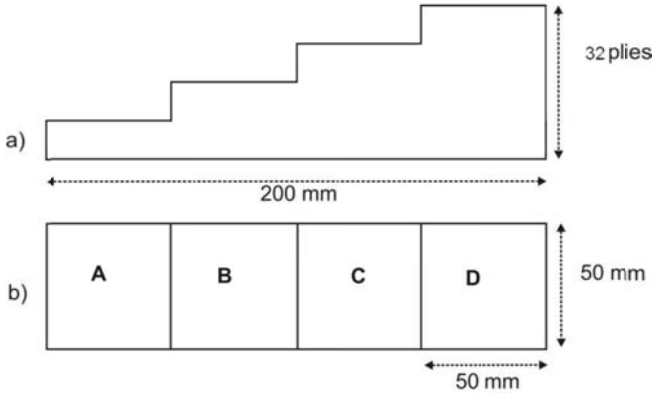

Figure5.2: Step wedge coupon for P1 and P2 stacking sequences. a) lateral view; b) frontal view.

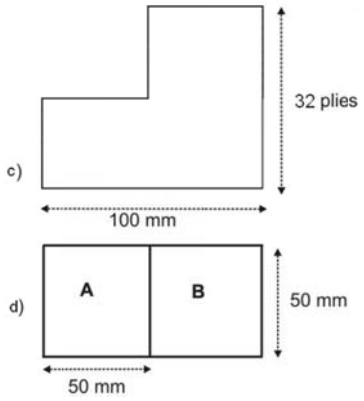

Figure 5.3: Step wedge coupon for P3 and P4 stacking sequences. a) lateral view; b) frontal view.

5.2 UT Set up

The UT is carried out using the facility named N.E.S.S.y. (Non destructive Evaluation Study System) schematized in the following figure 5.4:

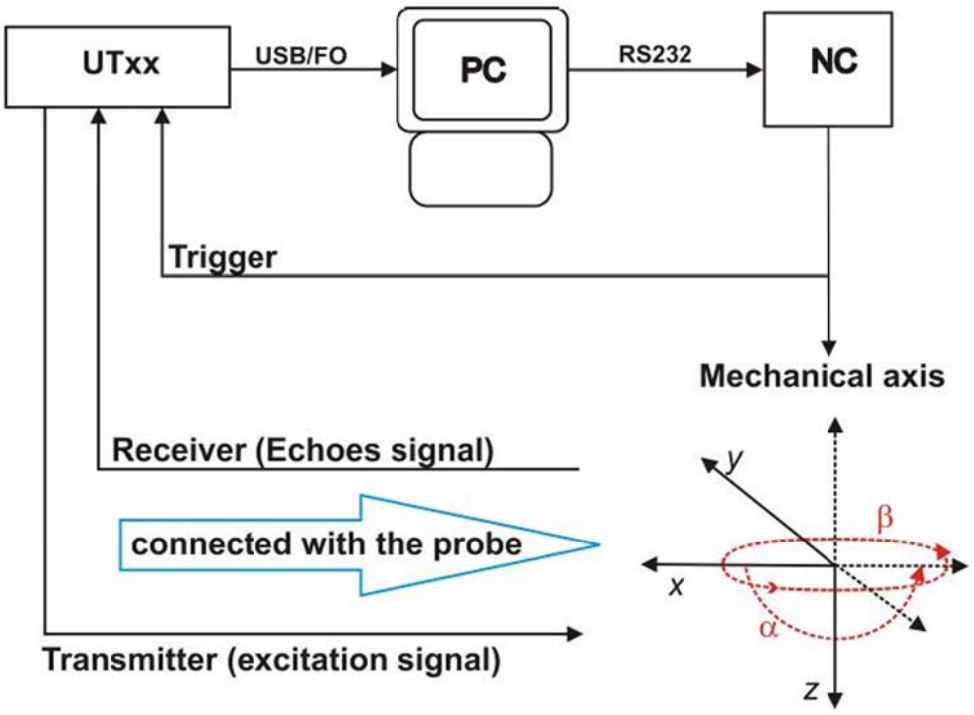

Figure 5.4: Schematic representation of the set up N.E.S.Sy..

The software supplied by Nukem® is able to:

- control the mechanical axis movements: the probe can be moved, in according with a proper geometry created by the customer. It is connected to the Numerical Controller, NC, (which actually talks with the axis) by an RS232 interface;
- establish the type of the emitted signal (excitation pulse duration and delay, transmitter impedance); high pass or low pass filter can be activated as well as impedance adaptation for the receiver probe;
- adjust the duration and the level of 4 independent gates on the A-scan signal, thanks to a digital oscilloscope. The trigger can be locked to the excitation pulse or to the Entry Echo, EE (the echo coming from the surface of the specimen);

- acquire and process the signals provided by the UTxx.

The unit UTxx is the main part of the system. It can transmit and receive signals through two independent channels. The received signal is analogically pre-amplified and then again amplified. Successively, it is digitized at a sampling frequency of 100 MHz and 8 bits of depth, for signals duration of 640 μs. The data are stored alternately into two RAM banks of 64 Kbyte memory capacity each, for signal processing by means of a Digital Signal Processor (DSP).

The mechanical part consists of a water pool (2400x2400x1200 mm) and 5 axis (x, y, z, α, β) to allow the movement of the probe in almost the whole pool volume. The axis are controlled by the NC, while the provided software assigns the geometrical coordinates and gives the movement commands. A double encoders system allows to assure the correct positioning of the probe and supplies the trigger signal for the UTxx. In this way the synchronism among the probe motion and the signal acquired is ensured point by point and the superimposition of transmitted and received signals (in the case of Reflection mode testing) is avoided.

5.2.1 Cares and criteria used for the test

As shown in the previous chapter 2, to inspect materials with the reflection technique, also commonly known as Pulse-Echo (PE) technique, both the coupons and the unique used transducer must be submerged in water. Due to the need to submerge also the coupons with induced porosity, their edges were properly hermetically sealed in order to avoid water infiltration from the flanks. This special caution allows to evaluate the attenuation due to the presence of pores, whilst, on the contrary, if the edges were not closed, pores could be partially or totally fulfilled with water. This must be avoided because the response of the ultrasonic signal at the two interfaces type, water-CFRP and air-CFRP, is completely different.

The coupons, due to the manufacturing process, have a surface smoother than the opposite one; the first was chosen as entry side for the ultrasonic signal, further, to reduce the influence of any possible surface discontinuity, the chosen ultrasonic probe was a planar type.

The frequency of the probe was selected bearing in mind some prescriptions:

- when ultrasounds go across a media they are subjected to frequency dispersion, and this phenomenon is amplified by the presence of the pores, that is why a narrow bandwidth probe was preferred;
- the graph 1.17 in chapter 1, shows clearly that the frequency of the probe has a strong influence on the measured attenuation for a certain level of porosity. Of course, the smaller is the wave length of the ultrasound, the higher will be its interaction with small pores, and vice versa. Moreover, the higher is the probe frequency the smaller will be its penetration capability. The thickness of all the coupons ranges from 4.4 mm to 6.5 mm, and in addiction, the pores quantity also ranges from smaller values to larger ones (see table 4.4), then, in order to be sure to inspect all the coupons with the same probe and to obtain measures comparable between them, a Karl Deutsch STS6WB4-20, 4-20 MHz, Flat, transducer was chosen with diameter D= 0,25" which was tuned at 5 MHz.

The probe was properly oriented perpendicularly to the entry surface of each coupon at a distance to assure the planar wave approximation within the material, i. e. the front wave entering into the material is planar and its intensity is almost constant.

The water in the pool was degassed and its thermal equilibrium was achieved.

The Greek-fret covered by the probe was designed in such a way to achieve20000 of acquired points for each coupon.

The data are acquired by using a gate (an amplitude-time window in which the signal peaks with the larger amplitude are acquired) starting from the Entry-Echo and not including it, and it stops on the Back-Wall echo, which is included. This allows to monitor the whole thickness of the coupons.

5.2.2 UT Results displaying

The results are shown in the form of couples of c-scans (false color maps), one for the attenuation measures and one for the *time of flight* (ToF) measures. Each of them is provided with a color scale allowing to translate, respectively, the colors of the c-scan into attenuation values (in dB) or into the ToF (in μs).

The total attenuation for each coupon is averaged on almost 2000 points. The software provides the *mean value* and the *standard deviation* for both the attenuation and the ToF.

5.2.3 Criteria for the inclusions/delaminations evaluation

In all the tested coupons obtained with 100%, 50% and 0% of curing pressure, as the manufacturing design was conceived, a kapton disk 20 mm in diameter was interleaved in the stacking sequence, whilst in the sets of coupons cured with the 75% and 25% of the curing pressure, two overlapped disks of the same diameter were put.

For the evaluation of these defects the following facts were beard in mind:

a) The area of the kapton disk is 314 mm^2, so this must be the dimension of the defect that will be checked;

b) If the defect causes just a reduction, i. e. an attenuation, of the back wall echo (in the attenuation c-scan) it is classified as an inclusion: a zone where the signal simply sees a different material; while if the back wall echo disappears in correspondence of the defect (in the ToF c-scans), it is classified as a delamination: a strong discontinuity of the material due to an air insertion, causing a mirror like reflection.

5.3 Ultrasonic Testing results

5.3.1 DAC construction

During ultrasonic characterization of the employed materials, the averaged attenuation of the signal is measured in correspondence of each step of the step wedges coupons. Then, the DAC was obtained for each of them as well as the slope and the intercept estimation via the linear regression method.

The results have shown that the symmetric stacking sequences are, in general, most attenuating, in fact they are characterized by a larger slope with respect to the ones obtained for the unidirectional laminates.

- **Step wedge P1**

In figure 5.5 the obtained DAC is shown. From it, the bulk attenuation β and the intercept, i.e. the *surface losses* (A_R) are calculated (table 5.2):

$\beta \pm \sigma_\beta$(dB/mm)	0.67 ±0.01
$A_R \pm \sigma_R$(dB)	12.35 ±0.09

Table 5.2.

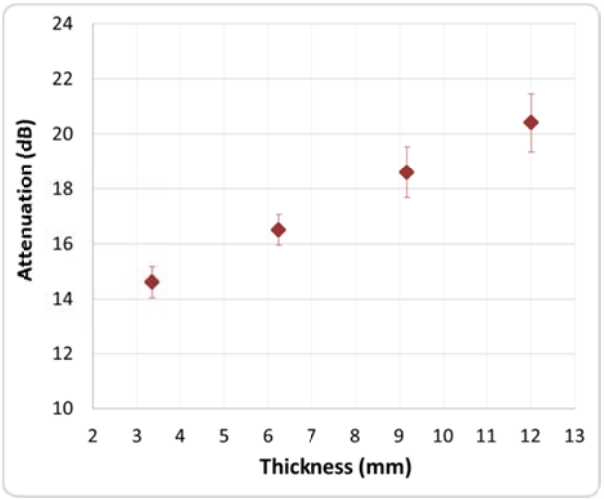

Figure 5.5: DAC of the step wedge P1.

- **Step wedge P2**

In figure 5.6 the obtained DAC is shown. From it, the bulk attenuation β and the intercept are calculated (table 5.3):

$\beta \pm \sigma_\beta$(dB/mm)	0.72 ±0.10
$A_R \pm \sigma_R$(dB)	11.50 ±0.84

Table 5.3.

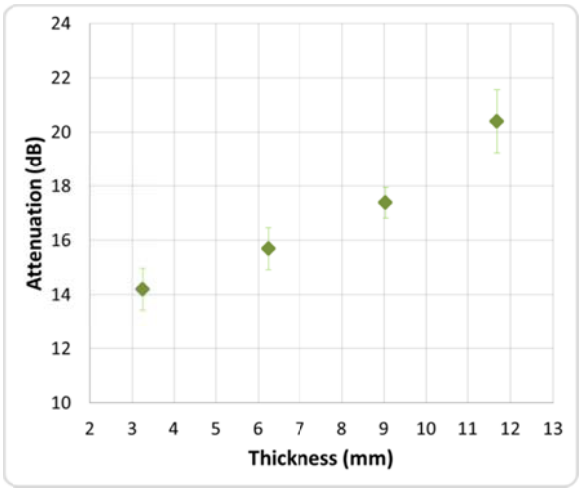

Figure 5.6: DAC of the step wedge P1.

- **Step wedge P3**

In figure 5.7 the obtained DAC is shown. From it, the bulk attenuation β and the intercept are calculated (table 5.4):

β(dB/mm)	1.13
A_R (dB)	8.24

Table 5.4.

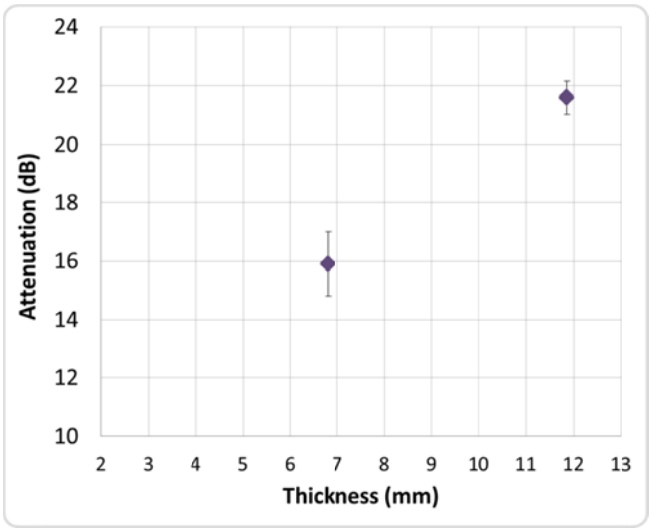

Figure 5.7: DAC of the step wedge P3.

The standard deviations on the calculated slope and intercept are practically negligible because the best fitting straight line is calculated only from a couple of data.

- **Step wedge P4**

In figure 5.8 the obtained DAC is shown. From it, the bulk attenuation β and the intercept are calculated (table 5.5):

β(dB/mm)	1.25
A_R(dB)	7.7

Table 5.5.

The standard deviations on the calculated slope and intercept are practically negligible because the best fitting straight line is calculated only from a couple of data.

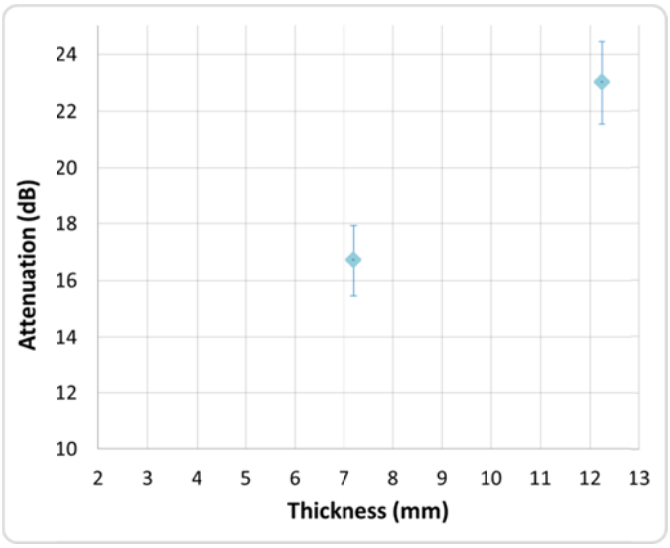

Figure 5.8: DAC of the step wedge P4.

5.3.2 C-scan of the coupons with induced porosity

In the following the c-scans obtained for each kind of coupons are reported. As previously explained, for each curing pressure, P_c, three sets of coupons were manufactured, but here only the most significant results are shown for each applied pressure. Both the attenuation and the ToF c-scans are shown with their correspondent color palette. All the shown c-scans refer to coupons positioned with the P1 type at the bottom until the P4 at the top.

It can be noticed that, when the defect is detected, it does not appear as disk shaped one. This is due to the fact that in most cases the disk is actually wrongly shaped (as the one shown in the previous fig. 4.4). Further, it is also possible a separation of the two disks for defects made by two overlapped disks. More specifically, this could be due to the slipping of one disk with respect to the other one, during the hand laying up of the coupons.

- **100% cured coupons**

In figure 5.9 the attenuation and the ToF c-scans are shown. In none c-scan the kapton disk was clearly detected, although it seems to be recognizable in the c-scans related to the coupon P4. The coupon P3 has the central part apparently more attenuating but it is probably due to a not perfectly planar surface.

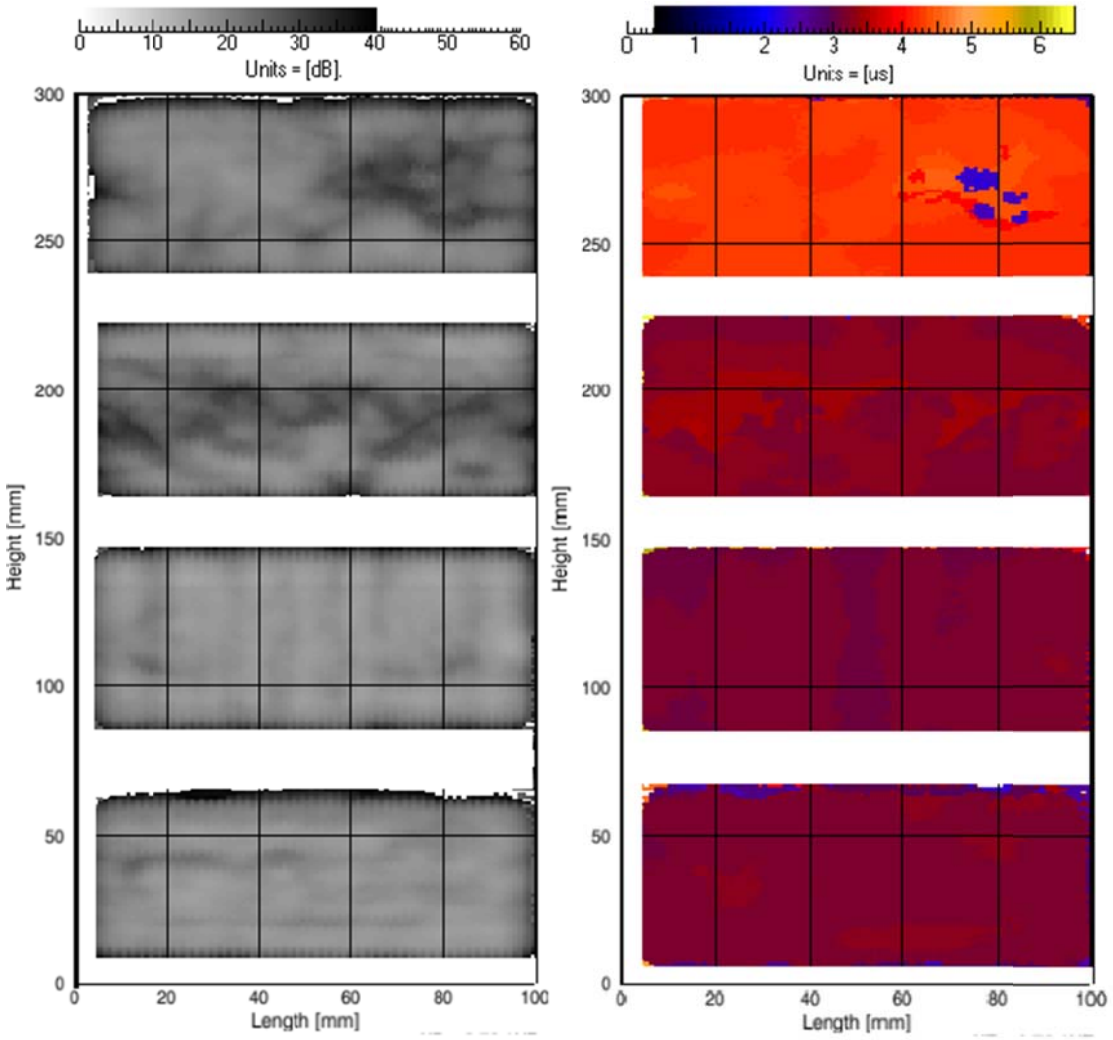

Figure 5.9: Attenuation (left) and ToF (right) c-scans of coupons cured with P_c=100%.

- **75% cured coupons**

In figures 5.10, the attenuation and the ToF c-scans are shown.

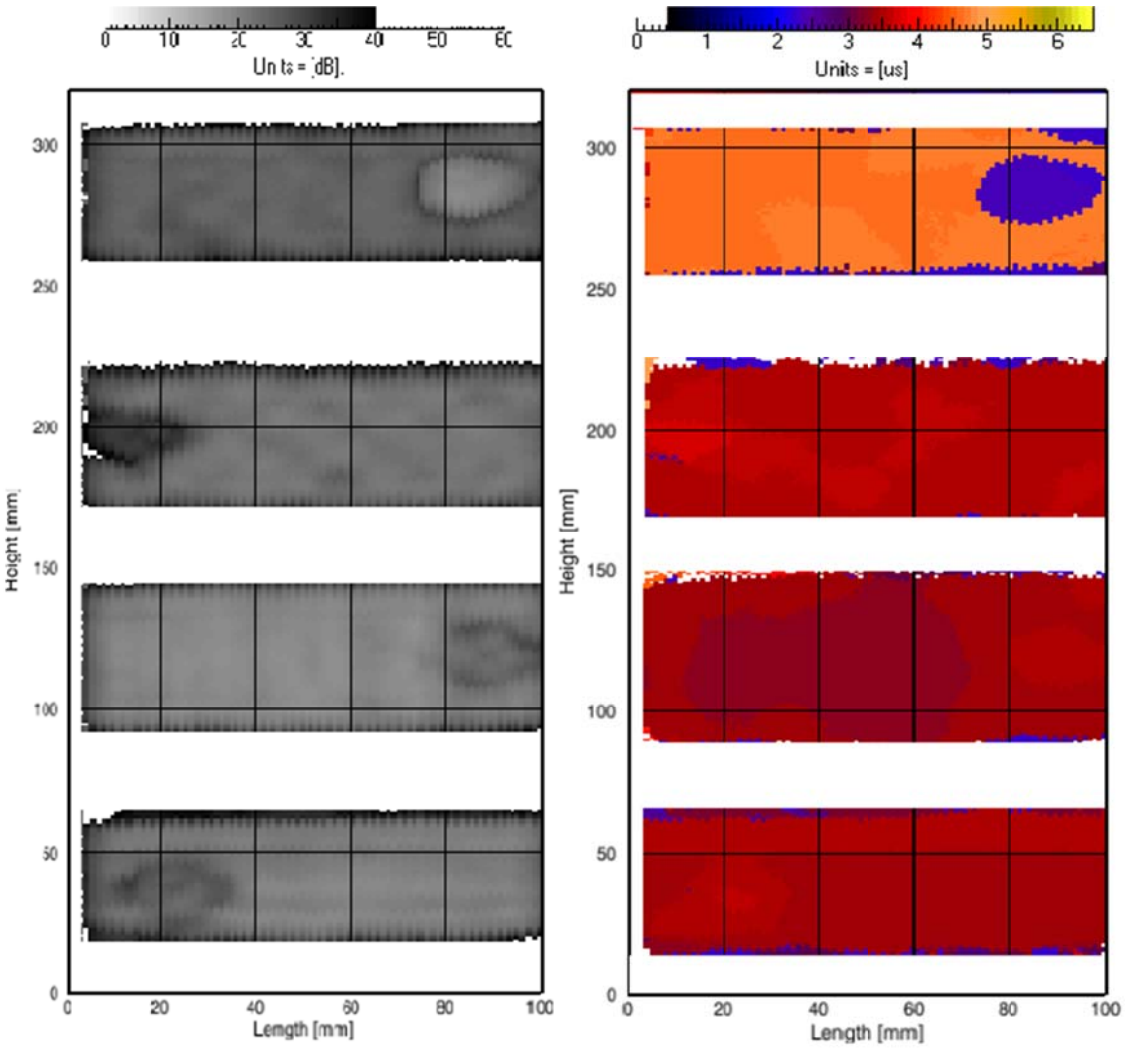

Figure 5.10: Attenuation (left) and ToF (right) c-scans of coupons cured with P_c=75%.

In the attenuation c-scan, the disk inclusion can be generally appreciated; in this case, the defect is made by two overlapped disks. Observing the ToF of the coupons, it can be noticed that only in the coupon P4 the disk is detected, then in this case the defect is considered a delamination (see paragraph 5.2.3). On the contrary in the coupons P1, P2 and P3, the kapton disk acts as just an inclusion of different material, acting as a different attenuating material.

- **50% cured coupons**

In figures 5.11, the attenuation and the ToF c-scans are shown.

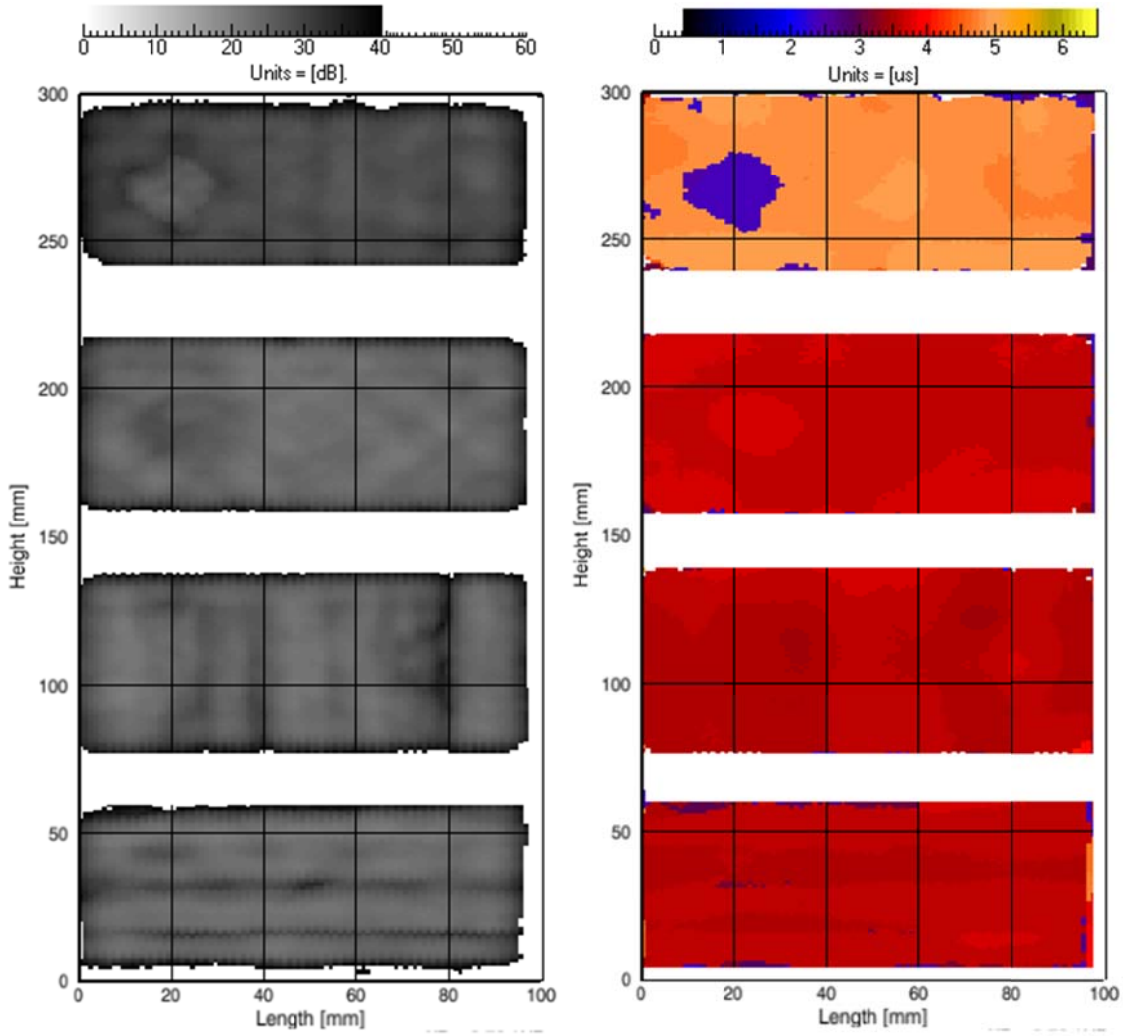

Figure 5.11: Attenuation (left) and ToF (right) c-scans of coupons cured with P_c=50%.

For coupons cured with P_c=50%, the signal seems to be more attenuated, which outlines the presence of an increased amount of induced porosity. In coupons type P1, P2 and P3 the attenuation increasing seems to be influenced by the fibres orientation. This can be also slightly appreciated in the ToF c-scan due to very small changes in the thickness. As for the previous case, observing the ToF of coupons, it can be noticed that only in the coupon P4 the disk is appreciable, consequently the defect is a delamination. This is corroborated by the attenuation c-scan due to the smaller attenuation in the defect area. The fact that the defect is not detected in the other coupons is due to the thinness of the single kapton disk

and to the presence of porosity; indeed porosity mitigates the signal due to possible mirror like reflections.

- **25% cured coupons**

In figures 5.12, the attenuation and the ToF c-scans are shown.

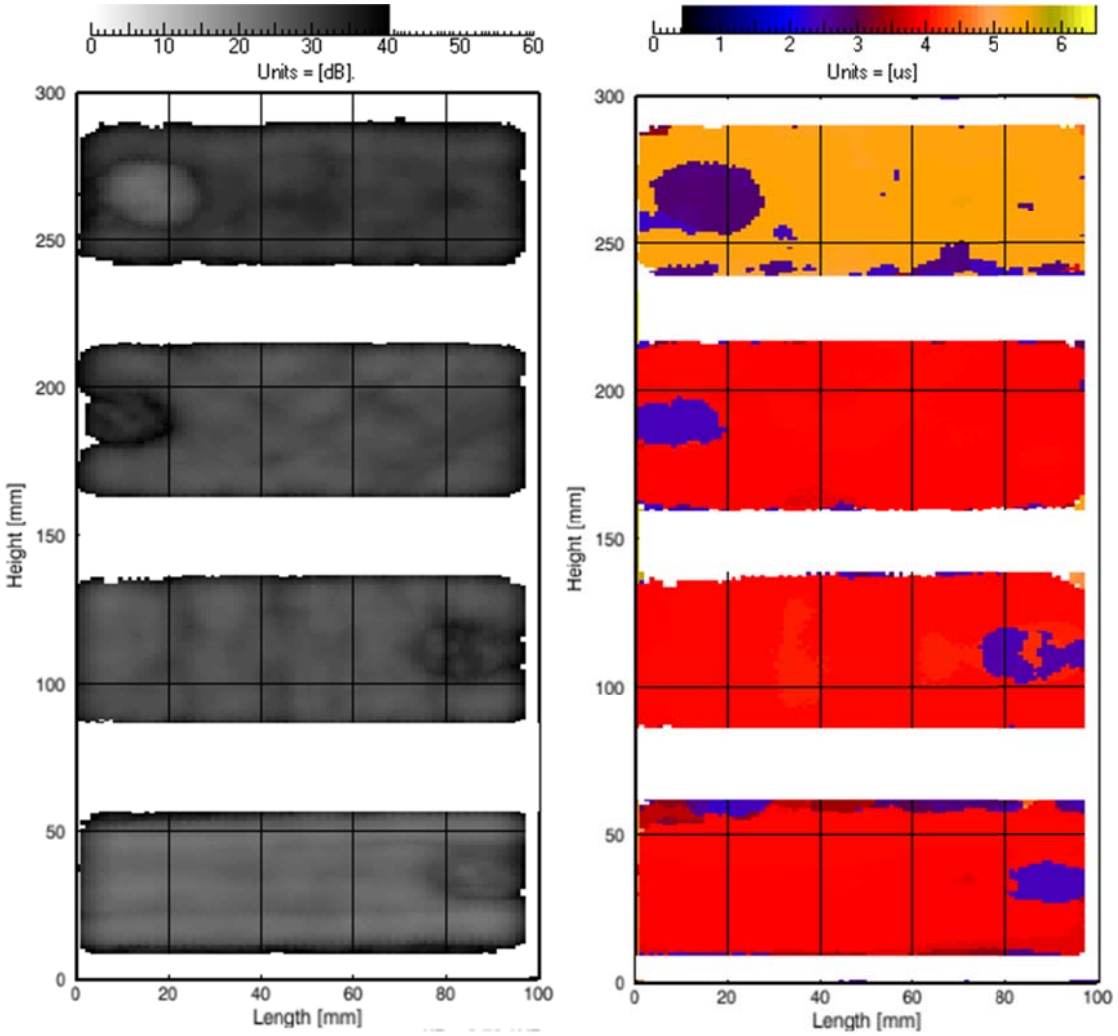

Figure 5.12: Attenuation (left) and ToF (right) c-scans of coupons cured with P_c=25%.

The increased reduction of the applied curing pressure has induced a more significant and distributed amount of porosity. This can be appreciated in the attenuation c-scans in figure 5.12; in fact, the overall attenuation is visibly higher than in the previous cases. The presence of porosity mitigates the signal reflected by the kapton disk especially for P1, P2 and P3 coupons. However, the defects can be appreciated as delamination in the ToF c-scans of all the coupons.

- **0% cured coupons**

In figures 5.13, the attenuation and the ToF c-scans are shown.

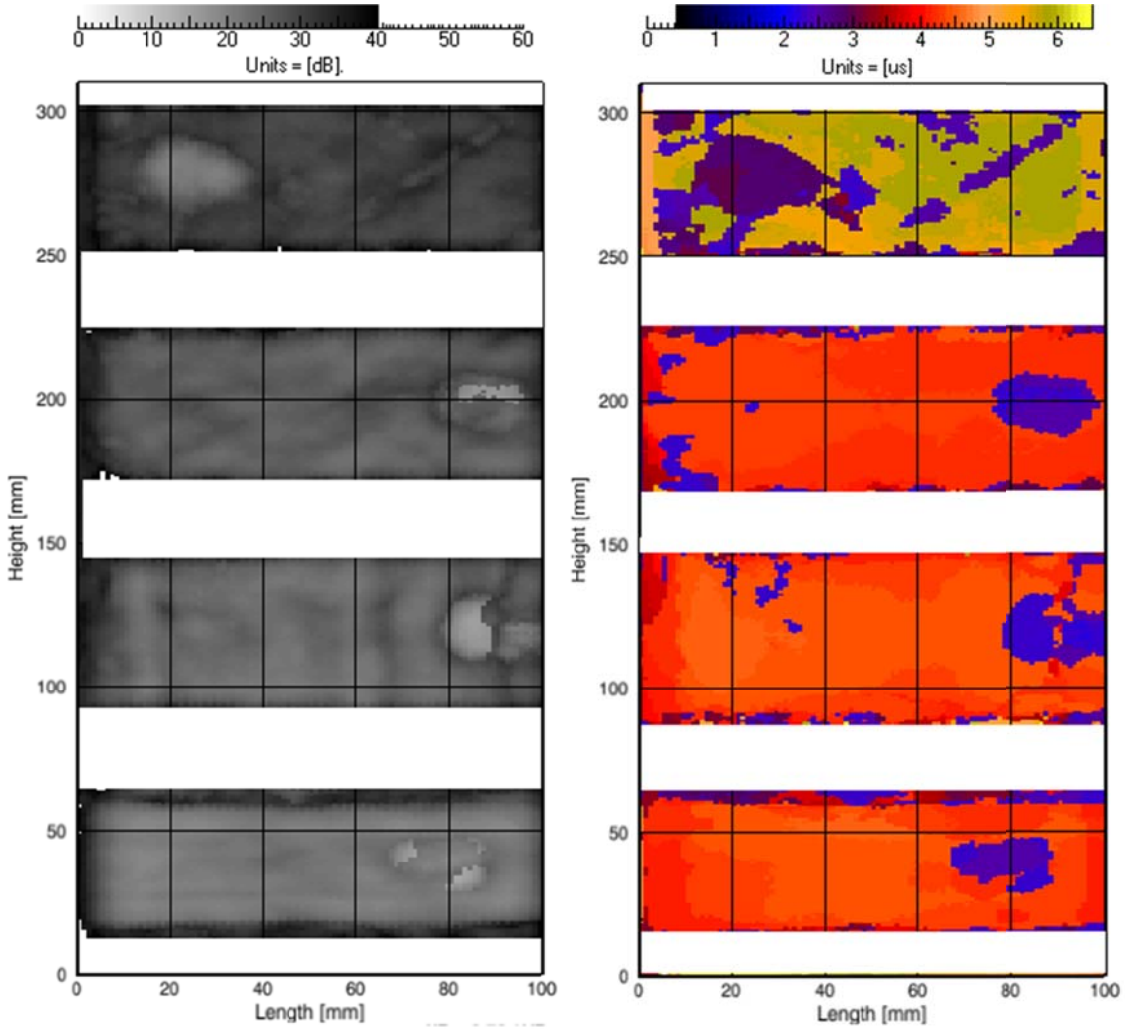

Figure 5.13: Attenuation (left) and ToF (right) c-scans of coupons cured with P_c=0%.

With a curing pressure P_c= 0% of the prescribed one, an increased amount of porosity is induced and, as a consequence, a stronger attenuation is measured. The presence of the defect is appreciable due to the smaller attenuation values with respects to the rest of the coupon area. The disk is clearly visible also in the ToF c-scan and other delaminated areas can be observed. This can be due to a local concentration of pores (or bigger connected pores) which, ultimately, produces a delamination.

5.3.3 Influence of the special manufacturing process on the UT results

From the attenuation c-scans, the average attenuation was calculated in the areas without the kapton disk. Such values are obtained by averaging 2000 acquired points. The obtained total average attenuation (A_T), the *bulk attenuation*, and the *attenuation coefficient* β of each set of coupons are collected in the following tables 5.6-5.9. The A_T is affected by an error of at most 15%.

P1 Pressure %	Aver. Atten. (dB)	σ (st. dev.) (dB)	Bulk atten. (dB)	β (dB/mm)
100	22.53	1.18	10.19	1.14
75	22.13	0.94	9.79	1.075
50	25.03	2.17	12.69	1.38
25	25.57	1.07	13.22	1.37
0	33.50	1.73	21.15	2.18

Table 5.6.

P2 Pressure %	Aver. Atten. (dB)	σ (st. dev.) (dB)	Bulk Atten. (dB)	β (dB/mm)
100	21.70	1.00	10.20	1.15
75	21.03	0.69	9.53	1.06
50	28.03	2.84	16.53	1.81
25	28.20	1.19	16.70	1.76
0	33.50	1.41	22.0	2.27

Table 5.7.

The bulk attenuation is obtained by subtracting, for each type of lamination sequence, the *surface losses* (A_R) from the average (total) attenuation. Then, to

obtain the attenuation coefficient β, the bulk attenuation is divided for the double thickness (due to the double passage of the signal across the coupon).

P3 Pressure %	Aver. Atten. (dB)	σ (st. dev.) (dB)	Bulk Atten. (dB)	β (dB/mm)
100	20.73	3.43	12.50	1.39
75	22.50	0.71	14.26	1.57
50	25.60	0.89	17.36	1.90
25	29.13	1.10	20.89	2.21
0	38.3	1.24	30.06	3.06

Table 5.8.

P4 Pressure %	Aver. Atten. (dB)	σ (st. dev.) (dB)	Bulk Atten. (dB)	β (dB/mm)
100	23.03	1.85	15.33	1.31
75	26.13	0.72	18.43	1.53
50	28.50	0.91	20.80	1.73
25	32.27	1.05	24.57	2.01
0	42.10	1.35	34.40	2.65

Table 5.9.

For each type of coupons, the obtained attenuation coefficient, are plotted against P_c in the graphs reported in the following figures 5.13-5.16. As can be seen, in every case an almost linear dependence on the decreasing pressure is outlined, although the trends are better fitted by a polynomial of the second order. In all the graphs both the linear and polynomial regression lines are reported: the first one in red and the second one in black.

The results of the two types of regression are resumed in table 5.10, where the best coefficient of determination R^2 is obtained for the polynomial regressions. It is interesting to outline that the larger sensitivity to the decreasing pressure is obtained for the coupon type P3, whose attenuation increases with the decreasing pressure much quickly than for the other stacking sequences. This is in partial contradiction with results obtained with the gravimetric method (see table 4.5), which shows that the P1 coupon has a stronger tendency to retain voids with respect to the other coupons types.

Coupon type	**Linear regression**		**Polynomial regression** ($y=ax+bx+cx^2$)			
	Slope	**R^2**	**a**	**b**	**c**	**R^2**
P1	-0.0084	0.73	1.85	0.02	$1x10^{-4}$	0.91
P2	-0.0102	0.85	1.86	0.01	$4x10^{-5}$	0.86
P3	-0.0115	0.91	2.17	0.02	$1x10^{-4}$	0.99
P4	-0.0097	0.93	2.00	0.02	$8x10^{-5}$	0.99

Table 5.10.

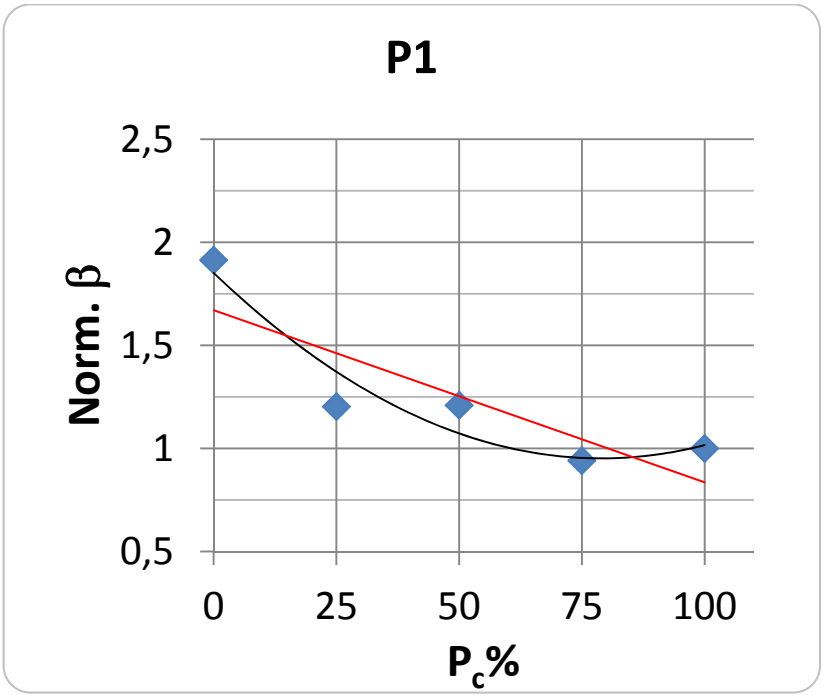

Figure 5.13: Normalized attenuation coefficient vs. P_c.

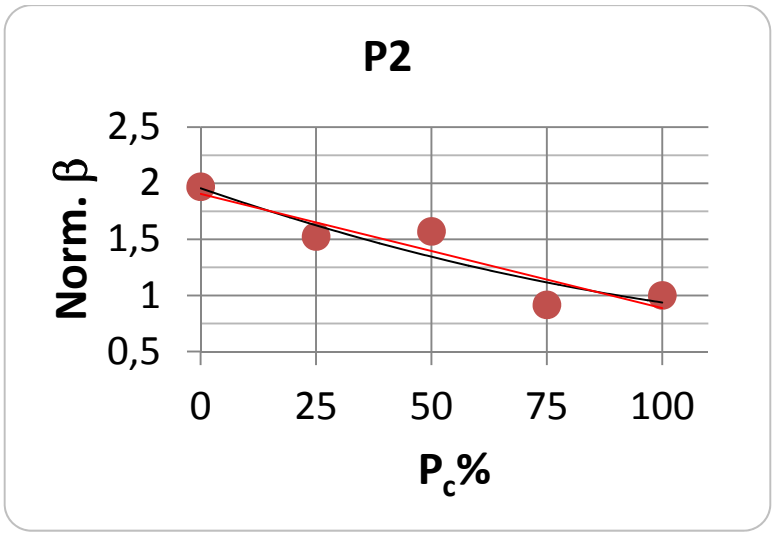

Figure 5.14: Normalized attenuation coefficient vs. P_c.

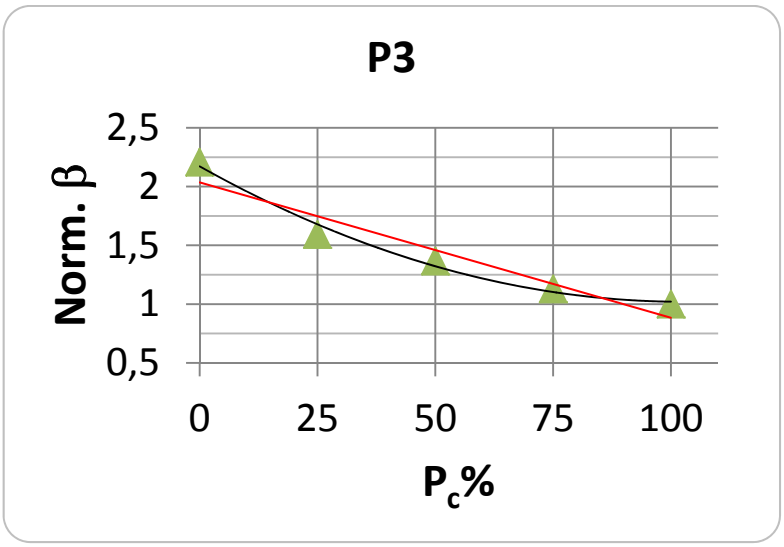

Figure 5.15: Normalized attenuation coefficient vs. P_c.

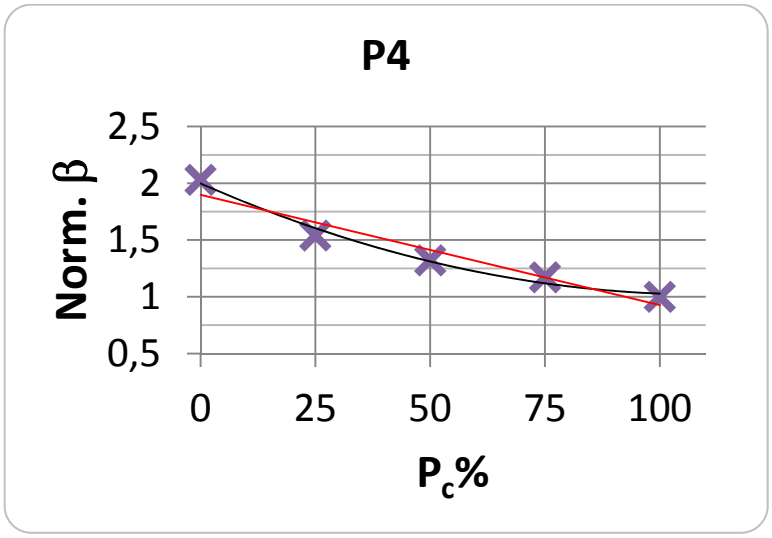

Figure 5.16: Normalized attenuation coefficient vs. P_c.

5.3.4 Comparison of results from UT and the gravimetric method

In order to check the influence of the volumetric percentage of pores measured with the gravimetric method, some graphs are shown in figures 5.17-5.20 . In each of them, the obtained ultrasonic attenuation coefficient, for each type of coupons, is plotted against the normalized $V_v\%$ (see chapter 4). As can be appreciated, in every case an almost linear dependence by the decreasing pressure is outlined, although the trends are much better fitted by a polynomial of the second order. In all the graphs both the linear and polynomial regression lines are reported: the first one in red and the second one in black.

The results of the two types of regression are resumed in table 5.11, where the best coefficient of determination R^2 is obtained for the polynomial regressions.

The most regular trend is shown by the P3 coupon, on the contrary the P4 reflects the stepped behavior shown by the porosity percentage in fig. 4.18 of the previous chapter. The apparent discrepancies between the behaviors obtained using the two methods, i.e. using the curing pressures as reference, or the porosity percentage, can be ascribed to the different response of UT and gravimetric methods to the distribution of pores in the coupons.

However, it must be remarked that UT is also sensitive to other parameters connected to the porosity, specifically the scattering of the ultrasonic wave beam due to the pores is strongly affected by the pores dimension, density and topological distribution. Indeed, if the pores diameter is of the same order of the ultrasonic wavelength, the scattering phenomenon is increased, and, in the worst case, if the pores are very large, the signal is almost totally reflected.

The gravimetric method, on the contrary, is practically not affected by the pores spatial distribution.

Moreover, the entire coupons were analyzed with the UT, whereas the gravimetric method only allows to evaluate smaller pieces.

Coupon type	Linear regression		Polynomial regression ($y=a+bx+cx^2$)			
	Slope	R^2	a	b	c	R^2
P1	0.092	0.59	1.07	-0.08	$1.8x10^{-2}$	0.67
P2	0.140	0.67	0.88	0.08	$7.5x10^{-3}$	0.70
P3	0.170	0.91	1.02	-0.03	$2.6x10^{-2}$	0.99
P4	0.100	0.56	-4.12	6.10	$-79x10^{-1}$	0.62

Table 5.11.

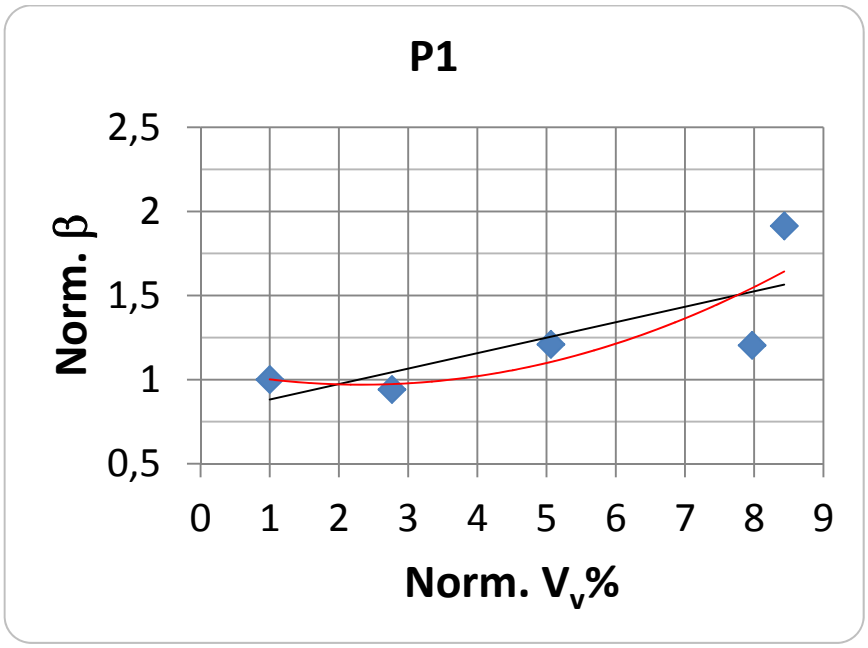

Figure 5.17: Normalized attenuation coefficient vs. the normalized V_v%.

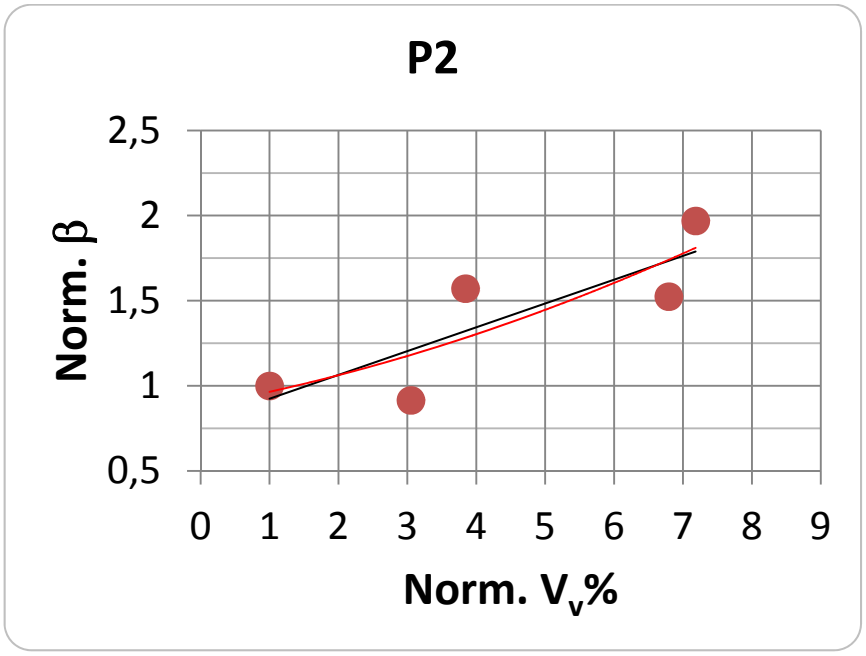

Figure 5.18: Normalized attenuation coefficient vs. the normalized V_v%.

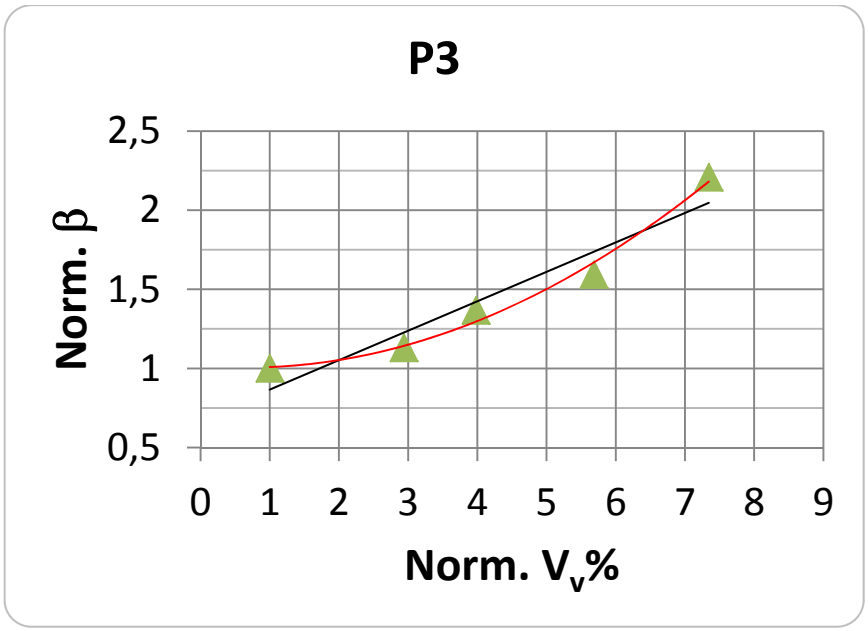

Figure 5.19: Normalized attenuation coefficient vs. the normalized V_v%.

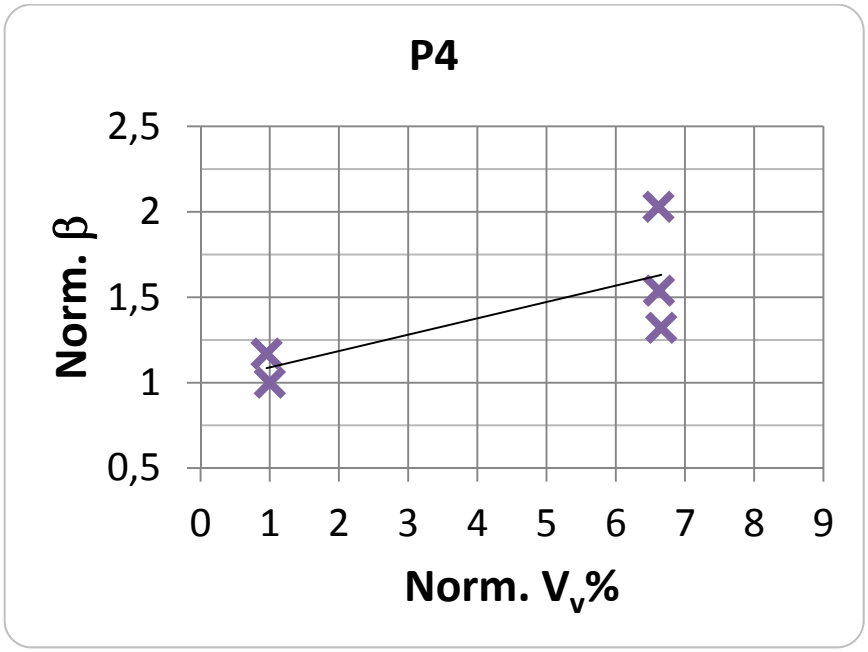

Figure 5.20: Normalized attenuation coefficient vs. the normalized V_v%.

5.3.5 Kapton disk detection

The nominal area of the kapton disk is 314 mm^2. The area of all the detected defects was measured by the software provided with the apparatus shown in fig. 5.4.

The detection of the kapton inclusion is more feasible for coupons cured with 75% and 25% of the curing pressure. This because, the defect was made by two

overlapped kapton disks. Indeed the axial resolution of the 5MHz transducer was estimated to be 0.5 mm which corresponds to the thickness of almost 2 plies, while a the detection of defects made by a single kapton disk is almost impossible. On the other hand in aeronautics, in order to calibrate the ultrasonic testing parameters for detection of delamination, i.e. the lack of adhesion between plies, this defect is simulated by two overlapped layers of a material different with respect to the pre-preg one.

Further, the fact that also for the 50% and 0% P_c cured coupons the defect detection was very probable is due to the double effect of the kapton disk and the local concentration of porosity.

Regardless the type of coupon and the pressure for which the defect was detected, the measured area was generally larger than expected. This is generally due to the effect of the interaction between the ultrasonic beam with the edges of the defect. This can be fine-tuned by applying a suitable criteria to distinguish the defect with respect to a sound area, which is what is generally done once the acceptance/rejection criteria are assigned.

Type	P_c	Defect area (mm^2)
P1	100%	–
P2		–
P3		–
P4		–
P1	75%	697
P2		495
P3		440
P4		476
P1	50%	–
P2		–
P3		458
P4		359
P1	25%	350
P2		399
P3		409
P4		454
P1	0%	–
P2		204
P3		440
P4		309

Table 5.12.

5.4 Remarks

The ultrasonic characterization of the coupons with embedded porosity, has allowed to re-demonstrate/confirm some data in literature, and it has open the door to some investigation aspects which have not yet been faced. This could led to reach a more comprehensive knowledge of the mechanisms involved with the formation of pores during autoclave curing.

In the following some important remarks are outlined:

- It is possible to obtain coupons with a different amount of porosity by simply regulating the pressure applied during autoclave curing.

Although the smallest applied pressure corresponds to 0% of the prescribed 7 bar one, which means no pressure applied in the autoclave cycle, the coupons were previously put in a vacuum bag and air was sucked off in order to create a difference of 1 bar with respect to the ambient pressure. That is why also coupons cured with P_c=0% maintained a certain level of compaction.

Of course, the simple change of pressure does not entail any other effect on the pores characteristics, such as distribution, size, and shape.

- Ultrasonic attenuation measures not only allow for indirect estimation of the pores density, but, involving the whole component, also provide more reliable results as compared to the ones obtained with the gravimetric method.
- Although the employed material is the same for all the coupons, including the step wedges, some discrepancies have been found in terms of surface losses and of slopes of the DACs. Surface losses are linked to the roughness of the inspected surfaces, which may change from coupon to coupon, depending on the manufacturing process.

The slope differences have to be ascribed, at this stage, principally to the inner structure of the material which attenuates the signal depending on the stacking sequence. This point deserves deeper insights .

- From the obtained results, it can be outlined that the lamination type P3 has a higher tendency to attenuate the ultrasonic signal with respect to the others lamination sequences. This entails that the different fibres distribution and

orientation could be responsible of a different distribution and concentration of pores. This last point needs a more deep knowledge of the resin flow mechanism involved in the autoclave curing coupled with a very accurate fractographic analysis.

Chapter 6

Infrared thermography testing and data analysis

In this chapter are shown all the results, obtained through non destructive evaluation with Infrared Thermography, of the porous coupons, which were already described in the previous chapter 4.

Firstly, tests are carried out by using Lock-in Thermography (LT) in order to get a general outlook on the detection of defects buried in the composite material under inspection. Then, the investigation goes on the measurement of thermal diffusivity with the Flash Thermography technique. This is done because the thermal diffusivity is directly linked to the density of the material and, in turn, to its porosity content.

The flash thermography measurements required a specific instrumentation and set-up, as well as a mathematical tool for processing the huge amount of data.

On the whole, the obtained results show a clear dependence of the thermal diffusivity on the curing applied pressure; specifically, the embedded porosity is responsible for a decreasing of the thermal diffusivity. This outcome allows for an indirect characterization of the porosity amount in the laminate in a simple, fast and completely non-invasive way.

6.1 Analysis of porous coupons with IRT

After the UT in immersion testing campaign, all the coupons (see section 5) were properly dried in order to assure complete removal of the likely water infiltration. This precaution was necessary because the presence of water in the laminate structure can locally modify the thermal properties of the material making the IRT measurements not effective for the determination of the desired quantity. On the other side, the undesired presence of water acts as further embedded anomaly which may affect the discrimination of the voluntary enclosed defects.

Tests were carried out by using both Lockin Thermography (LT) and Flash Thermography (FT). A general scheme of the test setup is given in the fig. 3.9 and here again reported for convenience in fig.6.1. On the whole, it shows the main components involved and the position of heating source and infrared camera to perform tests with both LT and FT in both reflection and transmission modes. More details about the heating source and the infrared camera as well testing procedure and data reduction will be given in the next sections concerned with the specific test arrangement.

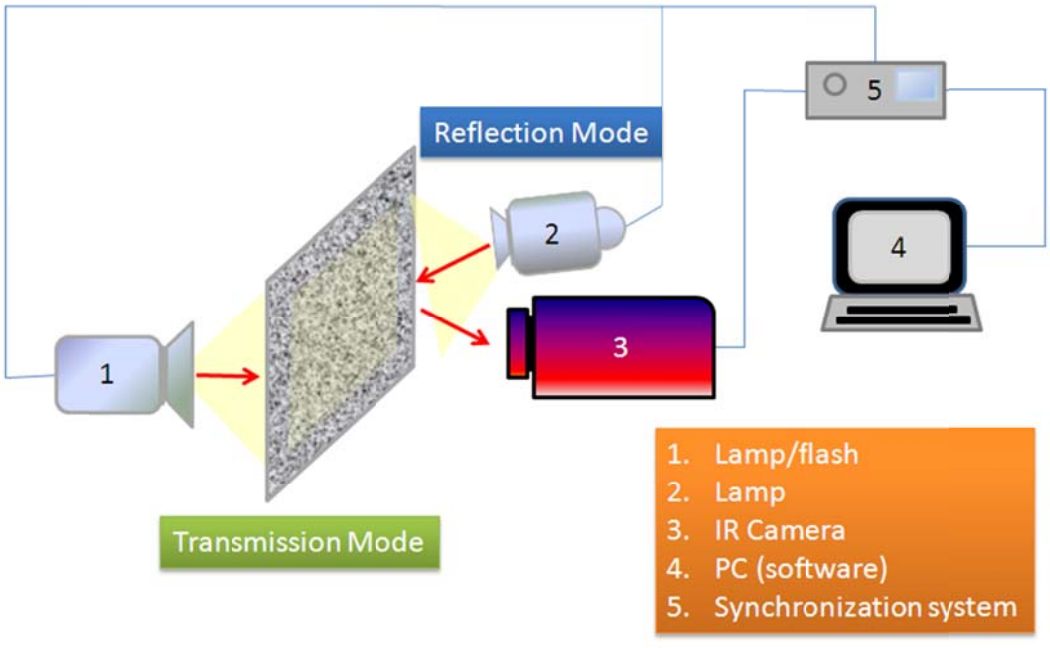

Figure 6.1: Set up for InfraRedThemography inspections.

6.1.1 Lockin Thermography

LT is used mainly to outline defects and to gain information about their depth. It was used in both reflection and transmission modes owing to the set-up schematically described in fig. 6.1. In both cases a halogen lamp (1 or 2) is sinusoidally modulated (5) and oriented toward one side of the coupon under inspection. This allows to heat up the material and to induce a heat wave travelling inside it. The thermal camera (3) acquires images in time sequence which account for the surface temperature variations either on the same side lighted by the lamp if the reflection mode is operated, or on the opposite side if the transmission mode is used. Then a specific software (4) algorithm allows to rapidly obtain amplitude and phase maps of the inspected object.

LT in reflection mode

The infrared Lock-In testing campaign was initially performed in the classical *reflection* mode (fig.6.1). This was the first chosen technique because, it allows (see eq. 3.33 and 3.37 in section 3) for fast determination of the defects depth. Unfortunately no significant results were obtained, because of a combination of factors such as the large thickness of the inspected coupons and the large amount of buried inhomogeneities that prevent a clear outline of the slag inclusion.

The same tests were also repeated at the Department of Aerospace Engineering (DIAS) University of Naples, Federico II.

The used instrumentation includes:

1. Halogen lamp of 500 W
2. ThermaCam FLIR SC6000
3. Computer with Software to process data IrNDT (1.7.0.0);
4. Frequency Modulator

Thermacam SC6000 characteristics:

- 640 x 512 pixels QWIP focal plane array;
- Spectral range (LWIR): 8÷9.2 μm;
- Cooling: Stirling pump; Sensitivity < 20mK;

The first observation to be made regards the power lamp which was smaller, but it was also of low encumbrance allowing for a close up heating.

Also in this case, on the whole, the obtained results were unsatisfactory since it was not possible to clearly visualize the kapton disk in all the coupons. However, some important information were achieved, which will be discussed in the following. To this end, some phase images, relating to the smooth side of the P1 coupon cured with curing pressure P_c=100% are reported in fig. 6.2

It is worth noting that within this technique the used heating stimulation frequency is decreased at each test in order to find the best phase contrast able to outline the presence of the defects. From the theory shown in section 3.5.3, this also allows to reconstruct the depth of the defects. The defect can be seen starting from a certain frequency value *f*, then its contrast improves with decreasing *f* till a critical *f* value, the so called *blind frequency* for which the defect is no more visible, after that the defect appears again but with a change of colour (change of phase angle value with respect to the background) and it generally remains visible also for smaller values of the frequency till the entire material thickness is traversed. As can be seen, the defect, although of poor contrast is detected since at a frequency of 2 Hz (Fig.6.2a); it appears with better phase contrast as the frequency is decreased to 1 Hz (Fig.6.2b) and to 0.5 Hz (fig. 6.2c). The sign of the phase contrast changes (fig. 6.2d) for *f* = 0.15Hz meaning that the blind frequency has been overpassed. At the stimulation frequency of 0.02 Hz (fig. 6.f) the defect practically disappears meaning that the entire thickness has been overpassed. These observations are better described by the graph in fig. 6.3. The same coupon was inspected also by viewing its opposite side which was more rough than the previous one (fig. 6.4). From this side it was practically impossible to find out the defect. This is due to a wrong positioning of the kapton disk in the lamination sequence: instead of being put in the middle of the stacking sequence, it was put one layer more close to the smoother surface. This aspect will be recalled later and discussed more in depth. Another interesting aspect come out for the P2 coupon cured with P_c=100% of the pressure.

From the phase map obtained with f = 0.15 Hz and by framing its smooth surface (fig. 6.5) it seems that the kapton disk is smaller than expected. It could be due to a mistake in the manufacturing. It has to be noted that the hand lay-up method involves a compression force applied with a special roller tool in order to remove as much as possible the air contained between the layers. Most probably, during such a compression operation, the kapton sheet wrinkled up; such a wrinkling up being favored by the horizontal orientation of the fibres.

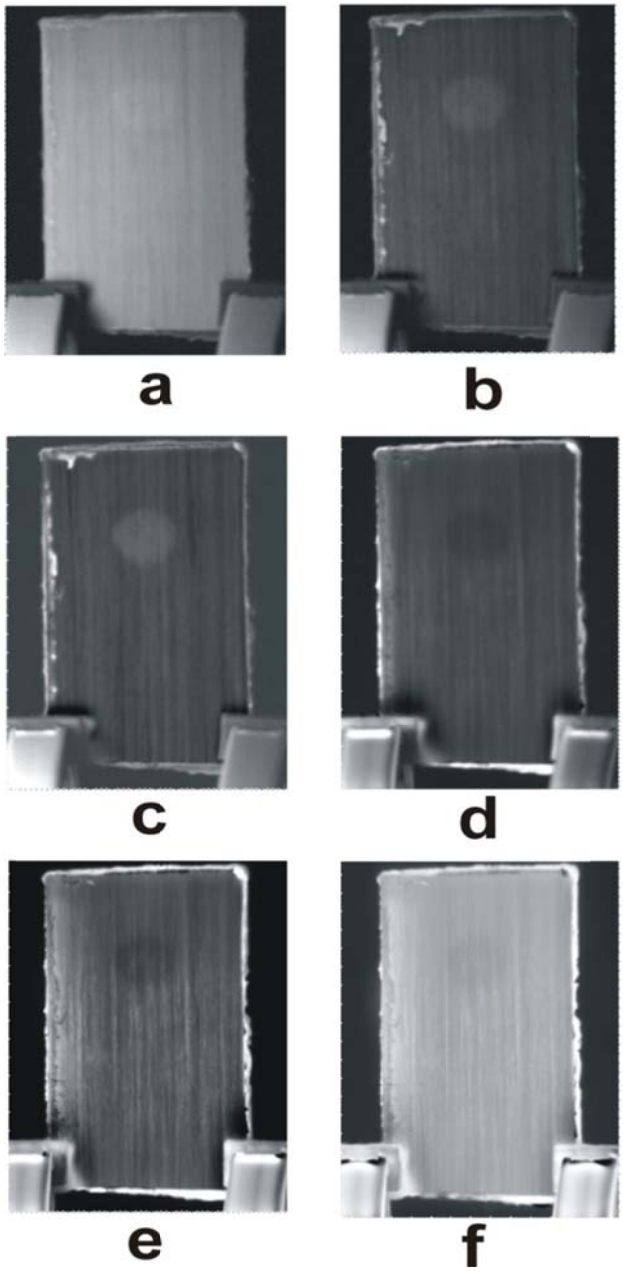

Figure 6.2: Phase maps of the smooth side of the P1 coupon cured with *Pc*=100%, at different stimulation frequencies: in a) *f*=2Hz; in b) *f*=1Hz; in c) *f*=0.5Hz; in d) *f*=0.15Hz; in e) *f*=0.05Hz, in f) *f*=0.02.

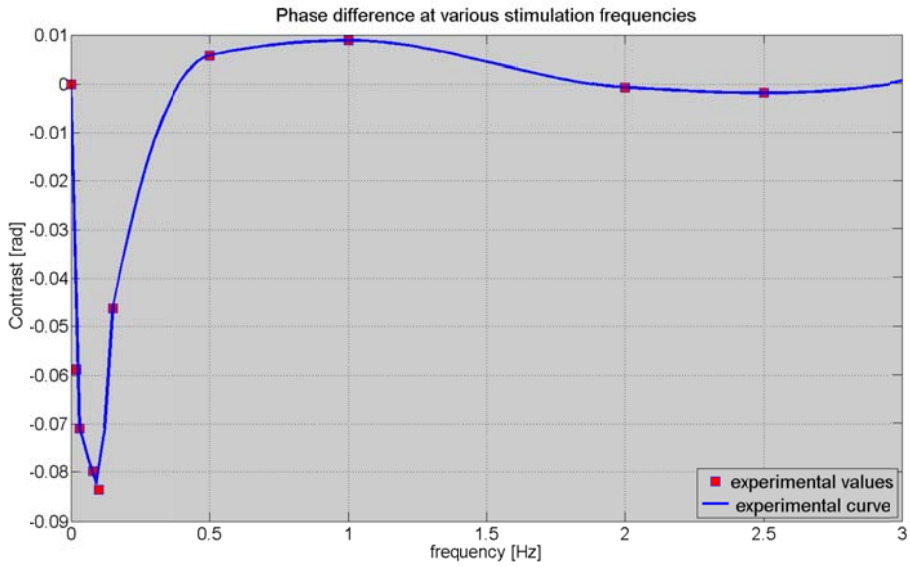

Figure 6.3: Distribution of the phase contrast with the stimulation frequency.

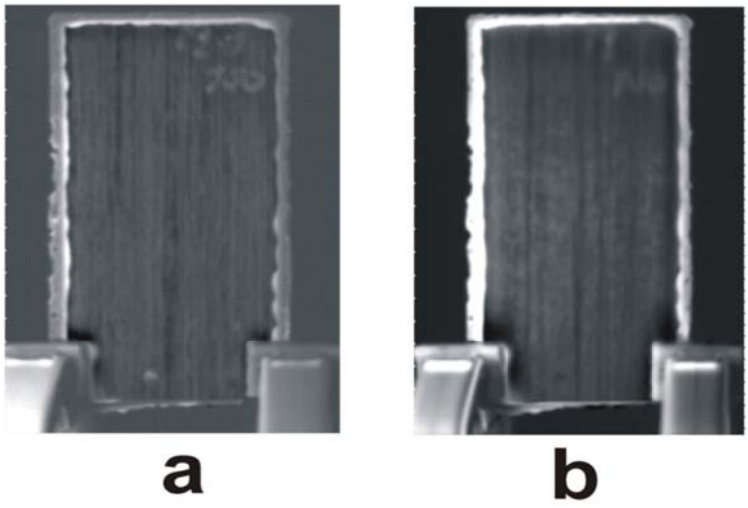

Figure 6.4: Phase maps of the rough side of the P1 coupon cured with *Pc*=100%, at different stimulation frequencies: in a) *f*=0.5Hz; in b) *f*=0.15Hz

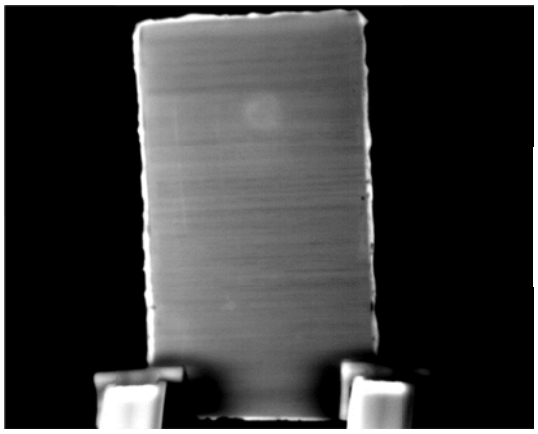

Figure 6.5: Phase map of the smooth side of the P2 coupon cured with P_c =100% of the pressure.

Also in the case of the P2 coupon cured with P_c=75% of the pressure, the kapton disk appears smaller than expected in both types of tests performed by viewing either the smooth surface (fig. 6.6a), or the rough one (fig. 6.6b).

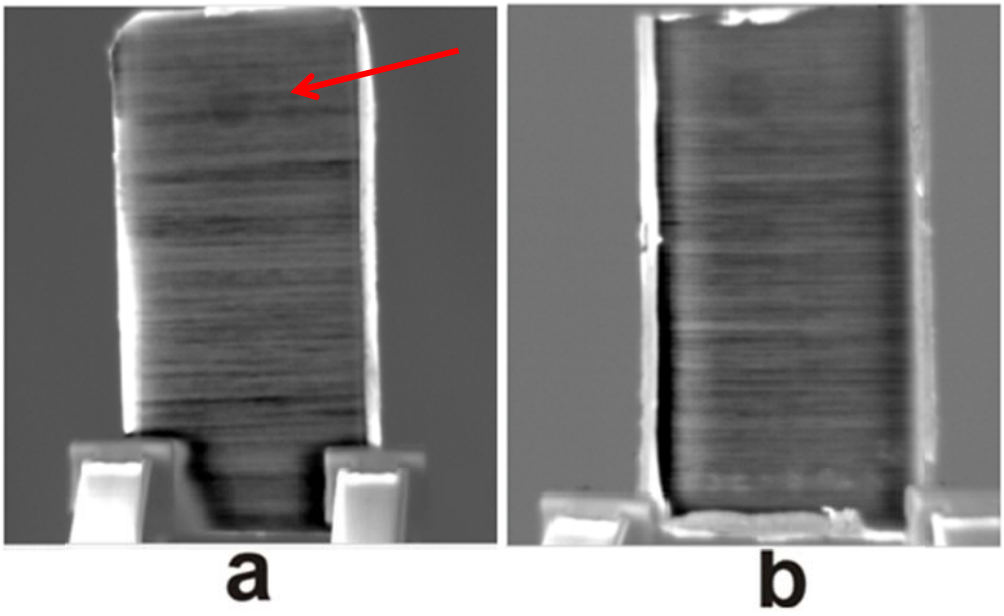

Figure 6.6: Phase maps of the smooth surface (a), and the rough surface (b) of the P2 coupon cured with P_c =75% using *f*=0.2.

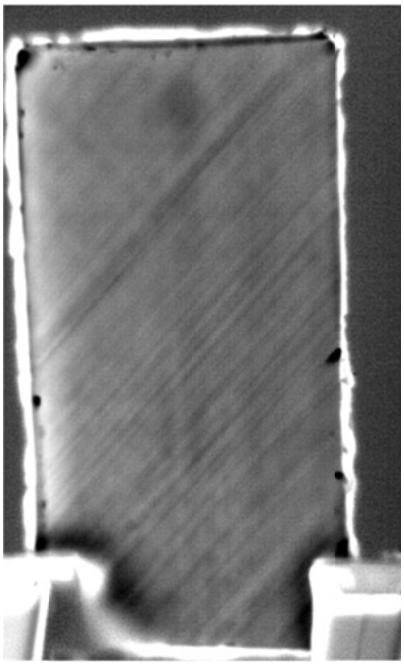

Figure 6.7: Phase maps of the P4 coupon cured with P_c =100% of the pressure, at *f*=0.2Hz.

What it is more, by comparing the two phase images in fig. 6.6, it can be noted that the disk in fig. 6.6b appears moved on the left side. As a probable explanation a splitter up of the kapton disk, which is, in reality, composed of two overlapped ones (see fig. 4.4) , has occurred. One part is clearly visualized

from the smoother specimen side (fig. 6.6a) and appears almost centered within the specimen width. Instead, the second part is only hardly perceptible on the right side (indicated by an arrow) also because masked by the wrapping up of the carbon fibres; the latter effect is also clearly visible in the phase image (fig. 6.6a). Of course, this second part of the kapton disk is better visualized when viewing the rear rough specimen side (fig. 6.6 b).

At last, fig. 6.7 shows a phase map of the P4 coupon cured with P_c=100%. As can be seen the defect appears displaced upside, of elliptical shape and of smaller size even if a lighter halo might be envisaged accounting for the real size. Again the disk was affected by the rolling up force during fabrication of the specimen.

It is worth noting that we are considering a very thin kapton sheet embedded in a carbon/epoxy with enclosed also a certain amount of porosity. Owing to the fact that, in presence of porosity, the thermal diffusivity of the carbon/epoxy laminate decreases substantially towards that of the epoxy resin and that the thermal diffusivity of kapton is close to that of the epoxy resin, it is obvious the difficulty in discriminating sound areas from defected areas.

LT in transmission mode

In the transmission mode, the thermal camera is put framing the opposite side of the lighted surface. Therefore, the thermal camera monitors and acquires the surface temperature on the side which is not directly warmed up by the lamp. Similarly to the reflection mode, also in this case phase maps can be obtained, but, being the path travelled by the thermal wave the same in each point of the material, the knowledge about the depth of the defect is missing. Nevertheless these tests are of interest because the phase delay between the excitation thermal wave, produced by the sinusoidal modulated light, and the thermal wave exiting from the material under analysis, depends not only on the covered path, but also on the material thermal properties. Indeed, as reported in chapter 3, and rewritten here for convenience, it is:

$$\varphi(x) = \frac{x}{\mu} \tag{6.1}$$

the relation between the phase delay and the diffusion length, which is given by:

$$\mu = \sqrt{\frac{2\alpha}{\omega}} = \sqrt{\frac{\alpha}{\pi f}} = \sqrt{\frac{k}{\rho c_p}\frac{1}{\pi f}} \tag{6.2}$$

Then, from eq. 6.1 and eq. 6.2 it can be observed that the phase delay strongly depends on the material properties, and, the local changes of the phase maps certainly can be ascribed to a different composition of the material in that area. Unfortunately, the available acquisition software does not allow to quantitatively measure the phase.

The used set up for the LT in transmission is that shown in fig. 6.1 with the used elements being:

1. halogen lamp (1) emitting at most 1kW light power;
2. Flir® SC5000 Infrared camera with the following main characteristics:
   - 320 x 256 pixels Indium Antimonide (InSb) focal plane array;
   - Spectral range (MWIR): 3.7÷5.1μm;
   - Cooling: Stirling pump;
   - Sensitivity< 25mK;
   - Frequency frame: 5-400 Hz full frame; up to 20kHz in the windowing mode;
3. Software provided by Flir, made by two blocks. One is devoted to the acquisition, visualization and several option for data displaying and saving (ALTAIR), the other block is devoted to the analysis of the data involving the lockin treatment algorithms (ALTAIR LI); this last is the part of the software producing, through an FFT like algorithm, both module and phase maps;
4. This part is made by a function generator for the sinusoidal modulation of the lamp light emission and by a synchronization block allowing to independently drive at most four lamps 1kW each.

Tests were carried out by putting the halogen lamp almost 50 cm distant from the surface of each coupon.

Each set of coupons was arranged in a proper casing in order to avoid the direct camera exposition to the light (fig. 6.9).

Figure 6.9: Setup for LT in transmission mode.

In the following figures 6.10–6.14 are shown some phase maps obtained with LT in transmission mode and by using a heating modulation equal to 0.025 Hz.

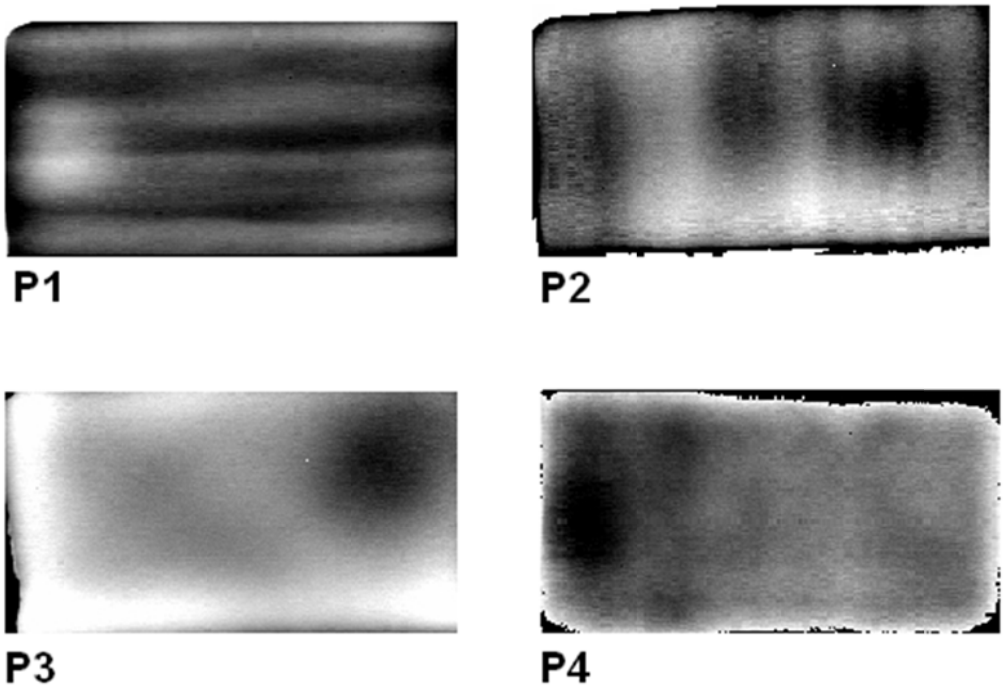

Figure 6.10: Phase map of the coupons cured with P_c =100%.

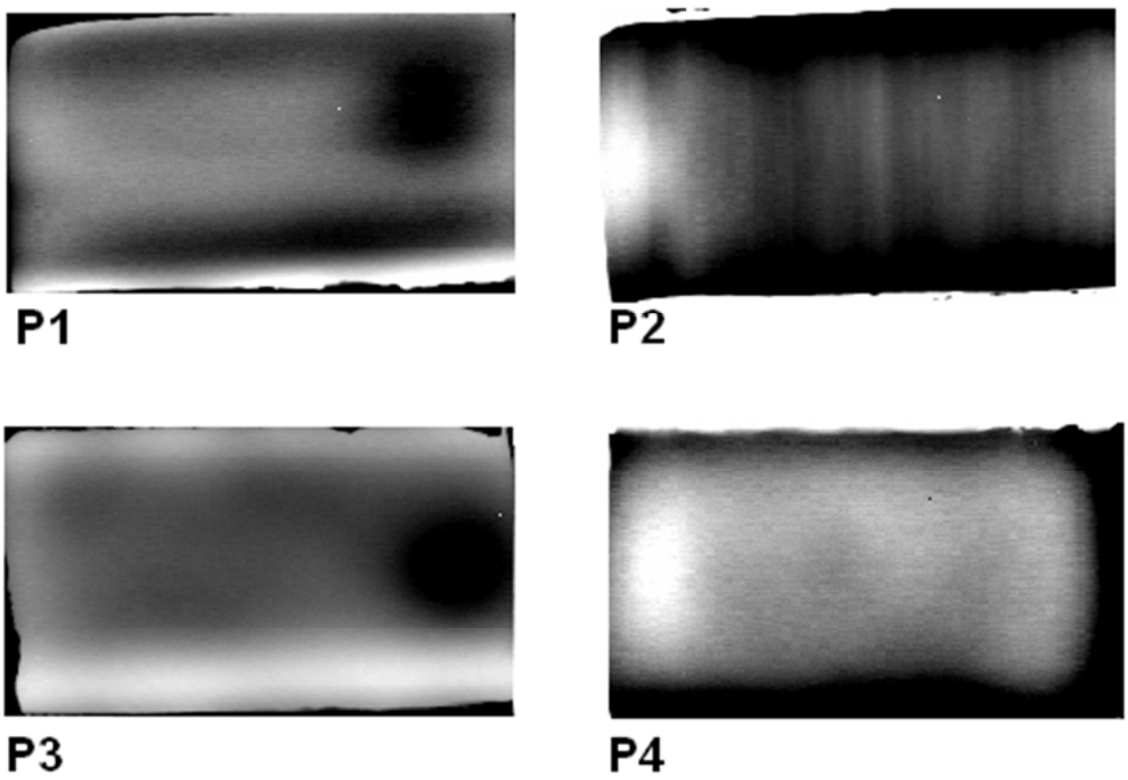

Figure 6.11: Phase map of the coupons cured with P_c =75%.

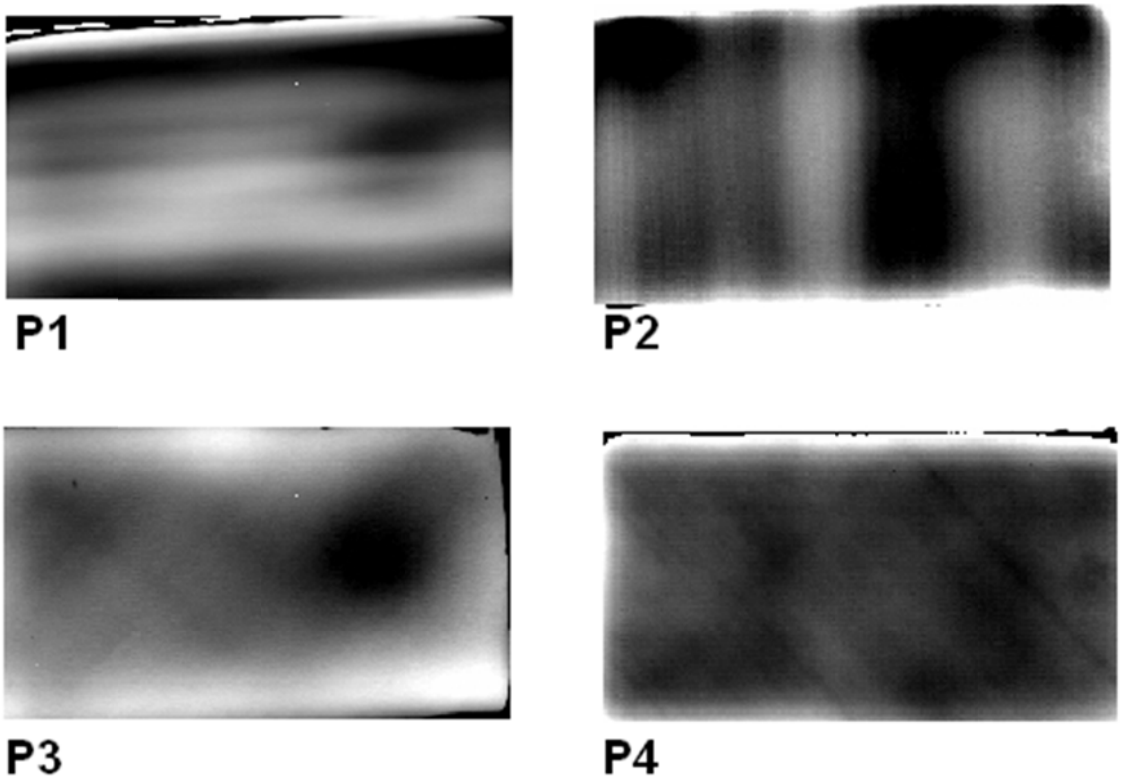

Figure 6.12: Phase map of the coupons cured with P_c =50%.

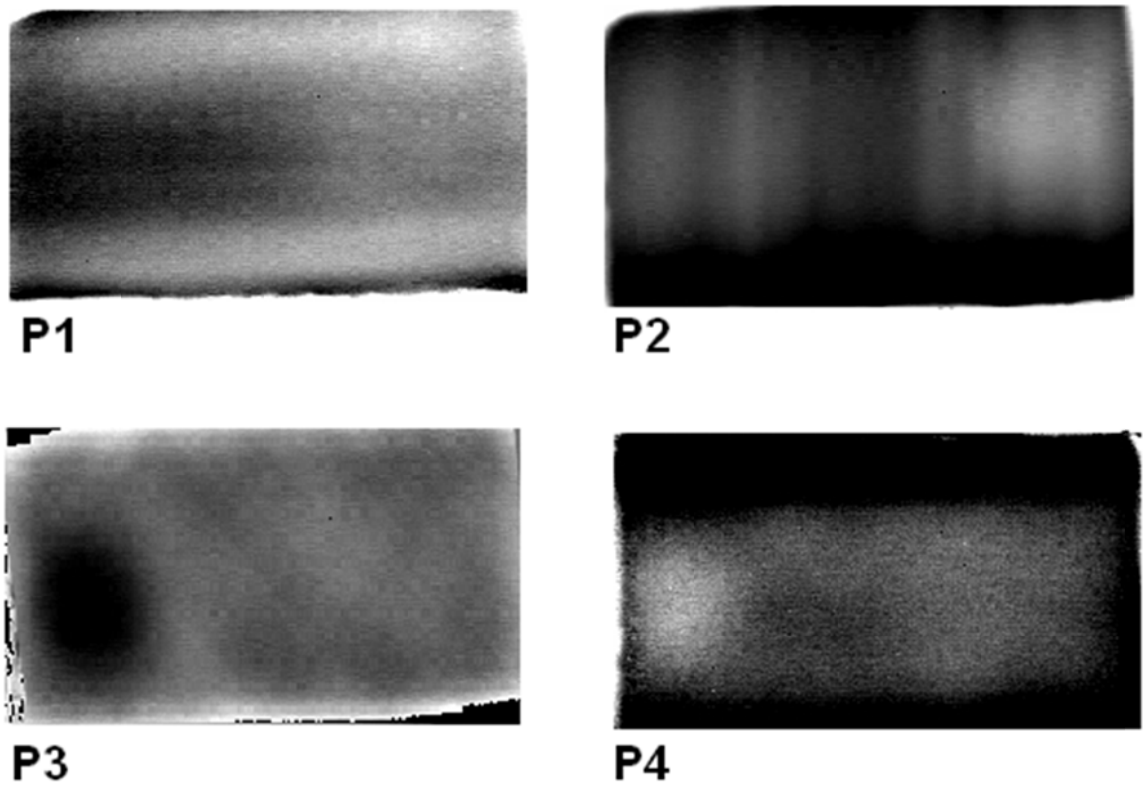

Figure 6.13: Phase map of the coupons cured with P_c =25%.

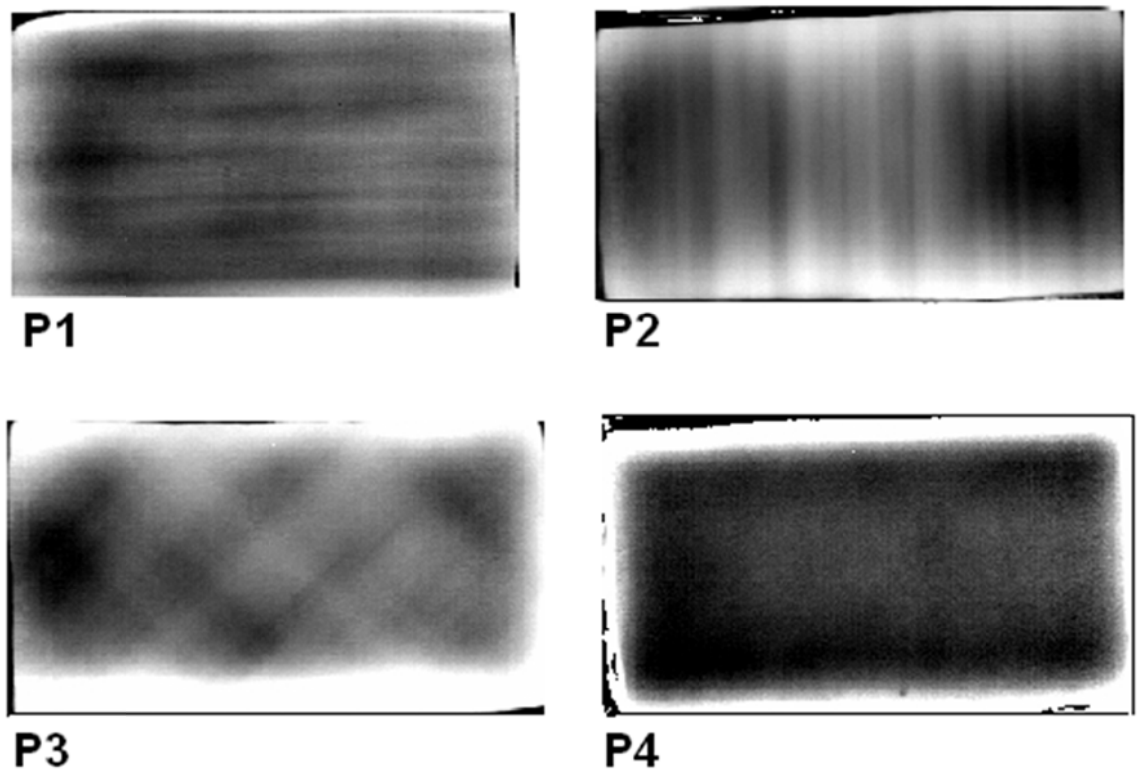

Figure 6.14: Phase map of the coupons cured with P_c =0%.

From a comparison between all the shown phase images it can be observed that:

- as a general comment the fibres orientation is clearly distinguishable in almost all the coupons whatever is the curing pressure;
- in all the coupons cured with P_c=100% (fig. 6.10), the kapton disk is clearly recognizable;
- in both the phase maps of the coupons cured with P_c=75% and P_c=50% (fig. 6.11 and 6.12) the kapton disk is clearly outlined only in the phase maps of P1 and P3 coupons;
- in the case of the coupons cured with P_c=25% of the pressure (fig. 6.13) the kapton disk can be distinguished in all the coupons, although it is not clearly outlined in coupons P1 and P2 ;
- the phase maps of the coupons cured with P_c=0% of the pressure (fig. 6.14), show that the kapton disk is almost wherever detected, but it is difficult to establish its real position in the coupon P4.

6.1.2 Flash thermography

As already seen in chapter 3, it seems that the most reliable IRT method for porosity characterization in CFRP is Flash Thermography .

The most important condition to be satisfied in order to apply the theory described in the paragraph 3.5.2 is that the inspected material is heated by a Dirac-like heat pulse which is instantaneously absorbed by the material. This requires a very fast and powerful heat source, which may be achieved by using special professional photography flash heads.

So, the set up arrangement used in this case was substantially that described in fig. 6.1, with tests performed in the transmission mode and the lamp 1 substituted with a flash head. Specifically the flash system, made by Hensel® and provided as a courtesy by Flir® systems Italy was assembled as follows:

- MH 6000 flash head with 6000 J maximum power emission;
- TRIA 6000 S power supply.

The synchronism was achieved by a triggering remote control.

The used experimental arrangement was exactly the same shown in fig. 6.9, with the halogen lamp replaced by the flash one. Also in this case the distance of almost 50 cm from the coupons was maintained.

The TRIA power pack allows to supply different levels of energy to the flash head, and, as a consequence, flashes of energies ranging from 187 J up to 6000 J can be obtained with a maximum flash duration of almost 2 ms.

Flash thermography measurements were carried out through the following steps:

- The flash was shoot on the surface of each coupon and consequently the thermal camera via the ALTAIR software acquired the temperature on the opposite surface. The starting time of the acquisition coincided with the flash shoot, whilst the acquisition was stopped when the cooling down period started.
- The temperature-time history of each coupon was acquired during a time interval long enough to let the viewed surface reaching the maximum temperature plateau; as an example, a graph is shown in fig. 6.15.

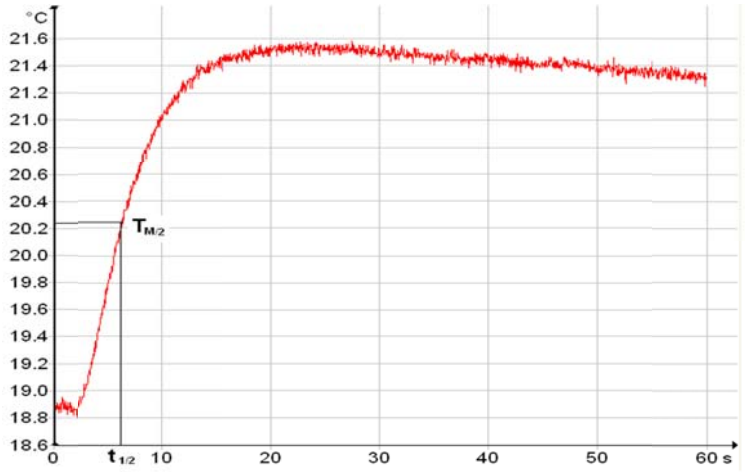

Figure 6.15: Temperature-time graph.

In this way, over the entire surface of every coupon, it is possible to observe, pixel by pixel, a graph like the one shown in figure 6.15. In order to obtain the diffusivity pixel by pixel using the formula in eq. 6.3:

$$\alpha = \frac{1.38L^2}{\pi^2 t_{1/2}} \qquad (6.3)$$

it is needed to find out the time instant for which the maximum temperature, $T_{M,}$ is reached; then, the time corresponding to $T_{M/2}$, i. e. $t_{1/2}$, must be calculated. L in eq.6.3 is the already specified thickness of the coupon. This action is done with the help of an algorithm written in Matlab ambient. Specifically, the calculation tool is made by two blocks:

a) the first block reads the temperature-time history acquired through the infrared camera then it is saved in an ascii format, which specifically is a matrix vector (each matrix is the single acquired frame) whose length is equal to the number of the acquired frames. Each point (i,j) in a single matrix is the temperature of the pixel (i,j) at a certain frame (i.e. time).

b) The second block is able to treat the temperature-time history of each single pixel. It finds out the time instant when the heating up period starts and then T_M and computes $T_{M/2}$ and so $t_{1/2}$.

Due to the thermal noise of the curves, $T_{M/2}$ is found with an error of 0.03°C. At last, a thermal diffusivity map is produced.

Thermal diffusivity maps

The thermal diffusivity maps of the different coupons are shown in the following figures 6.16-6.37; a dashed-contour circle indicates the probable position of the kapton disk.

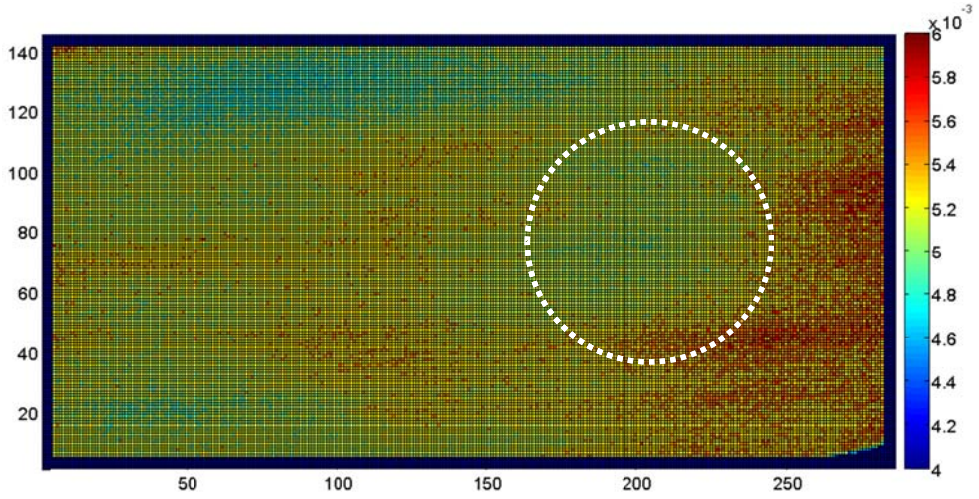

Figure 6.16: P1 cured with P_c =100%.

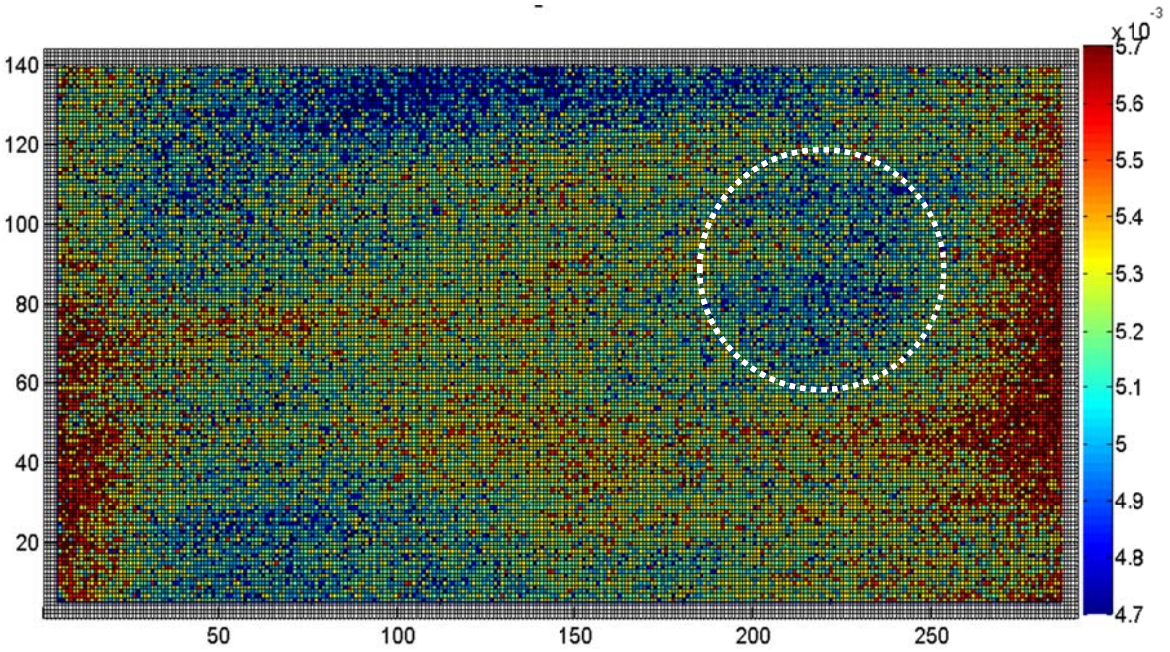

Figure 6.17: P1 cured with P_c = 100%. The diffusivity color palette has been changed in order to highlight the defect.

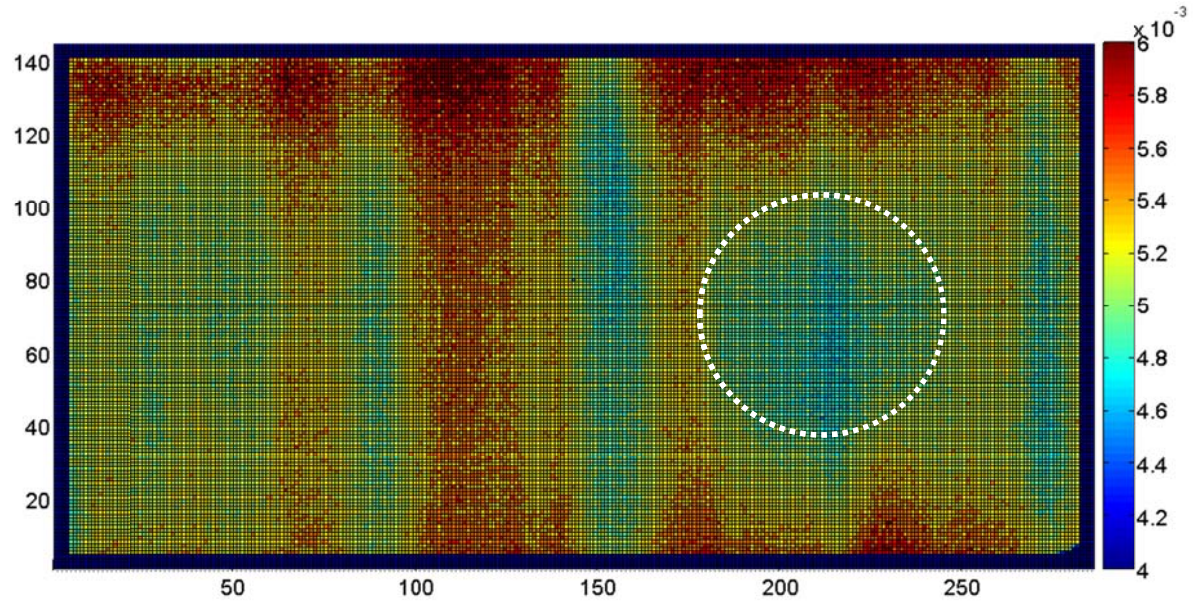

Figure 6.18: P2 cured with P_c = 100%.

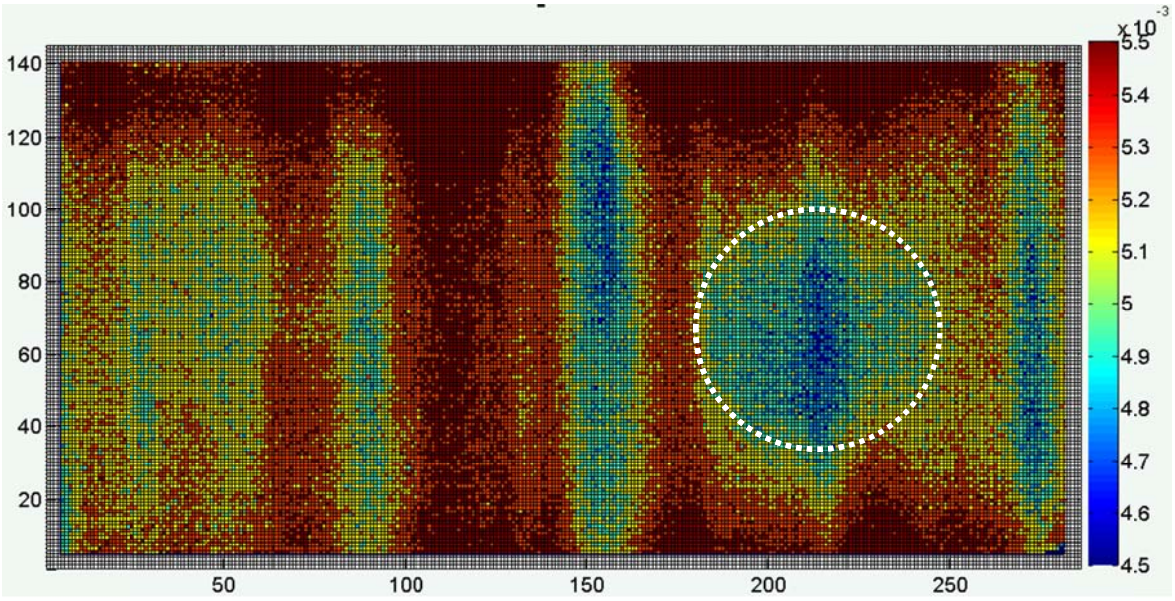

Figure 6.19: P2 cured with P_c =100%. The diffusivity color palette has been changed in order to highlight the defect.

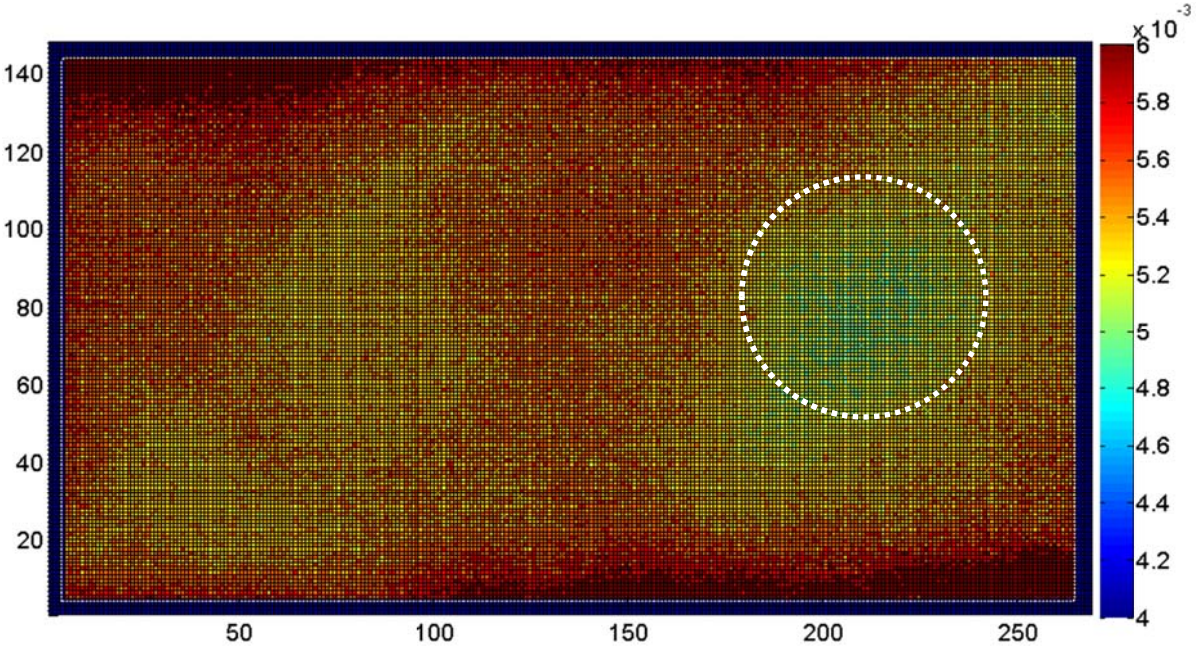

Figure 6.20: P3 cured with P_c = 100%.

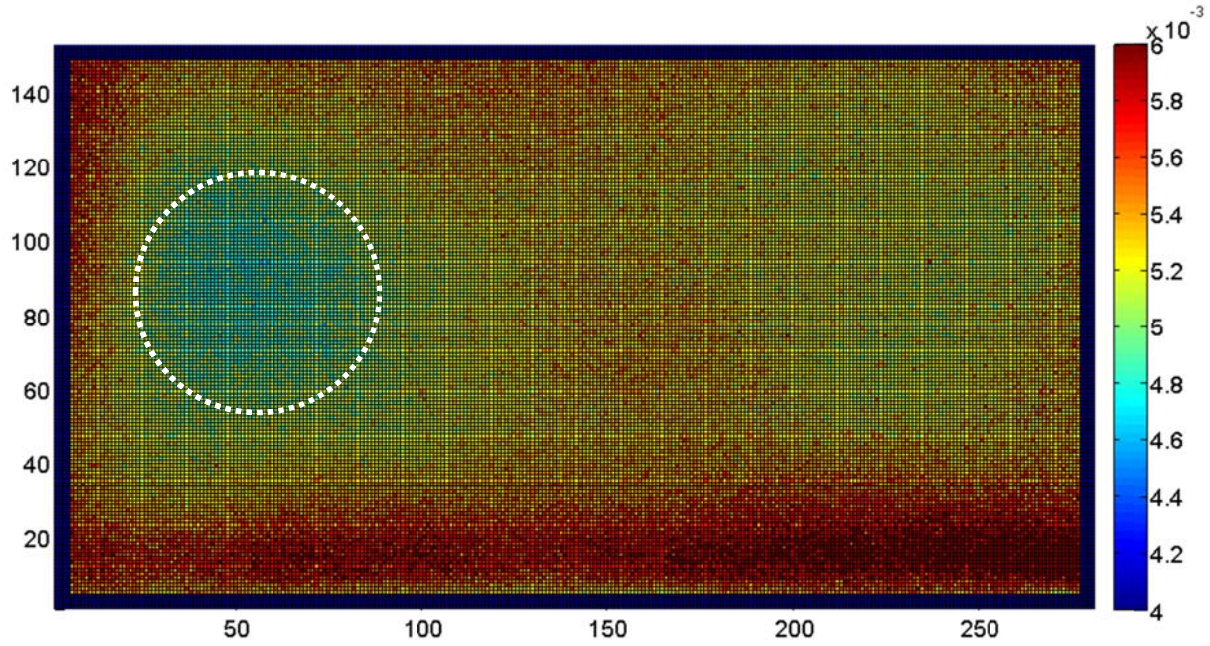

Figure 6.21: P4 cured with P_c = 100%.

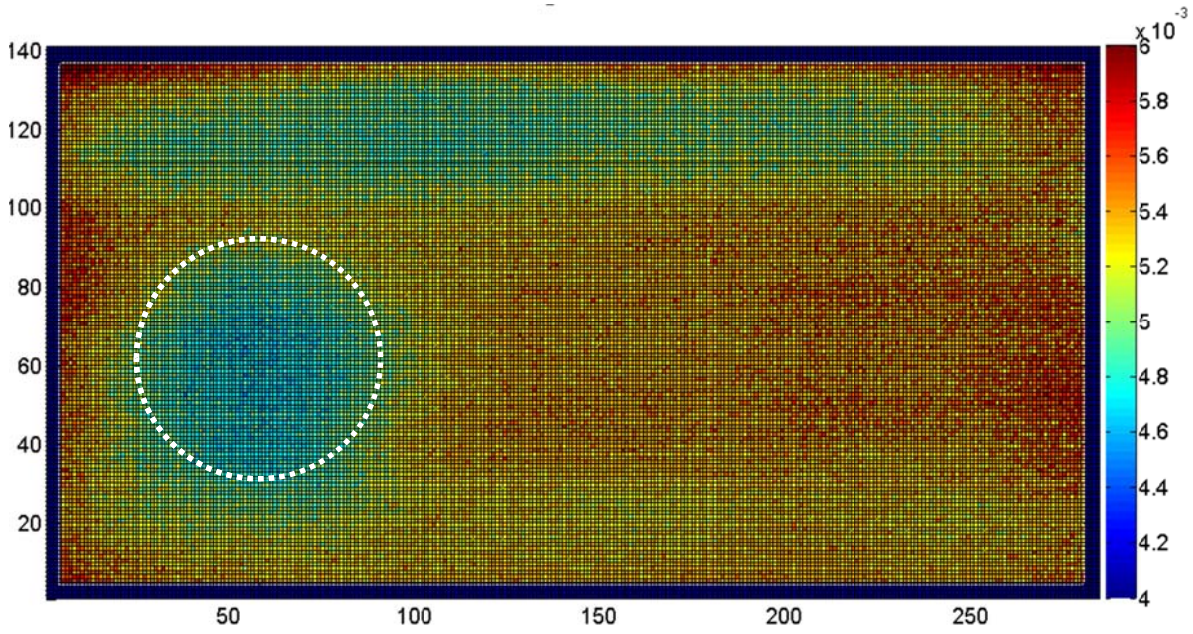

Figure 6.22: P1 cured with P_c = 75%.

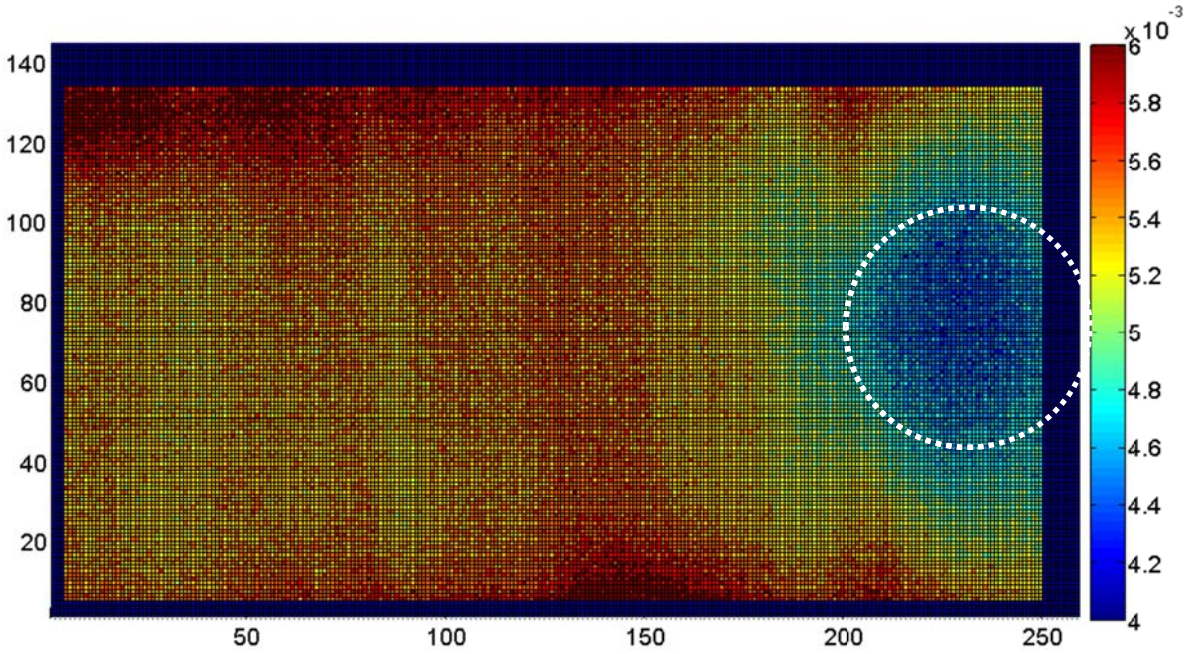

Figure 6.23: P2 cured with P_c =75%.

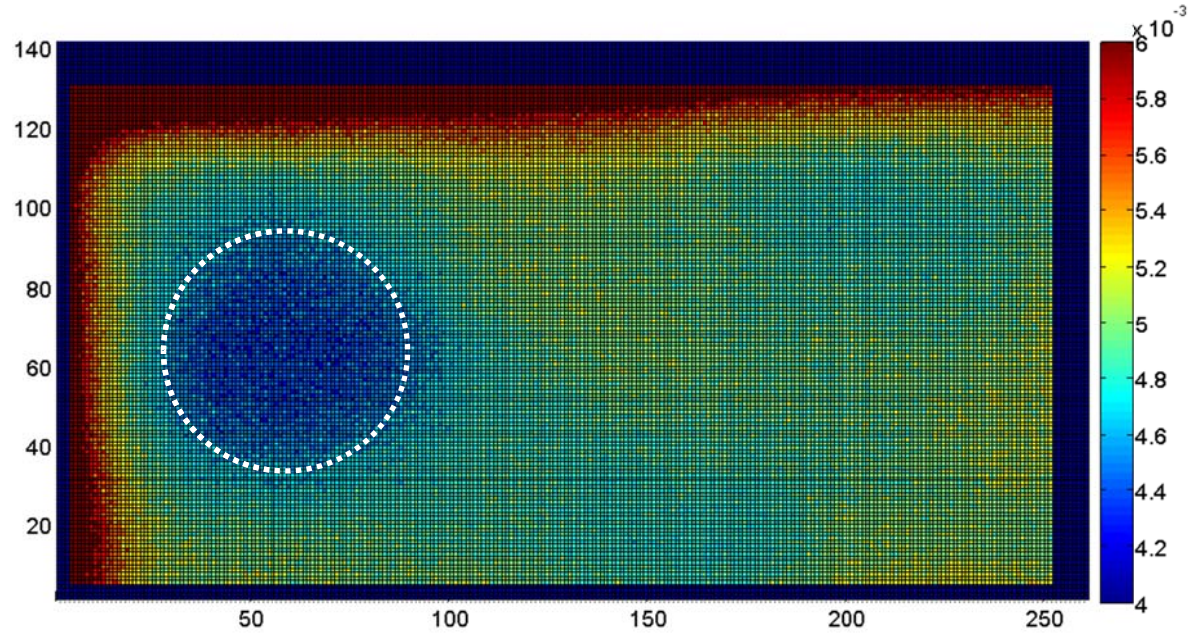

Figure 6.24: P3 cured with P_c = 75%.

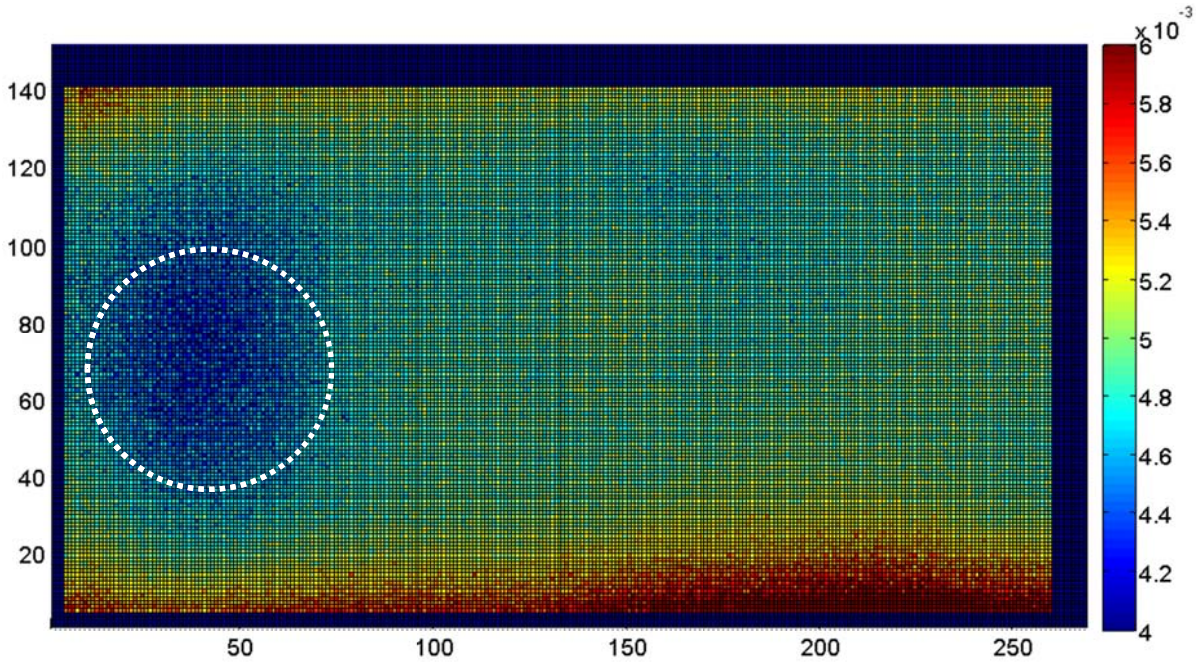

Figure 6.25: P4 cured with P_c = 75%.

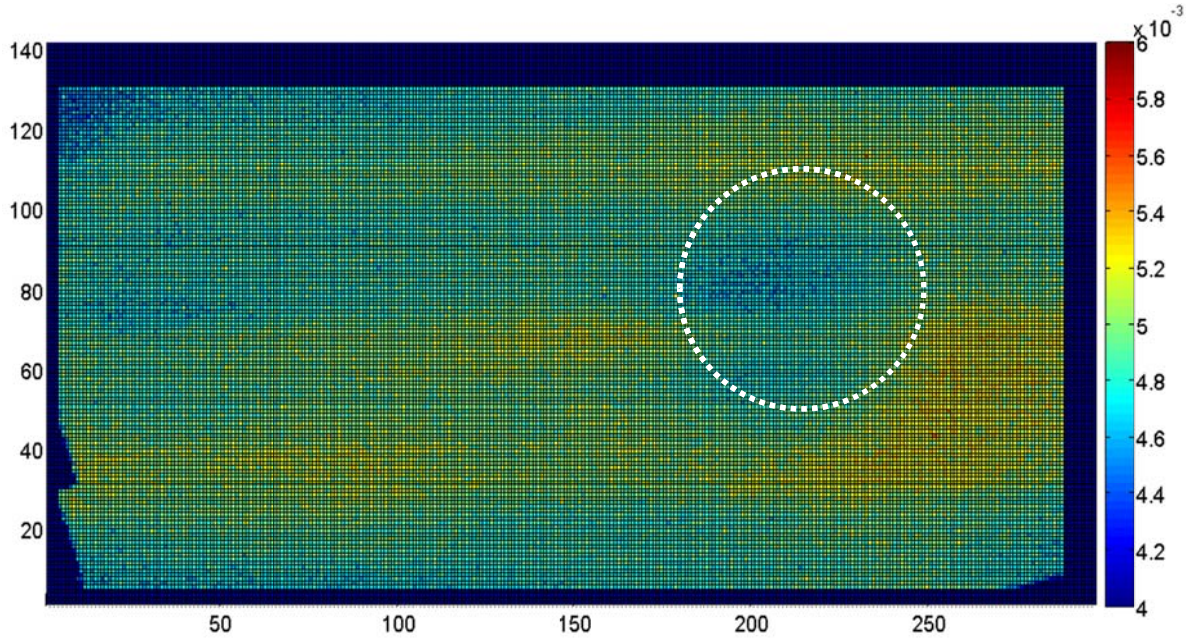

Figure 6.26: P1 cured with P_c = 50%.

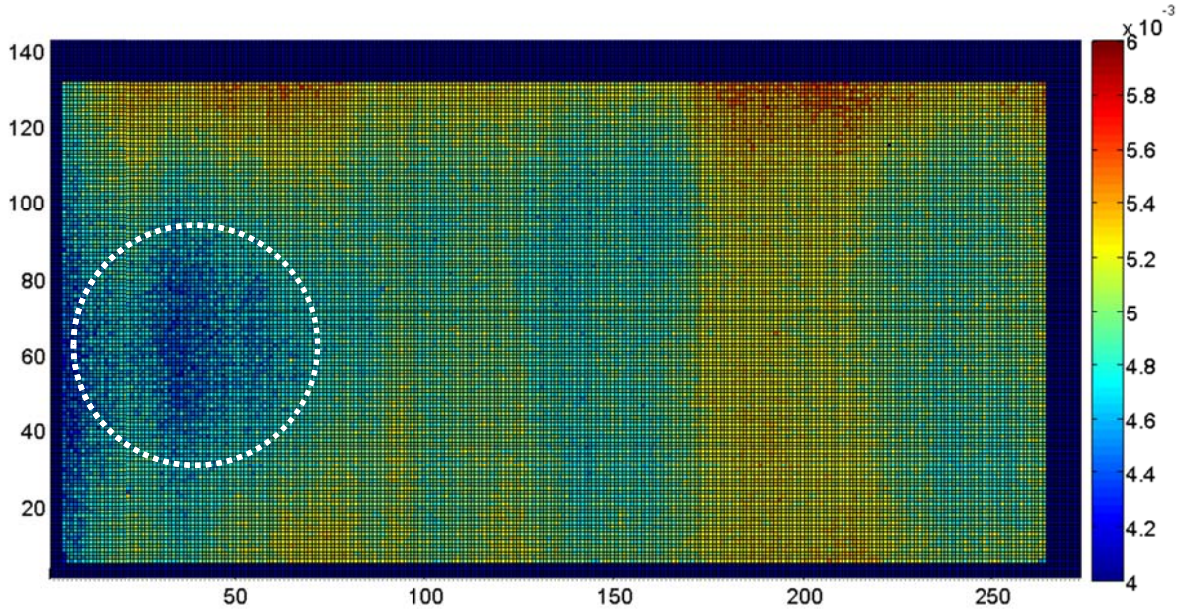

Figure 6.27: P2 cured with P_c = 50%.

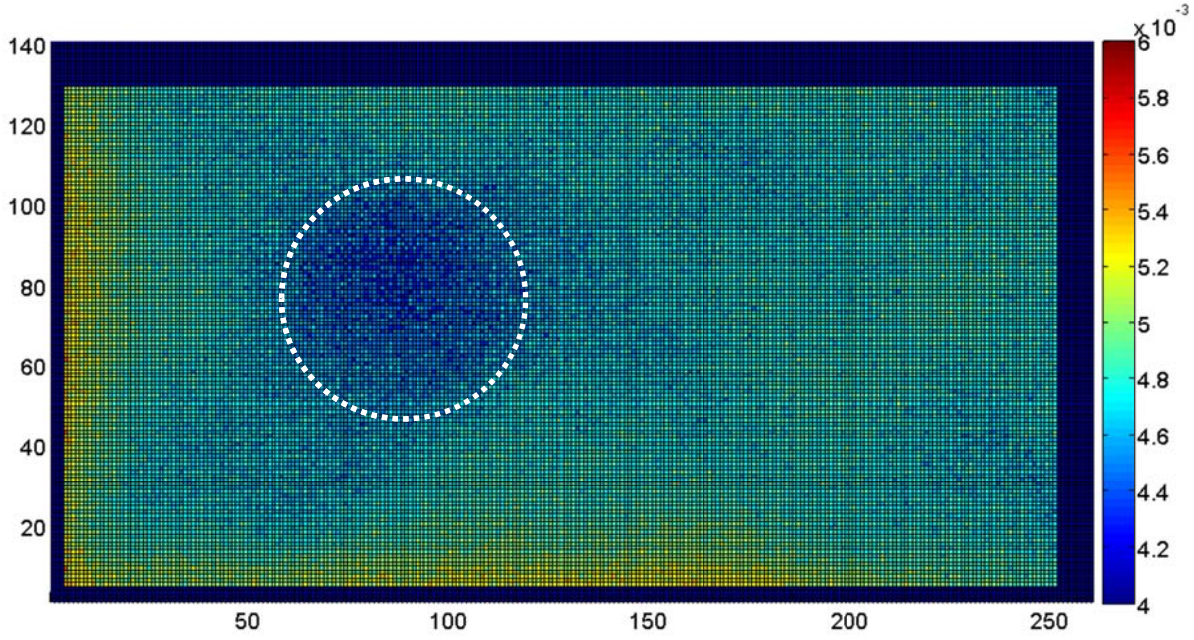

Figure 6.28: P3 cured with P_c = 50%.

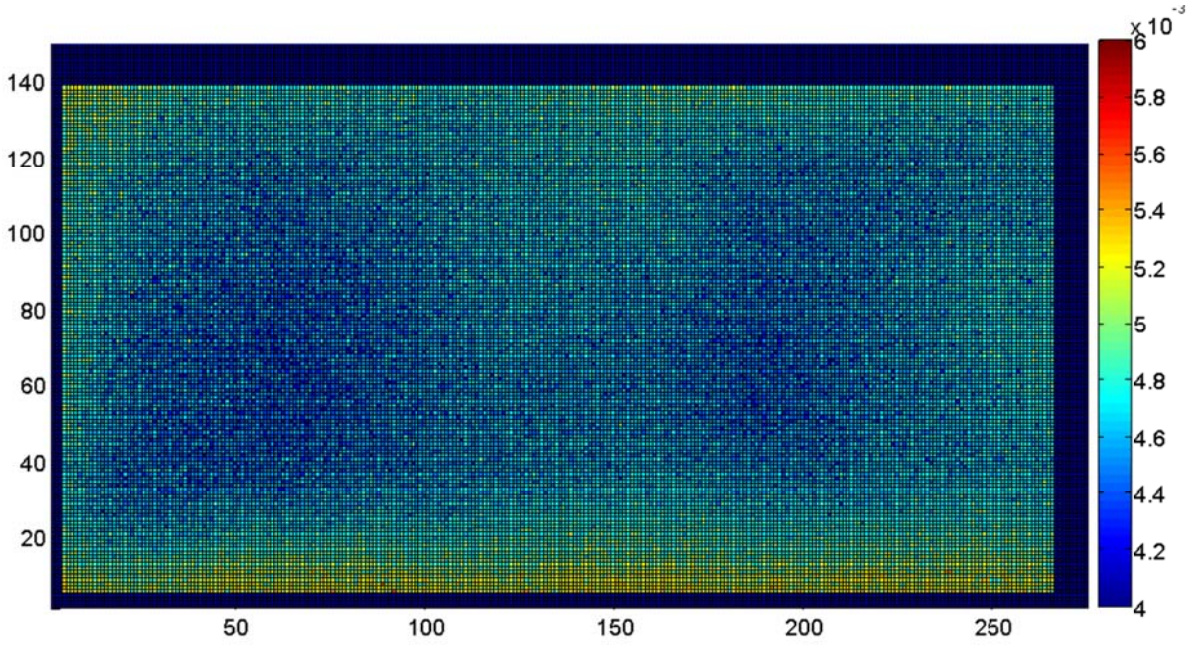

Figure 6.29: P4 cured with P_c =50%.

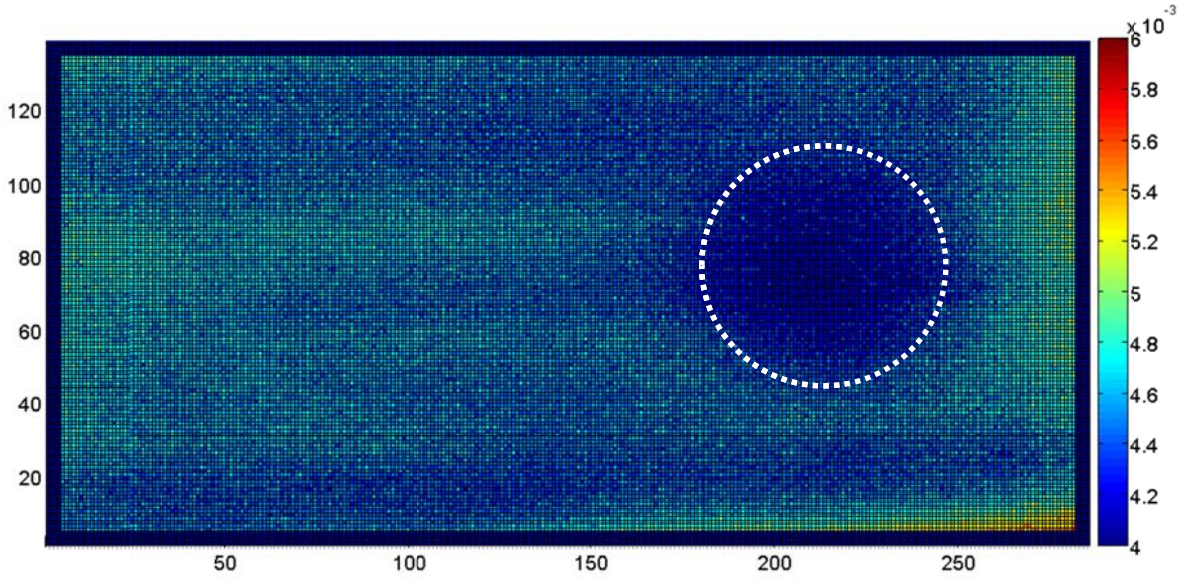

Figure 6.30: P1 cured with P_c = 25%.

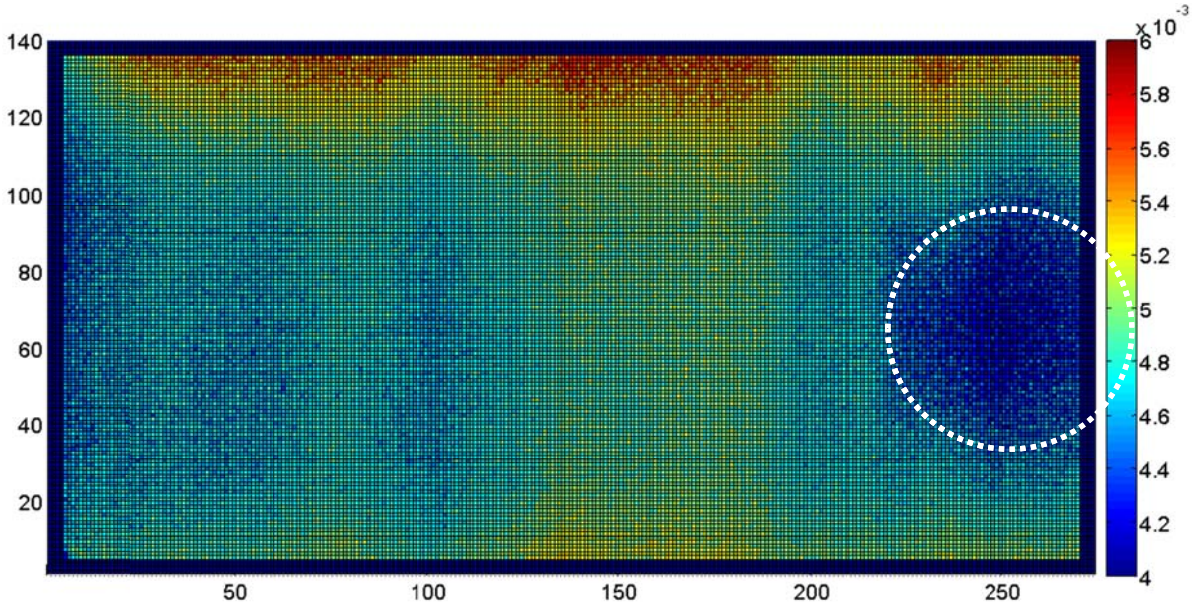

Figure 6.31: P2 cured with P_c = 25%.

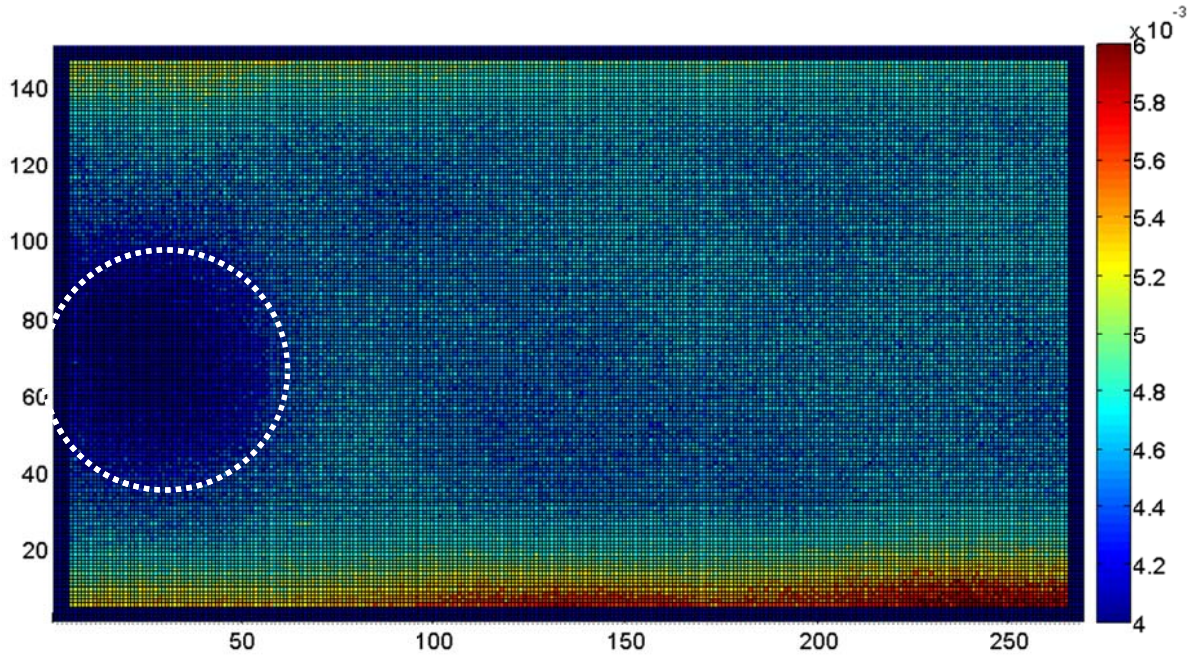

Figure 6.32: P3 cured with P_c = 25%.

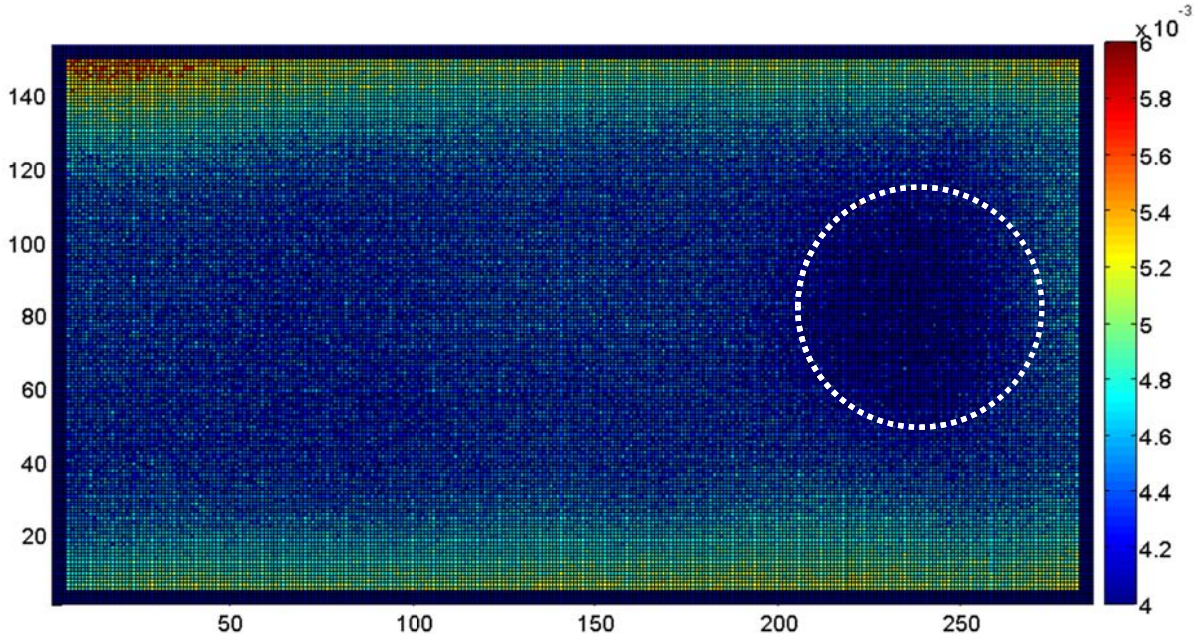

Figure 6.33: P4 cured with P_c = 25%.

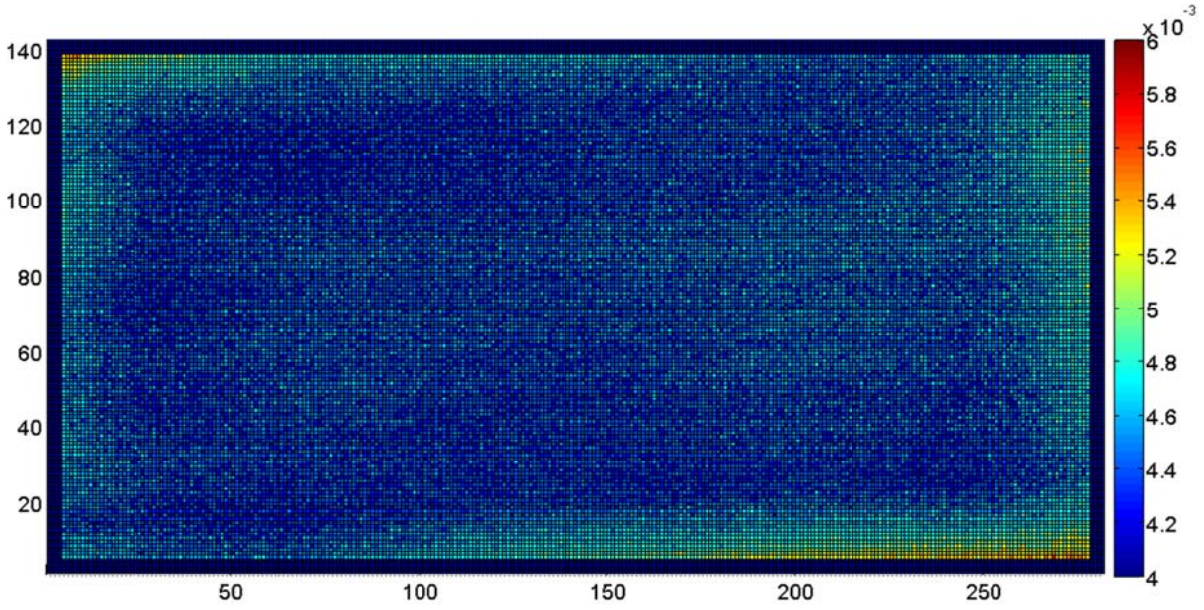

Figure 6.34: P1 cured with P_c = 0%.

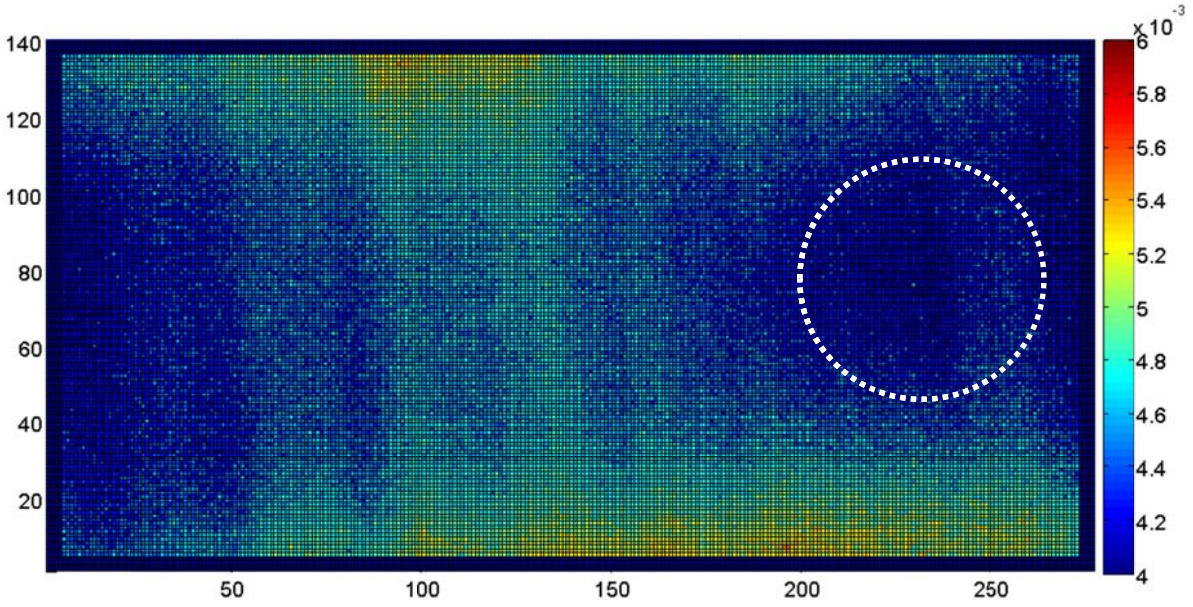

Figure 6.35: P2 cured with P_c =0%.

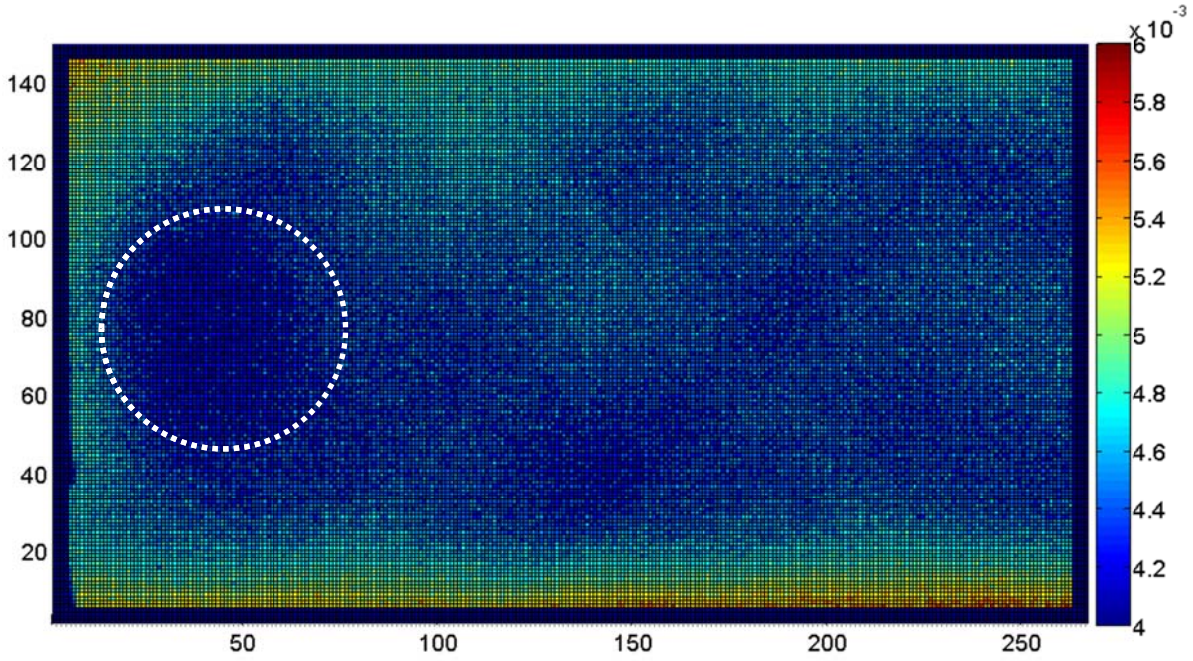

Figure 6.36: P3 cured with P_c = 0%.

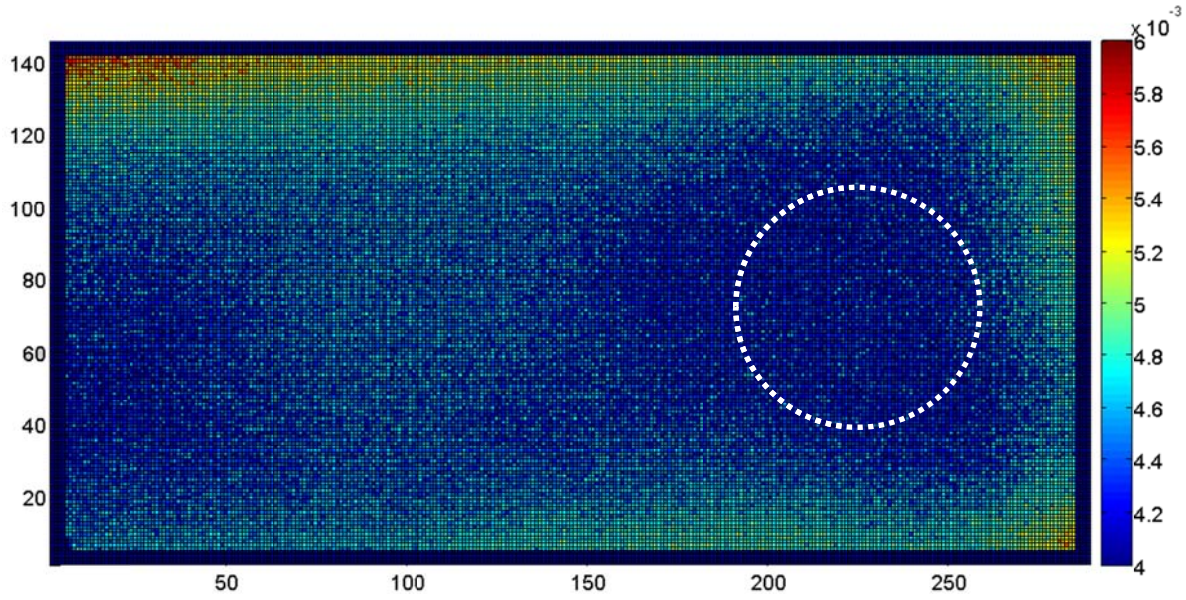

Figure 6.37: P4 cured with P_c =0%.

As can be immediately noticed, low values of thermal diffusivity are attained in correspondence of the kapton disk, which is visible in almost all the coupons, although in some cases its position can be only supposed. In these cases, the relevant amount of porosity and its special distribution have caused a sort of blurring effect, making ambiguous the discrimination of the kapton disk.

It must be remarked that the thermal diffusivity is larger along the fibres direction, then the heat diffusion can follow preferential directions which could mask the defect edges.

The anisotropic behavior of thermal diffusivity combined with the non-homogeneous porosity distribution probably favors discrimination of the fibres orientation in the diffusivity maps in figures 6.18, 6.30, 6.35 and 6.36. In fact, it seems that in these cases, there is a greater amount of porosity along the fibres, which has caused a reduction of thermal diffusivity in that direction. On the contrary in the coupons P4 which are characterized by a *balanced symmetrical* stacking sequence, the diffusivity, and so the porosity are more homogeneously spread in all directions.

Further, from figures 6.16-6.37 it can be easily noticed that the thermal diffusivity tends to decrease with decreasing the curing pressure (i.e. increased

embedded porosity). This can be better appreciated looking at the average thermal diffusivity values reported in the following table 6.1. In particular, the mean value of thermal diffusivity is calculated on an area of almost 15000 points relating to a sound zone without the kapton disk, and it is affected by an uncertainty of almost 3%.

The obtained average values of thermal diffusivity are plotted against the applied curing pressures (expressed, as usual, as percentage of the prescribed one) in fig. 6.38 and against the volume percentage of porosity obtained by the gravimetric method in fig. 6.39. In both graphs a best fitting curve of all the experimental points is also reported.

From table 6.1 and the graphs in figs. 6.38 and 6.39 it can be noticed that:

- For the coupon P3, the thermal diffusivity tends to reduce by almost 20% of its value attained at P_c=100%;
- a reduction of about 15% and 17% is respectively achieved for coupons P2 and P4;
- the larger reduction value of 23% is registered for the coupon P1.

Pressure %	DIFFUSIVITY α(cm²/s)			
	P1	P2	P3	P4
100	0.0052	0.0053	0.0055	0.0053
75	0.0054	0.0054	0.0047	0.0049
50	0.0049	0.0050	0.0047	0.0046
25	0.0045	0.0048	0.0045	0.0044
0	0.0040	0.0045	0.0044	0.0044

Table 6.1.

For all coupons, the values of thermal diffusivity are normalized with respect to the thermal diffusivity relative to the coupons cured with P_c =100%; such a normalized values are plotted against P_c and shown in the following figures 6.38-6.41. As can be seen, in every case an almost linear dependence with the decreasing pressure may be individuated, although the trends are slightly better fitted by a second order polynomial regression. In all the graphs both

linear and polynomial regression lines are reported: the first one in red and the second one in black.

The parameters coming up from the two types of fitting are resumed in table 6.2, as expected, the best coefficient of determination R^2 applies for the polynomial regressions.

By the data, it is outlined that the thermal diffusivity for P2 coupon types is more sensitive to the increasing of the embedded porosity.

In addition, it can be noticed that the curves relative to the polynomial regressions for P1 (fig.6.38) and P2 (fig.6.39) coupons type have an inverse concavity with respect to the curves obtained for the P3 (fig.6.40) and P4 (fig.6.41) types.

Coupon type	Linear regression		Polynomial regression ($y=a+bx+cx^2$)			
	Slope	R^2	a	b	c	R^2
P1	0.0022	0.93	0.77	0.0040	$2x10^{-5}$	0.99
P2	0.0017	0.90	0.84	0.0030	$1x10^{-5}$	0.94
P3	0.0016	0.79	0.82	0.0005	$2x10^{-4}$	0.91
P4	0.0017	0.90	0.83	0.0002	$2x10^{-5}$	0.90

Table 6.2.

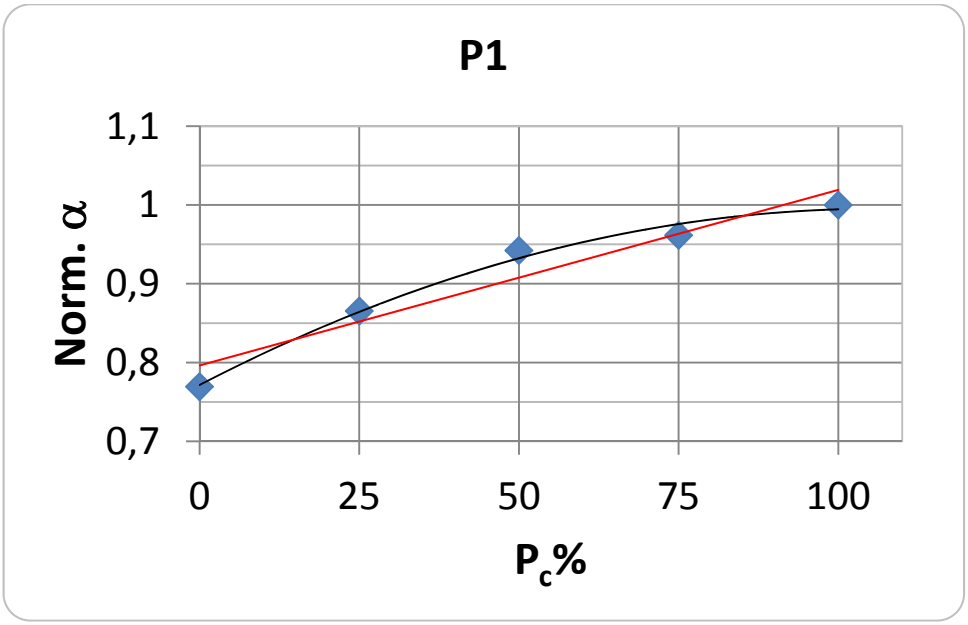

Figure 6.38: Normalized diffusivity vs. P_c.

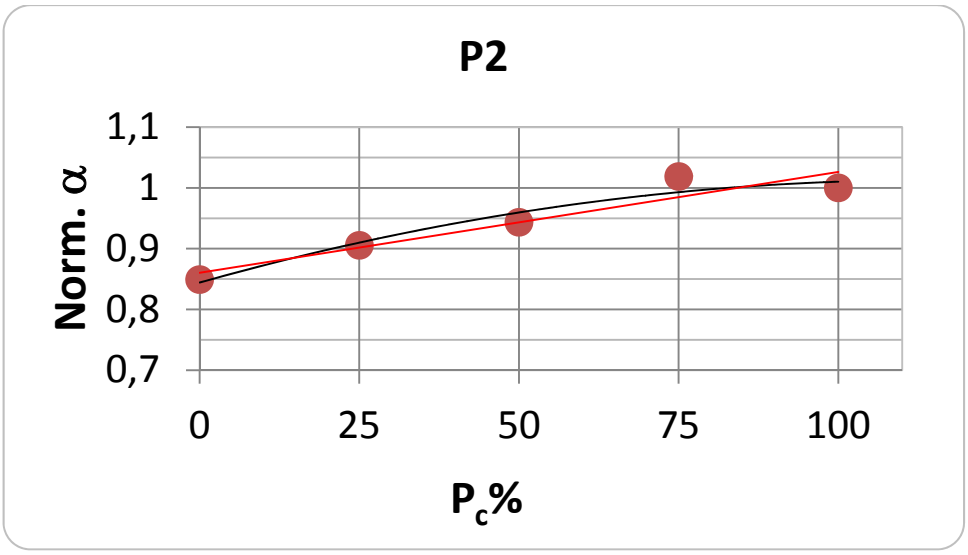

Figure 6.39: Normalized diffusivity vs. P_c.

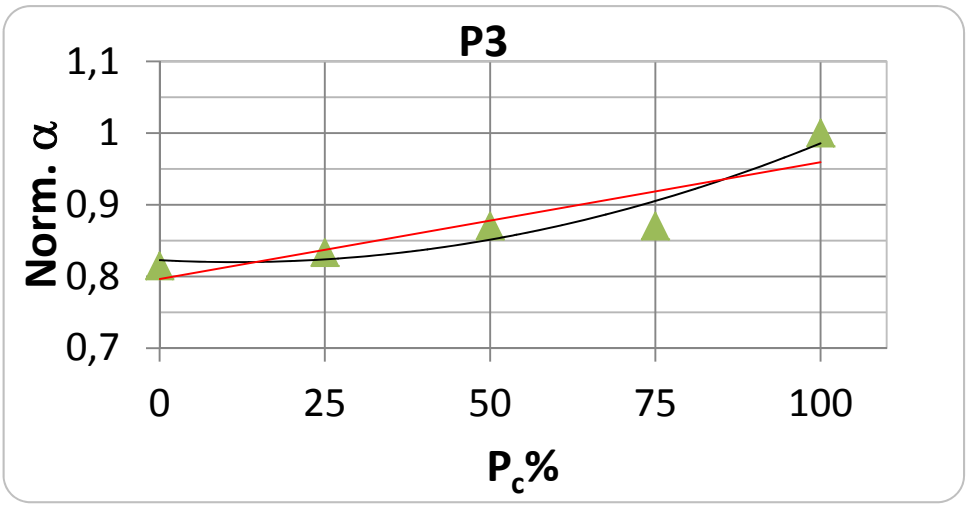

Figure 6.40: Normalized diffusivity vs. P_c.

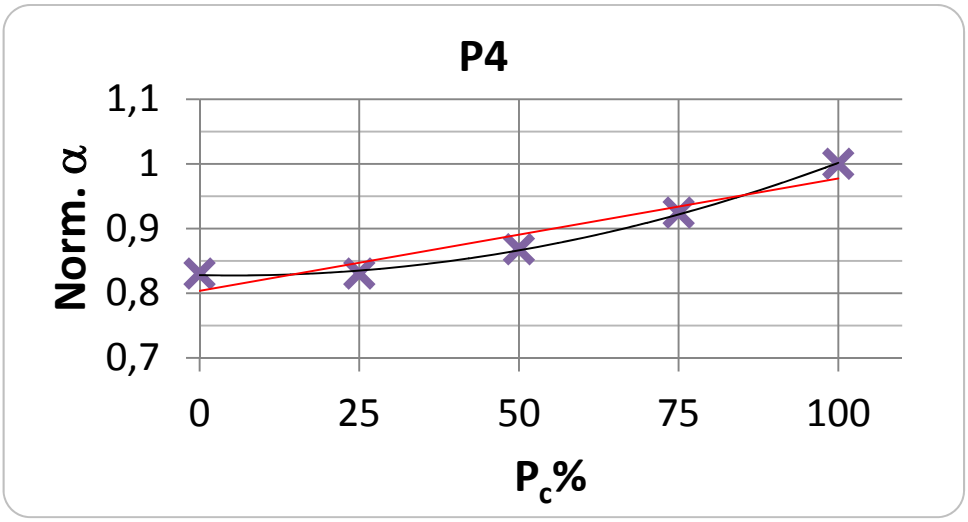

Figure 6.41: Normalized diffusivity vs. P_c.

The same occurs if the normalized thermal diffusivity values are plotted against the normalized percentage of porosity V_v%, obtained by the gravimetric method (see chapter 4), as can be seen from graphs in figures 6.42-6.45. Similarly to the previous graphs, also in this case both a linear and a second order polynomial regressions are used to fit data. The regressions parameters, as well as the coefficient of determination R^2 are reported in table 6.3. Also in this case the data are slightly better fitted by the second order polynomial.

Coupon type	Linear regression		Polynomial regression ($y=a+bx+cx^2$)			
	Slope	R^2	a	b	c	R^2
P1	-0.03	0.85	0.98	0.0087	$4x10^{-3}$	0.90
P2	-0.02	0.80	0.84	0.0077	$4x10^{-3}$	0.86
P3	-0.03	0.82	0.82	0.0005	$5x10^{-3}$	0.96
P4	-0.02	0.81	0.46	0.5897	$8x10^{-2}$	0.83

Table 6.3.

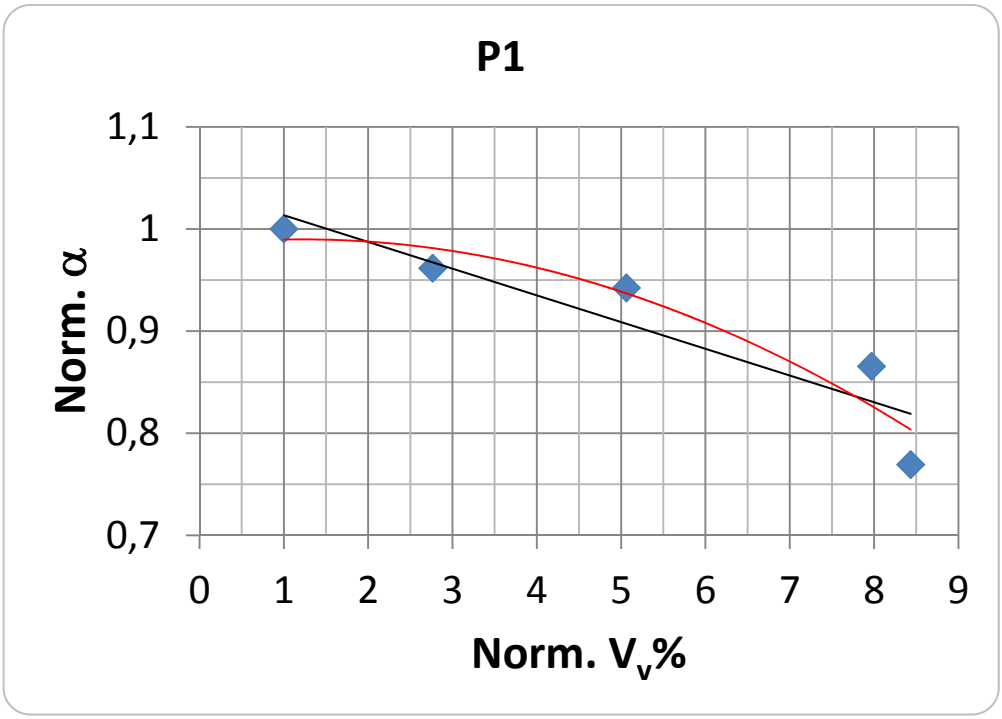

Figure 6.42: Normalized diffusivity vs. V_v%.

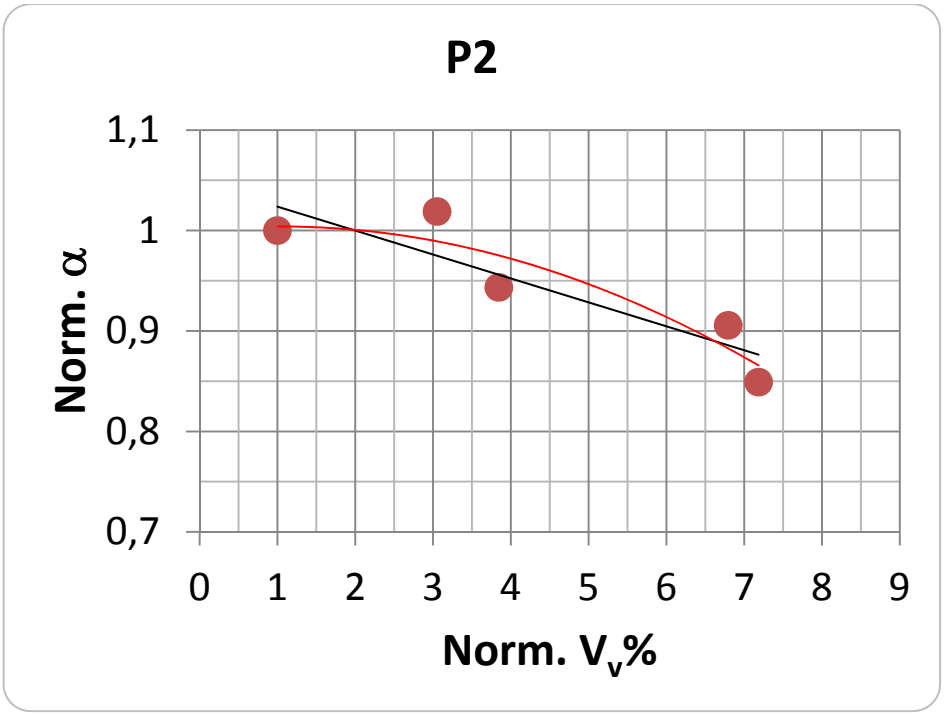

Figure 6.43: Normalized diffusivity vs. V_v%.

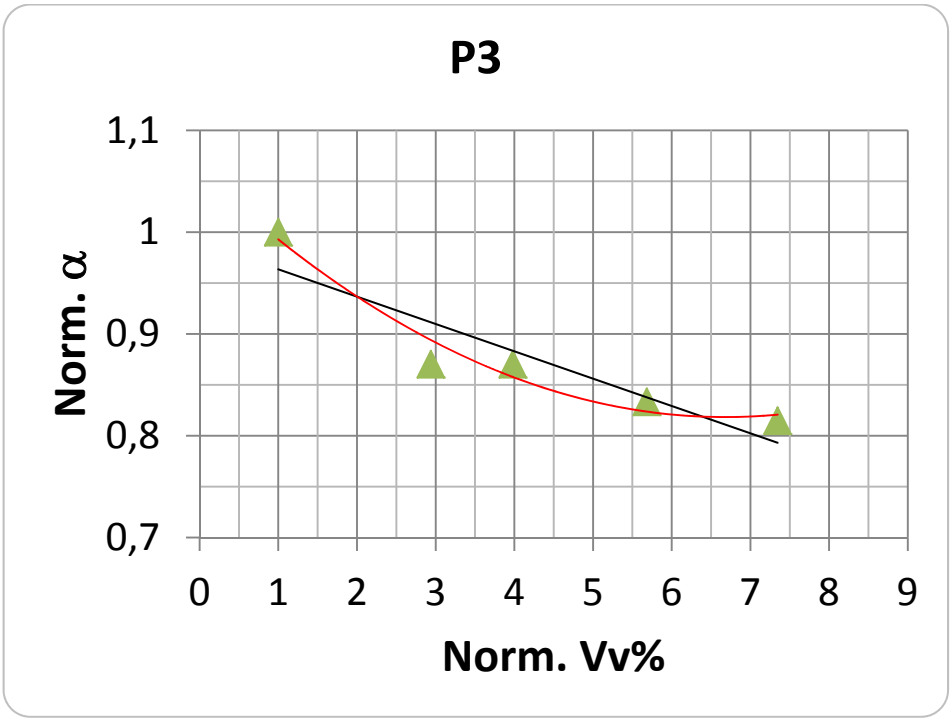

Figure 6.44: Normalized diffusivity vs. V_v%.

It has been proven [196,201] that the thermal diffusivity in a CFRP material depends on the fibres orientation. This may explain the inversion of concavity observed when passing from coupons with unidirectional fibres orientation (P1 and P2) to coupons with a more complex stacking sequence (P3 and P4).

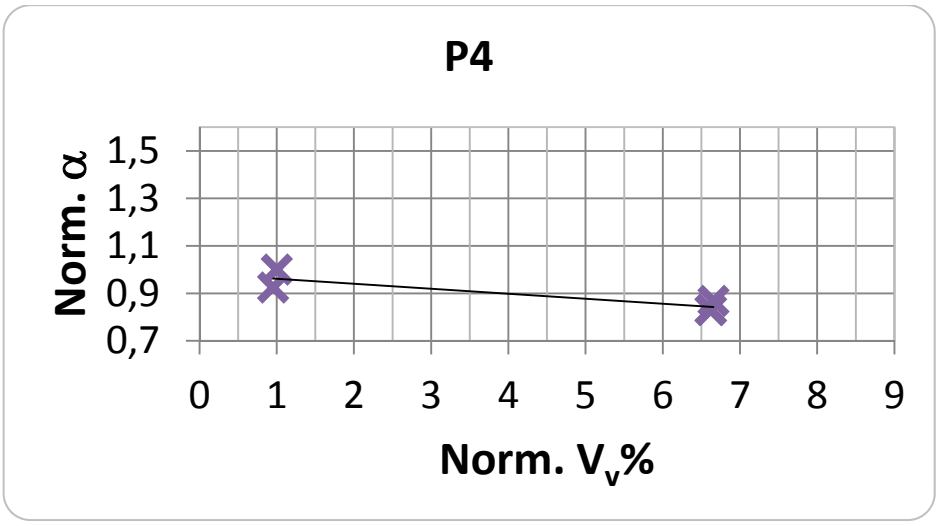

Figure 6.45: Normalized diffusivity vs. V_v%.

At last, the rate of the diffusivity decrement with respect to the embedded porosity ($\alpha/V_{v\%}$) is plotted against the applied pressure in fig. 6.46-6.49. Starting from the value relative to P_c = 100%, it can be noticed that, regardless of the stacking sequence, the rate drops first rapidly until P_c = 50% and after slowly towards an almost constant value as P_c approaches zero.

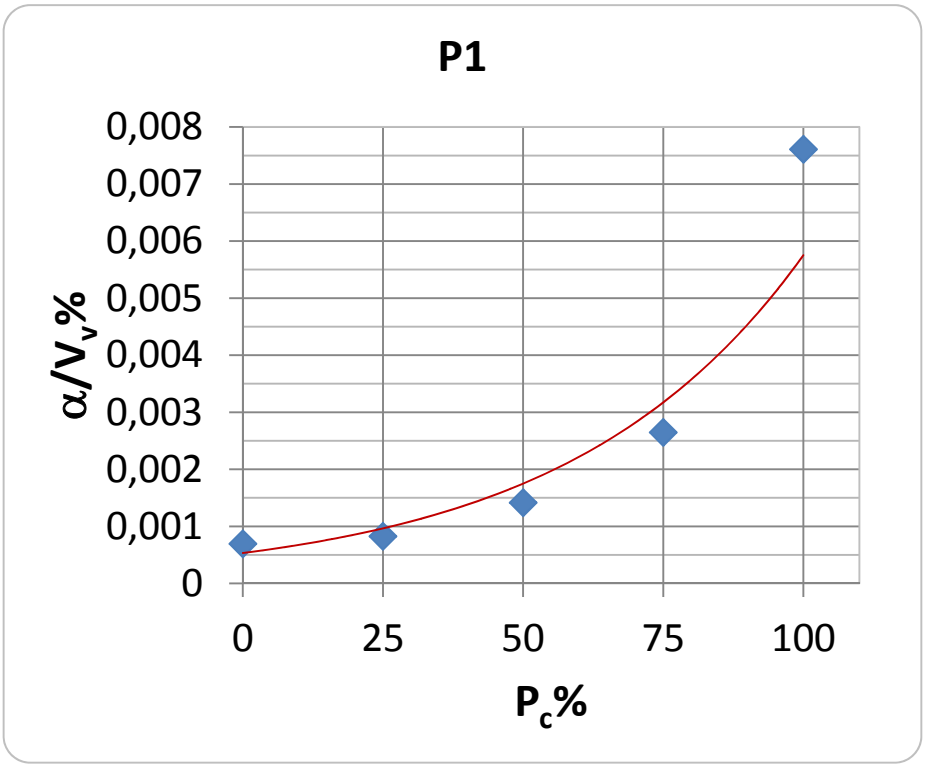

Figure 6.46: Rate of diffusivity decrement with respect porosity vs. percentage of applied curing pressure.

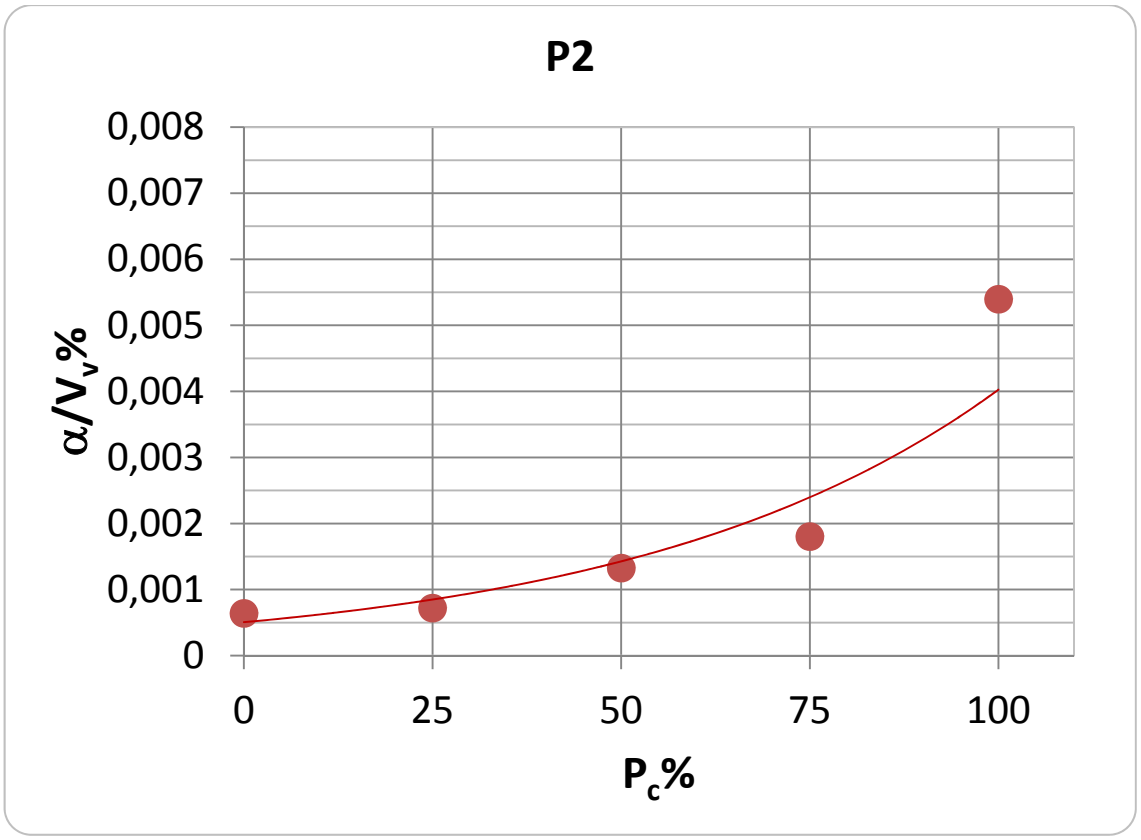

Figure 6.47: Rate of diffusivity decrement with respect porosity vs. percentage of applied curing pressure.

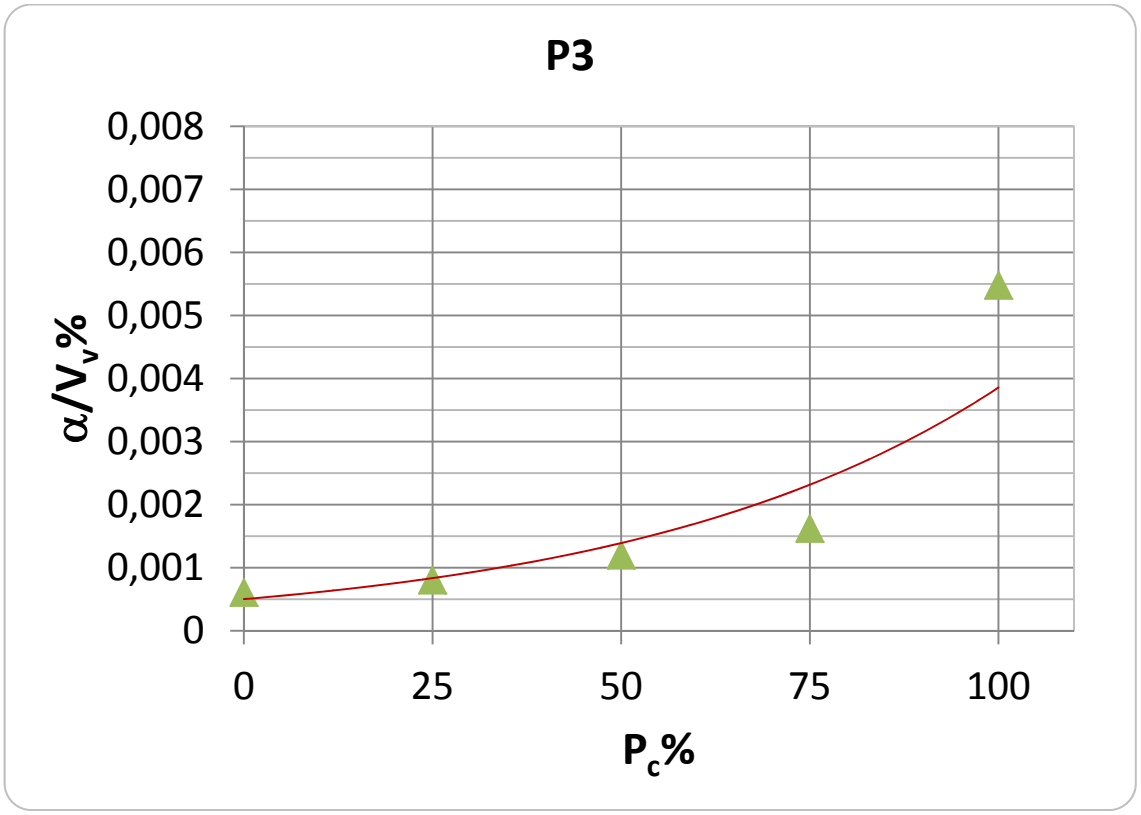

Figure 6.48: Rate of diffusivity decrement with respect porosity vs. percentage of applied curing pressure.

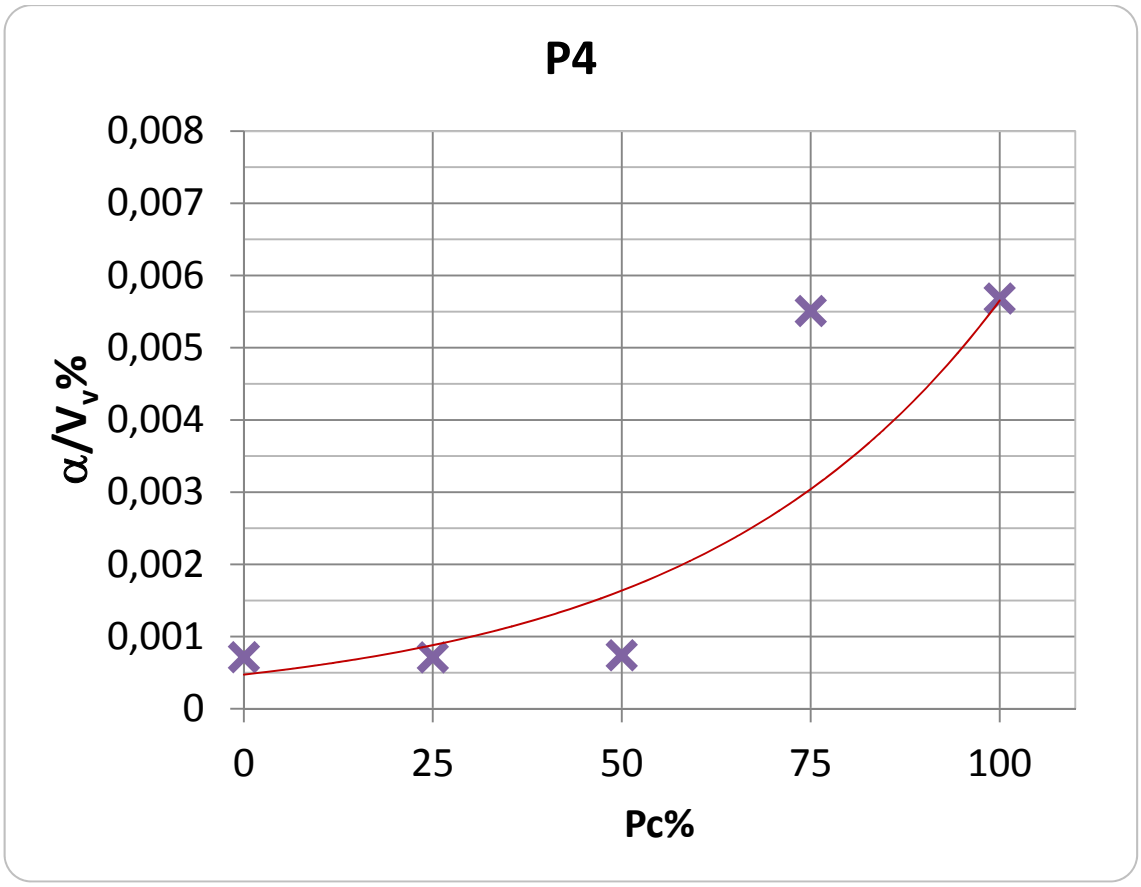

Figure 6.49: Rate of diffusivity decrement with respect porosity vs. percentage of applied curing pressure.

Quantitative measurements of defects size

Going back to Figs.6.16-6.37, the thermal diffusivity maps display low values in correspondence of the kapton disk. Of course, a clear discrimination of the disk is rather difficult because of many factors. One is due to the porosity amount in the bulk hosting material which tends to lessen the difference between the thermal diffusivity of the buried insert and of the hosting material. Another factor is due to an increase of porosity percentage, which, owing to the hand lay-up manufacturing technique, is likely to occur around the kapton disk making even more difficult the disk discrimination. In addition, to complicate the situation, lateral heat diffusion is associated with the heat transfer through the material thickness.

An attempt is made to measure the size of the kapton disk from the maps of thermal diffusivity. To this end, measurements are performed from data plots along horizontal lines through the defect center as shown in Fig. 6.50. As can be

seen, such a line, apart from irregularities due to the non uniform porosity distribution, displays a concavity over the defect. By measuring the extension of such a concavity as outlined by the two vertical lines intercepting the horizontal one through the average thermal diffusivity the diameter of the disk is obtained. What indicated in Fig.6.50 is a graphical way to show the criterion used, more specifically, an α value below the average one is considered as limit between sound and defective areas. All the measured diameter values are collected in table 6.4.

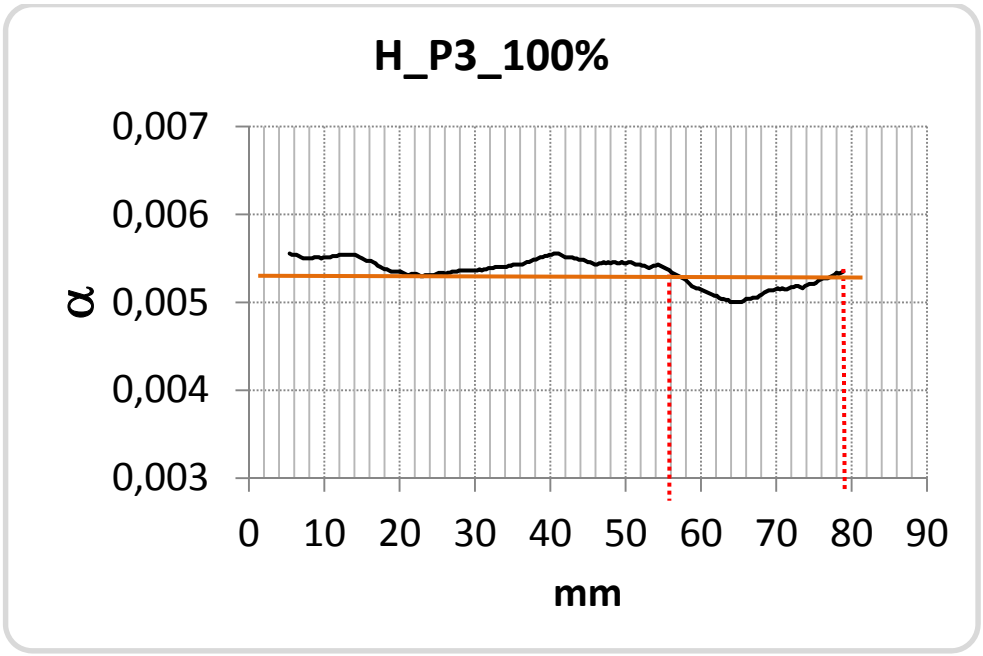

Figure 6.50: Horizontal line related to the defect in the coupon P3 cured with P_c=100%.

Pc	Coupon type	Diameter (mm)
100%	P3	20
	P4	22
75%	P1	23
	P2	24
	P3	24
25%	P1	25
	P2	22
	P3	25

Table 6.4.

From table 6.4 it can be observed that, some values exceed the nominal one that is 20 mm; this, as already said, is to be ascribed to different factors and mainly to the lateral thermal diffusion within the material. Further, it is obvious that the probability to detect and well outline a defect is higher for thicker defects, or better when the kapton insert is made by two overlapped disks. Another important factor is the depth at which a defect is located since shallow defects are more easy detected than the deeper ones. This means that the kapton disk is clearly outlined if it is correctly positioned in the middle of the stacking sequence due to the strong reduction of thermal diffusivity induced there by such a interleaved discontinuity. Instead, the probability to discover the kapton disk strongly decreases if one disk slipped away during manufacturing, or the disks were not correctly positioned. In general, the defect is better outlined for coupons type P3 most probably due to the stacking symmetrical sequence (-45°/45°) which allowed for a more isotropic distribution of porosity and, in turn of thermal diffusivity.

6.2 Some general remarks

The IRT testing of the coupons with embedded porosity, has allowed to re-demonstrate/confirm that this inspection approach is effective for both detection of inclusions and porosity evaluation. Of course, each of the different techniques used has shown to be more effective under specific conditions.

In the following some important remarks are outlined:

- LT in reflection has allowed detection of defects only in some of the coupons; for example, in the P1 cured with P_c=100% in which the kapton insert was wrongly positioned. More specifically, the insert was put closer to the smooth surface and not in the middle of the stacking sequence. In the coupons P2 and P4 cured with P_c=100% (fig. 6.10, 6.11) the kapton disk appeared of small size giving the idea of a probable wrapping up effect, most probably occurred during application of the rolling up force, with a resultant local thickening. Again, for the coupon P2 cured with P_c=75% two marks are distinguishable letting to suppose that a slipping of one kapton disk has occurred accompanied also by a local material compactness. For increasing the embedded porosity the detection of the defect failed. Further, the general unsuccessful detection can also be justified owing to the defect thickness. In fact, as observed by Meola et al. the ratio between the thickness and the depth of the defect *s/p* is a critical parameter, which in the present case is much smaller than the value of 0.1 which was established in [202] as a limit for deep defect detection. In particular, the limiting value of *s/p* = 0.1 was recently further decreased to approximately 0.06 [203]; however, this was achieved with a Teflon® insert in a low porosity CFRP.
- It is interesting to notice that, the observations made with LT in reflection are confirmed by those obtained with LT in transmission and with FT. In fact, the best defect detection with LT in reflection (fig. 6.2) in P1 for P_c = 100% comes out to be the worst with both LT in transmission (fig. 6.10) and FT (fig. 6.16). This because a defect which is shallow when viewing the smooth side (fig. 6.2)

became deeper when the rough side is observed (figs. 6.10 and 6.16). Again, the supposed wrapping effect (figs. 6.5) is confirmed looking at figs. 6.10 and 6.19. Conversely, defects which remain undetected through LT in reflection are better resolved with the other two techniques to mean that the defect was correctly positioned within the limiting *s/p* value for the given porosity amount.

- LT in transmission was successful in almost all the cases. Thus it can be used to inspect highly porous CFRP when both sides of the part are accessible.
- Flash Thermography in transmission, from the provided maps of thermal diffusivity, is able to supply information about the porosity distribution. The study carried out owing to four different stacking sequences has shown that thermal diffusivity is quite sensitive to the fibres orientation.

This technique has proved also effectiveness in detecting thin inclusions in a high porous medium as is the case of coupons cured with only 25% of the pressure, or lower. Moreover, this technique is effective for measuring the defect size.

At last, it has been found that LT in transmission and Flash thermography provides very similar results with regard to the detection of slag inclusions, although in some cases, as for coupons cured with P_c=100%, LT in transmission seems to be more effective in outlining the defect contour. Of course, for both techniques the effectiveness to discriminate a defect increases as the defect thickness increases too.

Conclusions

The attention of the present dissertation was devised towards the assessment of porosity content and distribution in Carbon fibres Reinforced Polymers (CFRP) by non destructive testing techniques.

As explained in the first Chapter, porosity is a typical defect that can arise during production of the component as a consequence of incorrect, or non fully optimized, manufacturing procedures. It is responsible of degradation of the mechanical properties as well of the overall performance of the manufactured structure and so it is matter of great interest.

Two nondestructive testing techniques have been herein investigated for suitability in the evaluation of porosity in CFRP. One is the Ultrasonic Testing (UT), which is the most commonly used technique in the aeronautical industry, but has some limitations in presence of porous materials. The other one is Infrared Thermography (IRT) which is becoming always more attractive due to its two-dimensional and non contact character. In particular, flash thermography is being investigated as the best candidate for porosity assessment. A description of both UT and IRT, from theoretical and practical points of view, has been given respectively in Chapters 2 and 3.

In an attempt to account for the main factors, which may cause the formation of porosity, or may affect its detection, special coupons were fabricated by varying the stacking sequence and the curing pressure, as described in Chapter 4. The amount of porosity in the coupons was firstly ascertained through destructive methods as illustrated in Chapter 4. More specifically, gravimetric measures for density evaluation and optical microscopy for estimation of the porosity percentage were carried out. In particular, the results obtained with the gravimetric method show a linear dependence of the volumetric percentage of porosity versus the decreasing curing pressure P_c. This may be also regarded as further validation to the curing pressure as fundamental parameter to be handled for the control of the porosity amount.

The results obtained with UT and shown in Chapter 5 show that, as a general trend, the ultrasonic attenuation coefficient β increases with decreasing the curing pressure P_c and with increasing the voids content V_v%. The plots of β against V_v% display a larger data spread which is mainly due to the random character of porosity in terms of both pores size and distribution within the material; this may affect ultrasonic data. More specifically, as explained in Section 5.3.4, the scattering of the ultrasonic wave beam due to the pores is strongly affected by the pores size, density and topological distribution. Regarding the detection of local thin delaminations simulated with kapton disks, UT is more effective in presence of large amounts of porosity as may happen for coupons cured with low pressure values. This because the kapton disk, being very thin, does not affect the passage of the ultrasonic signal in a well consolidated material.

From results obtained with IRT and reported in Chapter 6, it is possible to observe that each of the used techniques (FT, LT in reflection, or in transmission) is more effective under specific conditions. In particular, Lockin Thermography in reflection is able to discover the thin insert if the ratio *s/p* does not drop off a critical value. Conversely, the insert is generally recognizable with both Flash Thermography and Lockin Thermography in transmission. However, the contrast decreases with increasing the defect depth. In addition, FT is able to supply information about amount and distribution of porosity through measurements of thermal diffusivity α.

From a comparison of data coming out from the different methods used in this work, the following general comments can be made.

Owing to the detection of the thin insert, LT is more effective in presence of a well consolidated material contrarily to the UT, which is more effective in outlining a thin insert when surrounded by a porous medium. Of course, this makes the two techniques complementary in view of a complete nondestructive evaluation of CFRP parts involving both porous and more compact materials.

Regarding the evaluation of porosity, FT is to be preferred since it is effective, non contact, fast and it is also not affected by the surface finishing meaning that, unlike UT, a part can be inspected viewing indifferently the smooth, or the

rough side. In addition, flash thermography allows to contemporaneously detect manufacturing defects and assess the porosity amount within only one test with of course economic advantages. As a last but important remark, nondestructive testing with IRT is carried out using a simple and safe (for the personnel) set-up arrangement with further advantages in terms of safety at work concerns.

Bibliography

1. Kelly A. and Zweben C., Comprehensive Composite Materials, Pergamon, 1st edition (2000)
2. Miracle D.B. and Donaldson S.L., ASM Handbook Volume 21: Composites, ASM International, 2001
3. Lee S.M., Reference Book for Composites Technology, Technomic Publishing, Lancaster, USA, 1989
4. Schwartz M.M., Composite Material Handbook, McGraw-Hill Book Company, New York, 1984
5. Krenkel W., Ceramic Matrix Composites: Fiber Reinforced Ceramics and their Applications, John Wiley & Sons, 2008
6. http://ntrs.nasa.gov/archive/nasa/casi.ntrs.nasa.gov/20080017096_2008016802.pdf)
7. Dadd G., Owen R., Hodges J., Atkinson K., Sustained Hypersonic Flight Experiment (SHyFE), Proceedings of the 14th AIAA/AHI space planes and hypersonic systems and technologies conference, Canberra, Australia, November 6-9, 2006
8. Goodman J., Ireland P., Thermal Modeling for the Sustained Hypersonic Flight Experiment, Proceedings of the 14th AIAA/AHI space planes and hypersonic systems and technologies conference, Canberra, Australia, November 6-9, 2006
9. Kainer K.U., in Metal Matrix Composites. Custom-made Materials for Automotive and Aerospace Engineering, WILEY-VCH, 2006
10. http://www.f-16.net/news_article4145.html (Accessed on: March 24, 2011)
11. Miracle D.B., Maruyama B., Metal Matrix Composites for Space Systems: Current Uses and Future Opportunities, Proceedings of National Space and Missile Materials Symposium San Diego (CA), Feb. 28-March 2, 2000
12. Baker A.A., Dutton S., Kelly D., Composite Materials for Aircraft Structures, 2nd ed., AIAA Education Series, 2004

13. http://www.boeing.com/commercial/787family/programfacts.html (Accessed on: March 22, 2011)

14. http://ntrs.nasa.gov/archive/nasa/casi.ntrs.nasa.gov/20080014103_2008013648.pdf (Accessed on: March 22, 2011)

15. Patridge I. K., in Damage tolerance in composite structure, in Automotive Engineering Lightweight, Functional, and Novel Materials, ed. by Cantor B., Grant P., Johnston C., Taylor & Francis, 241–252, 2008

16. Mallick P., Fiber-reinforced composites: Materials, Manufacturing, and Design. 3rd ed., CRC Press Inc., New York, 2008

17. Sekido T., Kitaoka K., Odani H., Nishiyama S., Shimizu M., Method of RTM molding, US 0125155 A1 (2006)

18. Hayashi N., Mizuno H., Hasegawa K., Ota K., RTM molding method, US7785525 (2010)

19. http://www.carbonfiberglass.com/CompositesManufacturing/Composites-Manufacturing-Processes.html (Accessed on: March, 2013)

20. Letterman L.E., Resin film infusion process and apparatus, US4622091 (1986)

21. http://www.compositesworld.com/articles/an-elegant-solution-for-a-big-composite-part.aspx (Accessed on: March 15, 2010)

22. http://www.composites.ugent.be/home_made_composites/documentation/FibreGlast_Vacuum_infusion_process.pdf

23. Greenwood M.E., Gauchel J.V., Beckman J.J., Hankin,A.G., Process for filament winding composite workpieces, US6179945 (2001)

24. http://www.compositesworld.com/articles/brandt-goldsworthy-composites-visionary (Accessed on: October 10, 2010)

25. http://www.substech.com/dokuwiki/lib/exe/fetch.php?w=&h=&cache=cache&media=pultrusion.png (Accessed on: March, 2013)

26. Chan W. S. and Wang J. S., Influence of fiber waviness on the structural response of composite laminates, J. of Thermop. Compos. Mater., 7, 243-260, 1994

27. Kugler D. and Moon T. J., Identification of the Most Significant Processing Parameters on the Development of Fiber Waviness Thin Laminates, J. of Compos. Mater., 36, 1451-1479, 2002

28. Truong T. C., Vettori M., Lomov S., Verpoest I., Carbon composites based on multi-axial multi-ply stitched performs. Part 4. Mechanical properties of composites and damage observation, Composites: Part A, 36, 1207-1221, 2005

29. Züleyha A., Ramazan K., Buket O., The response of laminated composite plates under low-velocity impact loading, Composite Structures, 59, 1, 119–127, 2003

30. Tiberkaka R., Bacheneb M., Rechakc S., Necibd B., Damage prediction in composite plates subjected to low velocity impact, Composite Structures, 83, 1, 73–82, 2008

31. Pagano N.J., Schoeppner G.A., in Comprehensive Composite Materials vol.2, Elsevier, 433–528, 2000

32. Toscano C. and Lenzi F., Impact Behaviour of Damped Composites, Proceedings of 7th EUROMECH Solid Mechanics Conference (ESMC2009) Lisbon, Portugal, September 7-11, 635-636, 2009

33. http://ftp.rta.nato.int/public//PubFullText/RTO/MP/RTO-MP-069-II///MP-069(II)-(SM1)-19.pdf (Accessed on: April 10 ,2011)

34. Loos A. C. and Springer G. S., in Composite Materials, Quality Assurance and Processing, ed. C. E. Browning, ASTM STP 797, 110-118, 1983

35. Tang J.M., Lee W.I., Springer G.S., Effect of cure pressure on resin flow, voids and mechanical properties, J. Compos. Mater., 21, 421-440, 1987

36. Springer G. S., in Progress in Science and Engineering of Composites, ed. By T. Hayashi, K. Kawata and S. Umewaka, Japan Society of Composite Materials, 23-35, 1982

37. Loos A.C., Springer G.S., Curing of epoxy matrix composites, J. of Compos. Mater., 17, 135–169, 1982

38. Brown G.G., McKague E.L., Processing Science of Epoxy Resin Composites, Defense Technical Information Center, 1984

39. Liu L., Zhang B.M., Wang D.F., Wu Z.J., Effects of cure cycles on void content and mechanical properties of composite laminates, Compos. Struct., 73, 303–309, 2006

40. Boey F.Y.C., Lye S.W., Void reduction in autoclave processing of thermoset composites, Composites, 23, 4, 261–265, 1992

41. Greszczuk L.B., Effect of voids on strength properties of filamentary composites, Proceedings of the 22nd Annual Meeting of the Reinforced Plastics Division of The Society of the Plastics Industry, February 1-3, 20.A-1-20.A-10, 1967

42. Harper B.D., Staab G.H., Chen R.S., A note on the effects of voids upon the hygral and mechanical properties of AS4/3502 graphite/epoxy, J. of Compos. Mater., 21, 280-289, 1987

43. Olivier P., Cottu J.P., Ferret B., Effects of cure cycle pressure and voids on some mechanical properties of carbon/epoxy laminates, Composites , 26, 7, 509–515, 1995

44. Ghiorse S.R., Effect of void content on the mechanical properties of carbon/epoxy laminates, SAMPE QUARTERLY, 24, 2, 54–59, 1993

45. Bowles K.J., Frimpong S., Voids effects on the interlaminar shear strength of unidirectional graphite-fiber-reinforced composites, J. Comp. Mater., 26, 10, 1487–1509, 1992

46. Almeida S.F.M., Nogueira Z.S.N, Effects of void content on the strength of composite laminates, Comp. Struct., 28, 139–148, 1994

47. Hsu D. K. and Uhl K. M., in Review of Progress in Quantitative NDE, ed. D, O. Thompson & D. E. Chimenti, 6B, 1175-1184, Plenum Press, New York, 1986

48. Uhl K.M., Lucht B., Jeong H., Hsu D.K., in Review of Progress in QNDE, ed. D.O. Thompson and D.E. Chimenti, 7B, 1075-1082, Plenum Press, New York, 1988

49. Suarez J.C., Molleda F., Güemes A., Void content in carbon fiber/epoxy resin composites and its effects on compressive properties, Proceedings of the 9th International Conference on composite materials ICCM-9, VI, 589–596, 1993

50. Moore P.O., and McIntire P., Non destructive testing Handbook, vol.10, American Society for Nondestructive Testing, Columbus, Ohio, 1996

51. Kline, R.A., Nondestructive Characterization of Composite Media, Technomic, Lancaster, PA, 1992

52. Amaro A., Santos J., Cirne J., Comparative study of different non-destructive testing techniques in the characterization and quantification of the damage effects in carbon-epoxy laminates, Insight, 46, 559-65, 2004

53. Fletcher E.M., Process for fluorescence detection of extremely small flaws, US 33869201(1968)

54. ASTM E1417/E1417M - 11e1 Standard Practice for Liquid Penetrant Testing

55. http://2.imimg.com/data2/IS/KQ/MY-4267746/liquid-penetrant-dye-penetrant-testing-dpt-250x250.jpg (Accessed on March, 2013)

56. ASTM E709 - 08 Standard Guide for Magnetic Particle Testing

57. http://www.ndt-ed.org/GeneralResources/MethodSummary/MT1.jpg (Accessed on March 2013)

58. Engmin J.C ., Eddy current surface mapping system for flaw detection, US4755753 (1988)

59. ASTM E426 - 12 Standard Practice for Electromagnetic (Eddy-Current) Examination of Seamless and Welded Tubular Products, Titanium, Austenitic Stainless Steel and Similar Alloys

60. http://www.cnde.iastate.edu/faacasr/engineers/Supporting%20Info/Supporting%20Info%20Pages/Eddy%20Pages/Eddyprinciples_files/pic_02.jpg (Accessed on March 2013)

61. Ktrautkrämer J. and Ktrautkrämer H., Ultrasonic Testing of Materials, 4th ed., Springer-Verlag, Heidelberg DE, 1990

62. ASTM E2580-07 Standard Practice for Ultrasonic Testing of Flat Panel Composites and Sandwich Core Materials Used in Aerospace Applications

63. http://www.cnde.iastate.edu/faacasr/engineers/Supporting%20Info/Supporting%20Info%20Pages/Ultrasonic%20Pages/Ultraprinciples_files/ultra_graph_01.jpg (Accessed on March 2013)

64. Sokolov S.Y., Ultrasonic methods of detecting internal flaws in metal articles, Zavodskaya Laoratoriya, 4, 1468-1473, 1935

65. Meola C. and Toscano C., NonDestructive Evaluation of Carbon Fiber Reinforced Polymers with Ultrasonics and Infrared Thermography: an Overview on Historical Steps and Patents, (invited review) Recent Patents on Materials Science, 5, 1, 48-67, 2012

66. ASTM E2580 - 12 Standard Practice for Ultrasonic Testing of Flat Panel Composites and Sandwich Core Materials Used in Aerospace Applications

67. Tapphorn R.M., Spencer P., Beeson H.D., Kirsch M., in Nondestructive Testing and Evaluation, Milton Park (UK) Taylor & Francis, 11, 139-147, 1994

68. Lingenferter D.E., A Radiation gauge for determining weight percentage of the constituent graphite-epoxy composite materials, US466867, 1987

69. Marshall T.G., Hurmuzlu Y., Detection and Quantification of Fiber Waviness in Thick Section Composite Components, Proceedings of AHS 55th International Annual Forum, May 25-27, 1, 818-24, 1999

70. http://www.phoenixxray.com/images/principles_of_operation/tomography_e.jpg (Accessed on March 2013)

71. Henini M. and Razeghi M., Handbook of Infra-red detection technologies, Elsevier, 2002

72. Maldague X., Theory and Practice of Infrared Technology for Nondestructive Testing, John Wiley & Sons, 2001

73. Meola C., in Infrared Thermography: Recent Advances and Future Trends, Bentham Science Publishers, 253, 2012

74. Vavilov V., Thermal nondestructive testing: short history and state-of-art, Proceedings of QIRT92; ed. D. Balageas, G. Busse and G.M. Carlomagno; EETI editions Paris, France; 179-193, 1992

75. Parker R.D., Thermic balance of radiometer, US1099199 (1914)

76. http://www.movimed.com/images/Solutions/thermography/lufthansa_plane.jpg (Accessed on Marc 2013)

77. ASTM E2581-07: Standard Practice for Shearography of Polymer Matrix Composites, Sandwich Core Materials and Filament-Wound Pressure Vessels in Aerospace Applications

78. Hung Y.Y., Shearography: A new optical Method for Strain Measurement and Non-destructive Testing, Opt. Engin. 21, 3, 391-395, 1982

79. Hung Y.Y., in Trends in Optical Non-destructive Testing and Inspection, ed. Pramond K. Rastogi and Daniele Inaudi, Elsevier, 287-308, 2000

80. http://www.sciencedirect.com/science/article/pii/S0263822300001094 (Accessed on March 2013)

81. Yang L., Recent Developments in Digital Shearography for Nondestructive Testing, Mater. Eval., 64, 7, 704-709, 2006

82. ASTM E2581-07: Standard Practice for Shearography of Polymer Matrix Composites, Sandwich Core Materials and Filament-Wound Pressure Vessels in Aerospace Applications

83. ASTM E2533-09: Standard Guide for Nondestructive Testing of Polymer Matrix Composites Used in Aerospace Applications

84. Stone D.E.W. and Clarke B., Ultrasonic attenuation as a measure of void content in carbon-fiber reinforced plastics, Non-Destr. Test., 8, 137-145, 1975

85. Daniel I.M., Wooh S.C., Komsky I., Quantitative porosity characterization of composite materials by means of ultrasonic attenuation measurements, J. Nondestr. Eval, 11, 1-8, 1992

86. Nair S.M., Hsu D.K., Rose J.H., Porosity estimation using the frequency dependence of the ultrasonic attenuation, J. Nondestr. Eval., 8, 13-26, 1989

87. Hsu D.K., Ultrasonic Nondestructive Evaluation of Void Content in CFRP, Proceedings of the 46th Annual Technical Conference (ANTEC), 1273-1275, 1988

88. Steiner K.V., in Damage Detection in Composite Materials, STP 1128, ed. John E. Masters, Philadelphia, PA: American Society for Testing and Materials (ASTM), 72-84, 1992

89. Karabuto A.A., Murashov V.V., Podymova N.B., Oraevsky A.A., Nondestructive Characterization of Layered Composite Materials with a Laser Optoacoustic Sensor, Proceedings of the SPIE, 3396, 103-111, 1998

90. Toscano C., Vitiello C., Caramuta P., Study of The Porosity Occurrence in Composite Materials by Means of Ultrasonic and In-Plane Shear Testing, Proceedings of 5th International Conference on Times of Polymers (TOP) & Composites, 76-78, 2010

91. Steiner K.V., Krieger K., Mehl J.B., Caron J.N., Yang Y., Infrared Thermography and Laser-Based Ultrasonic Methods for On-Line Porosity Sensing During Thermoplastic Composite Fabrication, Proceedings of the 2nd Conference on NDE Applied to Process Control of Composite Fabrication, NTIAC,115-122, 1996

92. Grinzato E.G., Marinetti S., Bison P.G., NDE of Porosity in CRFP by Multiple Thermographic Techniques, Proceedings of SPIE, 4710, Thermosense XXIV, 588-598, 2002

93. Ciliberto A, Cavaccini G, Salvetti O., Chimenti M., Azzarelli L., Bison P.G., Marinetti S., Freda A., Grinzato E., Porosity Detection in Composite Aeronautical Structures, Infrared Physics & Technology, 43, 3-5, 139-143, 2002

94. Brit E.A., Smith R.A., A Review of NDE Methods For Porosity Measurement in Fiber-reinforced Polymer Composites, Insight, 46, 11, 681-686, 2004

95. http://ntrs.nasa.gov/archive/nasa/casi.ntrs.nasa.gov/20090014807_2009014230.pdf (Accessed on March 2012)

96. www.ville-ge.ch/culture/mhs (Accessed on May 2010)

97. Rayleigh J. W. S., The Theory of Sound, Macmillan, 1894

98. http://www.hearingaidmuseum.com/gallery/Miscellaneous/Hearing%20Testing%20Equipment/info/galtonwhistle.htm (Accessed on September 2012)

99. Curie J. and Curie P. C. R., Développement, par pression, de l'électricité polaire dans les cristaux hémièdres à faces inclines, Acad. Sci. Paris, 91, 294-295, 1880

100. Lippmann G., Principe de conservation de l'électricité, Ann. Chim. Phy. 24, 145-178, 1881

101. Richardson M.L.F., Apparatus for warning a ship of its approach to large objects in a fog, Br. Pat. No. 9423 (1912)

102. Chilowsky C.M. and Langévin. M.P. Procídés et appareil pour production de signaux sous-marins dirigés et pour la localsation à distances d'obstacles sons-marins, French patent no. 502913 (1916)

103. Pohlman R., Possibility of an Acoustical Image Analogous to Optics, Z. Tech. Phys. 113, 697-709, 1939

104. Firestone F.J., The Supersonic Reflectoscope, an Instrument for Inspecting the Interior of Solid Parts by Means of Sound Waves, Acoust. Soc. Am., 17, 287-299, 1946

105. http://www.ob-ultrasound.net (Accessed on March 2010)

106. http://www.library.uiuc.edu/archives/archon/index.php?p=collections/controlcardandid=4662 (Accessed on March 2010)

107. Dussik K.T., On the possibility of using ultrasound waves as a diagnostic aid, Neurol. Psychiat., 174, 153-168, 1942

108. Ludwig G.D. and Struthers F.W., Naval Medical Research Institute Reports, Project #004 001, Report No. 4, June 1949

109. McNay M.B. and Fleming J.E.E., Forty years of obstetric ultrasound 1957-1997: From a-scope to three dimensions, Ultrasound in Med. & Biol., 25, 1, 3–56, 1999

110. Auld B.A., Acoustic Fields and Waves in Solids. Wiley, New York, 1973

111. Lamb H., On Waves in an Elastic Plate, Proc. Roy. Soc. London, Ser. A 93, 114–128, 1917

112. Rose J.L., Ultrasonic Waves in Solid Media, Cambridge University Press, 1999

113. Setter N., in Piezoelectric Materials in Devices, ed. Nava Setter, Lausanne, Switzerland, p. 518, 2002

114. Manbachi A. and Cobbold R.S.C., Development and Application of Piezoelectric Materials for Ultrasound Generation and Detection, Ultrasound, 19, 4, 187–196, 2011

115. Von Hippel, A. Ferroelectricity, Domain structure, and phase transitions of barium titanate.Reviews of Modern Physics., 22, 221-237, 1950

116. Rase D.E., Roy R., Phase equilibria in the system Bao-Tio2, J. Amer. Ceram. Soc., 38,102-113, 1955

117. Jaffe B., Roth R. S, Marzullo S., Piezoelectric properties of Lead Zirconate-Lead Titanate solid-solution ceramics, J. Appl. Phys., 25, 809-810, 1954

118. Mattiat O.E., Ultrasonic Transducer Materials, Plenum Press, New York, US (1971)

119. Batzinger T.J., Li W., Gilmore R.S., Nieters E.J., Hatfield W.T., Klaassen R.E., et al. Phased array ultrasonic inspection method for industrial applications US6789427 (2004)

120. http://www.bercli.net/images/principles_phased_array.png (Accessed on March 2010)

121. Bond L.J., Absorption of ultrasonic waves in air at high frequencies (10 – 20 MHz), J. Acoust. Soc. Am., 92, 4, 2006-2045, 1992

122. Hampton L.E., A Non-contact ultrasonic testing method and device for ceramic honeycomb structures, US 0266789 (2007)

123. C. Toscano, in Recent Advances in Non Destructive Inspection (C. Meola Editor) Nova Science Publisher Inc., 2010

124. Jones B.R. and Stone D.E.W., Towards an ultrasonic-attenuation technique to measure void content in carbon-fibre composites, Non-Destructive Testing, 9, 2, 71-79, 1976

125. Ichikawa J., Abe M., Ultrasonic image processing apparatus, US7697779 (2010)

126. Smith R.A., Marriott A.B., Jones L.D., Delamination Sizing in Fibre-Reinforced Plastics using Pulse-Echo Amplitude, Insight, 39, 5, 330-336, 1997

127. Degriech J., Declercq N.F., Leroy O., Ultrasonic Polar Scans as a Possible Means of Nondestructive Testing and Characterization of Composite Plates, Insight, 45, 3, 196-201, 2003

128. Sarr D.P., Pulse echo/through transmission ultrasonic testing, US7823451 (2010)

129. Djordjevic B., Traugott B., Stephen C., Ultrasonic liquid jet probe, US 4507969 (1985)

130. Don J., Roth D., Carney V., Thickness-independent ultrasonic imaging applied to ceramic materials, NDTnet, 2, 10, 1997

131. Lorraine P.W., Filkins R.J., Dubois M., Drake Jr T.E., Deaton Jr, J.B., System and method of determining porosity in composite materials using ultrasounds, US6684701 (2004)

132. Papadakis E.P., Ultrasonic Attenuation Caused by Scattering in Polycrystalline Metals, J. Acoust. Soc. Am., 37, 711-717, 1965

133. Meola C., Origin and theory of infrared thermography (Chap.1 in: Infrared Thermography: Recent Advances and Future Trends (ed. C. Meola), Bentham Science Publishers, p. 3-28, 2012

134. Vavilov V., Thermal nondestructive testing: short history and state-of-art, Proc. QIRT92; Ed. D. Balageas, G. Busse and G.M. Carlomagno, EETI Editions Paris, France, 179-193, 1992

135. Parker R.D., Thermic balance of radiometer, Patent US1099199 (1914)

136. Barker G.A., Apparatus for detecting forest fires, Patent US1959702 (1934)

137. Nichols G.T., Temperature measuring, Patent US2008793 (1935)

138. Rinaldi R., Infrared Devices: Short History and New Trends (chap.2) in: Infrared Thermography: Recent Advances and Future Trends, (C. Meola Editor), Bentham Science Publishers, p. 29-59, 2012

139. Beller W.S., Navy sees promise in infrared thermography for solid case checking, Missiles and Rochets,16-22, 1965

140. Green D.R., Principles and applications of emittance-independent infrared non-destructive testing, Appl. Opt., 7, 9, 1779-86, 1968

141. Carslaw H.S., Jaeger J.C., Conduction of Heat in Solids, Clarendon Press, Oxford, UK, 1959

142. ASTM E2582-07: Standard Practice for Infrared Flash Thermography of Composite Panels and Repair Patches Used in Aerospace Applications, 2007

143. Walter G., Quantum Mechanics: An Introduction, Springer, 2001

144. www.theses.ulaval.ca/2005/23016/23016.pdf (Accessed on July 2013)

145. Planck M., The Theory of Heat Radiation, in The History of Modern Physics 1800-1950, 11, American Institute of Physics, Tomash Publishers, N. Y., 1988

146. http://www.ee.iitb.ac.in/~esgroup/es_mtech04_sem/es_sem04_paper_04307417.pdf (Accessed on October 2012)

147. Soloman S., Sensors Handbook, McGraw Hill Professionals, 1998

148. Kreisler A.J. and Gaugue A., Recent progress in high-temperature superconductor bolometric detectors: from the mid-infrared to the far-infrared (THz) range, Supercond. Sci. Technol. 13, 1235-1245, 2000

149. Wachter E.A., Thundat T., Oden P.I., Warmack R.J., Datskos P.G., Sharp S.L., Remote optical detection using microcantilevers, Rev. Sci. Instrum., 67, 10, 3434–3439, 1996

150. Rogalski A., Piotrowski J., Intrinsic infrared detectors, Progress in Quantum Electronics 12, 87-289, 1988

151. Rose A., Concepts in photoconductivity and allied problems, Interscience, New York, 1963

152. Rogalski A., HgCdTe infrared detector material: history, status and outlook, Reports on Progress in Physics, 68, 2267 – 2336, 2005

153. Haegel N.M., Schwartz W.R., Zinter J., White A.M., Beeman J.W., Origin of the Hook Effect in Extrinsic Photoconductor, Appl. Opt., 34, 5748–54, 2001

154. Gunapala S.D., Bandara S.V., Liu J.K., Hill C.J., Rafol S.B. et alt., 1024 x 1024 Pixel mid-wavelength and long-wavelength infrared QWIP focal plane arrays for imaging applications, Semicond. Sci. Technol., 20, 473-480, 2005

155. Tribolet P., Destefanis G., Third generation and multicolor IRFPA developments: a unique approach based on DEFIR, Proc. SPIE, 5783, 37-53, 2005

156. Norton P.R., Campbell J.B. III, Horn S.B.; Reago D.A., Third-generation infrared imagers, Proc. SPIE, 4130, 226-236, 2000

157. Meola C., in Recent Advances in Non-Destructive Inspection, 89-123, ed. C. Meola, Nova Science Publishers Inc., 2010

158. Kaplan H., Zayicek P.A., Application of differential infrared thermography in power generation facilities, SPIE Proceedings 2473, 67-74, 1995

159. Hurley T.L., in Infrared Methodology and Technology, ed. X.P.V. Maldague, Gordon and Breach, New York, 265-317, 1994

160. Johnson R.B., Feng C., Fehrinbach J.D., On the validity and techniques of temperature and emissivity measurements, SPIE Proceedings 2934, 202-206, 1988

161. Weil G., Computer aided infrared analysis of bridge deck delaminations, Proceeding 5th Infrared Information Exchange, 1, 85-93, 1985

162. Cielo P., Pulsed photothermal evaluation of layered materials, J. Applied Physics, 56, 230-236, 1984

163. Cielo P., Maldague X., Déom A.A., Lewak R., Advances in signal processing for non destructive evaluation of materials, Materials Evaluation, 45, 452-460, 1987

164. Maldague X., Non destructive evaluation of materials by infrared thermography Springer Verlag, London, 1993

165. Aamodt L.C., Maclachlan Spice, J.W., Murphy J.C., Analysis of characteristic transit time for time-resolved infrared radiometry studies of multilayered coatings, J. Appl. Phys., 68, 6087-6098, 1990

166. Maclachlan-Spicer J.W., Kerns W.D., Aamondt L.C., Murphy J.C., Time Resolved infrared radiometry (TRIR) of multilayer organic coatings using surface and subsurface heating, Proceeding SPIE, 1467, 311-321, 1991

167. Carlomagno G.M. and Berardi P.G., Unsteady thermotopography in non-destructive testing, Proceedings of the III Infrared Information Exchange (St Louis), 33–40, 1976

168. Beaudoin J.L., Merienne E., Danjoux R., Egee M., Numerical system for infrared scanners and application to the subsurface control of materials by photo thermal radiometry Infrared Technology and Applications, Proc. SPIE, 590, 287–292, 1985

169. Kuo P.K., Feng Z.J., Ahmed T., Favro L.D., Thomas R.L., Hartikainen J., in Photoacoustic and Photothermal Phenomena, ed P. Hess and J. Pelzl, Springer, Heidelberg, 415–418, 1988

170. Busse G., Wu D., Karpen W., Thermal wave imaging with phase sensitive modulated thermography, J. Appl. Phys., 71, 3962–3965, 1992

171. Balageas D. L., Lévesque P., Déom A., Characterization of electromagnetic fields using a lock-in infrared thermographic system, Proc. SPIE, 1933, 274-285, 1993

172. http://w3.gel.ulaval.ca/~maldagx/r_1086.pdf (Accessed on October 2012)

173. Vavilov V. P., Marinetti S., Pulsed Phase Thermography and Fourier analysis thermal tomography, Russian Journal of Nondestructive Testing, 35, 2, 134-145, 1999

174. Carlomagno G.M., Meola C., Comparison between Thermographic Techniques for Frescoes NDT, NDT&E International, 35, 559-565, 2002

175. Tenek L.H., Henneke E.G. II, Gunzburger M.D., Vibration of delaminated composite plates and some application to non destructive testing, Compos. Struct., 23, 3, 253-262, 1993

176. Cattaneo C., A form of heat conduction equation which eliminates the paradox of instantaneous propagation, Comptes Rendues, 247, 431-433, 1958

177. Grad H., On the kinetic theory of rarefied gases, Commun. Pure Appl. Math., 2, 4, 331–407, 1949

178. Ali A. H., Statistical mechanical derivation of Cattaneo's heat flux law, J. Thermophys. Heat Trans., 13, 4, 544–546, 1999

179. Greffet J., in Topics in Applied Physics, edited by Voz S., Springer, Paris, 1-13, 2007

180. Marín E., On the role of photothermal techniques for the thermal characterization of nanofluids, Internet Electron. J. Nanoc. Moletrón., 5, 2, 1007-1014, 2007

181. Maldague X.P., Theory and Practice of Infrared Technology for Nondestructive Testing, John Wiley & Sons, N. Y., 2001

182. Grinzato E., Bison P.G., Bressan C., Mazzoldi A., NDE of frescoes by infrared thermography and lateral heating, Proceedings Qirt 98, Septemer 7-10, Lodz, Poland, 64-70, 1998

183. Meola C., Carlomagno, G.M., Di Foggia M., Natale O., Infrared Thermography to Detect Residual Ceramic in Gas Turbine Blades, Applied Physics A, 91, 685-691, 2008

184. Heath D.M., Winfree W.P., in Review of Progress in Quantitative Non Destructive Evaluation, Thompson D.O., Chimenti D.E., eds., 8B, 16131619, 1989

185. Connolly M. P., The Measurement of Porosity in Composite Materials using Infrared Thermography, J. Reinf. Plast. Compos., 2, 1367-1375, 1992

186. Zalameda J.N., Winfree W.P., in Review of Progress in Quantitative Non-Destructive Evaluation Proceeding, Thompson D.O., and Chimenti D.E. eds., 9, 1541-1548, 1990

187. Grinzato E., Marinetti S., Bison P.G., NDE of porosity in CFRP by multiple thermographic techniques, Thermosense XXIV Proceeding, vol.4710 (Maldague X.P.V., Rozlosnik A.E. eds.), 588-598, 2002

188. Ringermacher H.I., Howard D.R., Gilmore R.S., in Review of Progress in Quantitative Non-Destructive Evaluation Proceeding, Thompson D.O., Chimenti D.E. eds., 21, 528-535, 2002

189. Mayr, G., Hendorfer, G., Plank, B. and Sekelja, J., Porosity Determination in CFRP Specimens by Means of Pulsed Thermography Combined with Effective Thermal Diffusivity Models, 29th Review of Progress in Quantitative Non-Destructive Evaluation Proceeding, Kingston (USA), (Thompson D.O., Chimenti D.E. eds.), 1103-1110, 2010

190. Parker W.J., Jenkins R. J., Butler C. P., Abbott G.L., Flash method for determination of thermal diffusivity, heat capacity and thermal conductivity, J. Appl. Phys., 32, 9, 1679-1684, 1961

191. Rosencwaig A., Busse G., High-resolution photoacoustic thermal-wave microscopy, Appl. Phys. Lett., 36, 725-727, 1980

192. Thomas R.L., Pouch J.J., Wong Y.H., Favro L.D., Kuo P.K., Rosencwaig A., Subsurface flaw detection in metals by photoacoustic microscopy, J. Appl. Phys. 51, 1152–1156, 1980

193. Busse G. Optoacoustic phase angle measurement for probing a metal, Appl. Phys. Lett., 35, 759–760, 1979

194. Letho A., Jaarinen J., Tiusanen T., Jokinen M. Luukkala M., Magnitude and phase in thermal wave imaging, Electron. Lett., 17, 364–365, 1982

195. Bai W., Wong B.S., Evaluation of Defects in Composite Plates under Convective Environments using Lock-In Thermography, Meas. Sci. Technol. 12, 142-150, 2001

196. Meola C., Carlomagno G.M., Squillace A., Giorleo G., Nondestructive Control of Industrial Materials by Means of Lock-In Thermography, Meas. Sci. Technol., 13, 1583-1590, 2002

197. Giorleo G., Meola C., Squillace A., Analysis of Defective Carbon- Epoxy by Means of Lock-in Thermography, Res. Nondestr. Eval., 12, 241-250, 2000

198. Dillenz A., Zweschper T., Riegert G., Busse G., Progress in phase angle thermography, Rev. Sci. Instr., 74, 417-419, 2003

199. http://web.mit.edu/roylance/www/voids.pdf (Accessed on November 2012)

200. Lenoe E.M., The effect of voids on the mechanical properties of high modulus graphite fiber/ epoxy reinforced composites, AVSD-0170-70-RR, Avco corp. System division, Lowell, Mass., March 1970

201. Zalameda J. N., Measured through the thickness thermal diffusivity of carbon fiber reinforced composite materials, J. Compos. Technol. Res., 21, 98–102, 1999

202. Meola C., Carlomagno G. M., Giorleo L., Geometrical Limitations to Detection of Defects in Composites by Means of Infrared Thermography, J. Nondestruct. Eval., 23, 4, 125-132, 2004

203. Meola C., Grasso V., Toscano C., Carlomagno G. M., Nondestructive evaluation of fiber reinforced polymers with lockin thermography, accepted for oral presentation at the Society for Experimental Mechanics (SEM) Conference, Chicago, June 3-6, 2013